

**Heme Protein Engineering and Mechanistic Investigations**

**by**

**Matthew W. Wolf**

**A dissertation submitted in partial fulfillment  
of the requirements for the degree of  
Doctor of Philosophy  
(Chemistry)  
in the University of Michigan  
2018**

**Doctoral Committee:**

**Professor Nicolai Lehnert, Chair  
Professor Vincent L. Pecoraro  
Professor Stephen W. Ragsdale  
Associate Professor Nathaniel Szymczak**

Matthew W. Wolf

[mwwolf@umich.edu](mailto:mwwolf@umich.edu)

ORCID iD: [0000-0002-2231-1438](https://orcid.org/0000-0002-2231-1438)

© Matthew W. Wolf 2018

To my parents:  
Michael and Margaret Wolf

## **Acknowledgements**

Lehnert Group colleagues and friends, thank you for all your support and help over the years. You've always been there to talk about research, brighten my day, and laugh with.

Nicolai, your guidance and support has meant a lot to me over these six years. Thank you for always believing in me when I was low and thank you for your mentorship that has made me a better scientist and person.

Nancy, your encouragement and love have pushed me through the good times and the bad these past few years. I am so lucky and happy to have you in my life, I don't think I would have made it through without you.

I have several collaborators to thank and acknowledge. To Dr. Sean Elliott and Kim Rizzolo, thank you for continually expressing protein and being a part of a collaboration that became a large part of my thesis.

Dr. Sangchoul Im and Dr. Lucy Waskell, thank you for being patient with me and teaching me about protein expression and for being a part of the MCubed MCD study.

Dr. Stephen Ragsdale and members of the Ragsdale group, thank you for letting me use your glovebox, and for preparing excellent and interesting MCD samples for me to run.

Dr. Takashi Matsuo and the Matsuo group, thank you for welcoming me to your laboratory, doing everything you could to help me with my research, and for showing me a wonderful time in Japan.

Szymczak group members including Jacob Geri, Eric Dahl, and Grayson Ritch, thank you for helping me with my experiments and for being patient with my lack of NMR knowledge.

The Chemistry department staff, for all your assistance with instrumentation, fixing equipment, and your help with all the problems I ran into over the years.

## Table of Contents

|  |             |
|--|-------------|
| <b>Dedication</b> .....  | <b>ii</b>   |
| <b>Acknowledgements</b> .....  | <b>iii</b>  |
| <b>List of Tables</b> .....  | <b>vii</b>  |
| <b>List of Figures</b> .....   | <b>viii</b> |
| <b>List of Schemes</b> .....   | <b>xv</b>   |
| <b>Abstract</b> .....  | <b>xvi</b>  |
| <br>   |             |
| <b>Chapter 1: Introduction</b> .....   | <b>1</b>    |
| 1.1 Transition Metal Catalysis .....   | <b>1</b>    |
| 1.2 Approaches to Designing Artificial Enzymes .....                                   | <b>3</b>    |
| 1.3 Heme Proteins and Carbene Transfer Catalysis .....                                 | <b>11</b>   |
| 1.4 Scope of Thesis .....  | <b>14</b>   |
| 1.5 References .....   | <b>16</b>   |
| <br>   |             |
| <b>Chapter 2: Engineering Ruthenium Myoglobin for Carbene Transfer Reactions</b> ..... | <b>25</b>   |
| 2.1 Preparation of RuMpIX(X) .....   | <b>26</b>   |
| 2.2 Protein Preparation and Analysis .....   | <b>28</b>   |
| 2.3 Reactivity of Free Ru <sup>II</sup> MpIX .....                                     | <b>30</b>   |
| 2.4 N-H Insertion with RuMb and Mutants .....  | <b>32</b>   |
| 2.5 Cyclopropanation with RuMb and Mutants .....                                       | <b>34</b>   |
| 2.6 Substrate Scopes .....   | <b>37</b>   |
| 2.7 Stability of RuMb .....  | <b>41</b>   |
| 2.8 Experimental Section .....   | <b>53</b>   |
| 2.9 References .....   | <b>59</b>   |

|   |            |
|---|------------|
| <b>Chapter 3: Catalyst Lifetimes of Modified Myoglobins and Ligand Addition to H93G Myoglobin</b> .....   | <b>62</b>  |
| 3.1 Determining Fe and Ru Catalyst Lifetimes and Reaction Rates for the Cyclopropanation of Styrene ..... | <b>64</b>  |
| 3.2 Determining Fe and Ru Catalyst Lifetimes and Reaction Rates for the N-H Insertion of Aniline .....    | <b>72</b>  |
| 3.3 FeH93GMb and RuH93GMb Preparation and Characterization .....  | <b>79</b>  |
| 3.4 Cyclopropanation of Styrene Using RuH93GMb with the Addition of Various Exogenous Ligands .....       | <b>87</b>  |
| 3.5 Experimental Section .....  | <b>91</b>  |
| 3.6 References .....  | <b>96</b>  |
| <br>  |            |
| <b>Chapter 4: Spectroscopic Investigation of Diheme Cytochrome <i>c</i> Peroxidases</b> .....             | <b>99</b>  |
| 4.1 MCD Benchmark Studies .....   | <b>102</b> |
| 4.2 EPR Spectra of <i>NeCcP</i> .....   | <b>104</b> |
| 4.3 Resonance Raman Spectra of <i>NeCcP</i> .....   | <b>106</b> |
| 4.4 Magnetic Circular Dichroism of <i>NeCcP</i> .....   | <b>114</b> |
| 4.5 EPR Spectra of <i>SoCcP</i> .....   | <b>116</b> |
| 4.6 Resonance Raman Spectra of <i>SoCcP</i> .....   | <b>118</b> |
| 4.7 Magnetic Circular Dichroism of <i>SoCcP</i> .....   | <b>124</b> |
| 4.8 Diferric <i>NeCcP</i> and <i>SoCcP</i> .....  | <b>126</b> |
| 4.9 Semi-reduced <i>NeCcP</i> and <i>SoCcP</i> .....  | <b>130</b> |
| 4.10 Mechanistic Implications .....   | <b>134</b> |
| 4.11 Experimental Section .....   | <b>137</b> |
| 4.12 References .....   | <b>140</b> |
| <br>  |            |
| <b>Chapter 5: Conclusions and Future Work</b> .....   | <b>144</b> |
| 5.1 Conclusions .....   | <b>144</b> |
| 5.2 Future Work .....   | <b>150</b> |
| 5.3 References .....  | <b>154</b> |

## List of Tables

|   |            |
|---|------------|
| <b>Table 2.1</b> Catalytic activity of RuMpIX, wild-type sperm whale ruthenium myoglobin (RuMb), and the Mb mutants in the N-H insertion reaction with aniline and EDA. ....    | <b>34</b>  |
| <b>Table 2.2</b> Catalytic activity of RuMpIX, wild-type horse heart ruthenium myoglobin (RuMb), and the Mb mutants in the cyclopropanation reaction with styrene and EDA. .... | <b>37</b>  |
| <b>Table 2.3</b> Substrate scope for N-H insertion reaction catalyzed by RuH64AMb. ....   | <b>39</b>  |
| <b>Table 2.4</b> Substrate scope for cyclopropanation catalyzed by RuH64AMb. ....   | <b>40</b>  |
| <b>Table 3.1</b> Catalytic lifetime activity of Fe and Ru catalysts for the cyclopropanation of styrene. ....   | <b>64</b>  |
| <b>Table 3.2</b> Catalytic lifetime activity of Fe and Ru catalysts for the N-H insertion of aniline. ....  | <b>73</b>  |
| <b>Table 3.3</b> Catalytic activity of RuH93G with various ligands added. ....  | <b>88</b>  |
| <b>Table 3.4</b> Catalytic activity of FeH93G with various ligands added. ....  | <b>89</b>  |
| <b>Table 4.1</b> Organisms that belong to distinct CcP classes. ....  | <b>101</b> |



## List of Figures

- Figure 1.1** Several examples of transition metal catalysts used in the chemical industry. Wilkinson's catalyst effectively hydrogenates olefins and alkenes, Grubb's catalyst facilitates olefin metathesis, and several catalysts such as the rhodium catalyst shown above, are available for hydroformylation, an important process for the production of aldehydes. ....2
- Figure 1.2** a) Model structure of the Cu(I/II)(TRIL23H)<sub>3</sub> peptide that is a functional model for nitrite reductase. b) Top-down proposed structure of the TRI-EHK24E with Cu bound. In this structure, Glu22 H-bonds with His23, changing the redox potential of the metal center. Adapted from refs [40] and [49]. ....5
- Figure 1.3** Cartoon depicting the expression of periplasmic streptavidin (SAV) and subsequent incorporation of a biotin-modified Hoyveda-Grubbs catalyst that can catalyze intramolecular olefin metathesis. Adapted from ref [37]. ....7
- Figure 1.4** The cyclopropanation of olefins is catalyzed by a modified P450BM3. The enzyme active site is depicted on the right with key mutated residues highlighted. The axial ligand has been mutated from a cysteine to a serine, and the green mesh shows the electron density around the heme. Adapted from ref [67]. ....10
- Figure 1.5.** A pymol model of the active site of sperm whale myoglobin highlighting some of the important residues near the heme site that can influence abiological activity. ....14
- Figure 2.1.** a) Electronic Absorption spectra of free Mesoporphyrin IX Dimethyl Ester (MpIX DME) and Ruthenium Mesoporphyrin IX Dimethyl Ester Carbonyl ([Ru<sup>II</sup>MpIXDME(CO)]), obtained after metalation with Ru<sub>3</sub>(CO)<sub>12</sub>. b) Electronic Absorption spectra of Ruthenium Mesoporphyrin IX Dimethyl Ester ([Ru<sup>II</sup>MpIXDME]) in DMF after photolysis of CO by irradiation with ~350 nm light *in vacuo*. ....27
- Figure 2.2.** IR spectra of the KBr pellets of [Ru<sup>II</sup>MpIXDME(CO)] and [Ru<sup>II</sup>MpIXDME] obtained after photolysis of the CO complex. ....28

**Figure 2.3.** Close-up of the heme cofactor environment in wild-type sperm whale Mb (image generated using PDB file 1MBO). The His64 residue is in close proximity to the heme, and mutating this residue can greatly impact the function and catalytic properties of the protein. Several other nearby residues are highlighted in yellow. ....28

**Figure 2.4.** Electronic absorption spectra comparing free [RuMpIX(X)] to the reconstituted Mb variants (a-d). UV-vis spectrum of Ru<sup>II</sup>Mb after reduction with excess Na<sub>2</sub>S<sub>2</sub>O<sub>4</sub> (e). Spectral comparison of the CO-bound complex [Ru<sup>II</sup>MpIX(CO)] and Ru<sup>II</sup>Mb with CO bound (f). .....29

**Figure 2.5.** Circular dichroism spectra of the Mb variants (wild-type, H64A, H64D, H64V) with native heme bound, in the apo-form, and reconstituted with [Ru<sup>III</sup>MpIX(X)]. . ....30

**Figure 2.6.** Electronic absorption spectra of a) 5 μM native sperm whale myoglobin after adding 5000 equivalents of Na<sub>2</sub>S<sub>2</sub>O<sub>4</sub> and 2000 equivalents of ethyl diazoacetate and b) 5 μM RuMb under the same conditions. ....41

**Figure 2.7.** Electronic absorption spectra of 5 μM RuMpIX(X) after adding 5000 equivalents of Na<sub>2</sub>S<sub>2</sub>O<sub>4</sub> and 2000 equivalents of ethyl diazoacetate. ....42

**Figure 2.8.** Mass spectra of a) horse heart Mb, b) horse heart Mb after adding 500 equiv. reductant, 1000 equiv. styrene, and 2000 equiv. EDA, c) RuMb, d) RuMb after adding 500 equiv. reductant, 1000 equiv. styrene, and 2000 equiv. EDA. ....43

**Figure 2.9.** a) Electronic absorption spectra of Ru<sup>II</sup>Mb in 100 mM KPi buffer at different pH values. b) Circular dichroism of Ru<sup>III</sup>Mb at different pH values. ....44

**Figure 2.10.** Electronic Absorption spectra of [Ru<sup>II</sup>MpIX] at different pH values. ....45

**Figure 3.1.** Time course of the cyclopropanation of styrene catalyzed by FePpIX. The catalyst was prepared at a 10 μM concentration and reduced with 500 equiv. of Na<sub>2</sub>S<sub>2</sub>O<sub>4</sub> before adding 1000 equiv. of styrene and 2000 equiv. of EDA. 450 μL aliquots were taken at the following time points: 0.5, 1, 1.5, 2, 5, 10, 30, 60, 120, and 240 minutes. Organic products were extracted with 1 mL of ethyl acetate before quantifying the organic product by GC/MS. ....65

**Figure 3.2.** Time course of the cyclopropanation of styrene catalyzed by FeMb over 60 min. The catalyst was prepared at a 10  $\mu$ M concentration and reduced with 500 equiv. of  $\text{Na}_2\text{S}_2\text{O}_4$  before adding 1000 equiv. of styrene and 2000 equiv. of EDA. 450  $\mu$ L aliquots were taken at the following time points: 0.5, 1, 1.5, 2, 5, 10, 30, and 60 min. Organic products were extracted with 1 mL of ethyl acetate before quantifying the organic product by GC/MS. Reactions were run in triplicate. ....66

**Figure 3.3.** Time course of the cyclopropanation of styrene catalyzed by FeMb over 60 min. The catalyst was prepared at a 20  $\mu$ M concentration and reduced with 500 equiv. of  $\text{Na}_2\text{S}_2\text{O}_4$  before adding 1000 equiv. of styrene and 2000 equiv. of EDA. The reaction was worked up with the same methods used in the 10  $\mu$ M time course reaction. One data point was taken at each time point ..67

**Figure 3.4.** Time course of the cyclopropanation of styrene catalyzed by FeH64AMb over 60 min. The catalyst was prepared at a 10  $\mu$ M concentration and reduced with 500 equiv. of  $\text{Na}_2\text{S}_2\text{O}_4$  before adding 1000 equiv. of styrene and 2000 equiv. of EDA. 450  $\mu$ L aliquots were taken at the following time points: 0.5, 1, 1.5, 2, 5, 10, 30, and 60 min. Organic products were extracted with 1 mL of ethyl acetate before quantifying the organic product by GC/MS. Reactions were run in triplicate. ....68

**Figure 3.5.** Time course of the cyclopropanation of styrene catalyzed by FeH64AMb over 60 min. The catalyst was prepared at a 20  $\mu$ M concentration and reduced with 500 equiv. of  $\text{Na}_2\text{S}_2\text{O}_4$  before adding 1000 equiv. of styrene and 2000 equiv. of EDA. The reaction was worked up with the same methods used in the 10  $\mu$ M time course reaction. One data point was taken at each time point ..68

**Figure 3.6.** Time course of the cyclopropanation of styrene catalyzed by RuMpIX(X) over 240 min. The catalyst was prepared at a 10  $\mu$ M concentration and reduced with 500 equiv. of  $\text{Na}_2\text{S}_2\text{O}_4$  before adding 1000 equiv. of styrene and 2000 equiv. of EDA. 450  $\mu$ L aliquots were taken at the following time points: 0.5, 1, 1.5, 2, 5, 10, 30, 60, 120, and 240 minutes. Organic products were extracted with 1 mL of ethyl acetate before quantifying the organic product by GC/MS. ....69

**Figure 3.7.** Time course of the cyclopropanation of styrene catalyzed by 10  $\mu$ M RuMb over 60 min. Catalysts were reduced with 500 equiv. of  $\text{Na}_2\text{S}_2\text{O}_4$  before adding 1000 equiv. of styrene and 2000 equiv. of EDA. 450  $\mu$ L aliquots were taken at the following time points: 0.5, 1, 1.5, 2, 5, 10, 30, and 60 min. Organic products were extracted with 1 mL of ethyl acetate before quantifying the organic product by GC/MS. Reactions were run in triplicate. ....70

**Figure 3.8.** Time course of the cyclopropanation of styrene catalyzed by RuH64AMb over 60 min and. The catalyst was prepared at a 10  $\mu$ M concentration and reduced with 500 equiv. of Na<sub>2</sub>S<sub>2</sub>O<sub>4</sub> before adding 1000 equiv. of styrene and 2000 equiv. of EDA. 450  $\mu$ L aliquots were taken at the following time points: 0.5, 1, 1.5, 2, 5, 10, 30, and 60 minutes. Organic products were extracted with 1 mL of ethyl acetate before quantifying the organic product by GC/MS. ....71

**Figure 3.9.** Time course of the N-H insertion of aniline catalyzed by a) FePpIX, b) FeMb, and c) FeH64AMb over 240 min. The catalysts were prepared at a 10  $\mu$ M concentration and reduced with 500 equiv. of Na<sub>2</sub>S<sub>2</sub>O<sub>4</sub> before adding 1000 equiv. of aniline and 2000 equiv. of EDA. 450  $\mu$ L aliquots were taken at the following time points: 0.5, 1, 1.5, 2, 5, 10, 30, 60, 120, and 240 minutes. Organic products were extracted with 1 mL of ethyl acetate before quantifying the organic product by GC/MS. Red data points closer to the beginning of the reaction were collected on different days from the blue data points. ....75

**Figure 3.10.** Time course of the N-H insertion of aniline catalyzed by a) RuMpIX(X), b) RuMb, and c) RuH64AMb over 240 min. The catalysts were prepared at a 10  $\mu$ M concentration and reduced with 500 equiv. of Na<sub>2</sub>S<sub>2</sub>O<sub>4</sub> before adding 1000 equiv. of aniline and 2000 equiv. of EDA. 450  $\mu$ L aliquots were taken at the following time points: 0.5, 1, 1.5, 2, 5, 10, 30, 60, 120, and 240 minutes. Organic products were extracted with 1 mL of ethyl acetate before quantifying the organic product by GC/MS. Red data points closer to the beginning of the reaction were collected on different days from the blue data points. ....76

**Figure 3.11.** Electron absorption spectra of H93G Mb reconstituted with a) FePpIX and b) [RuMpIX(X)]. ....81

**Figure 3.12.** Circular dichroism spectra of the H93GMb with native heme bound, in the apo-form, and reconstituted with [RuMpIX(X)]. ....81

**Figure 3.13.** Mass spectra of a) FeH93GMb and b) RuH93GMb. ....81

**Figure 3.14.** Ligands added to FeH93GMb and RuH93GMb in order to improve catalytic activity. ....81

**Figure 3.15.** Electronic absorption spectra of Fe<sup>III</sup>H93GMb before and after the addition of excess exogenous ligands including a) imidazole, b) phenol, c) tris(hydroxymethyl)phosphine, d) cyclopentanethiol, e) thiophenol, and f) tetrafluorobenzenethiol. ....82

**Figure 3.16.** Electronic absorption spectra of Ru<sup>III</sup>H93GMb before and after the addition of excess exogenous ligands including a) imidazole, b) phenol, c) tris(hydroxymethyl)phosphine, d) cyclopentanethiol, e) thiophenol, and f) tetrafluorobenzenethiol. ....84

**Figure 3.17.** Electronic absorption spectra of Ru<sup>II</sup>H93GMb and Ru<sup>II</sup>H93GMb(CO) after the addition of excess exogenous ligands including a) CO, b) imidazole, c) phenol, d) tris(hydroxymethyl)phosphine, e) thiophenol, and f) tetrafluorobenzenethiol. ....86

**Figure 4.1.** Near-UV/visible-region MCD spectra of a) high-spin ferric horse heart myoglobin (10.6  $\mu$ M), b) low-spin ferric Cytochrome *c* (2.9  $\mu$ M) and c) low-spin ferrous Cytochrome *c* (2.3  $\mu$ M). Each sample was prepared with ~50% glycerol in TIP7 buffer at pH 7. Spectra were recorded at 2 K. ....102

**Figure 4.2.** EPR spectra of a) 420  $\mu$ M diferric *NeCcP*, b) 490  $\mu$ M semi-reduced *NeCcP*, c) 419  $\mu$ M diferric *NeH59G CcP*, and d) 460  $\mu$ M semi-reduced *NeH59G CcP*. Experiments were conducted at 9.27 GHz, a power of 20 mW, and a temperature of 12 K. ....104

**Figure 4.3.** Resonance Raman spectrum of diferric *NeCcP* from a) 200 to 1750  $\text{cm}^{-1}$ , and b) enlarged view of the 1200 to 1750  $\text{cm}^{-1}$  region. The sample was 105  $\mu$ M with 50% glycerol in pH 7 TIP7 buffer. The sample was excited at 413.1 nm using a Krypton ion gas laser at 77 K. ....106

**Figure 4.4.** Resonance Raman spectrum of semi-reduced *NeCcP* from a) 200 to 1750  $\text{cm}^{-1}$ , and b) enlarged view of the 1200 to 1750  $\text{cm}^{-1}$  region. The sample was 160  $\mu$ M with 50% glycerol in pH 7 TIP7 buffer. The sample was excited at 413.1 nm using a Krypton ion gas laser at 77 K. ....106

**Figure 4.5.** Resonance Raman spectrum diferric *NeH59G CcP* from a) 200 to 1750  $\text{cm}^{-1}$ , and b) enlarged view of the 1200 to 1750  $\text{cm}^{-1}$  region. The sample was 419  $\mu$ M with 30% glycerol in pH 7 TIP7 buffer. The sample was excited at 413.1 nm using a Krypton ion gas laser at 77 K. ....109

**Figure 4.6.** Power dependence resonance Raman spectra of diferric *NeH59G CcP* from a) 1150 to 1400  $\text{cm}^{-1}$ , and b) 1400 to 1750  $\text{cm}^{-1}$  and the power dependence spectra of semireduced *NeH59G CcP* from c) 1150 to 1400  $\text{cm}^{-1}$ , and d) 1400 to 1750  $\text{cm}^{-1}$ . The diferric sample was 419  $\mu$ M and the semireduced sample was 460  $\mu$ M both with 30% glycerol in pH 7 TIP7 buffer. The sample was excited at 413.1 nm using a Krypton ion gas laser at 77 K. ....110

**Figure 4.7.** Resonance Raman spectrum of semi-reduced *NeH59G CcP* from a) 200 to 1750  $\text{cm}^{-1}$ , and b) enlarged view of the 1200 to 1750  $\text{cm}^{-1}$  region. The sample was 460  $\mu\text{M}$  with 30% glycerol in pH 7 TIP7 buffer. The sample was excited at 413.1 nm using a Krypton ion gas laser at 77 K. ....111

**Figure 4.8.** Room temperature resonance Raman spectrum of a) diferric *NeCcP* and b) diferric *NeH59G CcP*. The samples were  $\sim 420 \mu\text{M}$  with 30% glycerol in pH 7 TIP7 buffer. The samples were rotated and excited at 413.1 nm using a Krypton ion gas laser. Plasma lines are indicated with an asterisk. ....113

**Figure 4.9.** a) Near-UV/visible-region MCD spectra of the diferric and semi-reduced states of *NeCcP*, and b) a close-up of the Q-band region of the spectra. Samples were 20  $\mu\text{M}$  with  $\sim 50\%$  glycerol in a TIP7 buffer at pH 7. Spectra were recorded at 2 K. ....114

**Figure 4.10.** a) Near-UV/visible-region MCD spectra of a semi-reduced *NeCcP* sample that was photolyzed with a mercury lamp, and after warming the sample to 70 K in the dark and then cooling the sample back to 2 K. The sample was 3.1  $\mu\text{M}$  with  $\sim 50\%$  glycerol in a TIP7 buffer at pH 7. Spectra were recorded at 2 K. ....114

**Figure 4.11.** Near-UV/visible-region MCD spectra of the diferric and semi-reduced states of *NeH59G CcP*. Samples were 2-2.6  $\mu\text{M}$  with  $\sim 50\%$  glycerol in a TIP7 buffer at pH 7. Spectra were recorded at 2 K at pH 7. Spectra were recorded at 2 K. ....114

**Figure 4.12.** EPR spectra of a) 330  $\mu\text{M}$  diferric *SoCcP*, b) 230  $\mu\text{M}$  semi-reduced *SoCcP*, c) 280  $\mu\text{M}$  diferric *SoH80G CcP*, and d) 340  $\mu\text{M}$  semi-reduced *SoH80G CcP*. Experiments were conducted at 9.27 GHz, a power of 20 mW, and a temperature of 12 K. ....116

**Figure 4.13.** Resonance Raman spectrum of diferric *SoCcP* from a) 200 to 1750  $\text{cm}^{-1}$  and b) enlarged view of the 1200 to 1750  $\text{cm}^{-1}$  region. The sample was 105  $\mu\text{M}$  with 50% glycerol in pH 7 TIP7 buffer. The sample was excited at 413.1 nm using a Krypton ion gas laser at 77 K. ....118

**Figure 4.14.** Resonance Raman spectrum of semi-reduced *SoCcP* from a) 200 to 1750  $\text{cm}^{-1}$  and b) enlarged view of the 1200 to 1750  $\text{cm}^{-1}$  region. The sample was 160  $\mu\text{M}$  with 50% glycerol in pH 7 TIP7 buffer. The sample was excited at 413.1 nm using a Krypton ion gas laser at 77 K. ....119

**Figure 4.15.** Resonance Raman spectrum of diferric *SoH80G CcP* from a) 200 to 1750  $\text{cm}^{-1}$ , and b) enlarged view of the 1200 to 1750  $\text{cm}^{-1}$  region. The sample was 280  $\mu\text{M}$  with 30% glycerol in pH 7 TIP7 buffer. The sample was excited at 413.1 nm using a Krypton ion gas laser at 77 K. ....122

**Figure 4.16.** Resonance Raman spectrum of semi-reduced *SoH80G CcP* from 1200 to 1750  $\text{cm}^{-1}$ . The sample was 280  $\mu\text{M}$  with 30% glycerol in pH 7 TIP7 buffer. The sample was excited at 413.1 nm using a Krypton ion gas laser at 77 K. ....122

**Figure 4.17.** Room temperature resonance Raman spectrum of a) diferric *SoCcP* and b) diferric *SoH80G CcP*. The samples were 280-330  $\mu\text{M}$  with 30% glycerol in pH 7 TIP7 buffer. The samples were rotated and excited at 413.1 nm using a Krypton ion gas laser. Plasma lines are indicated with an asterisk. ....123

**Figure 4.18.** a) Near-UV/visible-region MCD spectra of the diferric and semi-reduced states of *SoCcP* and b) a close-up of the visible region of the spectra. The sample was 20  $\mu\text{M}$  with ~50% glycerol in a TIP7 buffer at pH 7. Spectra were recorded at 2K. ....124

**Figure 4.19.** Near-UV/visible-region MCD spectra of a semi-reduced *SoCcP* sample that was photolyzed with a mercury lamp, and after warming the sample to 70 K in the dark and then cooling the sample back to 2 K. The sample was 2.0  $\mu\text{M}$  with ~50% glycerol in a TIP7 buffer at pH 7. Spectra were recorded at 2 K. ....124

**Figure 4.20.** Near-UV/visible-region MCD spectra of the diferric and semi-reduced states of *SoH80G CcP*. The samples were 1.2-1.4  $\mu\text{M}$  with ~50% glycerol in a TIP7 buffer at pH 7. Spectra were recorded at 2K. ....124

**Figure 5.1.** a) The product of *N*-alkylation of mesoporphyrin IX by  $\text{Ru}^{\text{II}}=\text{CHCOOEt}$  and loss of  $\text{Ru}^{\text{II}}$ , and b) the product of C-H insertion into the *meso* carbon of mesoporphyrin IX. ....151

**Figure 5.2.** Several different carbene precursors with acceptor and/or donor groups that could be added to RuMb. ....153

## List of Schemes

- Scheme 1.1** A depiction of metallocarbene formation and carbene transfer to an olefin to form cyclopropane products. A simple porphine molecule is used to represent a metalloporphyrin complex.....**12**
- Scheme 2.1** Putative mechanism for the N-H insertion of aniline and the cyclopropanation of styrene with ethyl diazoacetate catalyzed by a Ru(II) porphyrin with CO bound.....**32**
- Scheme 4.1** Proposed reaction mechanisms for Constitutively Active and Activatable bCcPs (Modified from refs [19] and [20]). .....**101**
- Scheme 4.2** Possible mechanism for a reductively activated bCcP enzyme. The L-heme remains low-spin in each step of the mechanism prior to substrate release. EPR results suggest that the distal His bound to the L-heme is deprotonated upon reduction of the H-heme. This His residue may then deprotonate hydrogen peroxide before peroxide binds to the heme, displacing the same His residue. ....**136**



## Abstract

Artificial enzymes have proven useful for catalyzing organic transformations in water with high product stereospecificity. Despite the high yields and selectivity exhibited by some of these catalysts, less is known about the differences in activity and catalytic lifetimes between various metal centers in these artificial enzymes. In this work, the small heme protein myoglobin (Mb) was modified through cofactor substitution and mutagenesis to develop a new set of catalysts for carbene transfer reactions. Due to the high activity of ruthenium porphyrins in organic solvents towards carbene transfer, it was hypothesized that a ruthenium porphyrin reconstituted into Mb (RuMb) would be a more active catalyst for carbene transfer reactions than Fe-containing (native) Mb. Indeed, the ruthenium porphyrin (RuMpIX) in water exhibits a higher yield for both the N-H insertion of aniline (48% vs. 27%) and the cyclopropanation of styrene (26% vs. 16%) compared to the similar iron porphyrin FePpIX found in native Mb (FeMb). RuMb and FeMb variants exhibit similar yields for the N-H insertion of aniline (30-60%) with slightly higher yields achieved by the more hydrophobic H64A and H64V mutants relative to wild-type and H64D Mb. In contrast, all RuMb variants exhibit low activity towards the cyclopropanation of styrene (0-4% yield) compared to FeMb variants (25-36% yield). My work demonstrates that this is due to the fact that RuMpIX and RuMb both exhibit short catalyst lifetimes ( $\leq 30$  minutes), and that the reactive metalcarbene formed during catalysis inserts into both the porphyrin and protein scaffold (as evidenced by UV-vis and mass spectrometry studies). RuMpIX also exhibits a higher rate constant of product formation ( $k_{\text{obs}} = 5.9 \times 10^{-2} \text{ min}^{-1}$ ) compared to FePpIX ( $k_{\text{obs}} = 2.9 \times 10^{-2} \text{ min}^{-1}$ ), but

suffers a shorter catalytic lifetime than FePplX (30 min vs. 120 min). Therefore, the Ru=CR<sub>2</sub> unit is quite reactive towards nucleophiles, but this high reactivity results in carbene insertion into the porphyrin and protein, leading to rapid catalyst decomposition. Efforts towards “taming” the Ru catalyst by using more electron-donating proximal ligands (in the H93G mutant of Mb) have not been successful so far. Future studies should focus on gaining a better understanding of the active site of RuMb and on the decomposition products after the addition of the carbene precursor. A crystal structure of RuMb would lend greater insight into the structure of the active site and the orientation of RuMpIX in the heme pocket. Modulating carbene insertion activity by adding carbene precursors with electron-donating groups could also result in lower activity towards porphyrin or protein insertion and therefore longer catalyst lifetimes.

In addition, this work investigates the mechanism of diheme bacterial cytochrome *c* peroxidases (CcPs). There are two classes of CcPs: some enzymes are active in the diferric form, and other enzymes must be reduced by one electron before catalytic activity commences. Using several different spectroscopic methods, the oxidation and spin states of the heme cofactors in two different CcPs were studied. This work suggests that the low-potential, peroxidatic heme remains low-spin ferric even in the active form of each enzyme. The active heme does not reside in a statically five-coordinate form and activation prior to peroxide binding is likely a more dynamic process than previously hypothesized. This could have implications for how the heme cofactors in other diheme enzymes interact and how activity is induced in different peroxidases.

## Chapter 1

### Introduction

#### 1.1 Transition Metal Catalysis

Catalysts provide invaluable tools for chemists in the continuing effort to transform organic molecules in new ways and to prepare compounds more efficiently. By lowering the activation energy for a reaction, catalysts increase the rate of reactions and facilitate reactions between reagents that are functionally inert under non-catalytic conditions. Catalysts are used in approximately 90% of the processes in the chemical industry, influencing the production of drugs, plastics, fuels, and fertilizers.<sup>1</sup> Much of the development towards novel catalysis seeks to simplify product synthesis, reduce waste, and use less energy while still maintaining or improving product yield or turnover number (TON), turnover frequency (TOF) and the lifetime of the catalyst. In addition, a catalyst should ideally be selective for a desired product when more than one stereoisomer can result. Significant effort has also been spent towards developing “green” catalysts; efforts include minimizing the use of environmentally-detrimental solvents, using more earth-abundant metals in transition metal catalysts, and producing less waste in the form of by-products, among other goals.<sup>2-3</sup>

Transition metal complexes are of particular use in the chemical industry for the catalysis of organic transformations including hydrogenation,<sup>4</sup> olefin metathesis,<sup>5</sup> and hydroformylation,<sup>6</sup> among many, many other reactions (**Figure 1.1**). The most useful transition metal catalysts are easy to synthesize, characterize, and modify through minor changes to the ligand system. In addition, many transition metal catalysts exhibit long lifetimes and have provided a wealth of

mechanistic information about a given organic transformation which can lead to the production of new catalysts and improved catalytic activity over time. Despite all the advantages of homogeneous transition metal catalysts, many of these catalysts are not water-soluble and require environmentally detrimental organic solvents as reaction media.<sup>7</sup> Some of these small-molecule catalysts are stereoselective for a desired organic transformation, but in order to achieve a high degree of product diastereoselectivity or enantioselectivity, chiral ligands are often required, and these ligands are more challenging to synthesize.<sup>8</sup> It can also be difficult to tune product stereoselectivity towards a different isomer without preparing an entirely different catalyst and/or ligand system.

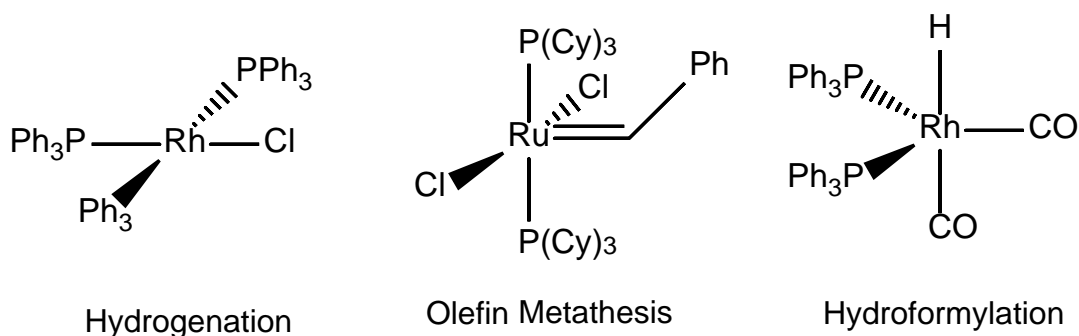


**Figure 1.1.** Several examples of transition metal catalysts used in the chemical industry. Wilkinson's catalyst effectively hydrogenates olefins and alkenes, Grubb's catalyst facilitates olefin metathesis, and several catalysts such as the rhodium catalyst shown above, are available for hydroformylation, an important process for the production of aldehydes.

In order to catalyze organic reactions in water and to control product stereoselectivity, chemists can make use of protein catalysts known as enzymes.<sup>9-11</sup> Enzymes catalyze a variety of organic transformations with high activity and selectivity for a specific product. These proteins facilitate the transformation of an organic molecule or substrate at a particular site (the active site) inside the protein. Both the chirality of the enzyme and an active site that is tailored for substrate binding influence product stereoselectivity.<sup>12</sup> In this way, enzyme active sites promote the

formation of a single product isomer. Metalloenzymes are of particular interest in the fields of biochemistry and catalysis as these proteins catalyze challenging reactions such as oxo-atom transfer to inactivated C-H bonds,<sup>13</sup> water oxidation to dioxygen,<sup>14</sup> and the formation of methane<sup>15-16</sup> among many others. In addition to the high activity of metalloenzymes, many enzymes are promiscuous towards non-natural substrates and reactions, although protein modifications are usually required to enhance this abiological activity.<sup>17-18</sup> There are a variety of organometallic reactions not observed in nature that are crucial for forming new C-C, C-H, C-N, and C-S bonds, and ultimately important for the development of new products in the chemical industry. To catalyze organometallic reactions and promote product stereoselectivity, metalloproteins and enzymes must be modified and designed to suit different substrates, reagents, and reaction conditions. In this way, researchers can access a variety of different catalysts from the same or similar protein scaffolds in order to catalyze different reactions or produce opposite product isomers.

## 1.2. Approaches to Designing Artificial Enzymes

Two broad strategies encompass the various approaches to preparing new artificial enzymes: rational design and directed evolution.<sup>19-21</sup> Rational design begins by building off of an existing enzyme, protein, or metal complex or by preparing a completely new protein structure. Synthesizing a new protein scaffold with a metal center,<sup>22-23</sup> reconstituting an existing protein with a new metal cofactor,<sup>18, 24-25</sup> or mutating key active site residues<sup>26-28</sup> are all strategies employed in successful rational design. *De novo* enzymes are constructed from combinations of peptides through the oligomerization of alpha-helices or other secondary protein structures to create a supramolecular assembly.<sup>22, 29</sup> Artificial metalloenzymes can also be developed through the

incorporation of new metal cofactors into protein scaffolds. Native cofactors have been replaced by similar yet distinct metal complexes,<sup>25, 30-33</sup> and metal complexes have been linked inside protein scaffolds that do not naturally contain metal centers.<sup>34-37</sup> Both of these approaches (*de novo* design and metal cofactor incorporation) require researchers to choose appropriate metal ions or complexes that can be readily incorporated into a protein scaffold. Limited mutagenesis is also often required to develop an active site that confers desired product stereoselectivity.<sup>25, 37</sup> In contrast, a directed evolution approach focuses on multiple rounds of mutagenesis.<sup>20, 38-39</sup> In this way, a library of enzyme mutants are quickly prepared and tested on a small-scale as further iterations build on the activity and stereoselectivity of the initial promising mutations. This method sometimes incorporates elements of rational design by targeting specific residues near the metal active site,<sup>37</sup> but also relies considerably on a sometimes unpredictable iterative mutagenesis process to deliver an active catalyst. Understanding some of the inherent advantages and drawbacks of these different approaches is key to developing new artificial metalloenzymes.

Through *de novo* enzyme design, entirely new protein scaffolds can be built for both enzyme mimicry and abiological catalysis. By synthesizing different peptide strands, and facilitating interactions between them, secondary and tertiary protein structures have been developed to bind different metal ions.<sup>22, 40-42</sup> Helical coiled coils and helical bundles are currently among the mostly widely prepared and investigated structures in the field of *de novo* design research owing to their relative ease of synthesis and assembly.<sup>29</sup> Coiled coils are formed from both hydrophobic and electrostatic interactions between the different helices<sup>43-44</sup> and key amino acids can be oriented inside the coil to bind metal centers after synthesis.<sup>45-46</sup> Various metal ions have been bound inside these peptide structures including Ni<sup>II</sup>, Cu<sup>I</sup>, Cu<sup>II</sup>, Zn<sup>II</sup>, Cd<sup>II</sup>, and Hg<sup>II</sup>.<sup>40, 47-49</sup> Pecoraro and coworkers have been at the forefront of this work, and have developed different

*de novo* protein systems including a functional nitrite reductase (NiR) model from a copper-bound  $\alpha$ -helical coiled coil (**Figure 1.2**).<sup>40, 49</sup> The designed copper NiR catalyzes the reduction of nitrite to nitric oxide, and while it does not achieve the activity of copper NiR found in anaerobic bacteria, it is still stable over several hours and exhibits structural similarity to the native enzyme near the copper center.<sup>40</sup> *De novo* design also allows for the careful tuning of active site secondary coordination spheres. Hydrogen-bonds to key amino acids can be introduced through the strategic placement of charged residues near the active site. The H-bonds can alter the donor strength of the ligands bound to the metal center and in turn affect the redox potential of the system as well. For the copper NiR model system, the introduction of two glutamate residues, of which one formed an H-bond with a histidine ligand to Cu, increased the redox potential of the enzyme which led to a four-fold increase in nitrite reduction activity.<sup>49</sup>

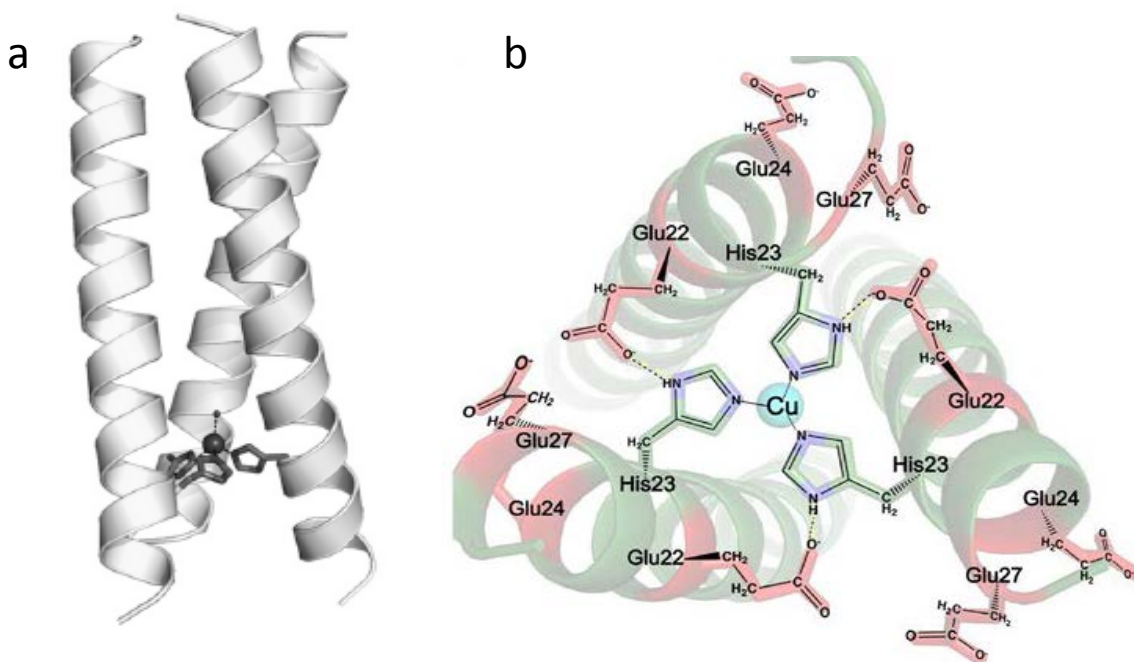


**Figure 1.2.** a) Model structure of the  $\text{Cu}(\text{I/II})(\text{TRIL23H})_3$  peptide that is a functional model for nitrite reductase. b) Top-down proposed structure of the TRI-EHK24E with Cu bound. In this structure, Glu22 H-bonds with His23, changing the redox potential of the metal center. Adapted from refs [40] and [49].

This model system illustrates some of the advantages to *de novo* enzyme design: by building a new protein scaffold from scratch, greater insight can be gained into the structure and activity of metalloenzyme active sites. The  $\alpha$ -helical coiled coils are also versatile scaffolds for the binding of different metals and different coordination environments in the active site, and secondary-coordination sphere interactions (such as H-bonding) can be controlled through the placement of charged and/or polar residues near the active site.<sup>22, 50</sup> However, the structural scope of proteins and enzymes produced through *de novo* design has thus far been focused on helical coiled coils and bundles due to the challenges presented in designing and synthesizing more complex protein structures from scratch. Most of the current studies have also either focused on the structure of these enzymes or on biologically-relevant reactivity instead of abiological reactions.<sup>22, 51</sup> More work needs to be done in order to understand how to build a larger library of *de novo* designed structures that can incorporate new metal sites and catalyze organometallic reactions.

Incorporation of metal complexes into protein scaffolds is another attractive method for preparing new metalloenzymes. Catalytically-competent transition metal complexes can benefit from both the active site chirality and substrate binding sites in proteins that can orient organic molecules towards the metal center and promote product stereoselectivity. Metal complexes and ions can be incorporated into protein scaffolds through several different methods. Complexes that are similar in size to a native metalloenzyme cofactor and have an available coordination site on the metal can bind to amino acid ligands such as histidine, cysteine, or tyrosine.<sup>18</sup> Heme proteins are particularly useful for this type of cofactor substitution, as native hemes can be extracted from several different proteins and replaced with other porphyrinoid complexes.<sup>30, 32-33, 52-54</sup> Metal complexes have also been linked inside proteins through the ligand system of the complex.



Extended ligand systems are designed to contain moieties that bind tightly to the protein system, either through supramolecular contacts or the formation of a covalent bond between the protein and ligand.<sup>18</sup> Streptavidin is a particularly useful protein scaffold for designing new metalloenzymes as it binds biotin tightly ( $K_d \sim 10^{-14}$  M).<sup>55</sup> Ward and coworkers have developed asymmetric transition metal complexes that incorporate biotin moieties at a distance from the metal center.<sup>24, 35, 37, 56-58</sup> A Hoyveda-Grubbs ruthenium catalyst modified with a biotin linkage was bound inside streptavidin to catalyze intramolecular olefin metathesis *in vitro* and *in vivo* (**Figure 1.3**).<sup>37</sup> After introducing several active site mutations near the modelled position of Ru, product yield increased four-fold compared to a water-soluble second-generation Hoyveda-Grubbs catalyst outside of the protein environment.<sup>37</sup> This work demonstrates the potential of using rational design of a metal cofactor and directed evolution through site saturation mutagenesis as complementary approaches to improve catalyst activity.

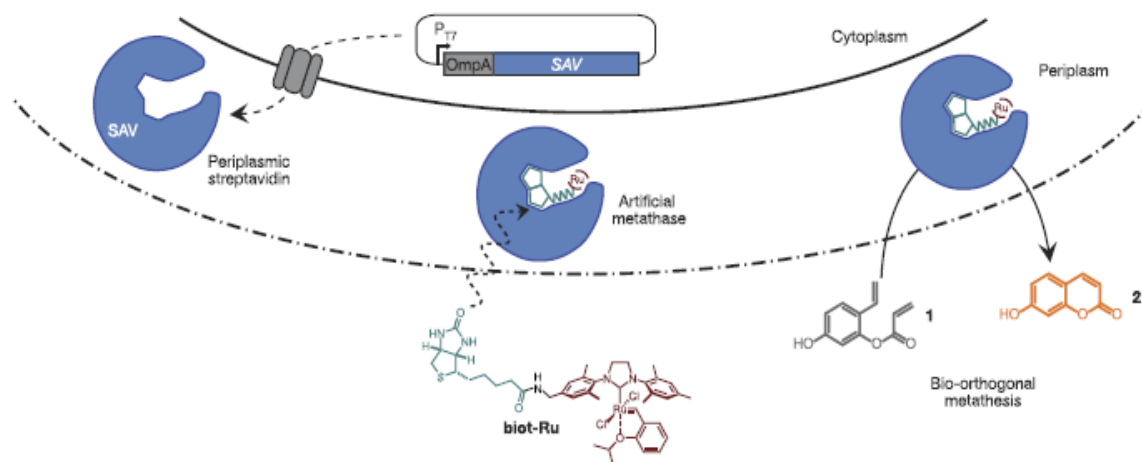


**Figure 1.3.** Cartoon depicting the expression of periplasmic streptavidin (SAV) and subsequent incorporation of a biotin-modified Hoyveda-Grubbs catalyst that can catalyze intramolecular olefin metathesis. Adapted from ref [37].

Supramolecular contacts between metal complexes and proteins are useful for preparing several new metalloenzymes from scaffolds such as streptavidin, but this technique is limited by the number of protein scaffolds that exhibit tight binding to a specific biomolecule and the ease

with which these biomolecules are synthetically incorporated into a ligand system. Transition metal complexes have also been incorporated into protein scaffolds through covalent linkage between the protein and metal complex ligands. Most efforts have focused on linking brominated ligands to native or artificially-introduced cysteine residues through nucleophilic exchange.<sup>18</sup> Salen complexes have been incorporated into myoglobin through cysteine linkages to catalyze sulfoxidation,<sup>59-60</sup> a Rh complex has been bound to a cysteine protease in order to catalyze hydrogenation of alkenes,<sup>61</sup> and a simple Cu complex has been linked into a lipase in order to catalyze Diels-Alder cycloadditions,<sup>62</sup> among other examples. Despite these successes, the challenge of designing ligand systems (often asymmetric ligands) that readily reconstitute into protein scaffolds remains a drawback to the incorporation of covalently or supramolecularly-linked metal complexes. With metalloenzymes that already contain a metal cofactor, it is sometimes easier to modify the native metal complex or design a similar cofactor to coordinate to the protein through the metal center. Even when successfully incorporating a metal complex into a protein, product stereoselectivity often needs to be tuned through mutagenesis, either by targeting a few key active site residues or a variety of residues throughout the protein using directed evolution.

Directed evolution can be regarded as a complementary approach to the strategies above, but it has also been used to enhance both biological and abiological activity in natural metalloenzymes.<sup>39</sup> Whereas successful *de novo* protein design or metal cofactor reconstitution require a significant understanding of the relationship between protein function and structure, directed evolution involves fewer design choices and improves enzyme catalytic activity by targeting a large selection of protein residues for repetitive and iterative mutagenesis.<sup>20, 38</sup> In this way, developing a new metal cofactor or a protein scaffold are not required for generating an enzyme capable of stereoselective and chemoselective catalysis. Directed evolution is an approach

aimed at quickly developing a highly active and selective catalyst whether this approach is used in conjunction with cofactor anchoring or *de novo* synthesis, or used with a natural protein or enzyme.

Directed evolution of natural enzymes for abiological catalysis has been pioneered in large part by Arnold and coworkers. Initial efforts were directed towards the family of heme enzymes known as Cytochrome P450s.<sup>63-68</sup> Biologically, these enzymes are important for the synthesis of biomolecules, the metabolism of certain drugs, and the detoxification of xenobiotics.<sup>13</sup> In the native enzyme, the heme binds oxygen and forms a reactive high-valent Fe<sup>IV</sup>-oxo unit that inserts an oxygen atom into an organic substrate. The Fe<sup>IV</sup>-oxo unit formed in the native enzyme is isoelectronic to organometallic iron-carbene or iron-nitrene units that act as intermediates in carbene and nitrene transfer reactions catalyzed by iron porphyrins (and other group 8 and group 9 metals).<sup>68</sup> Using previous studies of iron porphyrin carbene transfer reactions as a framework,<sup>69-71</sup> Arnold and coworkers initially modified P450<sub>BM3</sub> in order to develop a carbene transfer catalyst for the cyclopropanation of olefins (**Figure 1.4**).<sup>68</sup> The natural enzyme catalyzed the cyclopropanation of styrene in 1% yield, and the product exhibited low diastereoselectivity and enantioselectivity. A single T268A mutation near the active site of the heme increased the cyclopropanation yield to 65% and delivered 99% *trans* cyclopropane product. Product diastereoselectivity could be also reversed through further mutagenesis (13-14 point mutations) to provide 92% *cis* cyclopropane, and other mutations improved the enantioselectivity of the *cis* and *trans* products up to 97% and 96%, respectively.<sup>68</sup> Subsequent studies on P450<sub>BM3</sub> by the Arnold group focused on other carbene and nitrene transfer reactions such as N-H,<sup>65</sup> S-H,<sup>72</sup> and C-H insertion,<sup>73</sup> cyclopropanation with other substrates and carbene sources,<sup>63</sup> and catalyzing carbene transfer reactions *in vivo*.<sup>67</sup> In one particularly interesting example, the axial cysteine ligand in P450<sub>BM3</sub> was mutated to a serine residue (C400S) in order to raise the reduction potential of the

heme by +127 mV and allow for the reduction of the heme by biologically-relevant NAD(P)H reductants (**Figure 1.4**).<sup>67</sup> The cyclopropanation reaction could then proceed in live cells which increased product yield due to ease of producing the catalyst at larger scales.

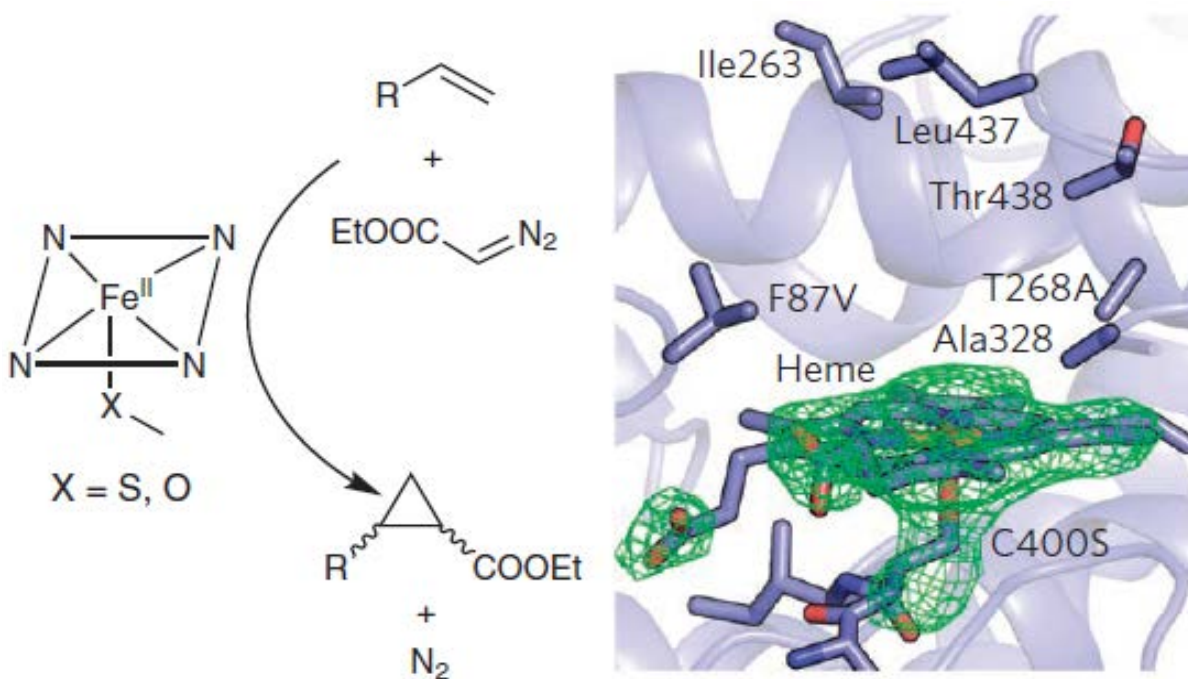


**Figure 1.4.** The cyclopropanation of olefins is catalyzed by a modified P450<sub>BM3</sub>. The enzyme active site is depicted on the right with key mutated residues highlighted. The axial ligand has been mutated from a cysteine to a serine, and the green mesh shows the electron density around the heme. Adapted from ref [67].

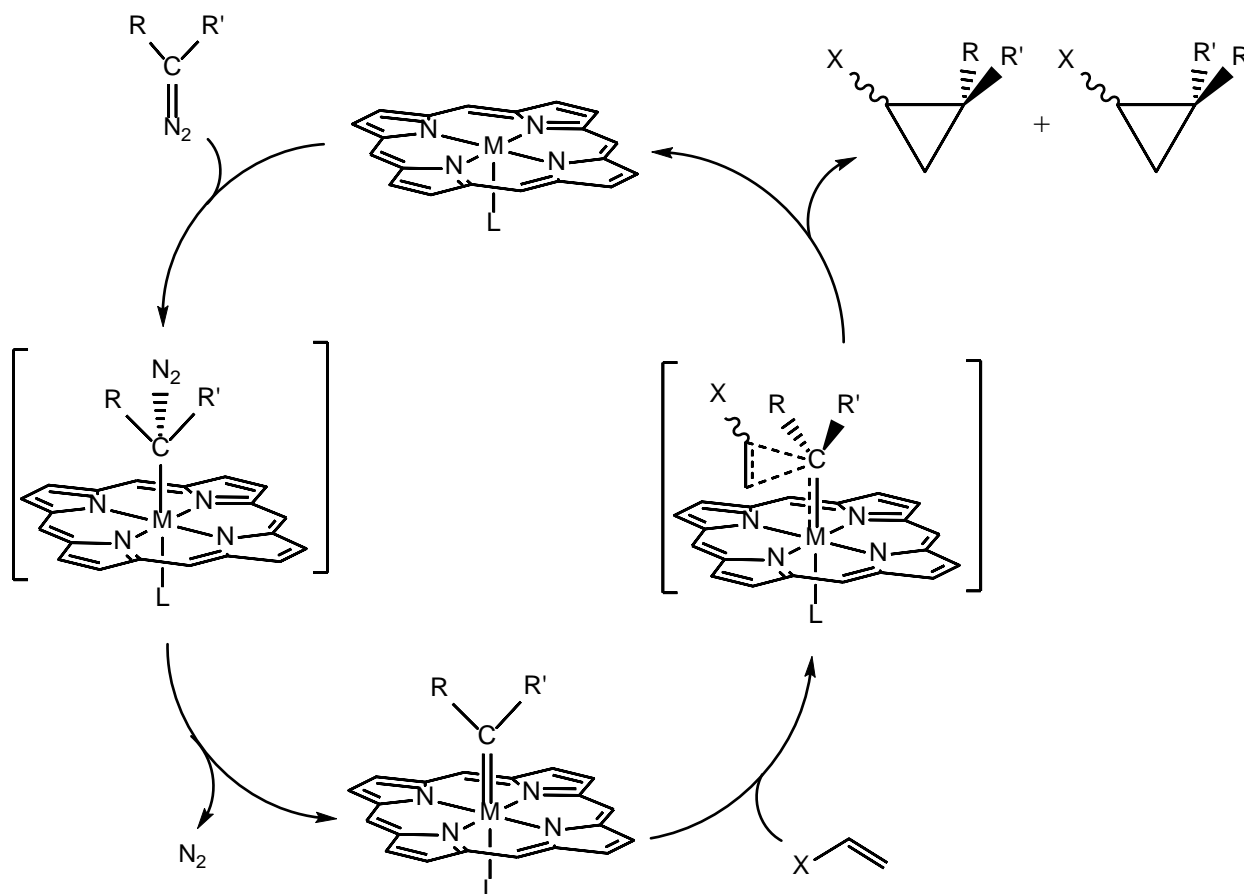
The higher carbene transfer activity and improved control over product stereoselectivity achieved by modified P450<sub>BM3</sub> demonstrate that directed evolution is indeed a powerful technique for developing new catalysts capable of abiological activity. Despite the benefits of this technique for tuning catalyst activity and altering protein structure, directed evolution arguably provides less insight into the factors governing the high catalytic activity of these enzymes when compared to rational design. Directed evolution relies on the collective effects of sequential mutagenesis at a variety of sites throughout the protein, and it is sometimes difficult to discern how the structural and chemical changes that result from mutagenesis lead to increased activity. In order to better

understand how the structure of artificial enzymes influences catalytic activity and organic transformations, a rational design approach is more suitable, even if directed evolution leads to faster development of active and selective catalysts.

### 1.3. Heme Proteins and Carbene Transfer Catalysis

As described above, heme proteins and enzymes can be particularly useful platforms for modification due to the wealth of literature on heme proteins, the sheer variety of heme proteins to choose from, and the ease of cofactor removal and replacement for some heme proteins.<sup>74</sup> Heme proteins serve a variety of functions in biology including oxygen transport and storage, electron transfer to and from enzymes, and catalyzing important reactions.<sup>13, 30, 75</sup> The structural and functional variety of heme proteins provides a wealth of opportunity for designing different catalysts for abiological activity. Though P450<sub>BM3</sub> is currently the most well-studied modified heme protein for carbene and nitrene transfer reactions, other heme proteins have also proved useful for organometallic catalysis including other P450 enzymes,<sup>76-77</sup> the electron transport protein cytochrome c,<sup>78</sup> and the oxygen storage protein myoglobin.<sup>28, 79-82</sup> Although several different reactions have been investigated using heme proteins including C-H,<sup>66, 77, 83</sup> N-H,<sup>65, 82</sup> S-H,<sup>72, 81</sup> and Si-H insertion,<sup>78</sup> cyclopropanation,<sup>64, 68, 80</sup> aziridination,<sup>84</sup> and aldehyde olefination,<sup>79</sup> all of these transformations have been mediated through the formation and transfer of a metallocarbene or metallonitrene intermediate. Group 8 and group 9 metals including iron,<sup>71, 85-87</sup> ruthenium,<sup>25, 88-91</sup> osmium,<sup>92-93</sup> cobalt,<sup>94-95</sup> rhodium,<sup>96-97</sup> and iridium<sup>98-99</sup> have long been investigated in both organic and aqueous environments<sup>100-102</sup> for the formation and reactivity of metallocarbenes and metallonitrenes. In a typical catalytic scheme (**Scheme 1.1**) for a porphyrin catalyzed carbene transfer reaction, a diazo reagent binds to the metal center through the carbene

carbon, and dinitrogen is released to form the electrophilic metallocarbene intermediate. A nucleophilic substrate, such as an olefin, then intercepts the electrophilic carbene intermediate. A three-atom centered transition state is formed before the product is released and an open coordination site on the metal center is regenerated.



**Scheme 1.1.** A depiction of metallocarbene formation and carbene transfer to an olefin to form cyclopropane products. A simple porphine molecule is used to represent a metalloporphyrin complex.

Though group 8 and group 9 metalloporphyrins exhibit high activity for carbene transfer reactions, it is difficult to control product stereoselectivity without the preparation of chiral porphyrins. For the cyclopropanation reaction in particular, most group 8 and 9 metals are more selective for the *trans* cyclopropane diastereomer<sup>101</sup> (with the exception of Rh porphyrins)<sup>96</sup> but significant enantioselectivity has only been achieved with chiral Halterman porphyrins which are more challenging to synthesize.<sup>8</sup> As Arnold and coworkers have demonstrated, protein scaffolds

can readily tune product stereoselectivity through point mutations located near the native heme. Though modified P450<sub>BM3</sub> has proven useful as catalyst for carbene and nitrene transfer reactions, it is easier to remove the native heme and reconstitute other porphyrins and metal cofactors into small heme proteins such as myoglobin.

Myoglobin is an attractive platform for protein engineering owing to its stability and ease of large-scale expression. In biology, myoglobin binds and stores oxygen in muscle tissue and is comprised of a relatively simple structure of eight alpha-helices.<sup>103-104</sup> The heme site in myoglobin is relatively open, allowing easy access for organic substrates, and for heme removal.<sup>105</sup> Concurrently with the work presented in this thesis, Fasan and coworkers prepared modified myoglobins as catalysts for several different carbene transfer reactions including cyclopropanation,<sup>80</sup> N-H insertion,<sup>82</sup> S-H insertion,<sup>81</sup> and aldehyde olefination.<sup>79</sup> By mutating key residues such as the distal histidine (His64) near the heme, higher activity, diastereoselectivity, and enantioselectivity were achieved (**Figure 1.5**). Different mutations proved important for transforming different substrates; the V68A mutation was crucial to improve enantioselectivity in the cyclopropanation of styrene,<sup>80</sup> whereas F43V and V68F mutations were necessary to increase activity in the olefination of benzaldehyde.<sup>79</sup> In addition to modifying myoglobin through mutagenesis, the apo-protein can be prepared through heme removal, or expression in metal-free broth.<sup>25, 105</sup> Metal complexes then coordinate to the proximal histidine (His93) during reconstitution. Myoglobin can readily incorporate different macrocycles into the empty heme site of the apo-protein. Porphyrinoids such as porphycenes and corroles have been reconstituted into apo-myoglobin to examine oxygen binding and peroxidase activity,<sup>30, 106</sup> as well as modified porphyrins with organic substrate binding domains and second and third-row transition metal porphyrins to facilitate catalysis.<sup>54, 83, 107-108</sup> Recently, Hartwig and coworkers reconstituted second

and third-row transition metal porphyrins into apo-myoglobin in order to catalyze cyclopropanation and intramolecular C-H insertion.<sup>83</sup> Despite the remarkable progress that has been made in modifying heme proteins through mutagenesis and cofactor replacement for carbene transfer reactions, further understanding about the differences in catalysis between different metal porphyrins is still required.

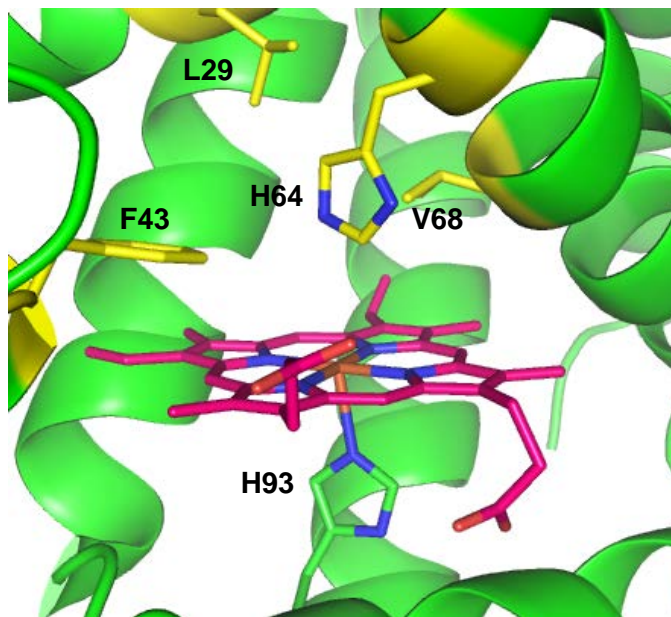


**Figure 1.5.** A pymol model of the active site of sperm whale myoglobin highlighting some of the important residues near the heme site that can influence abiological activity.

#### 1.4. Scope of Thesis

The scope of this thesis includes the incorporation of a ruthenium porphyrin into myoglobin (Mb) and the comparison between wild-type Mb (FeMb) and ruthenium Mb (RuMb) for catalytic carbene transfer reactions. This project is split into two different aims. The first aim focuses on the preparation of ruthenium mesoporphyrin IX (RuMpIX), the incorporation of this porphyrin into apo-Mb and the reactivity of RuMpIX and RuMb towards the cyclopropanation of styrene and the N-H insertion of aniline in comparison with the reactivity of FeMb and the native heme cofactor



(FePpIX). In addition, reactivity is examined as a function of pH and with different styrene and aniline derivatives as substrates. The difference in activity observed between FeMb and RuMb is investigated through the lens of catalyst decomposition. This work is in part reproduced from a manuscript published in the journal *Inorganic Chemistry*: Wolf, M. W.; Vargas, D. A.; Lehnert, N. *Inorganic Chemistry*, **2017**, *56*, 5623.

The second aim of this thesis focuses on further comparing FeMb and RuMb by looking into the catalyst lifetime and initial turnover frequency of several of the prepared Fe and Ru catalysts for both cyclopropanation and N-H insertion. In addition, this aim describes the preparation of H93G Mb, a Mb variant without the proximal histidine to which the heme or porphyrin is usually coordinated. In an attempt to improve the activity and stability of RuMb, exogenous ligands were added to these modified Mb proteins and cyclopropanation activity was compared between different ligands for both FeMb and RuMb.

The final aim of this thesis focuses on a different project apart from the modification of Mb. In collaboration with Dr. Sean J. Elliott and his graduate students at Boston University, the mechanisms of two different bacterial cytochrome *c* peroxidases (bCcPs) have been investigated using a variety of spectroscopic techniques. Despite the differences between constitutively-active and reductively activated bCcPs, these different enzymes have remarkably similar spectroscopic characteristics. This section represents a manuscript slated to be submitted for publication by May 2018.

## 1.5 References

- 1) Lim, X. Chemistry on the Fast Track. *Nature* **2016**, 537 (7619), 156-158.
- 2) Sinou, D. Metal catalysis in water. *Modern Solvents in Organic Synthesis* **1999**, 206, 41-59.
- 3) Horvath, I. T.; Anastas, P. T. Innovations and green chemistry. *Chem. Rev.* **2007**, 107 (6), 2169-2173.
- 4) Birch, A. J. W., D. H. Homogeneous Hydrogenation Catalysts in Organic Synthesis. In *Organic Reactions*, Dauben, W. G., Ed. John Wiley & Sons: New York, 1976; Vol. 24, pp 1-186.
- 5) Vougioukalakis, G. C.; Grubbs, R. H. Ruthenium-Based Heterocyclic Carbene-Coordinated Olefin Metathesis Catalysts. *Chem. Rev.* **2010**, 110 (3), 1746-1787.
- 6) Eilbracht, P.; Barfacker, L.; Buss, C.; Hollmann, C.; Kitsos-Rzychon, B. E.; Kranemann, C. L.; Rische, T.; Roggenbuck, R.; Schmidt, A. Tandem reaction sequences under hydroformylation conditions: New synthetic applications of transition metal catalysis. *Chem. Rev.* **1999**, 99 (11), 3329-3365.
- 7) Shanab, K.; Neudorfer, C.; Schirmer, E.; Spreitzer, H. Green Solvents in Organic Synthesis: An Overview. *Curr. Org. Chem.* **2013**, 17 (11), 1179-1187.
- 8) Nicolas, I.; Roisnel, T.; Le Maux, P.; Simonneaux, G. Asymmetric intermolecular cyclopropanation of alkenes by diazoketones catalyzed by Halterman iron porphyrins. *Tetrahedron Lett.* **2009**, 50 (36), 5149-5151.
- 9) Hammer, S. C.; Knight, A. M.; Arnold, F. H. Design and evolution of enzymes for non-natural chemistry. *Curr. Opin. Green. Sust.* **2017**, 7, 23-30.
- 10) Lu, Y. Biosynthetic Inorganic Chemistry. *Angew. Chem. Int. Ed.* **2006**, 45, 5588-5601.
- 11) Matsuo, T.; Hirota, S. Artificial enzymes with protein scaffolds: Structural design and modification. *Bioorg. Med. Chem.* **2014**, 22 (20), 5638-5656.
- 12) Whitesides, G. M.; Wong, C. H. Enzymes as Catalysts in Synthetic Organic-Chemistry. *Angew. Chem. Int. Ed.* **1985**, 24 (8), 617-638.
- 13) Ortiz de Montellano, P. R. *Cytochrome P450: structure, mechanism, and biochemistry*. Kluwer Academic/Plenum: New York, 2005.
- 14) McEvoy, J. P.; Brudvig, G. W. Water-splitting chemistry of photosystem II. *Chem. Rev.* **2006**, 106 (11), 4455-4483.

- 15) Kruger, M.; Meyerdierks, A.; Glockner, F. O.; Amann, R.; Widdel, F.; Kube, M.; Reinhardt, R.; Kahnt, R.; Bocher, R.; Thauer, R. K.; Shima, S. A conspicuous nickel protein in microbial mats that oxidize methane anaerobically. *Nature* **2003**, *426* (6968), 878-881.
- 16) Shima, S.; Krueger, M.; Weinert, T.; Demmer, U.; Kahnt, J.; Thauer, R. K.; Ermler, U. Structure of a methyl-coenzyme M reductase from Black Sea mats that oxidize methane anaerobically. *Nature* **2011**, *481*, 98-101.
- 17) Kazlauskas, R. J. Enhancing catalytic promiscuity for biocatalysis. *Curr. Opin. Chem. Biol.* **2005**, *9*, 195-201.
- 18) Steinreiber, J.; Ward, T. R., Artificial metalloenzymes as selective catalysts in aqueous media. *Coord. Chem. Rev.* **2008**, *252* (5-7), 751-766.
- 19) Petrik, I. D.; Liu, J.; Lu, Y. Metalloenzyme design and engineering through strategic modifications of native protein scaffolds. *Curr. Opin. Chem. Biol.* **2014**, *19*, 67-75.
- 20) Arnold, F. H. Directed Evolution: Bringing New Chemistry to Life. *Angew. Chem. Int. Ed.* **2017**, *56*, 2-8.
- 21) Bhagi-Damodaran, A.; Hosseinzadeh, P.; Mirts, E.; Reed, J.; Petrik, I. D.; Lu, Y. Design of Heteronuclear Metalloenzymes. *Method Enzymol* **2016**, *580*, 501-537.
- 22) Zastrow, M. L.; Pecoraro, V. L. Designing functional metalloproteins: From structural to catalytic metal sites. *Coord. Chem. Rev.* **2013**, *257* (17-18), 2565-2588.
- 23) Woolfson, D. N.; Bartlett, G. J.; Burton, A. J.; Heal, J. W.; Niitsu, A.; Thomson, A. R.; Wood, C. W. De novo protein design: how do we expand into the universe of possible protein structures? *Curr. Opin. Struct. Biol.* **2015**, *33*, 16-26.
- 24) Heinisch, T.; Ward, T. R. Artificial Metalloenzymes Based on the Biotin-Streptavidin Technology: Challenges and Opportunities. *Acc. Chem. Res.* **2016**, *49* (9), 1711-1721.
- 25) Sreenilayam, G.; Moore, E. J.; Steck, V.; Fasan, R. Metal Substitution Modulates the Reactivity and Extends the Reaction Scope of Myoglobin Carbene Transfer Catalysts. *Adv. Synth. Catal.* **2017**, *359* (12), 2076-2089.
- 26) Sigman, J. A.; Kwok, B. C.; Lu, Y. From myoglobin to heme-copper oxidase: Design and engineering of a Cu-B center into sperm whale myoglobin. *J. Am. Chem. Soc.* **2000**, *122* (34), 8192-8196.
- 27) Yeung, N.; Lin, Y. W.; Gao, Y. G.; Zhao, X.; Russell, B. S.; Lei, L. Y.; Miner, K. D.; Robinson, H.; Lu, Y. Rational design of a structural and functional nitric oxide reductase. *Nature* **2009**, *462* (7276), 1079-U144.
- 28) Bordeaux, M.; Singh, R.; Fasan, R. Intramolecular C(sp<sup>3</sup>)-H amination of arylsulfonyl azides with engineered and artificial myoglobin-based catalysts. *Bioorg. Med. Chem.* **2014**, *22* (20), 5697-5704.

- 29) Bryson, J. W.; Desjarlais, J. R.; Handel, T. M.; DeGrado, W. F. From coiled coils to small globular proteins: Design of a native-like three-helix bundle. *Protein Sci.* **1998**, *7* (6), 1404-1414.
- 30) Dejima, H.; Hayashi, T.; Matsuo, T.; Hisaeda, Y. New myoglobin reconstituted with an iron porphycene as a structural isomer of heme moiety. *J. Inorg. Biochem.* **2001**, *86* (1), 200-200.
- 31) Hayashi, T.; Sato, H.; Matsuo, T.; Matsuda, T.; Hitomi, Y.; Hisaeda, Y. Enhancement of enzymatic activity for myoglobins by modification of heme-propionate side chains. *J. Porph. Phthalo.* **2004**, *8* (1-3), 255-264.
- 32) Matsuo, T.; Hayashi, A.; Abe, M.; Matsuda, T.; Hisaeda, Y.; Hayashi, T. Meso-Unsubstituted Iron Corrole in Hemoproteins: Remarkable Differences in Effects on Peroxidase Activities between Myoglobin and Horseradish Peroxidase. *J. Am. Chem. Soc.* **2009**, *131* (42), 15124-+.
- 33) Ohora, K.; Meichin, H.; Kihira, Y.; Sugimoto, H.; Shiro, Y.; Hayashi, T. Manganese(V) Porphycene Complex Responsible for Inert C-H Bond Hydroxylation in a Myoglobin Matrix. *J. Am. Chem. Soc.* **2017**, *139* (51), 18460-18463.
- 34) Pierron, J.; Malan, C.; Creus, M.; Gradinaru, J.; Hafner, I.; Ivanova, A.; Sardo, A.; Ward, T. R. Artificial metalloenzymes for asymmetric allylic alkylation on the basis of the biotin-avidin technology. *Angew. Chem. Int. Ed.* **2008**, *47* (4), 701-705.
- 35) Hyster, T. K.; Knorr, L.; Ward, T. R.; Rovis, T. Biotinylated Rh(III) Complexes in Engineered Streptavidin for Accelerated Asymmetric C-H Activation. *Science* **2012**, *338* (6106), 500-503.
- 36) Monnard, F. W.; Nogueira, E. S.; Heinisch, T.; Schirmer, T.; Ward, T. R. Human carbonic anhydrase II as host protein for the creation of artificial metalloenzymes: the asymmetric transfer hydrogenation of imines. *Chem. Sci.* **2013**, *4* (8), 3269-3274.
- 37) Jeschek, M.; Reuter, R.; Heinisch, T.; Trindler, C.; Klehr, J.; Panke, S.; Ward, T. R. Directed evolution of artificial metalloenzymes for in vivo metathesis. *Nature* **2016**, *537* (7622), 661-+.
- 38) Reetz, M. T.; Peyralans, J. J. P.; Maichele, A.; Fu, Y.; Maywald, M. Directed evolution of hybrid enzymes: Evolving enantioselectivity of an achiral Rh-complex anchored to a protein. *Chem. Comm.* **2006**, (41), 4318-4320.
- 39) Renata, H.; Wang, Z. J.; Arnold, F. H. Expanding the Enzyme Universe: Accessing Non-Natural Reactions by Mechanism-Guided Directed Evolution. *Angew. Chem. Int. Ed.* **2015**, *54* (11), 3351-3367.
- 40) Tegoni, M.; Yu, F. T.; Bersellini, M.; Penner-Hahn, J. E.; Pecoraro, V. L. Designing a functional type 2 copper center that has nitrite reductase activity within alpha-helical coiled coils. *Proc. Natl. Acad. Sci.* **2012**, *109* (52), 21234-21239.

- 41) Zastrow, M. L.; Pecoraro, V. L. Influence of Active Site Location on Catalytic Activity in de Novo-Designed Zinc Metalloenzymes. *J. Am. Chem. Soc.* **2013**, *135* (15), 5895-5903.
- 42) Cangelosi, V. M.; Deb, A.; Penner-Hahn, J. E.; Pecoraro, V. L. A De Novo Designed Metalloenzyme for the Hydration of CO<sub>2</sub>. *Angew. Chem. Int. Ed.* **2014**, *53* (30), 7900-7903.
- 43) Degrado, W. F.; Lear, J. D. Induction of Peptide Conformation at Apolar Water Interfaces .1. A Study with Model Peptides of Defined Hydrophobic Periodicity. *J. Am. Chem. Soc.* **1985**, *107* (25), 7684-7689.
- 44) Kamtekar, S.; Schiffer, J. M.; Xiong, H. Y.; Babik, J. M.; Hecht, M. H. Protein Design by Binary Patterning of Polar and Nonpolar Amino-Acids. *Science* **1993**, *262* (5140), 1680-1685.
- 45) Ghadiri, M. R.; Fernholz, A. K. Peptide Architecture - Design of Stable Alpha-Helical Metallopeptides Via a Novel Exchange-Inert RuIII Complex. *J. Am. Chem. Soc.* **1990**, *112* (26), 9633-9635.
- 46) Ghadiri, M. R.; Choi, C. Secondary Structure Nucleation in Peptides - Transition-Metal Ion Stabilized Alpha-Helices. *J. Am. Chem. Soc.* **1990**, *112* (4), 1630-1632.
- 47) Zastrow, M. L.; Peacock, A. F. A.; Stuckey, J. A.; Pecoraro, V. L. Hydrolytic catalysis and structural stabilization in a designed metalloprotein. *Nat. Chem.* **2012**, *4* (2), 118-123.
- 48) Luczkowski, M.; Stachura, M.; Schirf, V.; Demeler, B.; Hemmingsen, L.; Pecoraro, V. L. Design of Thiolate Rich Metal Binding Sites within a Peptidic Framework. *Inorg. Chem.* **2008**, *47* (23), 10875-10888.
- 49) Yu, F. T.; Penner-Hahn, J. E.; Pecoraro, V. L. De Novo-Designed Metallopeptides with Type 2 Copper Centers: Modulation of Reduction Potentials and Nitrite Reductase Activities. *J. Am. Chem. Soc.* **2013**, *135* (48), 18096-18107.
- 50) Yu, F. T.; Cangelosi, V. M.; Zastrow, M. L.; Tegoni, M.; Plegaria, J. S.; Tebo, A. G.; Mocny, C. S.; Ruckthong, L.; Qayyum, H.; Pecoraro, V. L. Protein Design: Toward Functional Metalloenzymes. *Chem. Rev.* **2014**, *114* (7), 3495-3578.
- 51) Hirota, S.; Lin, Y. W. Design of artificial metalloproteins/metalloenzymes by tuning noncovalent interactions. *J. Biol. Inorg. Chem.* **2018**, *23* (1), 7-25.
- 52) Hayashi, T.; Dejima, H.; Matsuo, T.; Sato, H.; Murata, D.; Hisaeda, Y. Blue myoglobin reconstituted with an iron porphycene shows extremely high oxygen affinity. *J. Am. Chem. Soc.* **2002**, *124* (38), 11226-11227.
- 53) Matsuo, T.; Dejima, H.; Hirota, S.; Murata, D.; Sato, H.; Ikegami, T.; Hori, H.; Hisaeda, Y.; Hayashi, T. Ligand binding properties of myoglobin reconstituted with iron porphycene: Unusual O<sub>2</sub> binding selectivity against CO binding. *J. Am. Chem. Soc.* **2004**, *126* (49), 16007-16017.

- 54) Matsuo, T.; Fukumoto, K.; Watanabe, T.; Hayashi, T. Precise Design of Artificial Cofactors for Enhancing Peroxidase Activity of Myoglobin: Myoglobin Mutant H64D Reconstituted with a "Single-Winged Cofactor" Is Equivalent to Native Horseradish Peroxidase in Oxidation Activity. *Chem. Asian. J.* **2011**, *6* (9), 2491-2499.
- 55) Collot, J.; Gradinaru, J.; Humbert, N.; Skander, M.; Zocchi, A.; Ward, T. R. Artificial metalloenzymes for enantioselective catalysis based on biotin-avidin. *J. Am. Chem. Soc.* **2003**, *125* (30), 9030-9031.
- 56) Pordea, A.; Mathis, D.; Ward, T. R. Incorporation of biotinylated manganese-salen complexes into streptavidin: New artificial metalloenzymes for enantioselective sulfoxidation. *J. Organomet. Chem.* **2009**, *694* (6), 930-936.
- 57) Ward, T. R. Artificial Metalloenzymes Based on the Biotin-Avidin Technology: Enantioselective Catalysis and Beyond. *Acc. Chem. Res.* **2011**, *44* (1), 47-57.
- 58) Quinto, T.; Schwizer, F.; Zimbron, J. M.; Morina, A.; Kohler, V.; Ward, T. R. Expanding the Chemical Diversity in Artificial Imine Reductases Based on the Biotin- Streptavidin Technology. *Chemcatchem* **2014**, *6* (4), 1010-1014.
- 59) Zhang, J. L.; Garner, D. K.; Liang, L.; Barrios, D. A.; Lu, Y. Non-covalent Modulation of pH Dependent Reactivity of a MnSalen Cofactor in Myoglobin with Hydrogen Peroxide. *Chemistry* **2009**, *15*, 7481-7489.
- 60) Garner, D. K.; Liang, L.; Barrios, D. A.; Zhang, J. L.; Lu, Y. The Important Role of Covalent Anchor Positions in Tuning Catalytic Properties of a Rationally Designed MnSalen-Containing Metalloenzyme. *ACS Catal.* **2011**, *1* (9), 1083-1089.
- 61) Madern, N.; Queyriaux, N.; Chevalley, A.; Ghasemi, M.; Nicolotti, O.; Ciofini, I.; Mangiatordi, G. F.; Salmain, M. Piano-stool d(6)-rhodium(III) complexes of chelating pyridine-based ligands and their papain bioconjugates for the catalysis of transfer hydrogenation of aryl ketones in aqueous medium. *J. Mol. Catal. B. Enzym.* **2015**, *122*, 314-322.
- 62) Deuss, P. J.; Popa, G.; Slawin, A. M. Z.; Laan, W.; Kamer, P. C. J. Artificial Copper Enzymes for Asymmetric Diels-Alder Reactions. *Chemcatchem* **2013**, *5* (5), 1184-1191.
- 63) Wang, Z. J.; Renata, H.; Peck, N. E.; Farwell, C. C.; Coelho, P. S.; Arnold, F. H. Improved Cyclopropanation Activity of Histidine-Ligated Cytochrome P450 Enables the Enantioselective Formal Synthesis of Levomilnacipran. *Angew. Chem. Int. Ed.* **2014**, *53* (26), 6810-6813.
- 64) Renata, H.; Wang, Z. J.; Kitto, R. Z.; Arnold, F. H. P450-catalyzed asymmetric cyclopropanation of electron-deficient olefins under aerobic conditions. *Catal. Sci. Technol.* **2014**, *4* (10), 3640-3643.
- 65) Wang, Z. J.; Peck, N. E.; Renata, H.; Arnold, F. H. Cytochrome P450-catalyzed insertion of carbenoids into N-H bonds. *Chem. Sci.* **2014**, *5* (2), 598-601.

- 66) McIntosh, J. A.; Coelho, P. S.; Farwell, C. C.; Wang, Z. J.; Lewis, J. C.; Brown, T. R.; Arnold, F. H. Enantioselective Intramolecular C-H Amination Catalyzed by Engineered Cytochrome P450 Enzymes In Vitro and In Vivo. *Angew. Chem. Int. Ed.* **2013**, *52* (35), 9309-9312.
- 67) Coelho, P. S.; Wang, Z. J.; Ener, M. E.; Baril, S. A.; Kannan, A.; Arnold, F. H.; Brustad, E. M. A serine-substituted P450 catalyzes highly efficient carbene transfer to olefins in vivo. *Nat. Chem. Biol.* **2013**, *9* (8), 485-U33.
- 68) Coelho, P. S.; Brustad, E. M.; Kannan, A.; Arnold, F. H. Olefin Cyclopropanation via Carbene Transfer Catalyzed by Engineered Cytochrome P450 Enzymes. *Science* **2013**, *339* (6117), 307-310.
- 69) Khade, R. L.; Fan, W. C.; Ling, Y.; Yang, L.; Oldfield, E.; Zhang, Y. Iron Porphyrin Carbenes as Catalytic Intermediates: Structures, Mossbauer and NMR Spectroscopic Properties, and Bonding. *Angew. Chem. Int. Ed.* **2014**, *53* (29), 7574-7578.
- 70) Baumann, L. K.; Mbuvi, H. M.; Du, G.; Woo, L. K. Iron porphyrin catalyzed N-H insertion reactions with ethyl diazoacetate. *Organometallics* **2007**, *26* (16), 3995-4002.
- 71) Hamaker, C. G.; Mirafzal, G. A.; Woo, L. K. Catalytic cyclopropanation with iron(II) complexes. *Organometallics* **2001**, *20* (24), 5171-5176.
- 72) Farwell, C. C.; McIntosh, J. A.; Hyster, T. K.; Wang, Z. J.; Arnold, F. H. Enantioselective Imidation of Sulfides via Enzyme-Catalyzed Intermolecular Nitrogen-Atom Transfer. *J. Am. Chem. Soc.* **2014**, *136* (24), 8766-8771.
- 73) Prier, C. K.; Zhang, R. J. K.; Buller, A. R.; Brinkmann-Chen, S.; Arnold, F. H. Enantioselective, intermolecular benzylic C-H amination catalysed by an engineered iron-haem enzyme. *Nat. Chem.* **2017**, *9* (7), 629-634.
- 74) Fruk, L.; Kuo, C. H.; Torres, E.; Niemeyer, C. M. Apoenzyme Reconstitution as a Chemical Tool for Structural Enzymology and Biotechnology. *Angew. Chem. Int. Ed.* **2009**, *48* (9), 1550-1574.
- 75) Xiong, P.; Nocek, J. M.; Vura-Weis, J.; Lockard, J. V.; Wasielewski, M. R.; Hoffman, B. M. Faster Interprotein Electron Transfer in a [Myoglobin, b(5)] Complex with a Redesigned Interface. *Science* **2010**, *330* (6007), 1075-1078.
- 76) Key, H. M.; Dydio, P.; Liu, Z. N.; Rha, J. Y. E.; Nazarenko, A.; Seyedkazemi, V.; Cark, D. S.; Hartwig, J. F. Beyond Iron: Iridium-Containing P450 Enzymes for Selective Cyclopropanations of Structurally Diverse Alkenes. *ACS Central Sci.* **2017**, *3* (4), 302-308.
- 77) Dydio, P.; Key, H. M.; Hayashi, H.; Clark, D. S.; Hartwig, J. F. Chemoselective, Enzymatic C-H Bond Amination Catalyzed by a Cytochrome P450 Containing an Ir(Me)-PIX Cofactor. *J. Am. Chem. Soc.* **2017**, *139* (5), 1750-1753.

- 78) Kan, S. B. J.; Lewis, R. D.; Chen, K.; Arnold, F. H. Directed evolution of cytochrome c for carbon-silicon bond formation: Bringing silicon to life. *Science* **2016**, *354* (6315), 1048-1051.
- 79) Tyagi, V.; Fasan, R. Myoglobin-Catalyzed Olefination of Aldehydes. *Angew. Chem. Int. Ed.* **2016**, *55* (7), 2512-2516.
- 80) Bordeaux, M.; Tyagi, V.; Fasan, R. Highly Diastereoselective and Enantioselective Olefin Cyclopropanation Using Engineered Myoglobin-Based Catalysts. *Angew. Chem. Int. Ed.* **2015**, *54* (6), 1744-1748.
- 81) Tyagi, V.; Bonn, R. B.; Fasan, R. Intermolecular carbene S-H insertion catalysed by engineered myoglobin-based catalysts. *Chem. Sci.* **2015**, *6* (4), 2488-2494.
- 82) Sreenilayam, G.; Fasan, R. Myoglobin-catalyzed intermolecular carbene N-H insertion with arylamine substrates. *Chem. Comm.* **2015**, *51* (8), 1532-1534.
- 83) Key, H. M.; Dydio, P.; Clark, D. S.; Hartwig, J. F. Abiological catalysis by artificial haem proteins containing noble metals in place of iron. *Nature* **2016**, *534* (7608), 534-537.
- 84) Farwell, C. C.; Zhang, R. K.; McIntosh, J. A.; Hyster, T. K.; Arnold, F. H. Enantioselective Enzyme-Catalyzed Aziridination Enabled by Active-Site Evolution of a Cytochrome P450. *ACS Central Sci.* **2015**, *1* (2), 89-93.
- 85) Ohora, K.; Meichin, H.; Zhao, L. M.; Wolf, M. W.; Nakayama, A.; Hasegawa, J.; Lehnert, N.; Hayashi, T. Catalytic Cyclopropanation by Myoglobin Reconstituted with Iron Porphycene: Acceleration of Catalysis due to Rapid Formation of the Carbene Species. *J. Am. Chem. Soc.* **2017**, *139* (48), 17265-17268.
- 86) Cheng, G. L.; Mirafzal, G. A.; Woo, L. K. Iron porphyrin-catalyzed olefination of carbonyl compounds with ethyl diazoacetate. *Organometallics* **2003**, *22* (7), 1468-1474.
- 87) Wolf, J. R.; Hamaker, C. G.; Djukic, J. P.; Kodadek, T.; Woo, L. K. Shape and Stereoselective Cyclopropanation of Alkenes Catalyzed by Iron Porphyrins. *J. Am. Chem. Soc.* **1995**, *117* (36), 9194-9199.
- 88) Galardon, E.; LeMaux, P.; Simonneaux, G. Insertion of ethyl diazoacetate into N-H and S-H bonds catalyzed by ruthenium porphyrin complexes. *J. Chem. Soc. Perk. Trans.* **1997**, (17), 2455-2456.
- 89) Galardon, E.; LeMaux, P.; Simonneaux, G. Cyclopropanation of alkenes with ethyl diazoacetate catalysed by ruthenium porphyrin complexes. *Chem. Comm.* **1997**, (10), 927-928.
- 90) Frauenkron, M.; Berkessel, A. A novel chiral ruthenium porphyrin as highly efficient and selective catalyst for asymmetric cyclopropanations. *Tetrahedron Lett.* **1997**, *38* (41), 7175-7176.



- 91) Collman, J. P.; Rose, E.; Venburg, G. D. Reactivity of Ruthenium 5,10,15,20-Tetramesitylporphyrin Towards Diazoesters - Formation of Olefins. *J. Chem. Soc. Chem. Comm.* **1993**, (11), 934-935.
- 92) Smith, D. A.; Reynolds, D. N.; Woo, L. K. Cyclopropanation Catalyzed by Osmium Porphyrin Complexes. *J. Am. Chem. Soc.* **1993**, *115* (6), 2511-2513.
- 93) Che, C. M.; Huang, J. S. Ruthenium and osmium porphyrin carbene complexes: synthesis, structure, and connection to the metal-mediated cyclopropanation of alkenes. *Coord. Chem. Rev.* **2002**, *231* (1-2), 151-164.
- 94) Chen, Y.; Zhang, X. P. Asymmetric cyclopropanation of styrenes catalyzed by metal complexes of D-2-Symmetrical chiral porphyrin: Superiority of cobalt over iron. *J. Org. Chem.* **2007**, *72* (15), 5931-5934.
- 95) Dzik, W. I.; Xu, X.; Zhang, X. P.; Reek, J. N. H.; de Bruin, B. 'Carbene Radicals' in Co-II(por)-Catalyzed Olefin Cyclopropanation. *J. Am. Chem. Soc.* **2010**, *132* (31), 10891-10902.
- 96) Callot, H. J.; Piechocki, C. Cyclopropanation Using Rhodium(III)Porphyrins - Large Cis Vs Trans Selectivity. *Tetrahedron Lett.* **1980**, *21* (36), 3489-3492.
- 97) Callot, H. J.; Metz, F.; Piechocki, C. Sterically Crowded Cyclopropanation Catalysts - Syn-Selectivity Using Rhodium(III)Porphyrins. *Tetrahedron* **1982**, *38* (15), 2365-2369.
- 98) Anding, B. J.; Woo, L. K. Catalytic carbene transfer reactions with iridium(III) porphyrins. *Abstr. Pap. Am. Chem. Soc.* **2010**, 240.
- 99) Anding, B. J.; Ellern, A.; Woo, L. K. Olefin Cyclopropanation Catalyzed by Iridium(III) Porphyrin Complexes. *Organometallics* **2012**, *31* (9), 3628-3635.
- 100) Nicolas, I.; Le Maux, P.; Simonneaux, G. Synthesis of chiral water-soluble metalloporphyrins (Fe, Ru): new catalysts for asymmetric carbene transfer in water. *Tetrahedron Lett.* **2008**, *49* (40), 5793-5795.
- 101) Nicolas, I.; Le Maux, P.; Simonneaux, G. Asymmetric catalytic cyclopropanation reactions in water. *Coord. Chem. Rev.* **2008**, *252* (5-7), 727-735.
- 102) Ho, C. M.; Zhang, J. L.; Zhou, C. Y.; Chan, O. Y.; Yan, J. J.; Zhang, F. Y.; Huang, J. S.; Che, C. M. A Water-Soluble Ruthenium Glycosylated Porphyrin Catalyst for Carbenoid Transfer Reactions in Aqueous Media with Applications in Bioconjugation Reactions. *J. Am. Chem. Soc.* **2010**, *132* (6), 1886-1894.
- 103) Kendrew, J. C.; Dickerson, R. E.; Strandberg, B. E.; Hart, R. G.; Davies, D. R.; Phillips, D. C.; Shore, V. C. Structure of Myoglobin - 3-Dimensional Fourier Synthesis at 2 Å Resolution. *Nature* **1960**, *185* (4711), 422-427.
- 104) Lin, L.; Pinker, R. J.; Kallenbach, N. R. Alpha-Helix Stability and the Native-State of Myoglobin. *Biochemistry* **1993**, *32* (47), 12638-12643.

- 105) Teale, F. W. J. Cleavage of the Haem-Protein Link by Acid Methylethylketone. *Biochim. Biophys. Acta* **1959**, 35 (2), 543-543.
- 106) Oohora, K.; Hayashi, T. Reconstitution of Heme Enzymes with Artificial Metalloporphyrinoids. *Method Enzymol.* **2016**, 580, 439-454.
- 107) Paulson, D. R.; Addison, A. W.; Dolphin, D.; James, B. R. Preparation of Ruthenium(II) and Ruthenium(III) Myoglobin and the Reaction of Dioxygen, and Carbon-Monoxide, with Ruthenium(II) Myoglobin. *J. Biol. Chem.* **1979**, 254 (15), 7002-7006.
- 108) Li, C. Z.; Taniguchi, I.; Mulchandani, A. Redox properties of engineered ruthenium myoglobin. *Bioelectrochemistry* **2009**, 75 (2), 182-188.

## Chapter 2

### Engineering Ruthenium Myoglobin for Carbene Transfer Reactions

Heme proteins are useful platforms to develop artificial enzymes as they can be modified through both cofactor replacement and mutagenesis. The Arnold and Fasan groups have demonstrated that heme proteins such as cytochrome P450<sub>BM3</sub> and myoglobin (Mb) can be modified in order to produce very active and stereoselective carbene transfer catalysts.<sup>1-8</sup> Multiple rounds of active-site mutagenesis and reactivity screening through directed evolution can lead to improved product yield and stereoselectivity, though at the expense of gaining a more fundamental understanding of how these modifications improve catalysis.<sup>1-2</sup> Rational design of a catalyst through active-site mutations and cofactor modification is a more time-intensive approach, but can also lead to increased activity and selectivity of the system, and a better understanding of how the second coordination sphere influences reactivity.<sup>3, 6-8</sup> Arnold and Fasan's catalysts are effective at catalyzing cyclopropanation, N-H insertion and other carbene transfer reactions. Cyt. P450<sub>BM3</sub> mutants can catalyze carbene transfer reactions *in vitro* and *in vivo* and can achieve tens of thousands of turnovers.<sup>1-2</sup> In addition, the Arnold group has developed Cyt. P450 mutants for selectively producing *trans* or *cis* cyclopropanes.<sup>1-2</sup> The Fasan group has shown that a double mutant of Mb (H64V, V68A) can achieve over 45,000 total turnovers in the cyclopropanation reaction.<sup>3</sup> However, the use of the native Fe cofactor in these cases means that many of these catalysts are highly dioxygen sensitive, as ferrous hemes bind O<sub>2</sub> tightly in Mb and native Cyt. P450s. Compared to Fe, second and third row transition metal porphyrins such as Ru, Rh, and Ir

are less dioxygen sensitive and are highly active towards carbene transfer reactions as small molecule catalysts.<sup>9-12</sup> Through reconstitution of the apo-protein with a new metalloporphyrin, new catalysts for organometallic reactions can be prepared. Recently, this approach has been successfully used to generate CoMb, MnMb, and IrMb catalysts.<sup>13-14</sup> In parallel investigations, our work has focused on Ru catalysts for carbene insertion reactions. We speculated that modifying myoglobin through the insertion of a Ru porphyrin into the active site would lead to a more active and less dioxygen sensitive catalyst for carbene transfer reactions.

In this chapter, we follow the rational design approach and we report the design of Ru-modified Mb catalysts and their catalytic activity towards cyclopropanation and N-H insertion. For this purpose, we have incorporated Ru mesoporphyrin IX (RuMpIX) into wild-type (wt) Mb as has been previously reported,<sup>15-17</sup> and into Mb mutants and characterized these artificial enzymes using different spectroscopic methods. For reactivity studies, we used ethyl diazoacetate (EDA) as a carbene source, styrene derivatives for the cyclopropanation reactions and aniline derivatives for the N-H insertion reactions. We also studied the pH-dependence of these reactions and compared the results to RuMpIX outside of the protein scaffold. This chapter has been reproduced in part from a manuscript published in *Inorganic Chemistry* (Wolf, M. W.; Vargas, D. A.; Lehnert, N. *Inorg. Chem.* **2017**, *56*, 5623).<sup>18</sup>

## 2.1 Preparation of [RuMpIX(X)]

Mesoporphyrin IX dimethyl ester (MpIXDME) was metallated with Ru<sub>3</sub>CO<sub>12</sub> according to literature procedures to afford [RuMpIXDME(CO)] in 68% yield. The electron absorption spectrum exhibits a typical Soret band feature at 394 nm and Q bands at 517 and 548 nm (**Figure 2.1a**).<sup>15</sup> The IR spectrum shows a C-O stretch at 1925 cm<sup>-1</sup> (**Figure 2.2**). The Ru-CO bond was

photolyzed with 350 nm light *in vacuo* to provide an open coordination site on the Ru center after reconstitution into Mb. After photolysis, the 548 nm band decreases in intensity as the 521 nm band becomes sharper in the UV-vis spectrum (**Figure 2.1b**). The 1925  $\text{cm}^{-1}$  C-O stretch is almost entirely absent after photolysis, indicating that the CO ligand has dissociated from  $\text{Ru}^{\text{II}}$  (**Figure 2.2**). Upon exposure to air,  $\text{Ru}^{\text{II}}$  oxidizes to  $\text{Ru}^{\text{III}}$ . Addition of 1% KOH to  $[\text{Ru}^{\text{III}}\text{MpIXDME}]$  in a methanol/water mixture results in hydrolysis of the ester bonds and increases the solubility of the porphyrin in water. After hydrolysis, the porphyrin is dissolved in 100 mM potassium phosphate buffer and the pH of the solution is adjusted to 7 using HCl. The resulting complex,  $[\text{RuMpIX(X)}]$  is likely bound by a  $\text{Cl}^-$  or  $\text{OH}^-$  ligand in solution.

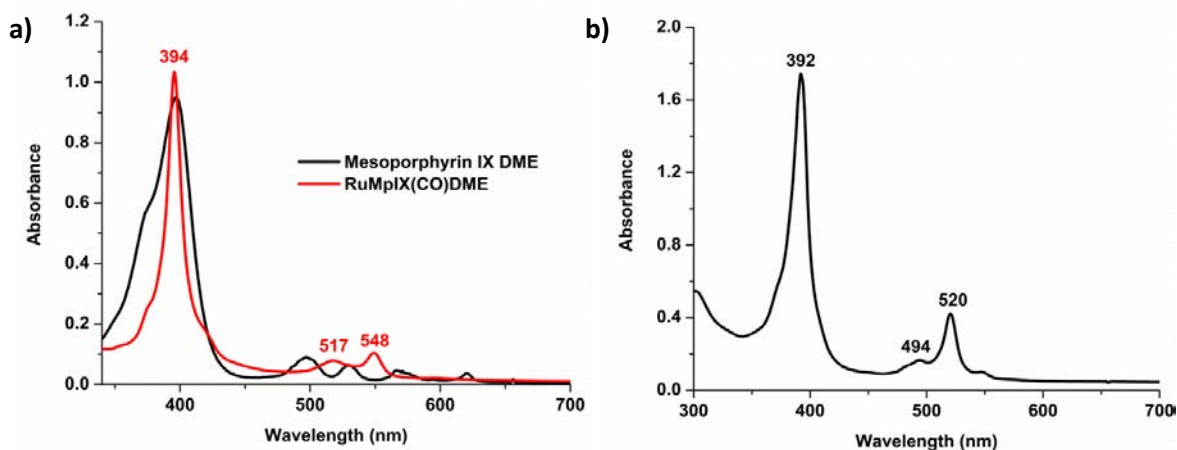


**Figure 2.1.** a) Electronic Absorption spectra of free Mesoporphyrin IX Dimethyl Ester (MpIX DME) and Ruthenium Mesoporphyrin IX Dimethyl Ester Carbonyl ( $[\text{Ru}^{\text{II}}\text{MpIXDME}(\text{CO})]$ ), obtained after metalation with  $\text{Ru}_3(\text{CO})_{12}$ . b) Electronic Absorption spectra of Ruthenium Mesoporphyrin IX Dimethyl Ester ( $[\text{Ru}^{\text{II}}\text{MpIXDME}]$ ) in DMF after photolysis of CO by irradiation with  $\sim 350$  nm light *in vacuo*.

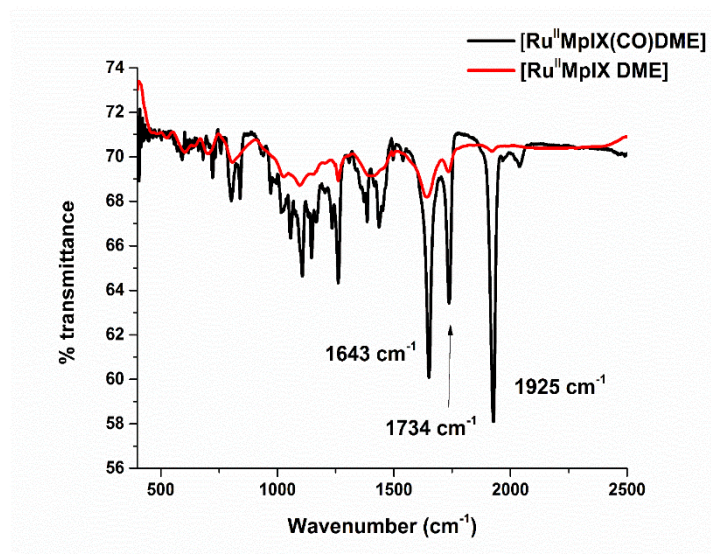


**Figure 2.2.** IR spectra of the KBr pellets of [Ru<sup>II</sup>MpIXDME(CO)] and [Ru<sup>II</sup>MpIXDME] obtained after photolysis of the CO complex.

## 2.2 Protein Preparation and Analysis

For the mutagenesis experiments performed here, we chose His64 as the key target site due to the proximity of His64 to the heme (**Figure 2.3**), and due to the enhancement in carbene transfer reactivity detailed in previous reports upon modification of this amino acid.<sup>3, 6-8</sup> The H64A and H64V mutants were chosen in order to increase the size of the protein active site and, in particular, to provide a more hydrophobic environment for the reactions investigated here. Since our substrates are rather hydrophobic (styrene and aniline derivatives), a more hydrophobic active site

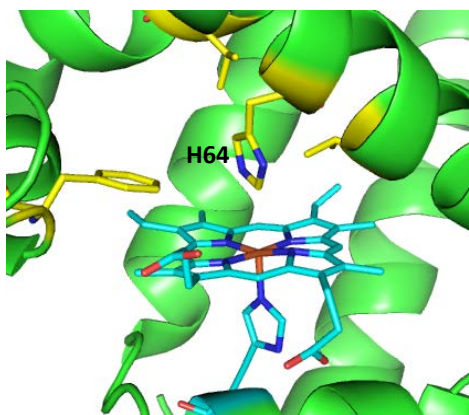


**Figure 2.3.** Close-up of the heme cofactor environment in wild-type sperm whale Mb (image generated using PDB file 1MBO). The His64 residue is in close proximity to the heme, and mutating this residue can greatly impact the function and catalytic properties of the protein. Several other nearby residues are highlighted in yellow.

pocket should allow for better substrate binding, and hence, increased TONs. In the crystal structures of deoxy H64A Mb and ferric H64V Mb no water molecules are present on the distal side of the heme pocket.<sup>19-20</sup> In contrast, the H64D mutant places the more polar Asp residue in the active site, making the active site more hydrophilic, and potentially allowing for stronger H-bonding interactions in the active site compared to His.

The various reconstituted proteins were characterized by UV-vis and CD spectroscopy. The porphyrin Soret band for free [RuMpIX(X)] at 389 nm shifts 1-5 nm to lower energy after incorporation into the protein, and upon reduction of the resulting Ru<sup>III</sup>Mb with Na<sub>2</sub>S<sub>2</sub>O<sub>4</sub>, the Soret band sharpens and Q bands appear at 495 and 520 nm (**Figure 2.4**). In particular, the sharp Q-band at 520 nm is a hallmark for the Ru(II) state of RuMb. The CD spectra show that various RuMb variants retain similar  $\alpha$ -helical structures as wild-type Mb after reconstitution (**Figure 2.5**).

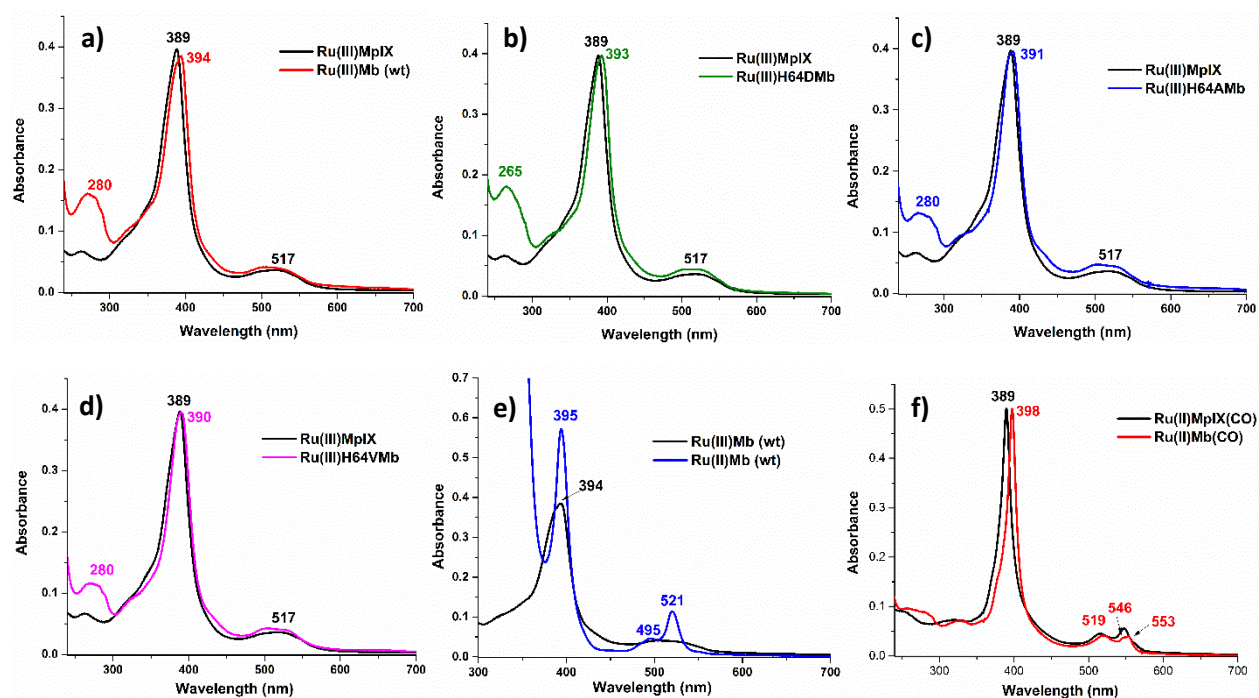


**Figure 2.4.** Electronic absorption spectra comparing free [RuMpIX(X)] to the reconstituted Mb variants (a-d). UV-vis spectrum of Ru<sup>II</sup>Mb after reduction with excess Na<sub>2</sub>S<sub>2</sub>O<sub>4</sub> (e). Spectral comparison of the CO-bound complex [Ru<sup>II</sup>MpIX(CO)] and Ru<sup>II</sup>Mb with CO bound (f).

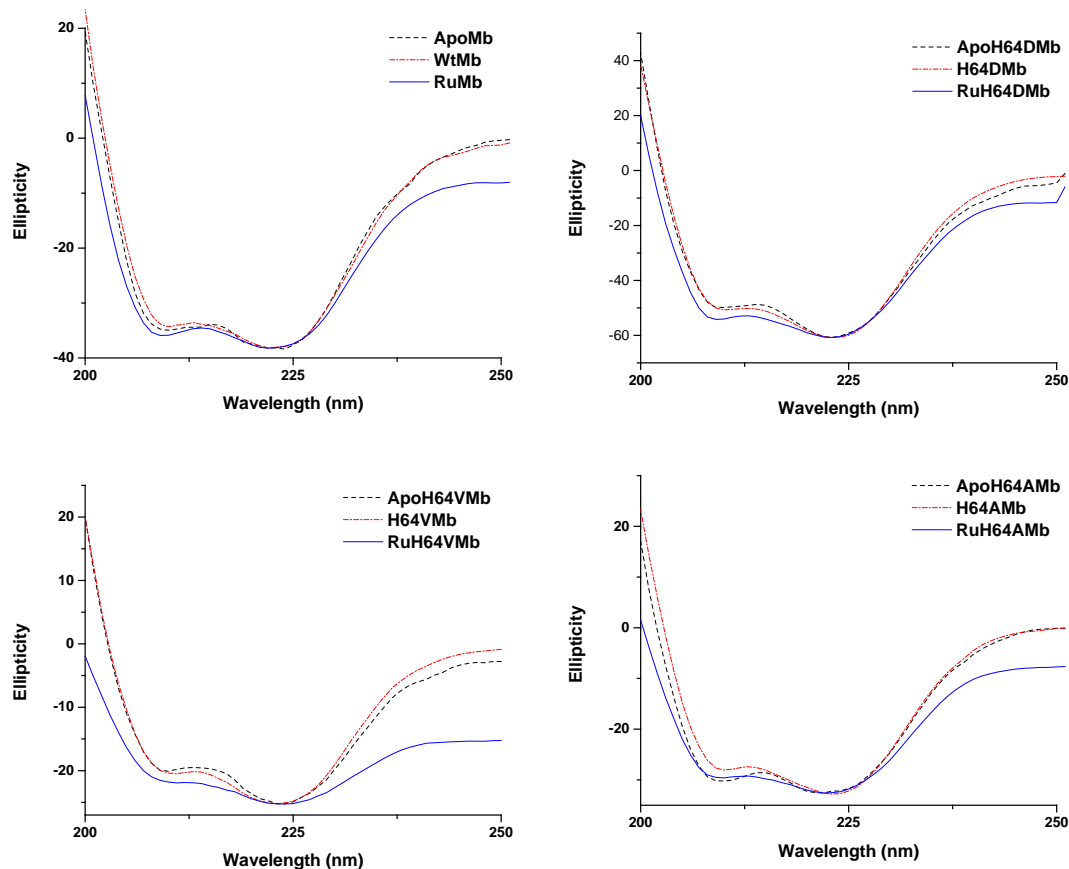


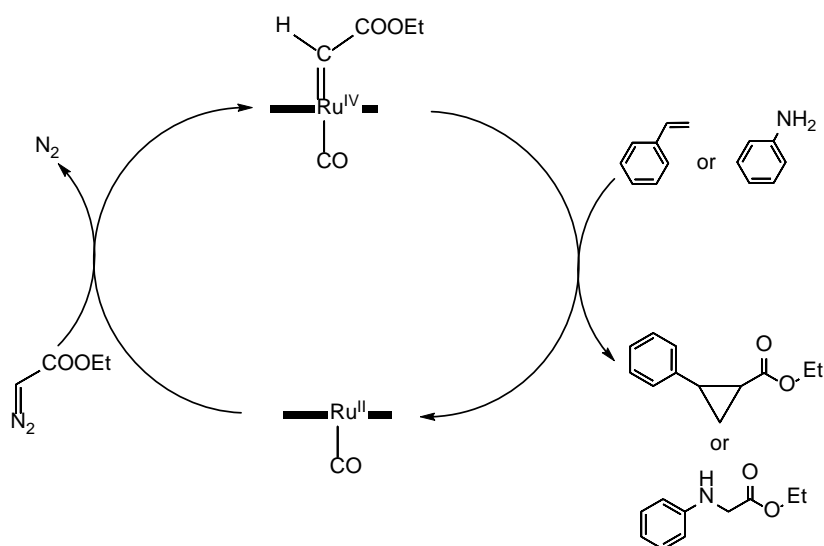
**Figure 2.5.** Circular dichroism spectra of the Mb variants (wild-type, H64A, H64D, H64V) with native heme bound, in the apo-form, and reconstituted with  $[\text{Ru}^{\text{III}}\text{MpIX}(\text{X})]$ .

### 2.3 Reactivity of Free $\text{Ru}^{\text{II}}\text{MpIX}$

Initial work focused on the catalysis of two different carbene transfer reactions by  $\text{Ru}^{\text{II}}\text{MpIX}$ : N-H insertion and cyclopropanation. Reactions were run under micro-anaerobic conditions of 30-45 ppm  $\text{O}_2$  and 1.5-3.0%  $\text{H}_2$ . Control reactions without catalyst were run for each substrate, and the results are listed in Table S1. During the course of these studies, we realized that the  $\text{Ru}^{\text{III}}$  was being reduced to  $\text{Ru}^{\text{II}}$  by the  $\text{H}_2$  inside the glovebox, thus the reactions could be catalyzed without external reductant added. Despite this finding, excess reductant ( $\text{Na}_2\text{S}_2\text{O}_4$ ) was included in each of the subsequent reactions to keep the reaction conditions consistent. At pH 7, the free  $\text{Ru}^{\text{II}}\text{MpIX}$  complex converts aniline to 2-(phenylamino)acetate (**3a**) in 48% yield (Table



**2.1).** The yield increases to 49% when running the reaction at pH 5, and to 67% at pH 3. Ru<sup>II</sup>MpIX further catalyzes the cyclopropanation of styrene to ethyl 2-phenylcyclopropanecarboxylate (**5a**) in 26% yield at pH 7 (Table 2). The free porphyrin in buffer does not induce substantial diastereoselectivity, with only 62% *trans* cyclopropane product observed. When the reaction is performed at pH 5, the yield decreases to 16%, and then further decreases to 11% at pH 3. The stereoselectivity of the products increases slightly at lower pH to 65% *trans* cyclopropane product. In comparison with [RuMpIX(X)], FePpIX (hemin) exhibits lower yields of 27% and 16% for the N-H insertion and cyclopropanation reactions, respectively. However, Fe<sup>II</sup>PpIX does demonstrate significantly higher diastereoselectivity in the cyclopropanation reaction – 87% *trans* product compared to 62% *trans* product produced by [RuMpIX(X)] at pH 7. Carbene transfer reactions were also run with [Ru<sup>II</sup>MpIX(CO)] in pH 7 buffer to compare to the CO-free porphyrin complex (data not shown). [Ru<sup>II</sup>MpIX(CO)] catalyzes the N-H insertion reaction in up to 84% yield and the cyclopropanation of styrene in 27% yield. Using [Ru<sup>II</sup>MpIX(CO)] as the catalyst results in slightly higher diastereoselectivity relative to Ru<sup>II</sup>MpIX with 73% vs. 62% *trans* cyclopropane product. This result implies that the CO group is not replaced when the Ru=CR<sub>2</sub> carbene intermediate is formed in the first step of the reaction, but instead, that the *trans* CO ligand influences the reactivity of the bound carbene with substrate in the second step of the reaction (**Scheme 2.1**). Hence, using porphyrin derivatives, a further fine-tuning of the reactivity of the system should be possible.



**Scheme 2.1.** Putative mechanism for the N-H insertion of aniline and the cyclopropanation of styrene with ethyl diazoacetate catalyzed by a Ru(II) porphyrin with CO bound.

## 2.4 N-H Insertion with RuMb and Mutants

Ru<sup>II</sup>Mb and the other RuMb variants catalyze the N-H insertion of aniline in various yields (**Table 2.1**; all isolated yields). The N-H insertion with aniline is catalyzed by wild-type Ru<sup>II</sup>Mb in 36% yield at pH 7, and in contrast to free Ru<sup>II</sup>MpIX, the yield decreases in the lower pH reactions to 17% and 27% for pH 5 and 3, respectively. The Ru<sup>II</sup>H64DMb catalyst exhibits similar activity to Ru<sup>II</sup>Mb, converting aniline to the desired product in 32% yield at pH 7 and 5, and in 30% yield at pH 3. Hence, lowering the pH has no real effect on the N-H insertion reaction catalyzed by Ru<sup>II</sup>H64DMb. Ru<sup>II</sup>H64VMb, which has a larger and more hydrophobic pocket, exhibits a slightly higher yield of 39% compared to Ru<sup>II</sup>Mb and Ru<sup>II</sup>H64DMb at pH 7. Upon running the reactions at lower pH, the yield decreased dramatically to 19% and 17% for pH 5 and 3, respectively. The Ru<sup>II</sup>H64AMb catalyst exhibits the highest yield of any of the catalysts at pH 7 – 52%. Like Ru<sup>II</sup>H64VMb and Ru<sup>II</sup>Mb, it also catalyzes fewer turnovers at pH 5 and 3 (34% and 35% yield, respectively).

Native myoglobin (FeMb) variants catalyzed the N-H insertion of aniline in relatively similar yields compared to Ru<sup>II</sup>Mb. At 10  $\mu$ M concentration, sperm whale Fe<sup>II</sup>Mb catalyzes the reaction in 39% yield, similar to the 36% yield that Ru<sup>II</sup>Mb achieves. Fe<sup>II</sup>H64DMb and Fe<sup>II</sup>H64AMb exhibit slightly higher yields compared to their Ru-reconstituted counterparts, catalyzing the reaction with 46% and 55% yield, respectively. Wild-type horse heart apo-Mb was also reconstituted with RuMpIX(CO) in order to compare the N-H insertion activity to the CO-free Ru<sup>II</sup>Mb. Ru<sup>II</sup>Mb(CO) achieved up to ~10% yield, much lower than Ru<sup>II</sup>Mb. It's unclear if some of the CO was labilized upon hydrolysis of [RuMpIXDME(CO)] or if some CO leaves during the N-H insertion reaction. Nevertheless, CO inhibits activity, likely due to the fact that in order to form the carbene intermediate, the CO ligand has to be replaced. Removal of CO is inefficient,<sup>16</sup> and this differs from the free [RuMpIX(CO)] complexes, where the metal-carbene bond can be formed in the presence of the CO ligand (in trans position to CO).

**Table 2.1.** Catalytic activity of [RuMpIX], wild-type sperm whale ruthenium myoglobin (RuMb), and the Mb mutants in the N-H insertion reaction with aniline and EDA.

| Catalyst <sup>a</sup> | pH | Yield <sup>b</sup> (%) | TON      |
|-----------------------|----|------------------------|----------|
| RuMpIX                | 7  | 48                     | 482 ± 11 |
|                       | 5  | 49                     | 487 ± 58 |
|                       | 3  | 67                     | 671 ± 56 |
| RuMb                  | 7  | 36                     | 360 ± 37 |
|                       | 5  | 17                     | 172 ± 30 |
|                       | 3  | 27                     | 273 ± 39 |
| RuH64DMb              | 7  | 32                     | 320 ± 39 |
|                       | 5  | 33                     | 325 ± 58 |
|                       | 3  | 30                     | 296 ± 40 |
| RuH64VMb              | 7  | 39                     | 392 ± 37 |
|                       | 5  | 19                     | 191 ± 23 |
|                       | 3  | 17                     | 173 ± 16 |
| RuH64AMb              | 7  | 52                     | 518 ± 78 |
|                       | 5  | 34                     | 342 ± 22 |
|                       | 3  | 35                     | 346 ± 28 |
| FePpIX                | 7  | 27                     | 271 ± 38 |
| FeMb <sup>c</sup>     | 7  | 39                     | 392 ± 54 |
| FeH64DMb              | 7  | 46                     | 461 ± 35 |
| FeH64AMb              | 7  | 55                     | 553 ± 35 |

<sup>a</sup> 450  $\mu$ L scale reactions using 20  $\mu$ M catalyst (0.1 ml %), 10 mM Na<sub>2</sub>S<sub>2</sub>O<sub>4</sub>, 20mM **1a** and 40 mM **2** conducted for 18 hours at room temperature under micro-aerobic conditions. <sup>b</sup> Determined based on GC-MS conversion using a calibration curve with isolated 3a. <sup>c</sup>Data collected with 10  $\mu$ M catalyst.

## 2.5 Cyclopropanation with RuMb and Mutants

The various Ru catalysts also catalyze the cyclopropanation of styrene with ethyl diazoacetate (EDA; see **Table 2.2**), though mostly in relatively low yields. Ru<sup>II</sup>Mb is a poor catalyst, only catalyzing the reaction in 3.2% yield at pH 7. Yield decreases at pH 5 to 1.2%, and rebounded at pH 3 to 3.3%, but the Ru<sup>II</sup>Mb never exhibits high activity for this reaction. This is very surprising, considering the relatively higher activity observed for free [RuMpIX(X)] as

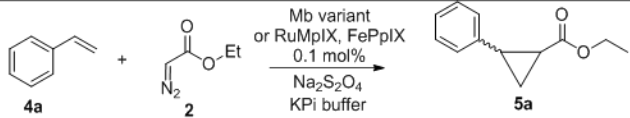
described above. This is also different from the N-H insertion reaction, where Ru<sup>II</sup>Mb shows similar activity compared to free [RuMpIX(X)]. This point is further addressed in the Discussion section, and originates from an unexpected lack of stability of the catalyst. Ru<sup>II</sup>H64DMb demonstrates lower activity but higher stereoselectivity (87% *trans* isomer) compared Ru<sup>II</sup>Mb. Unfortunately, Ru<sup>II</sup>H64D only achieves 0.6% yield at pH 7, and does not improve at lower pH values (0.3% at pH 5 and 0.7% at pH 3). As is the case with Ru<sup>II</sup>Mb, the stereoselectivity decreases at lower pH, but it should be noted that the stereoselectivity is difficult to measure accurately from the GC chromatogram with such low TON. The two variants with more hydrophobic active sites, Ru<sup>II</sup>H64VMb and Ru<sup>II</sup>H64AMb, exhibit higher TON compared to Ru<sup>II</sup>H64DMb. Ru<sup>II</sup>H64VMb exhibits 3.9% conversion at pH 7, which increases to 6.8% and 8.4% conversion at pH 5 and 3, respectively. Ru<sup>II</sup>H64AMb is a worse catalyst compared to Ru<sup>II</sup>H64VMb and Ru<sup>II</sup>Mb, exhibiting a yield of 1.7% at pH 7. Yields increase slightly to 3.0% and 2.3% at pH 5 and 3, respectively, but still do not match the activity of Ru<sup>II</sup>H64VMb.

None of our first-generation artificial enzymes demonstrate high product diastereoselectivity, but there are some notable differences between the proteins. Ru<sup>II</sup>Mb exhibits good stereoselectivity – 80% *trans* isomer at pH 7, and the stereoselectivity decreases at lower pH, down to 65% *trans* isomer at pH 3. The stereoselectivity of the wild-type variant at neutral pH is therefore higher compared to the intrinsic stereoselectivity of free [Ru<sup>II</sup>MpIX], which produces the *trans* diastereomer at 63 – 66% yield. Ru<sup>II</sup>H64DMb demonstrates the best product stereoselectivity of all catalysts tested here, producing 87% *trans* isomer at pH 7, significantly higher than free Ru<sup>II</sup>MpIX. The diastereoselectivity of the cyclopropane product induced by Ru<sup>II</sup>H64VMb is relatively small, ranging in between 70-74% at different pH values. Ru<sup>II</sup>H64AMb exhibits the lowest diastereoselectivity of the different protein catalysts, with only 69% *trans* isomer at pH 7,

59% at pH 5, and 68% at pH 3 produced. In conclusion, Ru<sup>II</sup>H64VMb and Ru<sup>II</sup>H64AMb, the two more hydrophobic proteins with the least sterically congested active sites, demonstrate similar stereoselectivity to the free Ru<sup>II</sup>MpIX complex. These results indicate that increased steric bulk in close proximity of the heme, as in the D mutant, may increase stereoselectivity, but in the case of the H64D mutant, product yield is compromised in our Ru-reconstituted catalyst. It remains to be seen whether a bulky, but non-polar amino acid at the H64 position could lead to increased product yield.

In contrast to RuMb and the RuMb variants, FeMb variants demonstrate increased TON and diastereoselectivity for the cyclopropanation of styrene. Fe<sup>II</sup>Mb (sperm whale) exhibits 25% conversion to product at pH 7, and produces 91% *trans* product. Horse heart myoglobin actually achieves a higher product yield (36%) compared to sperm whale myoglobin, though it exhibits the same diastereoselectivity (93% *trans* product) as is expected. Fe<sup>II</sup>H64DMb and Fe<sup>II</sup>H64AMb achieve 31% yield and 29% yield respectively. Similar to Ru<sup>II</sup>H64DMb, Fe<sup>II</sup>H64DMb induces the highest diastereoselectivity of the FeMb variants, but its selectivity is even more impressive compared to Ru<sup>II</sup>H64DMb, as it achieves up to 96% *trans* product. The Fasan lab investigated Fe<sup>II</sup>H64VMb, and were able to achieve 73% conversion to product and 92% *trans* product at pH 8, although these reactions were run at higher catalyst loading.<sup>3</sup> Nevertheless, it's clear that FeMb variants are much more effective at catalyzing the cyclopropanation of styrene and EDA compared to their RuMb counterparts.

**Table 2.2.** Catalytic activity of [RuMpIX], wild-type horse heart ruthenium myoglobin (RuMb), and sperm whale Mb(H64D, H64A, H64V) variants in the cyclopropanation reaction with styrene and EDA.



| Catalyst <sup>a</sup> | pH | Yield <sup>b</sup><br>(%) | TON       | % <i>trans</i><br>diastereomer |
|-----------------------|----|---------------------------|-----------|--------------------------------|
| [RuMpIX]              | 7  | 26                        | 263 ± 121 | 62                             |
|                       | 5  | 16                        | 162 ± 16  | 65                             |
|                       | 3  | 11                        | 114 ± 48  | 65                             |
| RuMb                  | 7  | 3.2                       | 32 ± 12   | 80                             |
|                       | 5  | 1.2                       | 12 ± 4.9  | 68                             |
|                       | 3  | 3.3                       | 33 ± 5.7  | 65                             |
| RuH64DMb              | 7  | 0.6                       | 5.8 ± 0.3 | 87                             |
|                       | 5  | 0.3                       | 2.9 ± 1.1 | 79                             |
|                       | 3  | 0.7                       | 7.4 ± 3.7 | 78                             |
| RuH64VMb              | 7  | 3.7                       | 39 ± 7.0  | 72                             |
|                       | 5  | 6.6                       | 68 ± 14   | 70                             |
|                       | 3  | 8                         | 84 ± 8.0  | 74                             |
| RuH64AMb              | 7  | 1.7                       | 17 ± 4.6  | 69                             |
|                       | 5  | 2.9                       | 29 ± 9.0  | 59                             |
|                       | 3  | 2.2                       | 22 ± 3.0  | 68                             |
| [FePpIX]              | 7  | 16                        | 158 ± 64  | 87                             |
| FeMb (sperm whale)    | 7  | 25                        | 248 ± 28  | 91                             |
| FeMb (horse heart)    | 7  | 36                        | 360 ± 22  | 93                             |
| FeH64DMb              | 7  | 31                        | 305 ± 25  | 96                             |
| FeH64VMb <sup>c</sup> | 8  | 73                        | 365       | 92                             |
| FeH64AMb              | 7  | 29                        | 287 ± 15  | 94                             |

<sup>a</sup> 450  $\mu$ L scale reactions using 20  $\mu$ M catalyst (0.1 ml %), 10 mM  $\text{Na}_2\text{S}_2\text{O}_4$ , 20mM **4a** and 40 mM **2** conducted for 18 hours at room temperature under micro-aerobic conditions. <sup>b</sup> Determined based on GC-MS conversion using a calibration curve with isolated **5a**. <sup>c</sup> Data from ref (3), reaction conditions were slightly different from this work.

## 2.6 Substrate Scopes

In order to conduct a substrate scope determination for the N-H insertion and cyclopropanation reactions, several *para*-substituted aniline and styrene derivatives were used. Ru<sup>II</sup>H64AMb achieves the highest TON for the N-H insertion reaction and provides a larger active

site pocket for bulkier aniline and styrene derivatives, and thus Ru<sup>II</sup>H64AMb was chosen as the catalyst for investigating substrate scopes. Ru<sup>II</sup>H64AMb catalyzes the N-H insertion of 4-methylaniline, 4-chloroaniline, 4-trifluoromethylaniline, and 4-vinylaniline in moderate yield (36%, 33%, 45% and 15%, respectively), whereas the substrates 4-nitroaniline and 4-methoxyaniline exhibit very low yields (2.9% and 5.7%) for their respective amine products (**Table 2.3**). The high yield for the reaction with 4-trifluoromethylaniline is particularly surprising, as it was expected that aniline derivatives with more electron-withdrawing groups such as -CF<sub>3</sub> would be worse nucleophiles and thus worse substrates for interacting with the electrophilic metal-carbene bond. Correspondingly, 4-nitroaniline with the electron-withdrawing -NO<sub>2</sub> group exhibits a very low yield, in agreement with these expectations. In contrast, the 4-methoxyaniline with an electron-donating -OCH<sub>3</sub> group also exhibits a very low yield for the N-H insertion reaction, again negating the simple explanation that product yield is solely correlated with the electronic nature of the aniline. Clearly, other factors must also be at work (see Discussion). As a substrate, 4-vinylaniline can potentially undergo both N-H insertion and cyclopropanation. The N-H insertion product is the only product observed in the GC/MS chromatogram (15% yield), which concurs with Ru<sup>II</sup>H64AMb exhibiting much higher product conversion when using aniline as the substrate compared to styrene. Ru<sup>II</sup>Mb also exhibits the same preference for N-H insertion over cyclopropanation when adding aniline and styrene to the reaction mixture simultaneously; the catalyst achieves 37% yield for the N-H insertion of aniline, and only 1% yield for the cyclopropanation of styrene (at 0.2 mol% catalyst loading for each substrate, data not shown). This is also the case for Fe<sup>II</sup>Mb, achieving up to 81% yield for the N-H insertion of aniline at 0.2 mol% catalyst loading and 3% yield for the cyclopropanation of styrene.



**Table 2.3.** Substrate scope for N-H insertion reaction catalyzed by RuH64AMb.

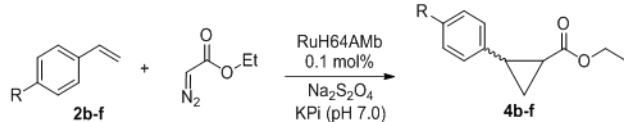
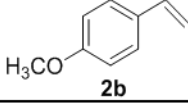
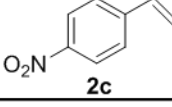
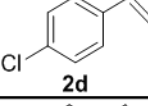
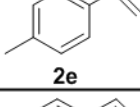
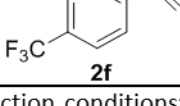
| Substrate | Product   | Yield <sup>b</sup> (%) | TON      |
|-----------|-----------|------------------------|----------|
|           | <b>3b</b> | 5.7                    | 57 ± 24  |
|           | <b>3c</b> | 3.0                    | 29 ± 8.3 |
|           | <b>3d</b> | 33                     | 327 ± 34 |
|           | <b>3e</b> | 36                     | 358 ± 13 |
|           | <b>3f</b> | 45                     | 451 ± 62 |
|           | <b>3g</b> | 15                     | 145 ± 31 |

Reaction conditions: 20 μM RuH64AMb (0.1 mol%), 20mM **1b-f**, 40 mM EDA, and 10 mM sodium dithionite conducted for 18 hours at room temperature in micro-aerobic conditions. <sup>b</sup> Determined based on GC-MS conversion using a calibration curve with isolated **3b-3f**.

The cyclopropanation substrate scope was also investigated using Ru<sup>II</sup>H64AMb. Several styrene derivatives were examined for cyclopropanation activity, with the functional groups analogous to the aniline derivatives discussed earlier (**Table 2.4**). All of the derivatives show higher activity compared to styrene. 4-methoxystyrene demonstrates by far the highest yield (36%) compared to the other substrates. 4-chlorostyrene shows a moderate conversion to the product (15%), and all other substrates exhibit lower yields – 7.3%, 7.1%, and 2.7% for 4-methylstyrene,

4-nitrostyrene, and 4-trifluoromethylstyrene, respectively. The lower yield is expected for 4-nitrostyrene and 4-trifluoromethylstyrene with the electron-withdrawing  $-\text{NO}_2$  and  $-\text{CF}_3$  groups, but not for 4-methylstyrene with the slightly electron-donating  $-\text{CH}_3$  group. Almost all the substrates exhibit similar diastereoselectivity, yielding 67-72% of the *trans* isomer. The only exception to this is 4-nitrostyrene, which exhibits only 52% generation of the *trans* cyclopropane product, nearly a 1:1 mixture of both diastereomers.

**Table 2.4.** Substrate scope for cyclopropanation catalyzed by RuH64AMb.

|                |           |                        |          |                             |
|--|-----------|------------------------|----------|-----------------------------|
| Substrate  | Product   | Yield <sup>a</sup> (%) | TON      | % <i>trans</i> diastereomer |
| <br><b>2b</b>  | <b>4b</b> | 36                     | 355 ± 12 | 72                          |
| <br><b>2c</b> | <b>4c</b> | 7.1                    | 71 ± 20  | 52                          |
| <br><b>2d</b> | <b>4d</b> | 15                     | 153 ± 27 | 69                          |
| <br><b>2e</b> | <b>4e</b> | 7.3                    | 73 ± 21  | 71                          |
| <br><b>2f</b> | <b>4f</b> | 2.7                    | 27 ± 9.1 | 67                          |

<sup>a</sup> Reaction conditions: 20 μM RuH64AMb (0.1 mol %), 20mM **2b-f**, 40 mM EDA, and 10 mM sodium dithionite conducted for 18 hours at room temperature in micro-anaerobic conditions.

<sup>b</sup> Determined based on GC-MS conversion using a calibration curve with isolated 4b-4f.

## 2.7 Stability of RuMb

In order to better understand the low catalytic activity of Ru<sup>II</sup>Mb towards cyclopropanation, especially in comparison to native FeMb as reported by the Fasan group (see Introduction), the stability of the modified protein after addition of EDA was investigated by UV-vis spectroscopy and mass spectrometry. After the addition of reductant and EDA to RuMb in a sealed cuvette, a rapid decrease in the Soret band absorbance at 396 nm occurs (**Figure 2.6b**). The Soret band absorbance decreases from 0.47 to 0.26 over the course of 20 min, and decreases further to 0.22 after 60 min. In addition, the Q band absorbance at 522 nm also decreases over the course of 60 min. In contrast, the Soret band of native horse heart Mb decreases only slightly over 60 min from 0.56 to 0.45, and minimal spectral changes occur for the Q band at 556 nm (**Figure 2.6a**). These results indicate that the Fe<sup>II</sup>Mb catalyst is still active for over an hour after the addition of EDA, whereas Ru<sup>II</sup>Mb appears to be quickly degrading under the same conditions. This indicated to us that the Ru<sup>II</sup>=CR<sub>2</sub> species that forms in the first step of catalysis may be attacking the porphyrin itself or amino acids in the active site of the protein.

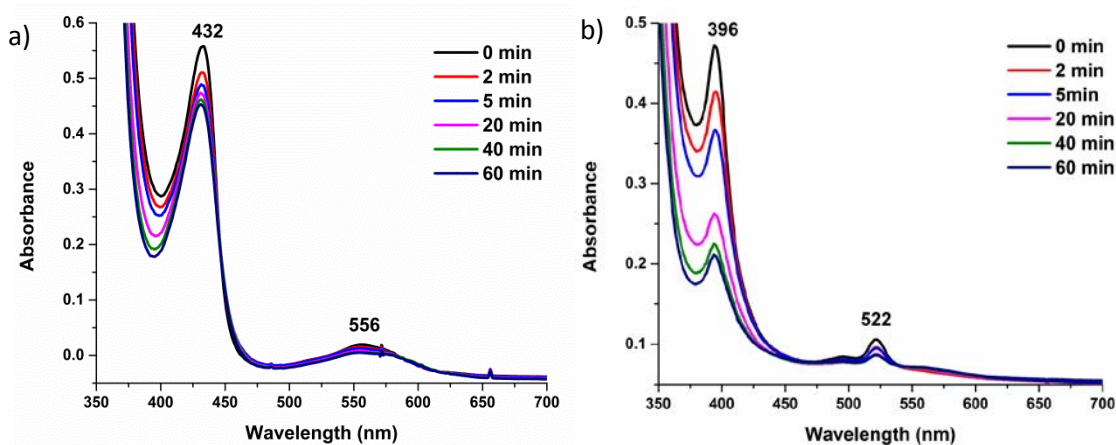


**Figure 2.6.** Electronic absorption spectra of a) 5  $\mu\text{M}$  native sperm whale myoglobin after adding 5000 equivalents of  $\text{Na}_2\text{S}_2\text{O}_4$  and 2000 equivalents of ethyl diazoacetate and b) 5  $\mu\text{M}$  RuMb under the same conditions.

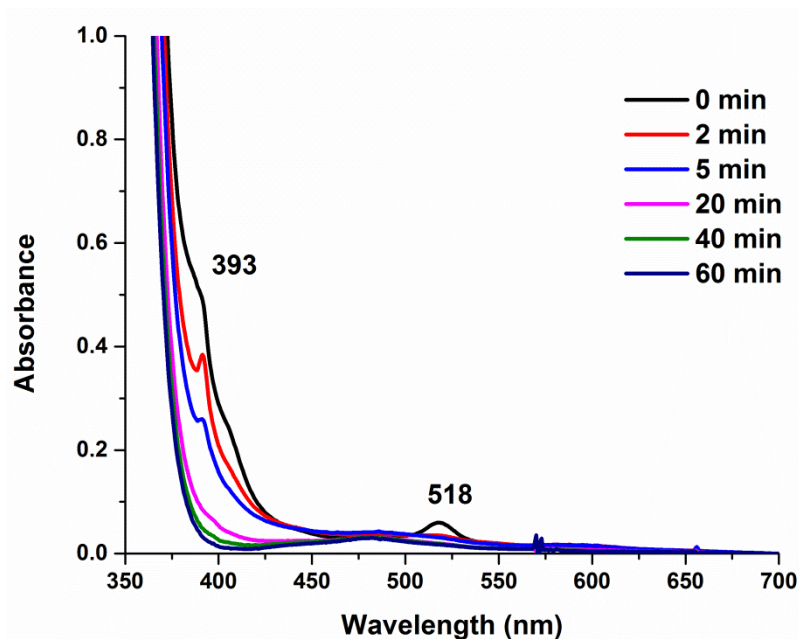


**Figure 2.7.** Electronic absorption spectra of 5  $\mu\text{M}$  [RuMpIX(X)] after adding 5000 equivalents of  $\text{Na}_2\text{S}_2\text{O}_4$  and 2000 equivalents of ethyl diazoacetate.

To investigate this further, mass spectra of sperm whale Mb and RuMb were taken before and after the cyclopropanation reactions to determine whether the metal-carbene unit could attack and modify the protein backbone. The mass spectrum of horse heart myoglobin shows a deconvoluted peak at 16951.7 amu, the mass of the protein scaffold without the native cofactor (which is likely lost from the protein during ionization) (**Figure 2.7a**). After a 3 hr reaction with styrene and EDA, two larger mass peaks are visible – at 16951.7 amu and 17037.9 amu (**Figure 2.7b**). The mass of the native protein increased by 86.2 amu, which is equivalent to the mass of EDA minus dinitrogen. Both the unmodified and carbene modified protein exist in solution 3 hours into the reaction, which shows that the catalyst is still active after this time period. The mass of RuMb (sperm whale) appears at 17995.4 amu (**Figure 2.7c**). Interestingly, RuMpIX appears to still be bound to the protein in this case. After reaction with styrene and EDA, a larger mass peak appears at 18081.4 amu, followed by a forest of smaller peaks with higher masses, indicative of heavy protein modification and degradation (**Figure 2.7d**). The main signal at 18081.4 amu shows

an increased mass of 86.0 amu compared to RuMb, once again corresponding to the addition of one carbene unit to the protein (or potentially the porphyrin). Some of the other smaller peaks likely result from multiple additions of EDA to the protein. It is unclear at this point which protein residue or residues get modified by the metal-carbene species, but it is clear that RuMb is heavily modified in the presence of EDA, with the metal-carbene likely inserting into both the protein scaffold and even the porphyrin. The latter is indicated by the fast bleaching of the Soret band as shown in **Figure 2.6b**. This leads to a quick loss of catalytic competency of RuMb.

The degradation of free RuMpIX(X) in the presence of EDA was also investigated by UV-vis spectroscopy and mass spectrometry. The UV-vis demonstrates a rapid decrease in the Soret band intensity over the course of just 20 minutes after the addition of 2000 EDA equivalents. (**Figure 2.7**). A complete disappearance of the free RuMpIX(X) mass at 666.18 m/z is observed 15 min into the catalytic reaction between EDA and styrene (data not shown). It's clear that the Ru porphyrin both inside and outside the protein scaffold quickly degrades upon the addition of EDA.

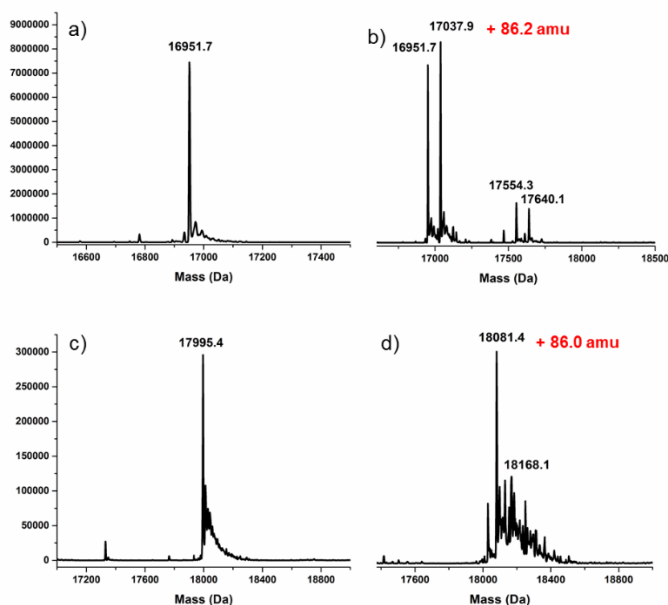


**Figure 2.8.** Mass spectra of a) horse heart Mb, b) horse heart Mb after adding 500 equiv. reductant, 1000 equiv. styrene, and 2000 equiv. EDA, c) RuMb, d) RuMb after adding 500 equiv. reductant, 1000 equiv. styrene, and 2000 equiv. EDA.

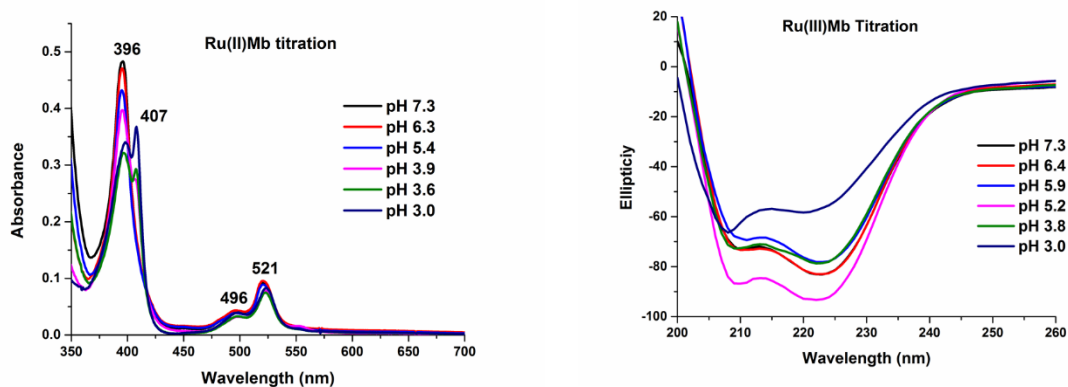


**Figure 2.9.** a) Electronic absorption spectra of Ru<sup>II</sup>Mb in 100 mM KPi buffer at different pH values. b) Circular dichroism of Ru<sup>III</sup>Mb at different pH values.

The stability of Ru<sup>II</sup>Mb was also investigated as a function of pH to potentially gain insight into reactivity differences at pH 7, 5, and 3. In between pH 5.4 and pH 3.9, the electronic absorption spectrum shows a significant change in the Soret band region (**Figure 2.9a**). The initial Soret band at 396 nm decreases and a new band appears at 407 nm. This directly indicates protonation of a basic residue in the active site of Mb, close to the Ru-porphyrin unit. The two resulting species coexist in the spectra at low pH. Importantly, neither one of the two species in solution shows an UV-vis spectrum that matches up with that of free Ru<sup>II</sup>MpIX at low pH (**Figure 2.10**), indicating that the Ru-porphyrin is not released from the protein. The circular dichroism spectra of Ru<sup>III</sup>Mb show a significant decrease in the well at 222 nm at pH 3.0 (**Figure 2.9b**). At pH 3, sperm whale myoglobin therefore exists in a partially unfolded intermediate state, and we observe a corresponding decrease in ellipticity.<sup>37</sup> However, it appears that much of the Ru<sup>II</sup>MpIX is still bound in the protein active site. Besides the UV-Vis data, further evidence that Ru-porphyrin is not released from Mb at pH 3.0 is provided by the fact that RuMpIX would catalyze the cyclopropanation reaction in much higher yield compared to RuMb. At pH 5.0, RuMb is still properly folded as expected.

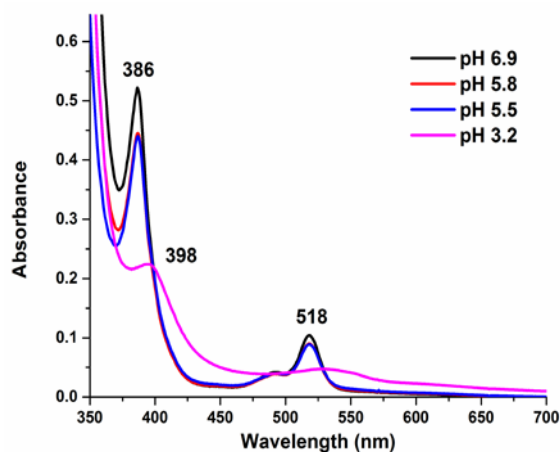


**Figure 2.10.** Electronic Absorption spectra of [Ru<sup>II</sup> MpIX] at different pH values.

## Discussion

In this chapter, the reactivity of Ru<sup>II</sup>Mb and corresponding distal His (H64) mutants to mediate carbene transfer reactions in water was investigated. Activity towards the N-H insertion of aniline is comparable between free Ru<sup>II</sup>MpIX, Ru<sup>II</sup>Mb variants, and Fe<sup>II</sup>Mb variants with Ru<sup>II</sup>H64AMb and Fe<sup>II</sup>H64AMb achieving the highest TON (520 and 550 at pH 7, respectively) for this reaction among our selected catalysts. In contrast, TONs decrease among all of the Ru<sup>II</sup>Mb variants compared to free [Ru<sup>II</sup>MpIX] and Fe<sup>II</sup>Mb variants for the cyclopropanation of styrene. The best Ru protein catalyst for the cyclopropanation of styrene is Ru<sup>II</sup>H64VMb, achieving up to ~39 TON at pH 7 and ~84 TON at pH 3, but the free Ru<sup>II</sup>MpIX demonstrates higher activity, catalyzing the reaction in up to ~260 TON at pH 7. Ru<sup>II</sup>Mb and Ru<sup>II</sup>H64DMb induce increased stereoselectivity during the cyclopropanation reaction, producing 80% and 87% *trans* isomer, respectively. Neither of the more hydrophobic variants, Ru<sup>II</sup>H64VMb and Ru<sup>II</sup>H64AMb, induce significant stereoselectivity compared to the intrinsic porphyrin stereoselectivity of 62-65% *trans* isomer. Despite the low activity observed for the cyclopropanation reaction, the Mb variants with larger and more hydrophobic active sites (Ru<sup>II</sup>H64AMb and Ru<sup>II</sup>H64VMb) achieve higher TON

for the N-H insertion reaction and Ru<sup>II</sup>H64VMb also exhibits higher TON for the cyclopropanation reaction compared to Ru<sup>II</sup>Mb and Ru<sup>II</sup>H64DMb (**Tables 2.1 and 2.2**). This is likely due to the hydrophobic nature of the substrates aniline and styrene, allowing for more facile entrance into the hydrophobic active site of Ru<sup>II</sup>H64VMb. This indicates that one way to prepare more active catalysts (for the substrates considered here) would be to further modify the active site to increase the hydrophobicity. Mutagenesis of other active-site residues to more hydrophobic amino acids will likely aid in this endeavor. Active-site mutations around the porphyrin would also aim to increase product stereoselectivity as the Ru<sup>II</sup>H64AMb and Ru<sup>II</sup>H64VMb catalysts only achieve 59-69% and 70-74% *trans* isomer, respectively, which is comparable to the selectivity of the free Ru<sup>II</sup>MpIX (63-65% *trans* isomer). The low stereoselectivity of the H64A and V mutants is likely due to the fact that they have very open active sites with little steric strain. Addition of more bulky, hydrophobic amino acids would be a straight-forward way to improve on this in the future.

It is also evident that the pH of the solution plays a role in determining the TON for these carbene transfer reactions, in particular in the case of the N-H insertion reaction. For most of the cyclopropanation reactions, it is difficult to discern a trend in reactivity as a function of pH due to low catalytic activity. In the case of Ru<sup>II</sup>H64VMb, however, there is a clear increase in observed reactivity as pH decreases (3.7% yield at pH7 to 8% yield at pH 3). Our results point towards two possible explanations for this observation. First, the acid titration study of Ru<sup>II</sup>Mb shows the appearance of a new Soret band at 407 nm at low pH, which indicates the formation of a protonated form of RuMb below pH 5.4 (**Figure 2.9**) where the vicinity of the Ru-porphyrin has been modified. We do not expect that this originates from the simple Ru<sup>II</sup>-OH<sub>2</sub>/Ru<sup>II</sup>-OH<sup>-</sup> equilibrium, since the pK<sub>A</sub> of water bound to divalent transition metal porphyrin complexes usually lies in the 9 – 11 range. This distal His may be protonated at this pH, but it is unclear if His protonation would



result in such a dramatic change in the absorption spectrum. At pH = 3, unfolding of the protein is further observed. Despite sperm whale myoglobin existing in a partially unfolded intermediate state below pH 5, our data show that the RuMpIX cofactor is not released at pH = 3, since free RuMpIX has characteristic UV-vis features. Though it is not entirely clear if the RuMpIX cofactor is binding at other sites of the slightly unfolded protein instead of just at His93 at lower pH. In any case, the protonation of the protein in the vicinity of the Ru-porphyrin unit and/or the more dynamic structure of the protein around pH = 3 are responsible for the observed changes in catalytic activity at low pH, leading to an increase in cyclopropanation activity. Second, for the N-H insertions at lower pH, the amine group of the styrene substrate will become protonated (and this is also a function of the exact nature of the aniline derivative), forming an anilinium cation. Aniline has a pK<sub>a</sub> of 4.58, and therefore, at pH <5 a significant percentage of the substrate is in the protonated anilinium form. Since the Mb active site is hydrophobic (especially in the H64A and H64V mutants), we can expect that the protonated anilinium ion cannot readily enter the Mb active site, and hence, the second step of the reaction now becomes unfavorable at lower pH. This is exactly what we observe for the N-H insertion reaction. In further agreement with this idea, this trend is reversed for free [Ru<sup>II</sup>MpIX], due to the fact that active site access is not a factor for the carbene insertion reactions of the free Ru-porphyrin complex. In addition, in the H64D mutant, an anionic carboxylate group is present in the active site. This might explain why H64D does not show any dependence of the TON on pH: in this case, the anionic carboxylate group might allow for a facile entrance of the anilinium cation into the active site, forming an ion pair, and the carboxylate side chain could assist in deprotonating the anilinium group during the N-H insertion step.

It is clear that the Ru<sup>II</sup>Mb catalysts are much better at catalyzing the N-H insertion of aniline compared to the cyclopropanation of styrene, despite both reactions using EDA as the carbene source and the fact that both reactions are catalyzed by free [Ru<sup>II</sup>MpIX] in good yields. However, aniline is 120 times more soluble than styrene in water, and thus aniline has easier access to the protein active site in comparison to styrene.<sup>21-22</sup> Addition of styrene to the buffer and protein solution causes the solution to become slightly cloudy, indicating the poor solubility of styrenes in the aqueous phase. This would explain why N-H insertion reactions with RuMb give much higher TON compared to cyclopropanation. This does, however, NOT explain the discrepancy in TON and stereoselectivity between RuMb and native sperm whale Mb and its variants that use iron in the active site (referred to as “FeMb” here for clarity): as first reported by the Fasan group (see Introduction), FeMb is a good catalyst for the cyclopropanation of styrenes with EDA. For direct comparison, we used sperm whale Fe<sup>II</sup>Mb and found that it catalyzes the cyclopropanation of styrene in 25% yield with 91% *trans* product formed, which is in stark contrast to the 3% yield and 80% *trans* product produced by Ru<sup>II</sup>Mb under equivalent conditions. We had anticipated that FeMb would not catalyze carbene transfer reactions under a 30-50 ppm O<sub>2</sub> atmosphere due to the high affinity of Fe<sup>II</sup>Mb towards binding O<sub>2</sub>, but the excess of reductant allows for consumption of any dissolved O<sub>2</sub> and for catalysis to proceed. The discrepancy in reactivity between FeMb and RuMb was initially attributed to an intrinsically lower carbene transfer activity of RuMpIX, but our data on the reactivity of free RuMpIX versus FePpIX actually show that the opposite is true, and that the Ru-porphyrin is the more active catalyst. We then turned to UV-vis and mass spectrometry to determine whether this difference between RuMb and FeMb could actually originate from differences in catalyst stability, which is an often overlooked aspect in the field of biocatalysis (but there is a notable exception from this: in a paper from the Arnold group that just

appeared in the literature, Cyt. P450 degradation under carbene transfer conditions was reported).<sup>23</sup> After adding EDA to both Fe<sup>II</sup>Mb and Ru<sup>II</sup>Mb under identical conditions, we observed a rapid decrease in the Soret band of Ru<sup>II</sup>Mb via UV-vis measurements, which we propose is due to the metal-carbene moiety modifying the active site of RuMb and the RuMpIX catalyst itself; the latter being indicated by the rapid bleaching of the Soret band (**Figure 2.6**). In stark contrast, Fe<sup>II</sup>Mb appears relatively stable over the course of at least one hour. Further insight into this issue is provided by mass spectrometry: after the reaction with styrene and EDA, RuMb shows that the mass of EDA (minus dinitrogen) has been added to the protein. The corresponding signal in the mass spectrum is accompanied by a forest of peaks at higher masses that indicate the presence of species where multiple EDA units have been added to the protein, plus heavy degradation of the protein itself (**Figure 2.8**). In contrast, the spectrum of Fe<sup>II</sup>Mb under the same conditions shows only two species: the unmodified (original) protein, plus a species where the mass of one EDA (minus dinitrogen) has been added to the protein matrix. These results demonstrate that opposite to our intuition, the Ru<sup>II</sup>=CR<sub>2</sub> unit is actually the more reactive carbene transfer catalyst compared to iron – leading to carbene transfer to the protein scaffold and the heme and in this way, causing relatively fast catalyst degradation. The rapid degradation of RuMb helps to explain both the low TON observed for cyclopropanation and the discrepancy in stereoselectivity between the Fe and Ru versions of the same protein. The low TON observed for cyclopropanation with RuMb and its variants is due to the fact that the concentration of substrate (styrene) is low (due to solubility) under the reaction conditions, leading to fast catalyst degradation. In contrast, the more stable FeMb is able to sustain catalysis much longer, resulting in higher TON after the typical 18 hours of reaction time. It is likely that the Ru<sup>II</sup>=CR<sub>2</sub> moiety also quickly modifies residues in the active site of the protein, changing the geometry of the active site, and thus leading to a difference in

product stereoselectivity. Our mass spectrometry gives evidence to support this hypothesis, as only minor modification of FeMb was observed relative to RuMb. Based on our results, all RuMb catalyst is in fact degraded in under 1 hour. On the other hand, the Ru<sup>II</sup>Mb catalysts exhibit similar reactivity to the free Ru<sup>II</sup>MpIX for N-H insertion, since in this case the more soluble and more reactive aniline substrate is able to intercept the Ru<sup>II</sup>=CR<sub>2</sub> unit before carbene transfer to the protein matrix or the heme can take place. We therefore conclude that the low solubility of styrene and some of the styrene derivatives under our reaction conditions is a major factor in the low activity for the cyclopropanation reaction of RuMb. RuMb therefore has great potential to be developed into a highly reactive carbene transfer catalyst, if these stability issues can be overcome. Arnold and coworkers have previously improved catalytic activity by studying the decomposition of Cyt. P450s,<sup>23</sup> making key modifications to the protein scaffold.

The substrate scope studies yielded a surprising result for the N-H insertion reaction: 4-trifluoromethylaniline exhibits a higher yield (45%) compared to the other substrates, with the exception of aniline. The electron-withdrawing -CF<sub>3</sub> group was expected to decrease the nucleophilicity of the aniline and thus exhibit less reactivity with the electrophilic Ru-carbene unit. On the other hand, the 4-methoxyaniline substrate exhibits a yield of only 5.7% for the reaction, which is much lower than expected for a substrate with the more electron-donating -OCH<sub>3</sub> group. For the styrene derivatives with the same *para*-substitutions, the relative reactivity is inverted: 4-methoxystyrene is the most reactive substrate (35% yield), whereas 4-trifluoromethylstyrene is the least reactive (2.7% yield). Clearly, besides electronic effects of the substrate, there are additional effects at work that influence the outcome of the reaction as discussed above. This includes, in particular, differences in pK<sub>A</sub> (anilines) and water solubility. In the case of the -OCH<sub>3</sub> group, 4-methoxystyrene may be more water soluble compared to styrene and some of the other substrates,

which would make it more available (higher effective concentration) at the very beginning of the reaction, increasing the yield before catalyst degradation occurs. On the other hand, 4-methoxyaniline acts as a poorer substrate in the N-H insertion reaction, because the methoxy group increases basicity, which leads to a higher  $pK_A$  ( $pK_A = 5.29$ ) and increased formation of the anilinium cation, hindering access of the substrate to the active site. It seems therefore evident that substrate solubility under catalytic conditions may play a significant role in reactivity. Despite 4-methylstyrene possessing a slightly electron-donating  $-CH_3$  group, it is expected to have lower solubility compared to some of the other substrates, and the yield with this substrate is comparable to 4-nitrostyrene (16% vs. 15%), much lower than for 4-chlorostyrene (37%). On the other hand, the size of the substrate does not seem to be an issue for reactivity as the larger  $-CF_3$  group in 4-trifluoromethylaniline does not lead to decreased reactivity for this substrate.

In comparison to the work of the Fasan group who has investigated carbene transfer reactions with iron-containing Mb and several Mb mutants, some significant differences between the two systems are evident.  $Ru^{II}MpIX$  and  $Ru^{II}Mb$  achieve similar TON in the N-H insertion of aniline compared to free hemin or wt Mb. However, the catalyst that the Fasan group tested for the N-H insertion of aniline was the  $Fe^{II}H64V/V68A$  Mb double mutant, which is able to achieve up to 6150 TON.<sup>8</sup> Future studies on a corresponding double mutant of RuMb will show if the Ru system can match or surpass this result for Fe.  $Ru^{II}MpIX$  exhibits slightly higher cyclopropanation activity to free hemin (26% yield vs. 16% yield, respectively), but  $Ru^{II}Mb$  and our His64 mutants all fare worse compared to wild-type Mb and the Mb mutants used by Fasan and coworkers, as well as to our  $Fe^{II}H64AMb$  and  $Fe^{II}H64DMb$  variants. This is largely due to the stability issues discussed above.<sup>3</sup>  $Ru^{II}H64DMb$  achieves the highest diastereoselectivity (87% *trans* product) but exhibits low activity regardless of pH, and lower diastereoselectivity compared to every one of the

FeMb variants (all >90% *trans* product). Ru<sup>II</sup>H64VMb exhibits higher cyclopropanation activity relative to the other Ru<sup>II</sup>Mb catalysts, but relatively low activity (only 4-8% yield depending on catalyst and pH) and diastereoselectivity (70-74%). The only substrate that is able to be efficiently converted to the cyclopropane product by Ru<sup>II</sup>H64AMb is 4-methoxystyrene, the most electron-rich and most soluble styrene derivative studied in this work.

In summary, wild-type Mb and three His64 mutants of Mb were reconstituted with RuMpIX(X). These catalysts exhibit moderate activity in the N-H insertion reaction of aniline derivatives, and low activity in the cyclopropanation of most of the styrene derivatives studied. RuH64DMb is able to achieve the best diastereoselectivity, but exhibits low activity. Our results show that one has to be cautious when analyzing the outcomes of organometallic reactions in water: besides the reactivity differences that result from electronic effects, solubility and acid/base equilibria can influence the outcome of reactions dramatically. We also observed an interesting difference between our RuMb catalysts and analogous iron systems studied in the literature, where application of Ru leads to significantly suppressed cyclopropanation reactivity. Our studies show that this is not due to a lack of carbene transfer reactivity of RuMb, but to the contrary, that this is caused by the catalyst being too reactive, leading to degradation of the protein and the porphyrin, and hence, fast catalyst deactivation. This is especially a factor when styrene substrates are used (for cyclopropanation) that exhibit low solubility in water. If the stability of RuMb can be improved, catalytic activity may increase and RuMb could become a useful catalyst for cyclopropanation. Our results also show that Mb mutants with hydrophobic active site pockets show moderate increases in activity, at least in conjunction with the non-polar styrene and aniline derivatives studied here. Hence, even more active catalysts should result from double or triple Mb mutants that further increase the hydrophobicity of the active site. To induce increased

stereoselectivity in the cyclopropane products, bulky hydrophobic groups should be used in these mutants. This is the next logical step in rational catalyst design that should lead to improved carbene transfer catalysts.

## 2.8 Experimental Section

### General Procedures

All chemicals and reagents were purchased from commercial suppliers (Sigma Aldrich, Fisher Scientific, Acros, Frontier Scientific) and used without further purification unless otherwise noted.  $^1\text{H}$  NMR spectra were measured on either a Varian MR400 (operating at 400 MHz), a Varian Inova 500 (operating at 500 MHz), or a Varian vnmrs 500 (operating at 500 MHz). Tetramethylsilane (TMS) served as the internal standard (0 ppm) for  $^1\text{H}$  NMR measurements. Alumina gel chromatography purifications were carried out using neutral aluminum oxide 90. Gas chromatography/ mass spectrometry (GC/MS) analyses were carried out using a Shimadzu QP-2010 GC/MS equipped with a 30 meter long DB-5 column with 0.25 mm I.D. Separation method: 1  $\mu\text{L}$  injection, injector temp.: 200  $^\circ\text{C}$ , detector temp.: 250  $^\circ\text{C}$ . Gradient: column temperature set to 60  $^\circ\text{C}$  for 3 min, then to 250  $^\circ\text{C}$  at 20  $^\circ\text{C}/\text{min}$ , and held at 250  $^\circ\text{C}$  for 2.5 min (7.5 min for derivatives). Total run time was 15.00 min for the aniline and styrene reactions, and was extended to 20.00 min for the aniline and styrene derivatives. Protein mass spectrometry analyses were carried out using an Agilent Q-TOF HPLC-MS equipped with a Poroshell 300SB-C8 column. Separation method: 20  $\mu\text{L}$  injection, flow rate: 0.5 mL/min, gradient: 95:5 water:acetonitrile for 3 min, followed by an increase over 10 min to 100% acetonitrile to elute the protein. Total run time was 13 min. Porphyrin mass spectrometry analyses were carried out using an Agilent 6230 TOF HPLC-MS.

## Protein Expression and Purification

Wild-type sperm whale myoglobin (Mb) H64A and H64D Mb variants were generously expressed and purified by Dr. Takashi Matsuo's group at the Nara Institute of Science and Technology (NAIST) in Ikoma, Japan. The H64V mutant was also expressed in the laboratory of Dr. Matsuo in *E. coli* BL21(DE3) cells, modified from standard procedures.<sup>24</sup> Briefly, cells were grown in LB media, (ampicillin, 50 µg/L) at 37 °C and 160 rpm until OD<sub>600</sub> reached ~ 0.8. The cell-containing media were placed on ice immediately after expression and cells were pelleted by centrifuging at 8800 rpm and 4 °C using a Beckman Coulter JA-10 fixed-angle rotor. Cell pellets were suspended in ~100 mL of 50 mM Tris buffer, pH = 8, and 10 mL of lysis buffer were added prior to sonication. Cells were sonicated using a Fisher Scientific Model 550 Dismembrator. The cells were pulsed 6 times at 15 s each time with 1 min intervals. After adding a stock solution of DNase (1 µg/mL) and stirring for one hour, the suspended cells were subjected to the sonication procedure again. The lysed cells and protein mixture was centrifuged at 8800 rpm and 4 °C for 80 min to extract the protein. The protein was initially purified by adding ammonium sulfate up to 50% saturation, centrifuging, and then adding more ammonium sulfate up to 90% saturation to precipitate myoglobin. After another round of centrifugation, the protein pellet was collected, suspended in 10 mM potassium phosphate (KPi) buffer, pH = 6, and then dialyzed against the same buffer. The protein was loaded onto a CM Sepharose column with 10 mM KPi buffer pH 6, and the collected protein fractions were then concentrated and loaded onto a Sephadex G-50 column with 100 mM KPi buffer, pH = 7, and eluted with the same buffer. The proteins were characterized by UV-vis and circular dichroism spectroscopy.



### **Synthesis of Ruthenium Mesoporphyrin IX Dimethyl Ester Carbonyl [RuMpIXDME(CO)]**

[RuMpIXDME(CO)] was synthesized as previously reported.<sup>25</sup> Under an Ar atmosphere, a solution of mesoporphyrin IX dimethyl ester (218 mg, 0.366 mmol) and Ru<sub>3</sub>(CO)<sub>12</sub> (400 mg, 0.626 mmol) in dimethylformamide (DMF, 60 mL) was refluxed at 160 °C. The conversion from free base porphyrin to metallated complex was followed by TLC and UV-vis spectroscopy. After ~21 hrs, the heat was turned off and the solvent was removed *in vacuo*. The resulting solid was dissolved in 50:50 CH<sub>2</sub>Cl<sub>2</sub>:ethanol (60 mL) and refluxed for another 30 min at 70 °C. The solvent was then removed by rotary evaporation. Unmetallated porphyrin was removed from the product on an alumina column in CH<sub>2</sub>Cl<sub>2</sub>. The product was eluted as a bright red band after adding 2% methanol to the column. 181 mg of the product were isolated (68% yield). The product was characterized by UV-vis, nm in CH<sub>2</sub>Cl<sub>2</sub>, (394, 517, 548), IR, cm<sup>-1</sup> in a KBr disk (1924 (CO), 1718, 1634) and <sup>1</sup>H-NMR, ppm in CDCl<sub>3</sub>: 1.88 (*t*, ethyl-CH<sub>3</sub>), 3.12 (*s*), 3.29 (*t*, propionate-CH<sub>2</sub>-), 3.54, 3.57, 3.59 (*s*, methyl-CH<sub>3</sub>), 3.64, 3.67 (*s*, methoxy-CH<sub>3</sub>), 4.00, (*q*, ethyl-CH<sub>2</sub>-), 4.29 (*t*, propionate-CH<sub>2</sub>-), 9.75, 9.80, 9.93, 9.94 (*s*, 1 each, meso-H). Elemental Analysis (C<sub>37</sub>H<sub>40</sub>N<sub>4</sub>O<sub>5</sub>Ru): Calculated: C 61.57, H 5.59, N 7.76. Found: C 60.48, H 5.63, N 7.87.

### **Photolysis of [RuMpIXDME(CO)]**

CO was labilized from the Ru porphyrin by measuring out ~1 mg of [RuMpIXDME(CO)], and dissolving the solid in ~3 mL of DMF in the glovebox. The solution was irradiated with a 100 W mercury lamp equipped with a UV filter to irradiate the sample with 351 nm light. The solution was irradiated for ~24 hrs, before removing the solvent *in vacuo*. The product, [RuMpIXDME], was characterized by UV-vis, nm in DMF (392, 494, 520) and IR spectroscopy, cm<sup>-1</sup> in a KBr disk by adding drops of the [RuMpIXDME] solution in DMF to the KBr (1735, 1635).

### **Hydrolysis of [RuMpIXDME]**

[RuMpIXDME] (~1 mg) was dissolved in 10 mL of 9:1 v:v methanol:water. NaOH (1% by volume) was added to the solution which was left refluxing for 1 hour in air. The reaction mixture was concentrated to ~1 mL under vacuum and the pH was adjusted with HCl (3 M) to a pH of about 7.0, which leads to the formation of a Ru(III) mesoporphyrin complex with OH<sup>-</sup> or Cl<sup>-</sup> bound. The [Ru<sup>III</sup>MpIX(X)] (X = OH<sup>-</sup> or Cl<sup>-</sup>) solution was stored at -20 °C prior to reconstitution or reactivity studies. The product was characterized by UV-vis, nm, in aqueous 100 mM pH 7 potassium phosphate (KPi) buffer (389, 517).

### **Preparation of apo-protein**

The heme cofactor was removed from Mb and the Mb mutants via Teale's method.<sup>36</sup> Briefly, the protein (in 100 mM potassium phosphate buffer) was unfolded by lowering the pH of the solution to ~2.3. The heme was extracted with 2-butanone, and after heme removal the protein was dialyzed against three buffers, each for two hours: 10 mM potassium phosphate (KPi) buffer at pH 6.0, 100 mM KPi buffer at pH 6.5, and 100 mM KPi buffer at pH 7.0. The apo-proteins were stored at 4 °C prior to reconstitution, yields typically ranged from 65% to 75%, calculated from the starting concentration of the heme-bound protein.

### **Preparation of RuMb and RuMb mutants**

[Ru<sup>III</sup>MpIX(X)] (1.1 equivalents) was added to ApoMb (1 equivalent) in KPi (100 mM, pH = 7.0) and the reconstituted protein was incubated at 0 °C for ~30-60 min before purification. The new Ru<sup>III</sup>Mb solution was purified by size-exclusion chromatography (Sephadex G-25) with 100 mM KPi pH = 7.0 as the mobile phase. The protein was concentrated, flash frozen, and stored at -20°C. The same procedure was applied for the preparation of the Ru<sup>III</sup>Mb mutants (H64D, A,

and V). Typical ratios between the absorbance of the porphyrin Soret band (~389-394 nm) and the absorbance at ~280 nm of the protein were 2.5 : 1 to 3.0 : 1. Protein concentration was determined from the Soret band absorbance in the UV-vis spectra, using an extinction coefficient of  $95.7 \text{ mM}^{-1} \text{ cm}^{-1}$  previously reported.<sup>15</sup>

### **N-H insertion reactions**

Reactions were carried out at a ~450  $\mu\text{L}$  scale using 20  $\mu\text{M}$  RuMb, 20 mM aniline (or aniline derivative), 40 mM ethyl diazoacetate (EDA), and 10 mM  $\text{Na}_2\text{S}_2\text{O}_4$ . The sodium dithionite (100 mM stock solution) in potassium phosphate buffer (100 mM, pH 7.0) was purged by bubbling argon through the solution for 10 min in a sealed vial. All reagents and proteins were brought into a Coy vinyl anaerobic chamber (30-50 ppm  $\text{O}_2$ , 1.5-3.0%  $\text{H}_2$ ) before running the reactions. The  $\text{Ru}^{\text{III}}$  protein was first reduced to  $\text{Ru}^{\text{II}}$  through addition of 40  $\mu\text{L}$  of  $\text{Na}_2\text{S}_2\text{O}_4$  solution, followed by the addition of 4  $\mu\text{L}$  of aniline or aniline derivative from a 2 M stock solution in methanol (with the exceptions of 4-nitroaniline and 4-vinylaniline which were less soluble in methanol and were therefore dissolved in dimethyl sulfoxide), and 8  $\mu\text{L}$  of EDA (2 M stock solution in methanol), which translates to a total MeOH content of 2.65%. The reactions were left under magnetic agitation for 18 hours at room temperature. Reactions with free  $[\text{Ru}^{\text{II}}\text{MpIX}]$  were carried out in an identical procedure with the exception that the  $\text{Ru}^{\text{III}}\text{Mb}$  was replaced by 400  $\mu\text{L}$  of  $[\text{Ru}^{\text{III}}\text{MpIX(X)}]$  (20  $\mu\text{M}$ ) in potassium phosphate buffer (100 mM, pH 7.0). Reactions at pH 5 and 3 were also carried out in the same manner. The pH of the protein, buffer, and  $\text{Na}_2\text{S}_2\text{O}_4$  solutions were all adjusted to pH 5 or 3 by addition of 3 M HCl before combining the protein, reductant, and reagents in the anaerobic chamber.

## **Cyclopropanation reactions**

Reactions were carried out in the same manner as the N-H insertion reactions, using 20 mM styrene (or styrene derivatives) instead of aniline. All 2 M styrene solutions were prepared in methanol apart from 4-nitrostyrene, which was more soluble in dimethyl sulfoxide.

## **Product Analysis**

The reactions were analyzed by addition of 20  $\mu$ L of internal standard (2-phenyl-ethanol, 1 M in methanol) to the reaction mixture, followed by extraction with 1.5 mL or 3 mL of ethyl acetate, depending on the reaction. The organic layer was dried with magnesium sulfate overnight and later filtered and analyzed by GC/MS (see **General Procedures** section for details on GC/MS analyses). Calibration curves for quantification of the N-H insertion products of aniline and aniline derivatives and the cyclopropanation products of styrene and styrene derivatives were constructed using authentic standards produced synthetically (using 1-2 mol%  $\text{Rh}_2(\text{OAc})_4$  as the catalyst). The exception to this was the quantification of the products of 4-vinylaniline which can undergo both N-H insertion and cyclopropanation. These products were quantified using the calibration curves for the standard aniline and styrene products in the reaction with EDA. These reactions to produce authentic standards were run according to the same methods in previous works.<sup>3, 8</sup> All measurements in the results tables were performed in triplicate. Negative control experiments were performed in the absence of catalyst, and the absence of reductant outside of the Coy glovebox.

## **Reactions with Ethyl Diazoacetate (EDA) in a Sealed Cuvette**

Native sperm whale Mb, RuMb, and [RuMpIX(X)] (5  $\mu$ M, pH 7) were prepared in the Coy glovebox in a sealed, screw-top cuvette. In the glovebox, 5000 equivalents of  $\text{Na}_2\text{S}_2\text{O}_4$  and 2000 equivalents of EDA in a 0.5 M stock solution in methanol were added. For each reaction, the

cuvette was sealed and removed from the wetbox before monitoring the kinetics by UV-vis for 1 hr.

### Protein and Porphyrin Mass Spectrometry after Cyclopropanation

Native sperm whale Mb and RuMb (10  $\mu$ M, pH 7) were prepared and reactions with 1 M EDA and 1 M styrene were carried out in the same manner as in the N-H insertion reactions. After 3 hrs, the reactions were stopped, and the protein masses were analyzed by HPLC-MS (see **General Procedures**). In a similar vein, [RuMpIX(X)] (20  $\mu$ M) was prepared and analyzed by LC-MS before and after a 15 min reaction with EDA and styrene.

### 2.9 References

- 1) Coelho, P. S.; Wang, Z. J.; Ener, M. E.; Baril, S. A.; Kannan, A.; Arnold, F. H.; Brustad, E. M. A serine-substituted P450 catalyzes highly efficient carbene transfer to olefins in vivo. *Nat. Chem. Biol.* **2014**, *10* (2), 485-487.
- 2) Coelho, P. S.; Brustad, E. M.; Kannan, A.; Arnold, F. H. Olefin Cyclopropanation via Carbene Transfer Catalyzed by Engineered Cytochrome P450 Enzymes. *Science* **2013**, *339* (6117), 307-310.
- 3) Bordeaux, M.; Tyagi, V.; Fasan, R. Highly Diastereoselective and Enantioselective Olefin Cyclopropanation Using Engineered Myoglobin-Based Catalysts. *Angew. Chem. Int. Ed.* **2015**, *54* (6), 1744-1748.
- 4) Renata, H.; Wang, Z. J.; Kitto, R. Z.; Arnold, F. H. P450-catalyzed asymmetric cyclopropanation of electron-deficient olefins under aerobic conditions. *Cat. Sci. Tech.* **2014**, *4* (10), 3640-3643.
- 5) Wang, Z. J.; Peck, N. E.; Renata, H.; Arnold, F. H. Cytochrome P450-catalyzed insertion of carbenoids into N-H bonds. *Chem. Sci.* **2014**, *5* (2), 598-601.
- 6) Tyagi, V.; Fasan, R. Myoglobin-Catalyzed Olefination of Aldehydes. *Angew. Chem. Int. Ed.* **2016**, *55* (7), 2512-2516.
- 7) Tyagi, V.; Bonn, R. B.; Fasan, R. Intermolecular carbene S-H insertion catalysed by engineered myoglobin-based catalysts. *Chem. Sci.* **2015**, *6* (4), 2488-2494.
- 8) Sreenilayam, G.; Fasan, R. Myoglobin-catalyzed intermolecular carbene N-H insertion with arylamine substrates. *Chem. Comm.* **2015**, *51* (8), 1532-1534.

- 9) Galardon, E.; LeMaux, P.; Simonneaux, G. Cyclopropanation of alkenes with ethyl diazoacetate catalysed by ruthenium porphyrin complexes. *Chem. Comm.* **1997**, (10), 927-928.
- 10) Che, C. M.; Huang, J. S. Ruthenium and osmium porphyrin carbene complexes: synthesis, structure, and connection to the metal-mediated cyclopropanation of alkenes. *Coord. Chem. Rev.* **2002**, 231 (1-2), 151-164.
- 11) Anding, B. J.; Ellern, A.; Woo, L. K. Olefin Cyclopropanation Catalyzed by Iridium(III) Porphyrin Complexes. *Organometallics* **2012**, 31 (9), 3628-3635.
- 12) Intrieri, D.; Caselli, A.; Gallo, E. Cyclopropanation Reactions Mediated by Group 9 Metal Porphyrin Complexes. *Eur. J. Inorg. Chem.* **2011**, (33), 5071-5081.
- 13) Key, H. M.; Dydio, P.; Clark, D. S.; Hartwig, J. F. Abiological catalysis by artificial haem proteins containing noble metals in place of iron. *Nature* **2016**, 534 (7608), 534-537.
- 14) Bordeaux, M.; Singh, R.; Fasan, R. Intramolecular C(sp<sup>3</sup>)-H amination of arylsulfonyl azides with engineered and artificial myoglobin-based catalysts. *Bioorg. Med. Chem.* **2014**, 22 (20), 5697-5704.
- 15) Paulson, D. R.; Addison, A. W.; Dolphin, D.; James, B. R. Preparation of Ruthenium(II) and Ruthenium(III) Myoglobin and the Reaction of Dioxygen, and Carbon-Monoxide, with Ruthenium(II) Myoglobin. *J. Biol. Chem.* **1979**, 254 (15), 7002-7006.
- 16) Srivastava, T. S. Carbon-Monoxide Derivative of Ruthenium(II) Myoglobin Probe of Heme Protein Conformation. *Biochim. Biophys. Acta* **1977**, 491 (2), 599-604.
- 17) Winter, M. B.; McLaurin, E. J.; Reece, S. Y.; Olea, C.; Nocera, D. G.; Marletta, M. A. Ru-Porphyrin Protein Scaffolds for Sensing O<sub>2</sub>. *J. Am. Chem. Soc.* **2010**, 132 (16), 5582-5583.
- 18) Wolf, M. W.; Vargas, D. A.; Lehnert, N. Engineering of RuMb: Toward a Green Catalyst for Carbene Insertion Reactions. *Inorg. Chem.* **2017**, 56 (10), 5623-5635.
- 19) Yi, J.; Heinecke, J.; Tan, H.; Ford, P. C.; Richter-Addo, G. B. The Distal Pocket Histidine Residue in Horse Heart Myoglobin Directs the O-Binding Mode of Nitrite to the Heme Iron. *J. Am. Chem. Soc.* **2009**, 131 (50), 18119-18128.
- 20) PDB ID: 5UT8, Wang, B.; Thomas, L.M.; Richter-Addo, G.B. Deoxy form of sperm whale myoglobin H64A.
- 21) Yalkowsky, S. H. H., Y.; Jain, P. In *Handbook of Aqueous Solubility Data 2ed.*; CRC Press: Boca Raton, FL, 2010; p 468.
- 22) Yalkowsky, S. H. H., Y. An Extensive Compilation of Aqueous Solubility Data for Organic Compounds Extracted from the AQUASOL DATABASE. In *Handbook of Aqueous Solubility Data*, CRC Press LLC: Boca Raton, FL, 2003; p 262.

- 23) Renata, H.; Lewis, R. D.; Sweredoski, M. J.; Moradian, A.; Hess, S.; Wang, Z. J.; Arnold, F. H. Identification of Mechanism-Based Inactivation in P450-Catalyzed Cyclopropanation Facilitates Engineering of Improved Enzymes. *J. Am. Chem. Soc.* **2016**, *138* (38), 12527-12533.
- 24) Springer, B. A.; Sligar, S. G. High-Level Expression of Sperm Whale Myoglobin in Escherichia-Coli. *Proc. Natl. Acad. Sci.* **1987**, *84* (24), 8961-8965.
- 25) Galardon, E.; Le Maux, P.; Simonneaux, G. Cyclopropanation of alkenes, N-H and S-H insertion of ethyl diazoacetate catalysed by ruthenium porphyrin complexes. *Tetrahedron* **2000**, *56* (4), 615-621.

## Chapter 3

### Catalyst Lifetimes of Modified Myoglobins and Ligand Addition to H93G Myoglobin

Artificial heme enzymes have proven remarkably successful for stereoselective carbene and nitrene transfer reactions, but less is known about the lifetime and decomposition pathways of these catalysts.<sup>1-10</sup> The reactive metallocarbene intermediate that is formed after the addition of ethyl diazoacetate (EDA) or other carbene precursors can readily insert into nucleophiles other than the desired substrate. In one key study, Arnold and coworkers catalyzed the cyclopropanation of styrene with an artificial P450<sub>BM3</sub> enzyme and identified specific amino acids that were modified by the iron-carbene unit using a trypsin digestion of the crude cyclopropanation mixture.<sup>11</sup> Histidine, cysteine, lysine, serine, and arginine residues near and further away from the metal center were chemically modified after the addition of EDA to the reduced enzyme. In addition, the iron carbene unit can insert into the porphyrin ligand itself, alkylating one or more of the porphyrin nitrogen atoms that coordinate to the iron center. Despite mutating some of the residues that were alkylated during catalysis, the catalytic lifetime of modified P450<sub>BM3</sub> did not improve and the heme cofactor was still alkylated after the addition of EDA. It is clear that artificial enzymes borne out of directed evolution and cofactor replacement can be active and stereoselective catalysts for different organometallic reactions, with some of the modified P450<sub>BM3</sub> catalysts even being used in reaction pathways to synthesis drugs.<sup>12</sup> However, more insight into catalyst lifetime and decomposition is needed for the development of more robust catalysts; catalysts that can be reused or regenerated. In this chapter, we investigate the lifetimes of iron and ruthenium porphyrins in



water as well as a couple of FeMb and RuMb variants. We demonstrate that all of the catalysts are very short-lived and the cyclopropanation reaction is finished within 30-60 minutes for all of the catalysts studied.

The catalytic activity and lifetime of RuMb for the cyclopropanation of styrene are much lower compared to FeMb (Chapter 2).<sup>13</sup> From both UV-vis and LC/MS data, it is evident that the lower activity of RuMb results from the rapid decomposition of the catalyst and the insertion of the metallocarbene unit into both the porphyrin and the protein scaffold. For metalloporphyrins in organic solvents, adding different axial ligands to the metal center and thereby altering the electronics of the metal results in higher or lower activity towards carbene transfer.<sup>14</sup> In wild-type Mb, the heme or porphyrin is bound by a proximal histidine ligand inside the protein pocket. By mutating this residue to a glycine, exogenous ligands can be bound to the heme.<sup>15-16</sup> A variety of different ligands have been bound to the proximal side of the heme in the H93G Mb mutant including imidazole, amines, ethers, phenolate, thioethers, thiolates, and phosphines, among others.<sup>16-24</sup> We hypothesized that through the reconstitution of RuMpIX into H93G Mb and the addition of exogenous ligands such as anionic phenolates and thiolates, and  $\sigma$ -donating phosphine ligands could alter the reactivity of the Ru center to make the Ru=CR<sub>2</sub> unit less reactive towards undesired decomposition reactions and thus achieve a longer catalyst lifetime. In this chapter we present results on the reconstitution of RuMpIX into apo-H93G Mb and the addition of exogenous ligands to RuH93G Mb to improve the catalytic activity of the cyclopropanation reaction. Carbon monoxide is also bound to the reduced Ru(II) center to see if this ligand affects catalytic activity.

### 3.1 Determining Fe and Ru Catalyst Lifetimes and Turnover Frequencies for the Cyclopropanation of Styrene

In this study, the catalytic lifetimes of FePpIX, FeMb, FeH64AMb, RuMpIX, RuMb, and RuH64AMb for the cyclopropanation of styrene and the N-H insertion of aniline were investigated. Reaction vials were prepared under reducing conditions (the same conditions as in Chapter 2) and substrate and EDA were added before taking aliquots from the reaction mixture at specific time points. Organic products were extracted with ethyl acetate before adding an organic standard (2-phenyl ethanol) and quantifying the product by GC/MS. A summary of the data is shown in **Table 3.1**.

**Table 3.1.** Catalytic lifetime activity of Fe and Ru catalysts for the cyclopropanation of styrene

| Catalyst | Concentration    | % Yield | Lifetime (min) | $k_{\text{obs}}$ ( $\text{min}^{-1}$ ) | $t_{1/2}$ (min) |
|----------|------------------|---------|----------------|--|-----------------|
| FePpIX   | 10 $\mu\text{M}$ | 7       | 120            | $2.9 \times 10^{-2}$                   | 17.3            |
| FeMb     | 10 $\mu\text{M}$ | 11      | 30             | $6.0 \times 10^{-2}$                   | 11.0            |
|          | 20 $\mu\text{M}$ | 43      | 30             | $8.7 \times 10^{-2}$                   | 7.2             |
| FeH64AMb | 10 $\mu\text{M}$ | 15      | 30             | $6.7 \times 10^{-2}$                   | 10.3            |
|          | 20 $\mu\text{M}$ | 50      | 30             | $1.2 \times 10^{-1}$                   | 4.1             |
| RuMpIX   | 10 $\mu\text{M}$ | 19      | 30             | $5.9 \times 10^{-2}$                   | 13.7            |
| RuMb     | 10 $\mu\text{M}$ | 1.3     | ~1             | N/A                                    | N/A             |
|          | 20 $\mu\text{M}$ | 1.9     | ~1             | N/A                                    | N/A             |
| RuH64AMb | 10 $\mu\text{M}$ | 3.6     | ~1             | N/A                                    | N/A             |

Reactions were set up in 3-4 mL pots with 0.1% catalyst loading, 500 equivalents of  $\text{Na}_2\text{S}_2\text{O}_4$ , 1000 equivalents styrene, and 2000 equivalents EDA. 450  $\mu\text{L}$  aliquots were collected at various time points and organic products were extracted with ethyl acetate. Percent yield was calculated with an internal standard of 3.3 mM 2-phenyl ethanol.

The moles of ethyl 2-phenylcyclopropanecarboxylate produced from the cyclopropanation of styrene catalyzed by Fe<sup>II</sup>PpIX over time are shown in **Figure 3.1**. At a catalyst concentration of 10  $\mu\text{M}$  (0.1% catalyst loading),  $9.1 \times 10^{-8}$  moles of product are produced within the first ten minutes of the reaction. Product yield increases to  $2.6 \times 10^{-7}$  moles (7% yield) over the course of two hours, when the reaction has reached its endpoint and the catalyst is likely decomposed. Though reactions in Chapter 2 and in literature studies have been run for 12-18 hours,<sup>5, 13, 25</sup> this shows that Fe<sup>II</sup>PpIX is only active for a fraction of that time. Fitting the data with an exponential curve results in a  $k_{\text{obs}}$  for product formation of  $2.9 \times 10^{-2} \text{ min}^{-1}$  and a  $t_{1/2}$  of 17.3 minutes.

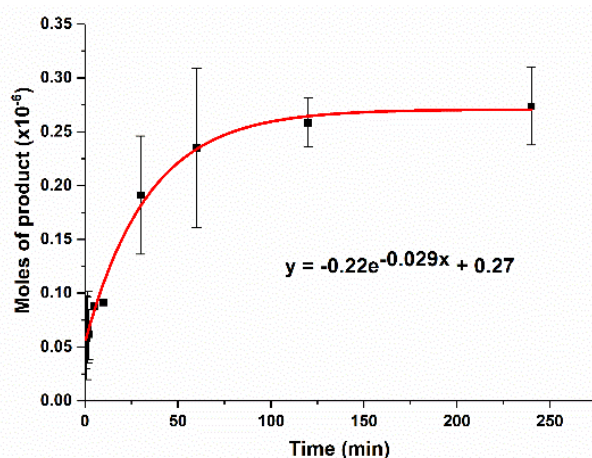


**Figure 3.1.** Time course of the cyclopropanation of styrene catalyzed by FePpIX. The catalyst was prepared at a 10  $\mu\text{M}$  concentration and reduced with 500 equiv. of  $\text{Na}_2\text{S}_2\text{O}_4$  before adding 1000 equiv. of styrene and 2000 equiv. of EDA. 450  $\mu\text{L}$  aliquots were taken at the following time points: 0.5, 1, 1.5, 2, 5, 10, 30, 60, 120, and 240 minutes. Organic products were extracted with 1 mL of ethyl acetate before quantifying the organic product by GC/MS.

Fe<sup>II</sup>Mb catalyzes the cyclopropanation of styrene in higher yield compared to Fe<sup>II</sup>PpIX (**Figure 3.2**). After ten minutes,  $2.3 \times 10^{-7}$  moles of cyclopropane are produced, and this yield improves to  $4.5 \times 10^{-7}$  moles of product (11% yield) at 30 minutes, when the reaction reaches its end. Running the same reaction at higher catalyst concentration (20  $\mu\text{M}$  catalyst, still 0.1 mol% loading) results in the same endpoint of 30 minutes for the reaction (**Figure 3.3**), though the yield for the reaction is much higher at  $3.4 \times 10^{-6}$  moles of product (43% yield). At 20  $\mu\text{M}$ , Fe<sup>II</sup>Mb

exhibits a higher  $k_{\text{obs}}$  of  $8.7 \times 10^{-2} \text{ min}^{-1}$  compared to  $6.0 \times 10^{-2} \text{ min}^{-1}$  at  $10 \mu\text{M}$  concentration and a shorter  $t_{1/2}$  of 7.2 minutes compared to 11.0 minutes. It is important to note that only single timepoints were collected for the reaction run with  $20 \mu\text{M}$  catalyst, and if the experiment was repeated several times, the average yield may be lower as previous data collected for  $\text{Fe}^{\text{II}}\text{Mb}$  indicate an average 20-30% overall yield for the cyclopropanation of styrene. Compared to  $\text{Fe}^{\text{II}}\text{PpIX}$ ,  $\text{Fe}^{\text{II}}\text{Mb}$  exhibits a higher rate of product formation with a higher  $k_{\text{obs}}$  of  $6.0 \times 10^{-2} \text{ min}^{-1}$  compared to  $2.9 \times 10^{-2} \text{ min}^{-1}$ .  $\text{Fe}^{\text{II}}\text{Mb}$  exhibits a higher TON but a shorter catalyst lifetime compared to  $\text{Fe}^{\text{II}}\text{PpIX}$ , indicating that styrene and EDA can readily access the metal center in Mb, but that the protein scaffold and heme decompose and/or become inactive over a shorter period of time.

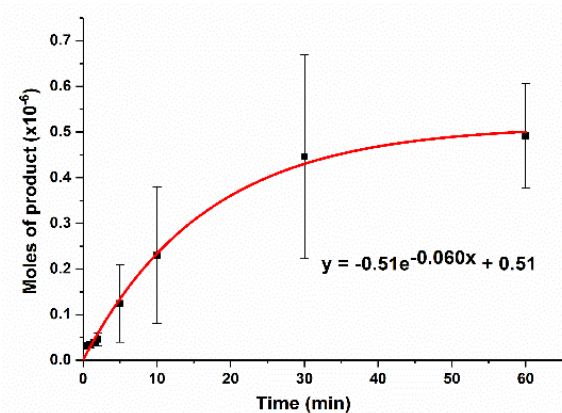


**Figure 3.2.** Time course of the cyclopropanation of styrene catalyzed by  $\text{FeMb}$  over 60 min. The catalyst was prepared at a  $10 \mu\text{M}$  concentration and reduced with 500 equiv. of  $\text{Na}_2\text{S}_2\text{O}_4$  before adding 1000 equiv. of styrene and 2000 equiv. of EDA.  $450 \mu\text{L}$  aliquots were taken at the following time points: 0.5, 1, 1.5, 2, 5, 10, 30, and 60 min. Organic products were extracted with 1 mL of ethyl acetate before quantifying the organic product by GC/MS. Reactions were run in triplicate.

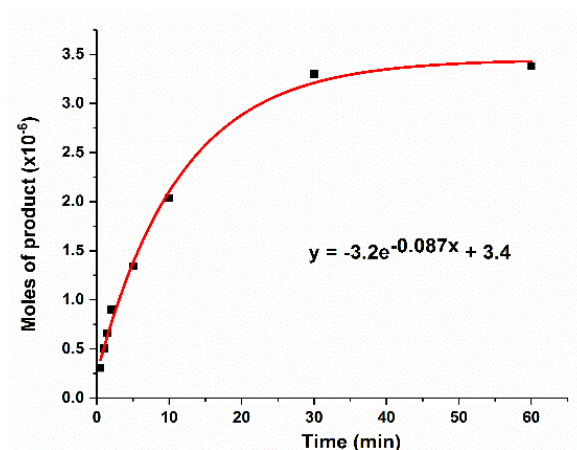


**Figure 3.3.** Time course of the cyclopropanation of styrene catalyzed by FeMb over 60 min. The catalyst was prepared at a 20  $\mu\text{M}$  concentration and reduced with 500 equiv. of  $\text{Na}_2\text{S}_2\text{O}_4$  before adding 1000 equiv. of styrene and 2000 equiv. of EDA. The reaction was worked up with the same methods used in the 10  $\mu\text{M}$  time course reaction. One data point was taken at each time point.

The H64A mutant of Mb decreases the steric bulk of the active site of the protein and makes the heme pocket more hydrophobic. In Chapter 2, this mutation resulted in higher yields for both the cyclopropanation of styrene and the N-H insertion of aniline compared to wild-type Mb. The reaction yields  $4.7 \times 10^{-7}$  moles of product after two minutes and  $6.1 \times 10^{-7}$  moles of product after 30 minutes (12% and 15% yield, respectively) when catalyzed by 10  $\mu\text{M}$   $\text{Fe}^{\text{II}}\text{H64AMb}$  (**Figure 3.4**). At 20  $\mu\text{M}$ , yield again improves considerably, up to  $4 \times 10^{-6}$  moles (50% yield) 30 minutes into the reaction (**Figure 3.5**). Similar to  $\text{Fe}^{\text{II}}\text{Mb}$ , catalysis ends after approximately 30 minutes and the percent yield determined after 18 hours (see Chapter 2) matches the percent yield found at the 30-minute time point using the 20  $\mu\text{M}$  catalyst. At 10  $\mu\text{M}$  concentration  $k_{\text{obs}}$  of product formation catalyzed by  $\text{Fe}^{\text{II}}\text{H64AMb}$  is  $6.7 \times 10^{-2} \text{ min}^{-1}$ , which is similar to  $\text{Fe}^{\text{II}}\text{Mb}$  with a  $k_{\text{obs}}$  of  $6.0 \times 10^{-2} \text{ min}^{-1}$ . As expected,  $\text{Fe}^{\text{II}}\text{H64AMb}$  also exhibits a slightly shorter  $t_{1/2}$  of 10.3 minutes compared to 11.0 minutes for  $\text{Fe}^{\text{II}}\text{Mb}$ . At 20  $\mu\text{M}$ ,  $\text{Fe}^{\text{II}}\text{H64AMb}$  exhibits a higher  $k_{\text{obs}}$  of  $1.2 \times 10^{-1} \text{ min}^{-1}$  and a  $t_{1/2}$  of 4.1 minutes compared to the reaction run at a concentration of 10  $\mu\text{M}$ . Both  $k_{\text{obs}}$

values are larger compared to Fe<sup>II</sup>Mb at the same concentrations. These results would seem to indicate that the larger and more hydrophobic pocket of Fe<sup>II</sup>H64AMb allows styrene to access the active site more readily or that that carbene formation is favored compared to wild-type Mb.

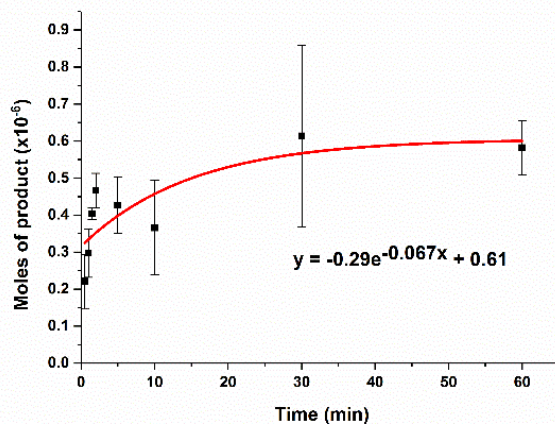


**Figure 3.4.** Time course of the cyclopropanation of styrene catalyzed by FeH64AMb over 60 min. The catalyst was prepared at a 10  $\mu\text{M}$  concentration and reduced with 500 equiv. of  $\text{Na}_2\text{S}_2\text{O}_4$  before adding 1000 equiv. of styrene and 2000 equiv. of EDA. 450  $\mu\text{L}$  aliquots were taken at the following time points: 0.5, 1, 1.5, 2, 5, 10, 30, and 60 min. Organic products were extracted with 1 mL of ethyl acetate before quantifying the organic product by GC/MS. Reactions were run in triplicate.

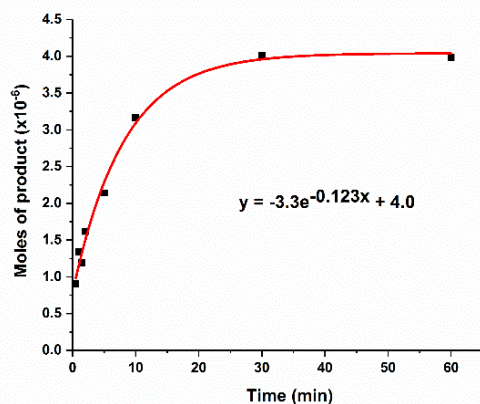


**Figure 3.5.** Time course of the cyclopropanation of styrene catalyzed by FeH64AMb over 60 min. The catalyst was prepared at a 20  $\mu\text{M}$  concentration and reduced with 500 equiv. of  $\text{Na}_2\text{S}_2\text{O}_4$  before adding 1000 equiv. of styrene and 2000 equiv. of EDA. The reaction was worked up with the same methods used in the 10  $\mu\text{M}$  time course reaction. One data point was taken at each time point.

Compared to Fe<sup>II</sup>PpIX, Ru<sup>II</sup>MpIX exhibits a higher yield of  $2.2 \times 10^{-7}$  moles after 10 min (6% yield) and  $7.5 \times 10^{-7}$  moles after 30 minutes (19% yield), which is also the endpoint of catalysis (**Figure 3.6**). Therefore, Ru<sup>II</sup>MpIX is a more active catalyst for cyclopropanation than Fe<sup>II</sup>PpIX but is also shorter-lived. An exponential fit of the data gives a  $k_{\text{obs}}$  of  $5.9 \times 10^{-2} \text{ min}^{-1}$  which is higher than the  $k_{\text{obs}}$  of  $2.9 \times 10^{-2} \text{ min}^{-1}$  determined for Fe<sup>II</sup>PpIX. A  $t_{1/2}$  of 13.7 minutes was calculated, shorter than the  $t_{1/2}$  of 17.3 minutes for Fe<sup>II</sup>PpIX. Despite the anomalies of the first few data points likely caused by artifacts in the experimental design (see Discussion), the data indicate that Ru<sup>II</sup>MpIX is a short-lived but active catalyst for cyclopropanation.

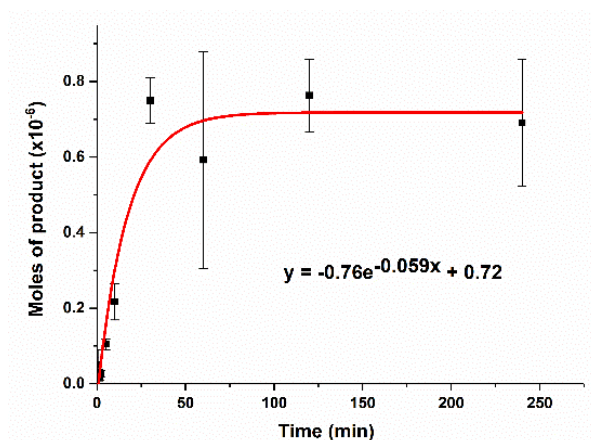


**Figure 3.6.** Time course of the cyclopropanation of styrene catalyzed by RuMpIX(X) over 240 min. The catalyst was prepared at a  $10 \mu\text{M}$  concentration and reduced with 500 equiv. of  $\text{Na}_2\text{S}_2\text{O}_4$  before adding 1000 equiv. of styrene and 2000 equiv. of EDA.  $450 \mu\text{L}$  aliquots were taken at the following time points: 0.5, 1, 1.5, 2, 5, 10, 30, 60, 120, and 240 minutes. Organic products were extracted with 1 mL of ethyl acetate before quantifying the organic product by GC/MS.

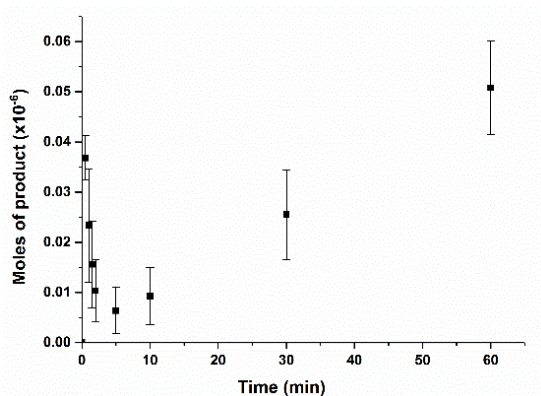


**Figure 3.7.** Time course of the cyclopropanation of styrene catalyzed by 10  $\mu\text{M}$  RuMb over 60 min. Catalysts were reduced with 500 equiv. of  $\text{Na}_2\text{S}_2\text{O}_4$  before adding 1000 equiv. of styrene and 2000 equiv. of EDA. 450  $\mu\text{L}$  aliquots were taken at the following time points: 0.5, 1, 1.5, 2, 5, 10, 30, and 60 min. Organic products were extracted with 1 mL of ethyl acetate before quantifying the organic product by GC/MS. Reactions were run in triplicate.

Compared to both  $\text{Fe}^{\text{II}}\text{Mb}$  and  $\text{Ru}^{\text{II}}\text{MpIX}$ ,  $\text{Ru}^{\text{II}}\text{Mb}$  is a poor catalyst for the cyclopropanation of styrene and only achieves up to 3% yield at 20  $\mu\text{M}$  concentration and a catalyst loading of 0.1%. As expected, the catalytic activity of  $\text{Ru}^{\text{II}}\text{Mb}$  at a 10  $\mu\text{M}$  concentration expires almost immediately with only  $3.7 \times 10^{-8}$  moles of product (0.9% yield) produced after 30 seconds, and  $2.5 \times 10^{-8}$  moles of product (0.6% yield) after 30 minutes (**Figure 3.7a**). After 60 minutes,  $5.1 \times 10^{-8}$  moles of product (1.3% yield) were measured by GC/MS. Despite the very slight increase in product in between the 30 and 60 minute time points, the low yield and high error indicate that the catalyst decomposes and catalysis ends almost immediately. Measurements at longer time points did not show improved product yield for the cyclopropanation reaction. Cyclopropanation reactions run with 20  $\mu\text{M}$  catalyst (**Figure 3.7b**) showed similar behavior with low yield (1.9%) and extremely short catalyst lifetime. The short lifetime likely results from rapid catalyst decomposition upon the addition of ethyl diazoacetate as discussed in Chapter 2. It should also be noted that running the reaction at a 4:1 ratio of styrene to EDA compared to a 0.5:1 ratio



did not result in appreciably higher yield; the reaction only proceeded in up to 3.7% yield (data not shown).

Similar to Ru<sup>II</sup>Mb, Ru<sup>II</sup>H64AMb is a poor catalyst for the cyclopropanation of styrene. Only  $5.6 \times 10^{-8}$  moles of cyclopropane (1.4% yield) are produced after 0.5 minutes, and this yield does not improve over the course of 30 minutes (**Figure 3.8**). Indeed, there is decrease in product yield in between 0.5 and 30 minutes, which was observed for Ru<sup>II</sup>Mb as well. This is a peculiar result, though the absolute difference between the yield at 0.5 minutes and at 5 minutes (the lowest yield measured) is only a difference of 1.1% yield due to the overall low-yielding nature of the reaction. In absolute terms, this is a small difference in percent yield. Yield increases up to  $1.5 \times 10^{-7}$  moles (3.6% yield) after 60 minutes which is close to the highest yields observed for 20  $\mu$ M RuMb variants over 18 hour reactions. The yield measured at 60 minutes also exhibits a large standard deviation, and a couple of the data points collected may be outliers.

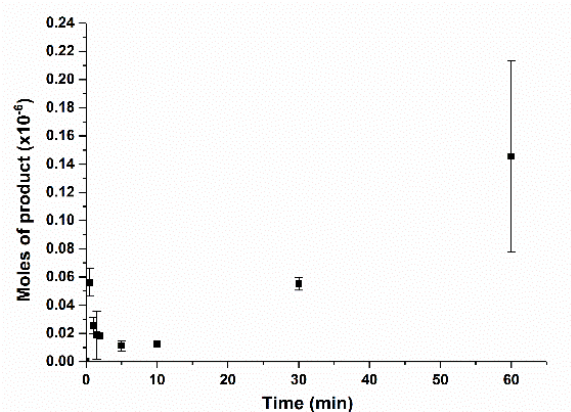


**Figure 3.8.** Time course of the cyclopropanation of styrene catalyzed by RuH64AMb over 60 min and. The catalyst was prepared at a 10  $\mu$ M concentration and reduced with 500 equiv. of  $\text{Na}_2\text{S}_2\text{O}_4$  before adding 1000 equiv. of styrene and 2000 equiv. of EDA. 450  $\mu$ L aliquots were taken at the following time points: 0.5, 1, 1.5, 2, 5, 10, 30, and 60 minutes. Organic products were extracted with 1 mL of ethyl acetate before quantifying the organic product by GC/MS.

### 3.2 Determining Fe and Ru Catalyst Lifetimes and Turnover Frequencies for the N-H Insertion of Aniline.

The N-H insertion of aniline with EDA generally results in a higher yield compared to the cyclopropanation of styrene, as exhibited in part by the production of some 2-(phenylamino)acetate without the presence of any metal catalyst in the reaction mixture. On average, a 15% yield of 2-(phenylamino)acetate is observed after 30 minutes without any catalyst present in the reaction mixture, and this yield remains constant over a period of 18 hours. In addition, aniline is more soluble in water compared to styrene, and thus catalysis was predicted to proceed at a faster initial rate. In order to determine the lifetime of each of the catalysts for the N-H insertion aniline, reactions were set up in the same manner as the cyclopropanation experiments and aliquots were taken at different time points before extracting the organic products with ethyl acetate and measuring the product concentration by GC/MS. N-H insertion data are summarized in **Table 3.2**. Experimental data were collected in two sets on different days – the longer timescale data from 30-480 minutes were collected prior to the shorter timescale data from 1-10 minutes. Data collected from different reaction vials are represented in **Figure 3.9** with different colors to distinguish separate experiments. Using Fe<sup>II</sup>PpIX as a catalyst,  $1.9 \times 10^{-6}$  moles of 2-(phenylamino)acetate (48% yield) were produced after 30 minutes, and time points collected later in the reaction did not demonstrate an appreciable increase in product yield (**Figure 3.9a**). It should be noted that the yield measured for this reaction with 10  $\mu$ M catalyst is higher compared to the 27% yield reported in Chapter 2 with 20  $\mu$ M.<sup>13</sup> It is unclear why the measured yield is much higher for catalyst at 10  $\mu$ M compared to previous data. Unfortunately, an initial rate cannot readily be calculated from the available data as the early time points collected at 1, 5, and 10 minutes do not exhibit a linear relationship. The product yield just one minute into the reaction is also much higher

than expected (40% yield) which may result in part from separate experiments being run to collect the shorter timescale data compared to the longer timescale data.

**Table 3.2.** Catalytic lifetime activity of Fe and Ru catalysts for the N-H insertion of aniline.

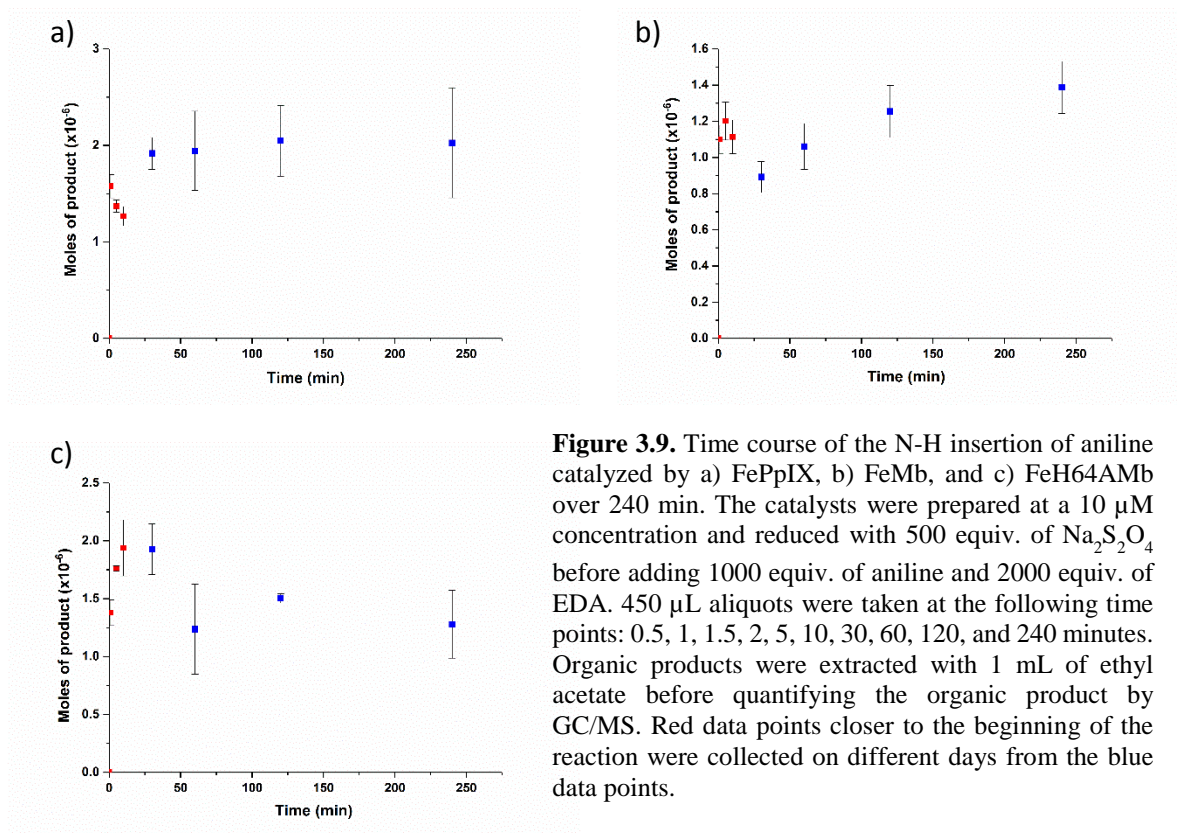
| Catalyst | Concentration | % Yield | Lifetime (min) |
|----------|---------------|---------|----------------|
| FePpIX   | 10 $\mu$ M    | 48      | $\leq$ 30      |
| FeMb     | 10 $\mu$ M    | 35      | 120            |
| FeH64AMb | 10 $\mu$ M    | 48      | $\leq$ 30      |
| RuMpIX   | 10 $\mu$ M    | 58      | $\leq$ 30      |
| RuMb     | 10 $\mu$ M    | 35      | $\leq$ 30      |
| RuH64AMb | 10 $\mu$ M    | 34      | $\leq$ 30      |

Reactions were set up in 3-4 mL pots with 0.1% catalyst loading, 500 equivalents of  $\text{Na}_2\text{S}_2\text{O}_4$ , 1000 equivalents aniline, and 2000 equivalents EDA. 450  $\mu$ L aliquots were collected at various time points and organic products were extracted with ethyl acetate. Percent yield was calculated with an internal standard of 3.3 mM 2-phenyl ethanol.

$\text{Fe}^{\text{II}}\text{Mb}$  exhibits lower yield for the N-H insertion of aniline compared to  $\text{Fe}^{\text{II}}\text{PpIX}$  (**Figure 3.9b**) at a 10  $\mu$ M catalyst concentration. After 30 minutes,  $8.9 \times 10^{-7}$  moles of 2-(phenylamino)acetate (22% yield) are generated which increases over the span of 120 minutes to  $1.4 \times 10^{-6}$  moles of product (35% yield). The long timescale data for  $\text{Fe}^{\text{II}}\text{Mb}$  indicate that the N-H insertion of aniline occurs over a longer period of time compared to the cyclopropanation of styrene, which was finished after 30 minutes. This could result from the higher solubility and therefore availability of aniline as a substrate in the reaction mixture compared to styrene. Increased availability of the substrate would likely allow for more facile interception of the metallocarbene intermediate and thus a slower rate of catalyst decomposition from the insertion of

the carbene ligand into the porphyrin or protein scaffold. Data collected at 1, 5, and 10 minutes once again do not show a linear relationship and exhibit higher product yield compared to data collected after 30 and 60 minutes of the reaction. This is likely an experimental artifact by running experiments on different days to collect the shorter timescale data. If the shorter timescale data points are accurate, N-H insertion activity occurs over a much shorter period of time, which may result from high initial activity with more aniline substrate available, followed by catalyst inactivation.

Fe<sup>II</sup>H64AMb catalyzes the N-H insertion of aniline in 48% yield ( $1.9 \times 10^{-6}$  moles of 2-(phenylamino)acetate) after 30 minutes (**Figure 3.9c**). Data collected at 60 and 120 minutes exhibit decreased yield of 31% and 38%, respectively. It seems unlikely that this decrease in yield results from the decomposition of product over time, as no decrease in yield was observed when using either Fe<sup>II</sup>Mb or Fe<sup>II</sup>PpIX. It is currently unclear why the measured product yield decreased after the 30 minute time point, but it should also be noted that the standard deviations of data points collected at 60 and 240 minutes are relatively high. Shorter timescale data collected at 1, 5, and 10 minutes also exhibit higher product yield than expected, as was the case for Fe<sup>II</sup>Mb. Increased product yield after 30 minutes compared to Fe<sup>II</sup>Mb was expected as the larger active site of Fe<sup>II</sup>H64AMb likely allows for easier substrate access. The reaction is also finished after 30 minutes compared to 120 minutes for Fe<sup>II</sup>Mb. Although the higher activity and initial rate of reaction for Fe<sup>II</sup>H64AMb compared to Fe<sup>II</sup>Mb is likely due to the larger and more hydrophobic active site, the reason for lower catalyst lifetime and decrease in product generation after 30 minutes is not clear at this point in time.



At a 10  $\mu\text{M}$  concentration,  $\text{Ru}^{\text{II}}\text{MpIX}(\text{X})$  catalyzes the N-H insertion of aniline in 58% yield, or  $2.3 \times 10^{-6}$  moles of product after 30 minutes (**Figure 3.10a**). As with the cyclopropanation of styrene,  $\text{Ru}^{\text{II}}\text{MpIX}(\text{X})$  is a more active catalyst compared to  $\text{Fe}^{\text{II}}\text{PpIX}$ . The reaction reaches its endpoint within the first 30 minutes of the reaction as yield did not increase over time, even past 240 minutes (data not shown). If the data collected from one to ten minutes is accurate, the reaction is finished almost instantly, likely concomitant with carbene insertion into the porphyrin and swift catalyst decomposition. Catalyst lifetime is short for all  $\text{Ru}^{\text{II}}$  catalysts that were tested for both the cyclopropanation of styrene and the N-H insertion of aniline, and this case is no exception. Initial data points (1-10 minutes) also demonstrated high yield (58-74%), but as indicated above,

these data points were collected on a different day, and it is not clear if they are accurate for a one-pot reaction.

Similar to Ru<sup>II</sup>MpIX(X), Ru<sup>II</sup>Mb is only active for the N-H insertion of aniline over a period of 30 minutes or less (**Figure 3.10b**). At the 30 minute time point,  $1.4 \times 10^{-6}$  moles of 2-(phenylamino)acetate (35% yield) are produced, and no further increase in product yield is observed over time. Once again, aniline is more available as a substrate in the reaction mixture compared to styrene, and thus even though Ru<sup>II</sup>Mb rapidly decomposes in the presence of EDA, aniline is able to intercept the metallocarbene intermediate on short timescales and more product is produced.

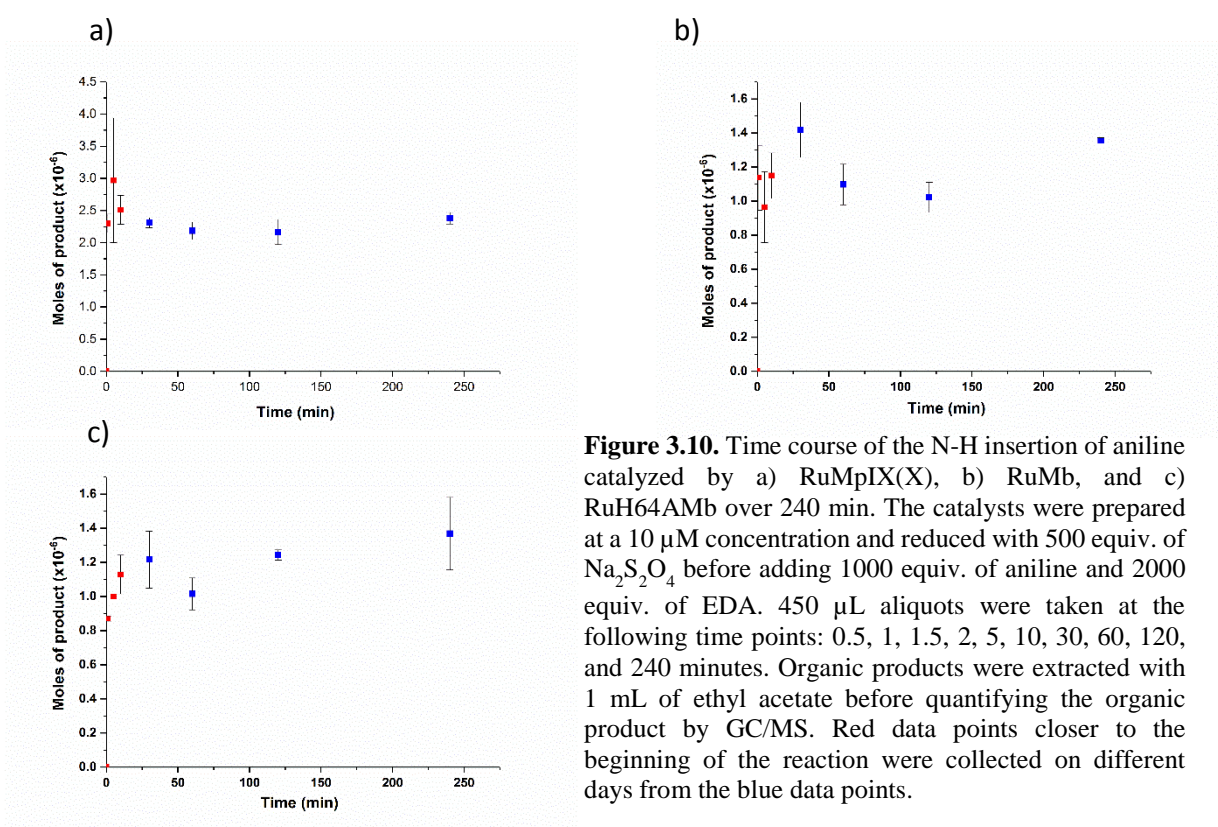


**Figure 3.10.** Time course of the N-H insertion of aniline catalyzed by a) RuMpIX(X), b) RuMb, and c) RuH64AMb over 240 min. The catalysts were prepared at a 10  $\mu$ M concentration and reduced with 500 equiv. of Na<sub>2</sub>S<sub>2</sub>O<sub>4</sub> before adding 1000 equiv. of aniline and 2000 equiv. of EDA. 450  $\mu$ L aliquots were taken at the following time points: 0.5, 1, 1.5, 2, 5, 10, 30, 60, 120, and 240 minutes. Organic products were extracted with 1 mL of ethyl acetate before quantifying the organic product by GC/MS. Red data points closer to the beginning of the reaction were collected on different days from the blue data points.

Remarkably similar results were achieved for the N-H insertion of aniline catalyzed by Ru<sup>II</sup>H64AMb in comparison with Ru<sup>II</sup>Mb (**Figure 3.10c**). After 30 minutes,  $1.2 \times 10^{-6}$  moles of 2-

(phenylamino)acetate were produced (31% yield), and although the yield improved slightly to  $1.4 \times 10^{-6}$  moles of product (34% yield) after 240 minutes, the values are both within one standard deviation of each other. Therefore, the reaction appears to finish within 30 minutes, as is the case for all of the N-H insertion reactions facilitated by the Fe<sup>II</sup> and Ru<sup>II</sup> catalysts tested. Time points taken at 1, 5, and 10 minutes exhibited 23-27% yield, but as was the case for the data collected for Fe<sup>II</sup> catalysts, it is unclear if these data are accurate.

## Discussion

In a variety of different investigations into carbene transfer catalysis by modified heme proteins (including work done in Chapter 2), reactions are run over an extended period of time, typically 12-18 hours.<sup>5, 13, 25</sup> Data here suggest that these catalytic reactions typically reach their endpoint in a much shorter period of time, many under one hour. For the cyclopropanation reaction, Fe<sup>II</sup>Mb, Fe<sup>II</sup>H64AMb, and Ru<sup>II</sup>MpIX cease catalysis after 30 minutes, and Ru<sup>II</sup>Mb and Ru<sup>II</sup>H64AMb exhibit extremely short lifetimes for the reaction, only catalyzing the cyclopropanation of styrene in low yield (1-3%) on the timescale of a couple minutes. The short catalytic lifetimes of Ru<sup>II</sup>Mb and Ru<sup>II</sup>H64AMb arise from rapid insertion of the metallocarbene unit into the ruthenium porphyrin and the protein scaffold, as discussed in Chapter 2. Ru<sup>II</sup>MpIX also exhibits a short lifetime for the cyclopropanation of styrene but in this case the catalyst is more accessible to both EDA and styrene, and high activity is observed 30 minutes into the reaction. Ru<sup>II</sup>MpIX exhibits a higher  $k_{\text{obs}}$  of  $5.9 \times 10^{-2} \text{ min}^{-1}$  compared to  $2.9 \times 10^{-2} \text{ min}^{-1}$  for Fe<sup>II</sup>PpIX, indicating a faster rate of product formation despite a shorter catalytic lifetime. This supports our hypothesis that the Ru=CR<sub>2</sub> unit is more reactive compared to Fe=CR<sub>2</sub>, and the carbene unit inserts rapidly into the porphyrin scaffold, decomposing the catalyst (see Chapter 2).

Fe<sup>II</sup>Mb and Fe<sup>II</sup>H64AMb are less susceptible to carbene insertion into the porphyrin or protein scaffold, and both catalysts exhibit higher TON and longer catalyst lifetimes of approximately 30 minutes compared to Ru<sup>II</sup>Mb and Ru<sup>II</sup>H64AMb. At the 20  $\mu$ M concentration, Fe<sup>II</sup>H64AMb exhibits both higher activity and a higher rate of product formation compared to Fe<sup>II</sup>Mb for the cyclopropanation of styrene, as indicated for the higher  $k_{\text{obs}}$  for Fe<sup>II</sup>H64AMb compared to Fe<sup>II</sup>Mb. This result is likely due to the larger and more hydrophobic active site of Fe<sup>II</sup>H64AMb which allows styrene to access the metal center more readily. For the N-H insertion of aniline, most of the catalysts appear to cease function in 30 minutes or less, with the exception of Fe<sup>II</sup>Mb. In this case the moles of 2-(phenylamino)acetate increased up to two hours, although it should be noted that these values fall within one standard deviation of one another. This analysis also ignores the data points collected at 1, 5, and 10 minutes. As stated above, these data points were collected in different experiments, and although the experiments were conducted in the same manner as the longer time points, it seems clear that some intrinsic error in EDA and aniline loading led to increased TON at these shorter timescale data points. Aniline is more soluble in water than styrene and thus is more available to intercept the metallocarbene unit formed after the addition of EDA. Also, the decomposition of EDA and the N-H insertion of aniline occurs without any catalyst present in the reaction mixture. Thus, it is possible that the N-H insertion of aniline is complete within mere minutes for the catalysts studied here, but with the experimental error for the data points collected on shorter timescales, that claim cannot be made at the moment. All six of the catalysts tested are functional for the N-H insertion of aniline, and Ru<sup>II</sup>Mb and Ru<sup>II</sup>H64AMb exhibit much higher activity for this reaction compared to the cyclopropanation of styrene. This is again due to the availability of aniline in the reaction mixture and the rapid interception of the metallocarbene bond prior to catalyst decomposition. To address the shortcomings of some of



these time course studies, other methods such as  $^1\text{H-NMR}$  kinetics or finding an appropriate poison to end catalyst functionality at different time points could be useful. These methods are not without their shortcomings, however. The first few minutes of the reaction would likely not be able to be measured by  $^1\text{H-NMR}$  kinetics. Also, pyridine and imidazole ligands were added in separate experiments to determine if these compounds would bind to the metal center and stop catalytic function, but these experiments were unsuccessful (data not shown). In either case, it is clear that the catalytic lifetime of artificial enzymes is an important parameter to consider in developing these novel catalysts. Studies in the future will continue to focus on improving both catalyst lifetime and activity.

### **3.3 FeH93GMb and RuH93GMb Preparation and Characterization**

As evidenced in Chapter 2 and above, the activity and catalytic lifetime for  $\text{Ru}^{\text{II}}\text{Mb}$  and other  $\text{RuMb}$  variants are quite low for the cyclopropanation of styrene in comparison to  $\text{Fe}^{\text{II}}\text{Mb}$ . The  $\text{Ru}=\text{CR}_2$  unit rapidly inserts into the porphyrin ligand itself as well as nucleophilic residues inside the protein, whereas the  $\text{Fe}=\text{CR}_2$  unit inserts at a much slower rate.<sup>13</sup> In wild-type Mb, an axial histidine coordinates to the metal center for both the native  $\text{FePpIX}$  and the reconstituted  $\text{RuMpIX}$ . By expressing the H93G mutant of Mb, a variety of exogenous ligands can be added such as alkoxides, thiolates, and phosphines, among others.<sup>16</sup> We hypothesized that anionic or more electron-donating ligands could help stabilize the metallocarbene by pushing electron density into the  $\text{Ru}=\text{CR}_2$  unit and making the carbene less electrophilic, and thus less likely to insert into the porphyrin or protein. In this study we prepared  $\text{FeH93GMb}$ , removed the heme and reconstituted the apo-protein with  $\text{RuMpIX}$ . After characterizing  $\text{RuH93GMb}$ , we added several

exogenous ligands to the reaction mixture to improve the catalytic activity of RuMpIX inside the protein scaffold.

The H93G Mb plasmid was prepared, the mutant was expressed in *E. coli*, and the protein was purified by column chromatography. After collecting the protein, the native heme was removed via Teale's method,<sup>26</sup> and fractions of apo-H93G Mb were reconstituted with FePpIX and RuMpIX(X) and characterized by electron absorption spectroscopy and circular dichroism. Fe<sup>III</sup>H93GMb has been studied extensively, and a typical electron absorption spectrum is shown in **Figure 3.11a**. The heme Soret band is observed at 405 nm, and a couple of absorption features are present at 490 and 603 nm. To our knowledge, Ru<sup>III</sup>H93GMb has not been prepared previously, at least not without CO bound to the Ru<sup>II</sup> center. The electronic absorption spectrum exhibits the Soret band at 397 nm, slightly red-shifted from Ru<sup>III</sup>Mb which exhibits the same band at ~392 nm (**Figure 3.11b**). The broad Q-band feature at 515 nm is the same for both Ru<sup>III</sup>H93GMb and Ru<sup>III</sup>Mb. Both prior to and after reconstitution, the circular dichroism spectra of apo-H93GMb, Fe<sup>III</sup>H93GMb, and Ru<sup>III</sup>H93GMb exhibit typical "double-well" features at 210 and 223 nm that indicate the anticipated alpha-helical folding (**Figure 3.12**). A mass of 17250.4 m/z was observed for H93GMb, indicating that His93 has been replaced with a glycine residue (**Figure 3.13a**). This is the protein mass without the metal cofactor; the FePpIX cofactor dissociates from the protein scaffold during time of flight measurements. Interestingly, this is not the case for RuH93GMb, as some of the RuMpIX remained bound to the protein scaffold during measurement as indicated by the mass peak at 17915.6 m/z. This is a bit surprising, as the cofactors should only be bound through hydrophobic contacts and salt bridges between the protein and the propionate side chains

of the porphyrin. Nevertheless, it is evident that the reconstitution of RuMpIX into apo-H93GMb was successful.

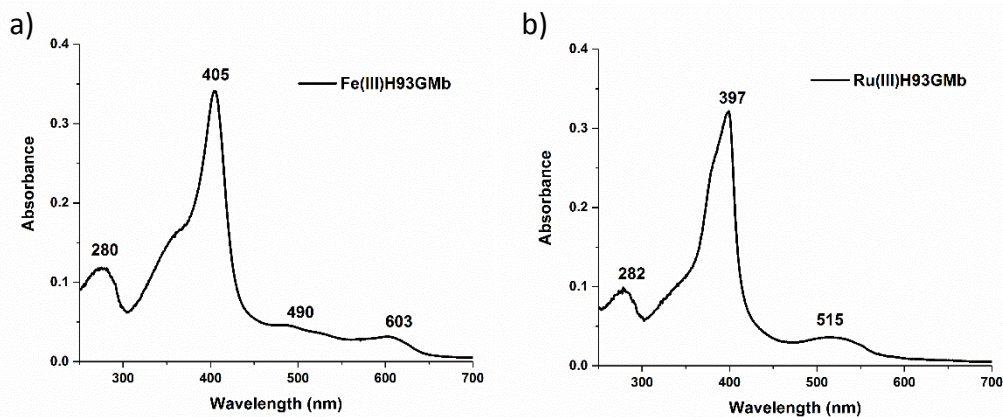


**Figure 3.11.** Electron absorption spectra of H93G Mb reconstituted with a) FePpIX and b) [RuMpIX(X)].

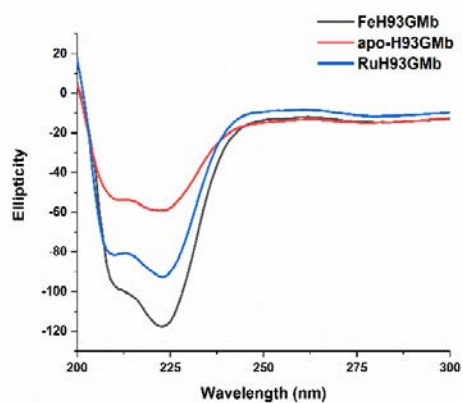


**Figure 3.12.** Circular dichroism spectra of the H93GMb with native heme bound, in the apo-form, and reconstituted with [RuMpIX(X)].

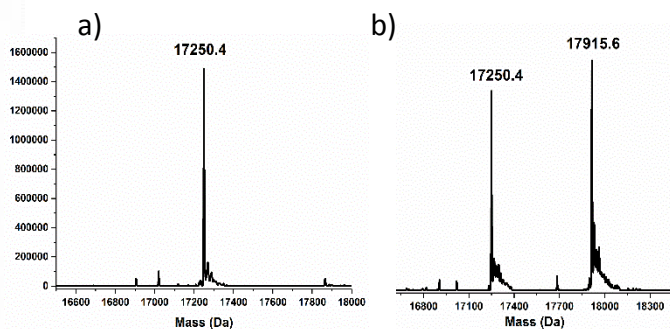


**Figure 3.13.** Mass spectra of a) FeH93GMb and b) RuH93GMb.

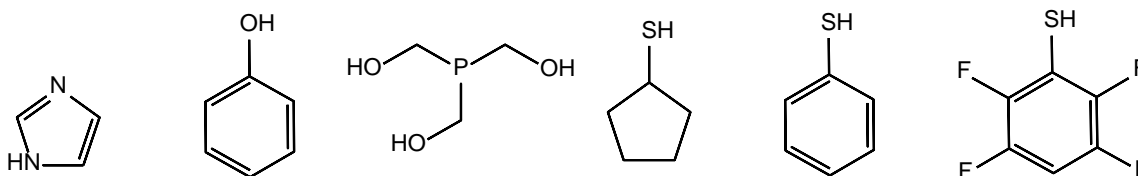


**Figure 3.14.** Ligands added to FeH93GMb and RuH93GMb in order to improve catalytic activity.

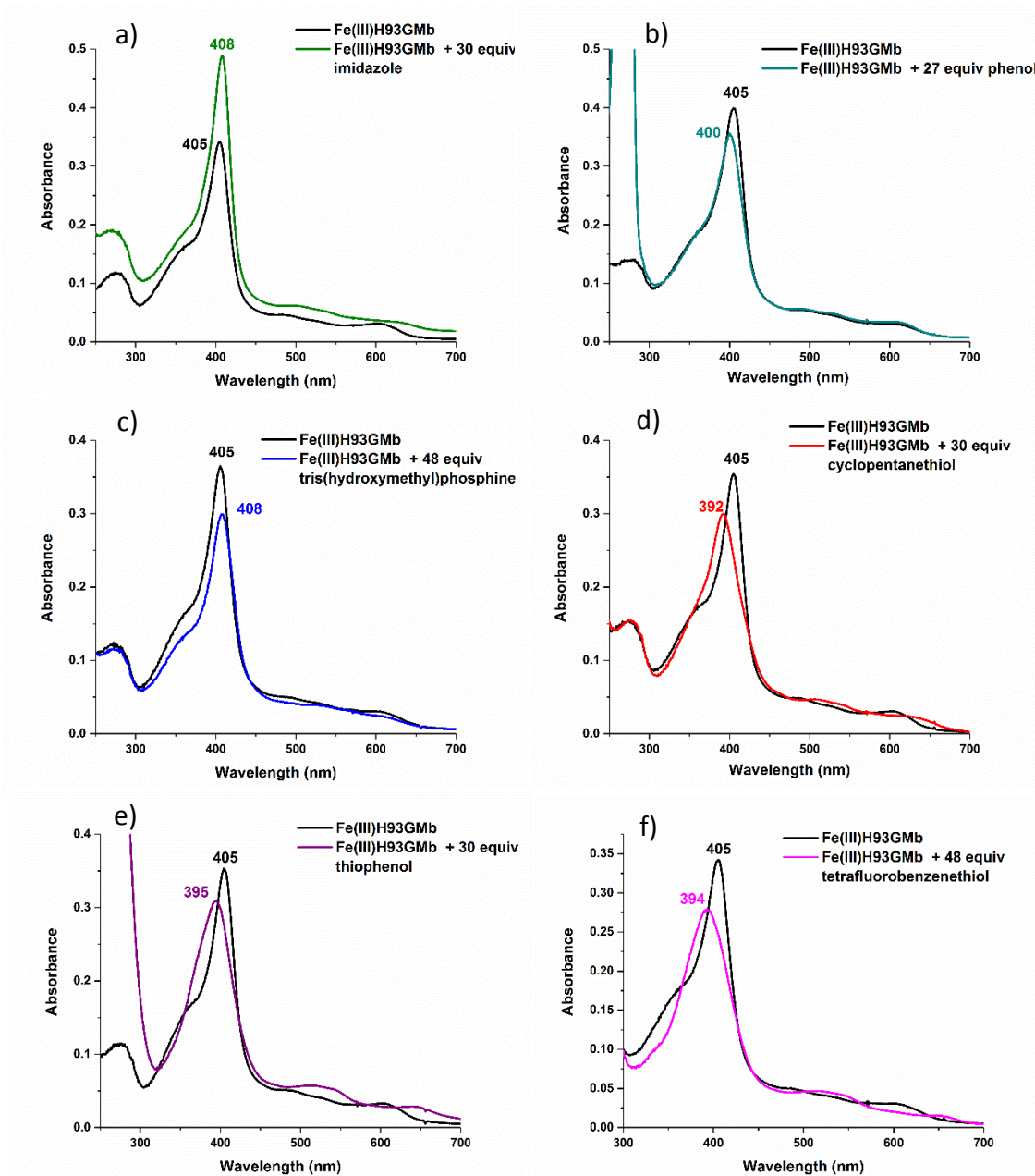


**Figure 3.15.** Electronic absorption spectra of Fe<sup>III</sup>H93GMb before and after the addition of excess exogenous ligands including a) imidazole, b) phenol, c) tris(hydroxymethyl)phosphine, d) cyclopentanethiol, e) thiophenol, and f) tetrafluorobenzenethiol.

After preparing Fe<sup>III</sup>H93GMb and Ru<sup>III</sup>H93GMb, different ligands were titrated or added to the reconstituted proteins in order to try and determine if the ligands would bind to the metal center. (Figure 3.14). Changes in the electronic absorption spectra of Fe<sup>III</sup>H93GMb upon ligand

addition have previously been studied for a wide variety of ligands.<sup>16</sup> Some of these ligand addition experiments were repeated in order to compare changes in electronic absorption spectra between Fe<sup>III</sup>H93GMb and Ru<sup>III</sup>H93GMb after the addition of ligands (**Figure 3.15**). As expected, shifts in the Soret band and Q bands were observed and results matched previous literature work. The one ligand that had not been previously studied was tetrafluorobenzenethiol, a more electron-deficient thiophenol derivative. Addition of tetrafluorobenzenethiol to Fe<sup>III</sup>H93GMb resulted in broadening of the Soret band as well as a shift from 405 to 394 nm, similar to the spectral features that result after the addition of thiophenol. (**Figure 3.15e and f**). New features also appear at 515 and 653 nm, again similar to the binding of thiophenol to Fe<sup>III</sup>H93GMb. It is clear from these results and previous work that the proximal pocket in H93G Mb can accommodate a wide variety of exogenous ligands. In contrast to Fe<sup>III</sup>H93GMb, the titration of exogenous ligands did not cause any appreciable shifts in the Soret band or the Q bands in the spectrum of Ru<sup>III</sup>H93GMb (**Figure 3.16**). After the titration of each ligand into Ru<sup>III</sup>H93GMb, the Soret band remained in between 393-398 nm and the broad Q band remained at 515 nm. It is unclear from the Ru<sup>III</sup>H93GMb spectra if the exogenous ligands are binding to the metal center or not. Ru<sup>III</sup>H93GMb was reduced to Ru<sup>II</sup> with the addition of excess dithionite, upon which the Soret band sharpens and shifts to 394 nm, and two sharp Q band features appear at 494 and 521 nm (**Figure 3.17a**). This spectrum is almost identical to the electron absorption spectrum of Ru<sup>II</sup>Mb. As was the case for Ru<sup>III</sup>H93GMb, no spectral changes were observed upon the addition of the same six ligands.



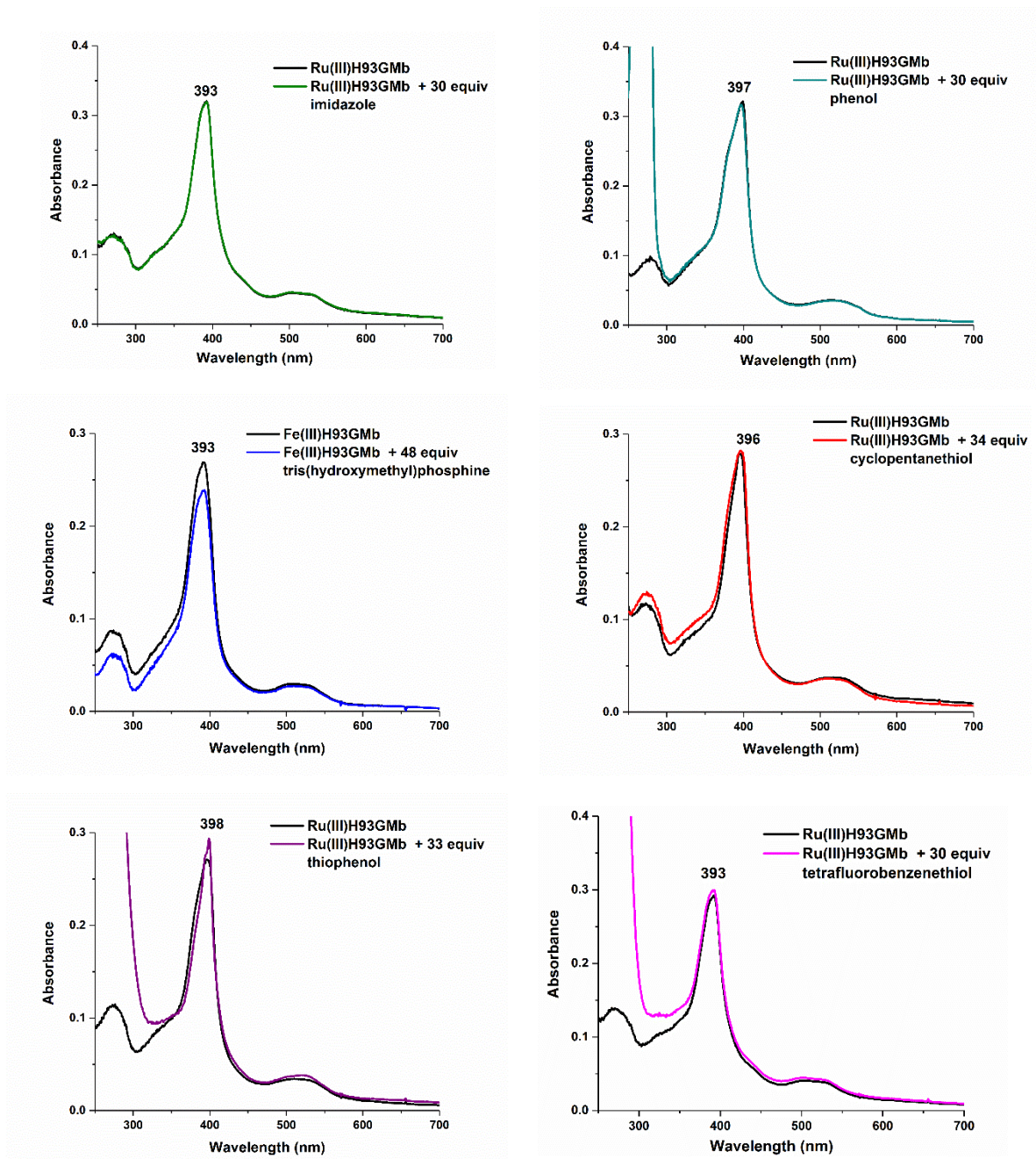


**Figure 3.16.** Electronic absorption spectra of Ru<sup>III</sup>H93GMb before and after the addition of excess exogenous ligands including a) imidazole, b) phenol, c) tris(hydroxymethyl)phosphine, d) cyclopentanethiol, e) thiophenol, and f) tetrafluorobenzenethiol.

Carbon monoxide was bound to the reduced Ru<sup>II</sup> center by bubbling CO through the solution for two minutes. After the addition of CO, a weak band at 550 nm appeared and the Soret

band shifted slightly to 397 nm (**Figure 3.17a**). The CO band is not split into two smaller Q bands as observed in wild-type RuMb, suggesting that the CO may be bound in the proximal site of the heme.<sup>27</sup> Unfortunately, no spectral changes were observed by adding exogenous ligands either before or after the bubbling of CO to Ru<sup>II</sup>H93GMb (**Figure 3.17**). Future work will focus on trying to detecting ligand binding to Ru through IR spectroscopy. By concentrating the protein, binding CO, and adding the ligands above to Ru<sup>II</sup>-CO, we may be able to observe a change in the energy of the C-O stretching frequency. To detect phosphine binding, <sup>31</sup>P NMR spectroscopy may also be used.

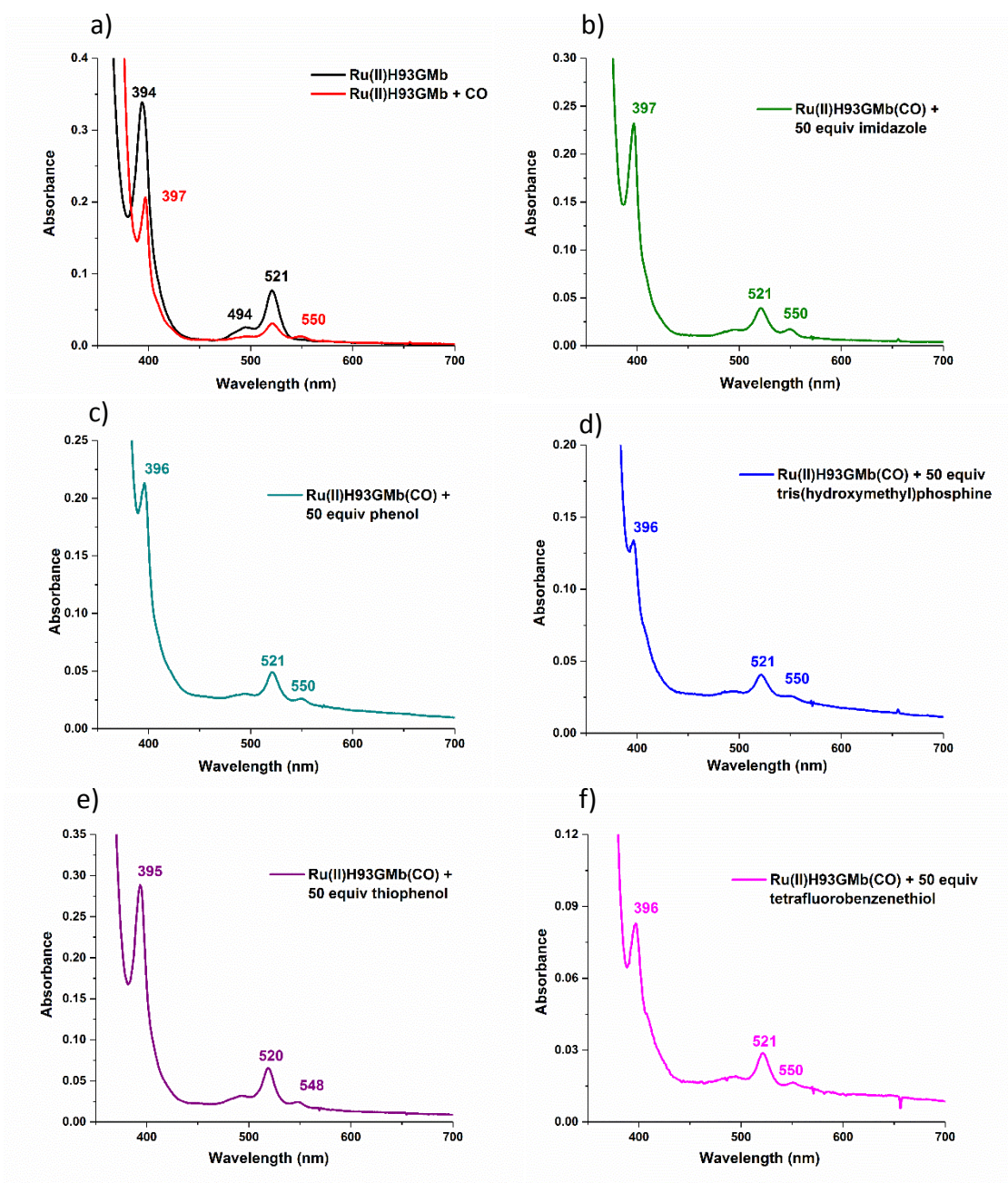


**Figure 3.17.** Electronic absorption spectra of Ru<sup>II</sup>H93GMb and Ru<sup>II</sup>H93GMb(CO) after the addition of excess exogenous ligands including a) CO, b) imidazole, c) phenol, d) tris(hydroxymethyl)phosphine, e) thiophenol, and f) tetrafluorobenzenethiol.

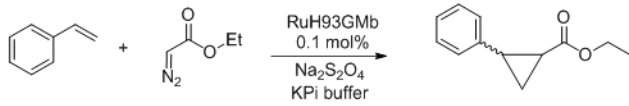


### 3.4 Cyclopropanation of Styrene Using RuH93GMb with the Addition of Various Exogenous Ligands

Despite not detecting if ligands were binding to the Ru center in RuH93GMb, the cyclopropanation activity of Ru<sup>II</sup>H93GMb was studied with the various ligands added to the reaction mixture. After reducing Ru<sup>III</sup> to Ru<sup>II</sup>, the ligands were immediately added to the aqueous reaction media followed by styrene and EDA after two minutes. Reactions were run for 18 hours to directly compare to the data collected in Chapter 2. Without any ligand added to the reaction mixture, Ru<sup>II</sup>H93GMb catalyzes the cyclopropanation of styrene in 3.4% yield, similar to Ru<sup>II</sup>Mb, which catalyzes the same reaction in 3.2% yield (**Table 3.3**). Ru<sup>II</sup>H93GMb achieves only 66% of the *trans* cyclopropane isomer, which could indicate that a small percentage of the RuMpIX dissociates from the Mb scaffold to catalyze the reaction. It is evident that most of the RuMpIX stays bound inside the protein as higher yield would be expected if RuMpIX dissociates during the reaction. Ligands were added into the reaction mixtures in either 1, 5, or 50 equivalents. Unfortunately, Ru<sup>II</sup>H93GMb achieves  $\leq 1.2\%$  yield for the cyclopropanation of styrene in each case for the six different ligands added to the reaction mixture. Ru<sup>II</sup>H93GMb with the addition of exogenous ligands achieves 77-84% *trans* isomer, though it should be noted that at such low yields the stereoselectivity is difficult to measure accurately. This may also help to explain why at 50 equivalents of ligand added, stereoselectivity decreases to 65-69%. Some variability in the stereoselectivity of RuMb for the cyclopropanation reaction has been observed previously, though in all cases, low yield for cyclopropanation has been a constant. Ru<sup>II</sup>H93GMb(CO) exhibits a particularly low yield for the cyclopropanation of styrene, close to 0%. Carbon monoxide was the only ligand that could readily be detected to bind to Ru<sup>II</sup> by electron absorption spectroscopy, and required the addition of excess Na<sub>2</sub>S<sub>2</sub>O<sub>4</sub> to reduce Ru<sup>III</sup> to Ru<sup>II</sup> before binding CO and adding

styrene and EDA. Whether the ligands are binding or not binding to the metal center in Ru<sup>II</sup>H93GMb, yields for the cyclopropanation of styrene remain extremely low.

**Table 3.3.** Catalytic activity of RuH93G with various ligands added



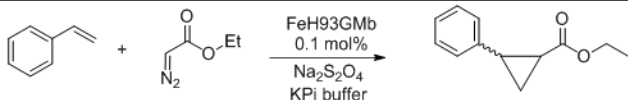
| Ligand                        | Equiv. added | Yield <sup>b</sup> (%) | TON | % <i>trans</i> diastereomer |
|-------------------------------|--------------|------------------------|-----|-----------------------------|
| No Ligand                     | N/A          | 3.4                    | 34  | 66                          |
| Imidazole                     | 1            | 0.5                    | 5   | 84                          |
|                               | 5            | 0.3                    | 3   | 86                          |
|                               | 50           | 0.5                    | 5   | 69                          |
| Phenol                        | 1            | 0.3                    | 3   | 80                          |
|                               | 5            | 0.5                    | 5   | 83                          |
|                               | 50           | 0.1                    | 1   | 65                          |
| Tris(hydroxymethyl) phosphine | 1            | 0.4                    | 4   | 80                          |
|                               | 5            | 1.2                    | 12  | 78                          |
| Cyclopentanethiol             | 1            | 0.3                    | 3   | 77                          |
|                               | 5            | 0.2                    | 2   | 83                          |
|                               | 50           | 0.1                    | 1   | 65                          |
| Thiophenol                    | 1            | 0.5                    | 5   | 82                          |
|                               | 5            | 0.3                    | 3   | 84                          |
| Tetrafluorobenzenethiol       | 1            | 0.6                    | 6   | 81                          |
|                               | 5            | 0.7                    | 7   | 81                          |
| CO                            | 1            | 0                      | 0.4 | 84                          |

450  $\mu$ L scale reactions using 20  $\mu$ M catalyst (0.1 ml %), 10 mM Na<sub>2</sub>S<sub>2</sub>O<sub>4</sub>, 20mM styrene and 40 mM EDA conducted for 18 hours at room temperature under micro-aerobic conditions. <sup>b</sup>Determined based on GC-MS conversion using a calibration curve with isolated cyclopropane product.

In contrast to Ru<sup>II</sup>H93GMb, Fe<sup>II</sup>H93GMb demonstrates moderate activity for the cyclopropanation of styrene (**Table 3.4**). Without ligand added, Fe<sup>II</sup>H93GMb catalyzes the cyclopropanation of styrene in 32% yield, which is slightly higher than Fe<sup>II</sup>Mb which catalyzes the same reaction in 25% yield. The addition of five equivalents of imidazole or phenol do not lead

to significant change in reaction yield, catalyzing cyclopropanation in 31% and 29% yield, respectively. Addition of tris(hydroxymethyl)phosphine and tetrafluorobenzenethiol result in a decrease in yield for the reaction to 15% and 11%, respectively. If these ligands act as stronger donors to the Fe=CR<sub>2</sub> unit, it may be the case that the metallocarbene becomes less electrophilic and less reactive with styrene or other nucleophiles. More catalyst lifetime studies and turnover frequency studies would have to be conducted to better understand this phenomenon. With or without ligand added, Fe<sup>II</sup>H93GMb achieves 88-92% *trans* cyclopropane which is similar to wild-type Fe<sup>II</sup>Mb. Despite the lower yields observed after the addition of the phosphine and thiol ligands to the protein, Fe<sup>II</sup>H93GMb is still a much more functional catalyst compared to Ru<sup>II</sup>H93GMb.

**Table 3.4.** Catalytic activity of FeH93G with various ligands added



| Ligand                           | Yield <sup>b</sup><br>(%) | TON | % <i>trans</i><br>diastereomer |
|----------------------------------|---------------------------|-----|--------------------------------|
| No Ligand                        | 32                        | 316 | 88                             |
| Imidazole                        | 31                        | 305 | 89                             |
| Phenol                           | 29                        | 294 | 89                             |
| Tris(hydroxymethyl)<br>phosphine | 15                        | 152 | 92                             |
| Tetrafluoro-<br>benzenethiol     | 11                        | 106 | 92                             |

<sup>a</sup> 450  $\mu$ L scale reactions using 20  $\mu$ M catalyst (0.1 ml %), 10 mM Na<sub>2</sub>S<sub>2</sub>O<sub>4</sub>, 20mM **4a** and 40 mM **2** conducted for 18 hours at room temperature under micro-aerobic conditions. <sup>b</sup>Determined based on GC-MS conversion using a calibration curve with isolated cyclopropane product.

## Discussion

After the preparation of Ru<sup>II</sup>H93GMb and the addition of various exogenous ligands, catalyst activity for the cyclopropanation of styrene remained low. The Ru=CR<sub>2</sub> unit inserts rapidly into the porphyrin itself and the protein scaffold in Ru<sup>II</sup>Mb and by adding more electron donating ligands we hoped to modulate this activity. If donating ligands such as thiols and phosphines could donate electron density to the Ru=CR<sub>2</sub> unit and decrease the electrophilicity of the carbene, then the carbene might be less reactive towards undesired decomposition products and improve catalyst lifetime and activity. Nevertheless, yield did not improve when adding thiols, phosphine, or phenol. It is unclear whether or not these ligands were actually binding to the Ru center, as binding could not readily be detected by electron absorption spectroscopy. Other spectroscopic methods such as monitoring the CO stretch by vibrational spectroscopy after the addition of ligands or detecting ligand binding via NMR spectroscopy need to be investigated in the future to determine if these ligands are binding to Ru or not. In contrast, ligand binding to the Fe<sup>III</sup> center in Fe<sup>III</sup>H93GMb could easily be detected by UV-vis spectroscopy. Activity for Fe<sup>II</sup>H93GMb towards the cyclopropanation of styrene remained moderately high, similar to Fe<sup>II</sup>Mb, with the exception of tris(hydroxymethyl)phosphine and tetrafluorobenzenethiol (the only thiol tested with Fe<sup>II</sup>H93GMb). It may be the case that the addition of these more electron donating ligands resulted in a decrease in the electrophilicity of the Fe=CR<sub>2</sub> unit, and thus the reactivity of the metallocarbene towards styrene also decreased. It is also important to note that these reactions were not run in triplicate, and thus some variability in yield may be expected when repeating these experiments. In addition, UV-vis absorption kinetics should be measured in order to determine if the exogenous ligand bound to Fe<sup>II</sup> remains bound after the addition of EDA to the reaction mixture. In the future, new Mb mutants such as H93C and H93Y can be prepared to ensure thiol

or phenolate binding to the Fe<sup>II</sup> or Ru<sup>II</sup> center, though it seems likely that RuMb variants will continue to decompose quickly in the presence of EDA and act as poor catalysts for the cyclopropanation of styrene.

### **3.5 Experimental Section**

#### **General Procedures**

All chemicals and reagents were purchased from commercial suppliers (Sigma Aldrich, Fisher Scientific, Acros, Frontier Scientific) and used without further purification unless otherwise noted. Gas chromatography/ mass spectrometry (GC/MS) analyses were carried out using a Shimadzu QP-2010 GC/MS equipped with a 30 meter long DB-5 column with 0.25 mm I.D. Separation method: 1  $\mu$ L injection, injector temp.: 200 °C, detector temp.: 250 °C. Gradient: column temperature set to 60 °C for 3 min, then to 250 °C at 20 °C/min, and held at 250 °C for 2.5 min (7.5 min for derivatives). Total run time was 10.75 min for both the N-H insertion and cyclopropanation reactions. Protein mass spectrometry analyses were carried out using an Agilent Q-TOF HPLC-MS equipped with a Poroshell 300SB-C8 column. Separation method: 20  $\mu$ L injection, flow rate: 0.5 mL/min, gradient: 95:5 water:acetonitrile for 3 min, followed by an increase over 10 min to 100% acetonitrile to elute the protein. Total run time was 13 min. All reagents and proteins were brought into a Coy vinyl anaerobic chamber (40-70 ppm O<sub>2</sub>, 1.5-3.0% H<sub>2</sub>) before running the reactions.

#### **Mutagenesis**

Mutagenesis of wild-type Mb was performed using the QuikChange XL protocol according to the manufacturer's instructions. The H93G mutation is shown in bold, and the reverse primer was

the exact reverse and complement of the primer given. The H93G variant was made by adding the forward primer CCGCTTGCGCAATCGGGTGCTACTAACATAAG prior to PCR.

### **Protein Expression and Purification**

Wild-type sperm whale Mb and H93G Mb were expressed from the pEMBL19(+) plasmid in *E. coli* BL21(DE3) cells, modified from standard procedures.<sup>28</sup> Briefly, cells were grown in LB media, (ampicillin, 50 µg/L) at 37 °C and 160 rpm until OD<sub>600</sub> reached ~ 0.8. The cell-containing media were placed on ice immediately after expression and cells were pelleted by centrifuging at 8800 rpm and 4 °C using a Beckman Coulter JA-10 fixed-angle rotor. Cell pellets were suspended in ~100 mL of 50 mM Tris buffer, pH = 8, and 10 mL of lysis buffer were added prior to sonication. Cells were sonicated using a Fisher Scientific Model 550 Dismembrator. The cells were pulsed 6 times at 15 s each time with 1 min intervals. After adding a stock solution of DNase (1 µg/mL) and stirring for one hour, the suspended cells were subjected to the sonication procedure again. The lysed cells and protein mixture was centrifuged at 8800 rpm and 4 °C for 80 min to extract the protein. The protein was initially purified by adding ammonium sulfate up to 50% saturation, centrifuging, and then adding more ammonium sulfate up to 90% saturation to precipitate myoglobin. After another round of centrifugation, the protein pellet was collected, suspended in 10 mM potassium phosphate (KPi) buffer, pH = 6, and then dialyzed against the same buffer. The protein was loaded onto a CM Sepharose column with 10 mM KPi buffer pH 6, and the collected protein fractions were then concentrated and loaded onto a Sephadex G-50 column with 100 mM KPi buffer, pH = 7, and eluted with the same buffer. The proteins were characterized by UV-vis and circular dichroism spectroscopy.

## Expression and Purification of 6x His-tagged Proteins

In addition to the above protocol for proteins without a His-tag, two plasmids (pET22-b) were ordered from GenScript to express 6x His-tagged versions of wild-type sperm whale Mb, and H93G Mb. These plasmids were hydrated in 100  $\mu$ L of Milli-Q water and stored at -20 °C prior to use. The expression and purification system for these proteins was slightly different than above.<sup>10</sup> Briefly, cells were grown in Terrific Broth (ampicillin, 100  $\mu$ g/mL) at 37 °C and 150 rpm until OD<sub>600</sub> reached 0.6-0.8 at which point 0.25 mM isopropyl  $\beta$ -D-1-thiogalactopyranoside (IPTG) was added to induce protein overexpression. In addition, 0.3 mM amino-leuvulinic acid was added at the same time to aid in heme synthesis. After a 17 hour incubation at 31 °C, the cell-containing media were placed on ice immediately and cells were pelleted by centrifuging at 8800 rpm and 4 °C using a Beckman Coulter JA-10 fixed-angle rotor. Cell pellets were suspended in ~100 mL of 50 mM Tris buffer, pH = 8, and 10 mL of lysis buffer were added prior to sonication. Cells were sonicated using a Fisher Scientific Model 550 Dismembrator. The cells were pulsed 6 times at 15 s each time with 1 min intervals. After adding a stock solution of DNase (1  $\mu$ g/mL) and stirring for one hour, the suspended cells were subjected to the sonication procedure again. The lysed cells and protein mixture was centrifuged at 8800 rpm and 4 °C for 80 min to extract the protein. After cell lysis, the supernatant was loaded onto a Ni-NTA agarose column and the red protein bound to the top of the column. The bound protein was washed with two buffers, first with a 50 mM potassium phosphate, 800 mM NaCl buffer at pH 6.2 followed by a 50 mM potassium phosphate, 800 mM NaCl, 250 mM glycine buffer at pH 6.2. The protein was eluted with a 50 mM potassium phosphate, 800 mM NaCl, 300 mM imidazole buffer at pH 7 before concentrating and characterizing by electron absorption spectroscopy, circular dichroism, and mass spectrometry.

Purity was determined by gel electrophoresis. Mb with and without an N-terminal His-tag catalyzes the cyclopropanation of styrene in the same yield.

### **Cyclopropanation and N-H Insertion Reactions Over Time**

Reactions were mostly carried out on a 3-4 mL scale using 10  $\mu$ M catalyst, 10 mM styrene or aniline, 20 mM ethyl diazoacetate (EDA), and 5 mM Na<sub>2</sub>S<sub>2</sub>O<sub>4</sub> (all of the concentrations are doubled for the 20  $\mu$ M catalyst reactions). The sodium dithionite (100 mM stock solution) in potassium phosphate buffer (100 mM, pH 7.0) was purged by bubbling argon through the solution for 10 min in a sealed vial. The Fe<sup>III</sup>/Ru<sup>III</sup> protein was first reduced to Fe<sup>II</sup>/Ru<sup>II</sup> through addition of 500 equivalents of Na<sub>2</sub>S<sub>2</sub>O<sub>4</sub> solution, followed by the addition of 1000 equivalents of styrene or aniline from a 1-2M stock solution in methanol (depending on the concentration of catalyst) and 2000 equivalents of EDA (1-2 M stock solution in methanol), which translates to a total MeOH content of 2.65%. The reactions were under magnetic agitation and 450  $\mu$ L aliquots were collected at various timepoints. To these aliquots, 1 mL of ethyl acetate was added to extract the organic products, and 600  $\mu$ L of the ethyl acetate layer was transferred to a GC/MS vial. As a GC/MS standard, 1-2  $\mu$ L of 1 M 2-phenyl ethanol were added to the 600  $\mu$ L of organic product to quantify the cyclopropanation or N-H insertion product. For the cyclopropanation reactions apart from those catalyzed by RuMb and RuH64AMb, product formation over time was fit with an exponential curve from which  $k_{\text{obs}}$  and  $t_{1/2}$  were determined

### **Cyclopropanation using RuH93GMb and FeH93GMb**

Reactions were carried out at a ~450  $\mu$ L scale using 20  $\mu$ M RuH93GMb or FeH93GMb, 20 mM styrene, 40 mM ethyl diazoacetate (EDA), and 10 mM Na<sub>2</sub>S<sub>2</sub>O<sub>4</sub>. The sodium dithionite (100 mM stock solution) in potassium phosphate buffer (100 mM, pH 7.0) was purged by bubbling argon through the solution for 10 min in a sealed vial. All reagents and proteins were brought into



a Coy vinyl anaerobic chamber (30-50 ppm O<sub>2</sub>, 1.5-3.0% H<sub>2</sub>) before running the reactions. The Ru<sup>III</sup> protein was first reduced to Ru<sup>II</sup> through addition of 40 μL of Na<sub>2</sub>S<sub>2</sub>O<sub>4</sub> solution, followed by the addition of one of the following six ligands: imidazole, phenol, tris(hydroxymethyl)phosphine, cyclopentanethiol, thiophenol, and tetrafluorobenzenethiol. Ligands were added in either 1, 5, or 50 equivalents. Stock solutions of imidazole and tris(hydroxymethyl)phosphine were prepared in pH 7 potassium phosphate buffer and stock solutions of phenol, cyclopentanethiol, thiophenol and tetrafluorobenzenethiol were prepared in dimethylformamide. Only 1 or 5 μL of ligand stock solution were added to each reaction. Carbon monoxide was also used as a ligand for one of the reactions, see below. Ligand addition was followed by the addition of 4 μL of styrene and 8 μL of EDA (2 M stock solution in methanol), which translates to a total MeOH content of 2.65%. The reactions were left under magnetic agitation for 18 hours at room temperature. After 18 hours, 1 mL of ethyl acetate was added to extract the organic products, and 600 μL of the ethyl acetate layer was transferred to a GC/MS vial. As a GC/MS standard, 1 μL of 1 M 2-phenyl ethanol were added to the 600 μL of organic product. Calibration curves for quantification of ethyl 2-phenylcyclopropanecarboxylate were constructed using authentic standards produced synthetically (using 1-2 mol% Rh<sub>2</sub>(OAc)<sub>4</sub> as the catalyst). Measurements were not performed in triplicate, data were collected from single reactions with different ligands.

### **Ligand addition to Fe<sup>III</sup>H93GMb and Ru<sup>III</sup>H93GMb**

The following six ligands were added to Fe<sup>III</sup>H93GMb and Ru<sup>III</sup>H93GMb in various concentrations and equivalents: imidazole, phenol, tris(hydroxymethyl)phosphine, cyclopentanethiol, thiophenol, and tetrafluorobenzenethiol. Up to 100 equivalents of ligand were added to the protein solutions, and electron absorption spectroscopy data were recorded. Imidazole

and tris(hydroxymethyl)phosphine stock solutions were prepared in 100 mM potassium phosphate buffer at pH 7, and stock solutions of the other four ligands were prepared in dimethylformamide.

### Carbon Monoxide Addition to RuH93GMb

Ru<sup>III</sup>H93GMb was reduced to Ru<sup>II</sup>H93GMb with excess solid Na<sub>2</sub>S<sub>2</sub>O<sub>4</sub>. Carbon monoxide was bubbled through the reduced protein solution for two minutes. After CO bubbling, a band at 550 nm in the UV-vis spectrum was observed, indicating that CO had bound to the Ru<sup>II</sup> center.

### 3.6 References

- 1) Prier, C. K.; Hyster, T. K.; Farwell, C. C.; Huang, A.; Arnold, F. H. Asymmetric Enzymatic Synthesis of Allylic Amines: A Sigmatropic Rearrangement Strategy. *Angew. Chem. Int. Ed.* **2016**, *55* (15), 4711-4715.
- 2) Farwell, C. C.; McIntosh, J. A.; Hyster, T. K.; Wang, Z. J.; Arnold, F. H. Enantioselective Imidation of Sulfides via Enzyme-Catalyzed Intermolecular Nitrogen-Atom Transfer. *J. Am. Chem. Soc.* **2014**, *136* (24), 8766-8771.
- 3) Coelho, P. S.; Wang, Z. J.; Ener, M. E.; Baril, S. A.; Kannan, A.; Arnold, F. H.; Brustad, E. M. A serine-substituted P450 catalyzes highly efficient carbene transfer to olefins in vivo (vol 9, pg 485, 2013). *Nat. Chem. Biol.* **2014**, *10* (2), 164-164.
- 4) McIntosh, J. A.; Coelho, P. S.; Farwell, C. C.; Wang, Z. J.; Lewis, J. C.; Brown, T. R.; Arnold, F. H. Enantioselective Intramolecular C-H Amination Catalyzed by Engineered Cytochrome P450 Enzymes In Vitro and In Vivo. *Angew. Chem. Int. Ed.* **2013**, *52* (35), 9309-9312.
- 5) Coelho, P. S.; Brustad, E. M.; Kannan, A.; Arnold, F. H. Olefin Cyclopropanation via Carbene Transfer Catalyzed by Engineered Cytochrome P450 Enzymes. *Science* **2013**, *339* (6117), 307-310.
- 6) Tinoco, A.; Steck, V.; Tyagi, V.; Fasan, R. Highly Diastereo- and Enantioselective Synthesis of Trifluoromethyl-Substituted Cyclopropanes via Myoglobin-Catalyzed Transfer of Trifluoromethylcarbene. *J. Am. Chem. Soc.* **2017**, *139* (15), 5293-5296.
- 7) Tyagi, V.; Fasan, R. Myoglobin-Catalyzed Olefination of Aldehydes. *Angew. Chem. Int. Ed.* **2016**, *55* (7), 2512-2516.
- 8) Tyagi, V.; Bonn, R. B.; Fasan, R. Intermolecular carbene S-H insertion catalysed by engineered myoglobin-based catalysts. *Chem. Sci.* **2015**, *6* (4), 2488-2494.

- 9) Sreenilayam, G.; Fasan, R. Myoglobin-catalyzed intermolecular carbene N-H insertion with arylamine substrates. *Chem. Comm.* **2015**, 51 (8), 1532-1534.
- 10) Bordeaux, M.; Singh, R.; Fasan, R. Intramolecular C(sp<sup>3</sup>)-H amination of arylsulfonyl azides with engineered and artificial myoglobin-based catalysts. *Bioorg. Med. Chem.* **2014**, 22 (20), 5697-5704.
- 11) Renata, H.; Lewis, R. D.; Sweredoski, M. J.; Moradian, A.; Hess, S.; Wang, Z. J.; Arnold, F. H. Identification of Mechanism-Based Inactivation in P450-Catalyzed Cyclopropanation Facilitates Engineering of Improved Enzymes. *J. Am. Chem. Soc.* **2016**, 138 (38), 12527-12533.
- 12) Wang, Z. J.; Renata, H.; Peck, N. E.; Farwell, C. C.; Coelho, P. S.; Arnold, F. H. Improved Cyclopropanation Activity of Histidine-Ligated Cytochrome P450 Enables the Enantioselective Formal Synthesis of Levomilnacipran. *Angew. Chem. Int. Ed.* **2014**, 53 (26), 6810-6813.
- 13) Wolf, M. W.; Vargas, D. A.; Lehnert, N. Engineering of RuMb: Toward a Green Catalyst for Carbene Insertion Reactions. *Inorg. Chem.* **2017**, 56 (10), 5623-5635.
- 14) Chan, K. H.; Guan, X. G.; Lo, V. K. Y.; Che, C. M. Elevated Catalytic Activity of Ruthenium(II)-Porphyrin-Catalyzed Carbene/Nitrene Transfer and Insertion Reactions with N-Heterocyclic Carbene Ligands. *Angew. Chem. Int. Ed.* **2014**, 53 (11), 2982-2987.
- 15) Depillis, G. D.; Decatur, S. M.; Barrick, D.; Boxer, S. G. Proximal Ligand Substitution in Sperm Whale Myoglobin - Exchange of Various Ligands in and out of the Cavity Mutant H93g. *Biophys. J.* **1994**, 66 (2), A400-A400.
- 16) Du, J.; Sono, M.; Dawson, J. H. The H93G myoglobin cavity mutant as a versatile scaffold for modeling heme iron coordination structures in protein active sites and their characterization with magnetic circular dichroism spectroscopy. *Coord. Chem. Rev.* **2011**, 255 (7-8), 700-716.
- 17) Sun, S. F.; Sono, M.; Dawson, J. H. Mono- and bis-phosphine-ligated H93G myoglobin: Spectral models for ferrous-phosphine and ferrous-CO cytochrome P450. *J. Inorg. Biochem.* **2013**, 127, 238-245.
- 18) Du, J.; Perera, R.; Dawson, J. H. Alkylamine-Ligated H93G Myoglobin Cavity Mutant: A Model System for Endogenous Lysine and Terminal Amine Ligation in Heme Proteins such as Nitrite Reductase and Cytochrome f. *Inorg. Chem.* **2011**, 50 (4), 1242-1249.
- 19) Du, J.; Sono, M.; Dawson, J. H. Ferric His93Gly myoglobin cavity mutant and its complexes with thioether and selenolate as heme protein models. *J. Porph. Phthal.* **2011**, 15 (1), 29-38.
- 20) Qin, J.; Perera, R.; Lovelace, L. L.; Dawson, J. H.; Lebioda, L. Structures of thiolate- and carboxylate-ligated ferric H93G myoglobin: Models for cytochrome P450 and for oxyanion-bound heme proteins. *Biochemistry* **2006**, 45 (10), 3170-3177.

- 21) Perera, R.; Dawson, J. H. Modeling heme protein active sites with the his93gly cavity mutant of sperm whale myoglobin: complexes with nitrogen-, oxygen- and sulfur-donor proximal ligands. *J. Porph. Phthal.* **2004**, *8* (1-3), 246-254.
- 22) Perera, R.; Sono, M.; Sigman, J. A.; Pfister, T. D.; Lu, Y.; Dawson, J. H. Neutral thiol as a proximal ligand to ferrous heme iron: Implications for heme proteins that lose cysteine thiolate ligation on reduction. *Proc. Natl. Acad. Sci.* **2003**, *100* (7), 3641-3646.
- 23) Dawson, J. H.; Pond, A. E.; Roach, M. P.; Thomas, M. R.; Boxer, S. G. Extending the use of H93G(Im) myoglobin for the preparation of mixed ligand ferrous, ferric and ferryl heme adducts and their characterization with MCD spectroscopy. *J. Inorg. Biochem.* **1999**, *74* (1-4), 110-110.
- 24) Roach, M. P.; Franzen, S.; Pang, P. S. H.; Boxer, S. G.; Woodruff, W. H.; Dawson, J. H. Thiolate adducts of cavity mutant myoglobin H93G as models for cytochrome P450. *Faseb. J.* **1997**, *11* (9), 820.
- 25) Bordeaux, M.; Tyagi, V.; Fasan, R. Highly Diastereoselective and Enantioselective Olefin Cyclopropanation Using Engineered Myoglobin-Based Catalysts. *Angew. Chem. Int. Ed.* **2015**, *54* (6), 1744-1748.
- 26) Teale, F. W. J. Cleavage of the Haem-Protein Link by Acid Methylethylketone. *Biochim. Biophys. Acta* **1959**, *35* (2), 543-543.
- 27) Paulson, D. R.; Addison, A. W.; Dolphin, D.; James, B. R. Preparation of Ruthenium(II) and Ruthenium(III) Myoglobin and the Reaction of Dioxygen, and Carbon-Monoxide, with Ruthenium(II) Myoglobin. *J. Biol. Chem.* **1979**, *254* (15), 7002-7006.
- 28) Springer, B. A.; Sligar, S. G. High-Level Expression of Sperm Whale Myoglobin in Escherichia-Coli. *Proc. Natl. Acad. Sci.* **1987**, *84* (24), 8961-8965.

## Chapter 4

### Spectroscopic Investigation of Diheme Cytochrome *c* Peroxidases

Hydrogen peroxide ( $\text{H}_2\text{O}_2$ ) is produced as an undesired by-product of the electron transport chain during aerobic respiration and can damage cells through decay into hydroxyl or superoxide radicals.<sup>1</sup> In many species of bacteria, excess  $\text{H}_2\text{O}_2$  is reduced to water by soluble cytochrome *c* peroxidases (bCcPs) in order to avoid buildup of toxic radical species.<sup>2</sup> Each canonical bCcP is a homodimer, where each protomer contains two covalently-bound, *c*-type heme cofactors in separate domains. One of the hemes exhibits a relatively high  $\text{Fe}^{\text{III/II}}$  redox potential, typically between 330 to 450 mV vs. NHE.<sup>3-4</sup> This high-potential (H-heme) is axially coordinated by His and Met residues, and facilitates electron transfer to the active site from small donor proteins and/or stores reducing equivalents.<sup>4-6</sup> The active site is a peroxidatic, low-potential heme (L-heme) where  $\text{H}_2\text{O}_2$  binds and is reduced to water.<sup>2</sup> The L-heme has a  $\text{Fe}^{\text{III/II}}$  redox potential that ranges in between -330 to -250 mV vs. NHE, like other heme peroxidases.<sup>3-4</sup> Most bCcP can be referred to as ‘activatable’: while the enzyme is isolated in the diferric form, it is catalytically inactive,<sup>7</sup> due to the ligation of two His residues at each apical position of the L-heme active site (see **Table 4.1**).<sup>6-13</sup> Activation is achieved by reducing the H-heme, producing a stable, activated state where the H-heme is ferrous and the L-heme remains ferric. Most bCcPs belong to this class, and the most well-studied example is the bCcP from *Pseudomonas aeruginosa* (*PaCcP*). Indeed, x-ray crystal structures of *PaCcP* either as-isolated or reduced to the activated, semi-reduced state show that the L-heme is six-coordinate (6C) in the diferric form of the enzyme, ligated by the two His

residues, and that upon reduction of the H-heme, local conformational changes occur in the enzyme, breaking one of the Fe-N<sub>His</sub> bonds of the L-heme, creating a five-coordinate (5C) site and allowing H<sub>2</sub>O<sub>2</sub> to bind to the iron center.<sup>7-8, 14</sup> Spectroscopic data from UV-vis and room temperature near-IR MCD indicate that the L-heme changes spin states from low-spin ferric to high-spin ferric upon semi-reduction at the H-heme.<sup>15-16</sup>

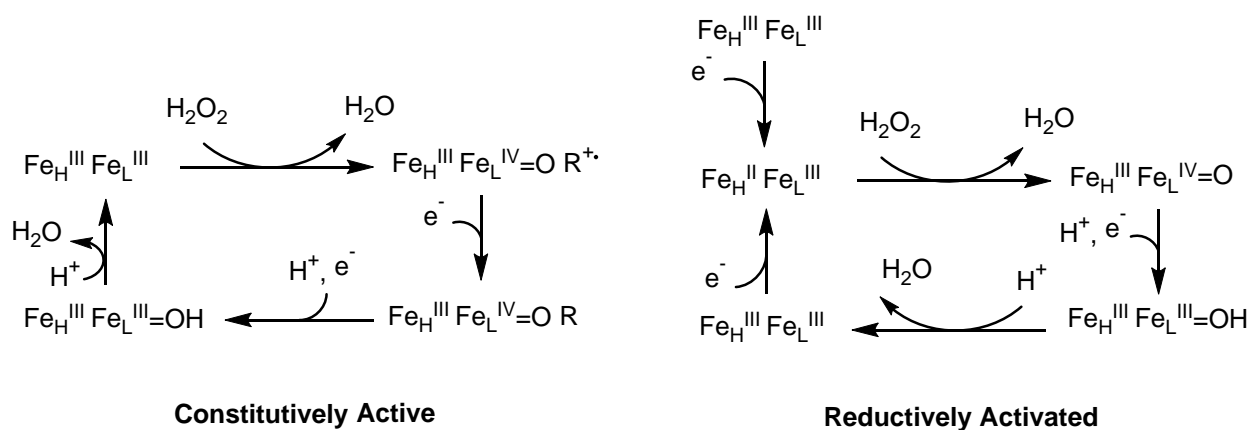
In contrast, the other class of bCcPs is the ‘constitutively active’ class, which contains peroxidases that are catalytically competent in both the diferric form of the enzyme and the semi-reduced oxidation state (**Table 4.1**).<sup>3, 17</sup> There are fewer examples of enzymes in this class compared to the ‘activatable’ class, but several have been studied previously, including the bCcP from *Nitrosomonas europaea* (*NeCcP*). *NeCcP* has been characterized by UV-vis and EPR spectroscopy, as well as protein crystallography.<sup>3, 18</sup> The crystal structure of the enzyme exhibits a 5C L-heme in the diferric form of the enzyme, ready to bind H<sub>2</sub>O<sub>2</sub>.<sup>18</sup> *NeCcP* shares sequence similarity (~60% primary sequence identity) and high structural homology with the bCcP from *Shewanella oneidensis* (*SoCcP*), which is a member of the ‘activatable’ class of bCcPs, and while they catalyze the same reaction, starting their reactivity at different redox states suggests that different mechanisms would be at work in the *Ne* and *So* enzymes (see **Scheme 4.1**).<sup>13, 19-20</sup> The catalytic mechanism of *NeCcP* is proposed to be similar to monoheme peroxidases with H<sub>2</sub>O<sub>2</sub> binding to the L-heme and an Fe<sup>IV</sup>=O R<sup>+</sup> “Compound I”-like intermediate with a cation radical located on either the porphyrin ring or an adjacent tryptophan residue. In the second step, reduction to a “Compound II”-like species occurs through a small electron-donor protein such as Cytochrome *c*<sub>551</sub> prior to the formation of a ferric-hydroxo species and release of a second equivalent of water. In contrast, it is proposed that “activatable” bCcPs, including *SoCcP*, must go

through the reduction of the H-heme first before binding H<sub>2</sub>O<sub>2</sub> at the L-heme and forming an Fe<sup>IV</sup>=O Compound II-like intermediate without having to go through a Compound I species.<sup>19</sup>

**Table 4.1 Organisms that belong to distinct CcP classes**

| Bacterial CcPs that require reduction         | Bacterial CcPs that are constitutively active |
|---|---|
| <i>Paracoccus denitrificans</i> <sup>6</sup>  | <i>Nitrosomonas europaea</i> <sup>3</sup>     |
| <i>Pseudomonas aeruginosa</i> <sup>7</sup>    | <i>Methyloccoccus casulatus</i> <sup>17</sup> |
| <i>Paracoccus pantrophus</i> <sup>8</sup>     |   |
| <i>Pseudomonas nautica</i> <sup>9</sup>       |   |
| <i>Rhodobacter capsulatus</i> <sup>10</sup>   |   |
| <i>Pseudomonas stutzeri</i> <sup>11</sup>     |   |
| <i>Geobacter sulfurreducens</i> <sup>12</sup> |   |
| <i>Shewanella Oneidensis</i> <sup>13</sup>    |   |

**Scheme 4.1.** Proposed reaction mechanisms for Constitutively Active and Activatable bCcPs (Modified from refs [19] and [20])



Evaluating the coordination chemistry and spin-state(s) of the peroxidative active site in bCcPs is an essential missing piece of our understanding of these enzymes. In this chapter, we use EPR, resonance Raman and MCD spectroscopy to evaluate whether or not canonical bCcPs, when active, are indeed 5C at the active site, using the enzymes from *N. europaea* (constitutively active) and *S. oneidensis* (activatable) as examples. Single point mutation variants of *NeCcP* and *SoCcP* (H59G and H80G, respectively) were also prepared in order to prevent the native distal His residue from coordinating the L heme. The spectra of the native protein and the variants that lack the distal

His could then be compared to help assign the oxidation and spin states of the catalytically-relevant L-heme. Spectroscopic data were collected on both the diferric and semi-reduced forms of each of these enzymes, and analyzed in detail. This work was done in collaboration with Dr. Sean Elliott and Kim Rizzolo at Boston University. In the Elliott laboratory proteins were expressed purified before the spectroscopic work conducted in our laboratory.

#### 4.1 MCD Benchmark Studies

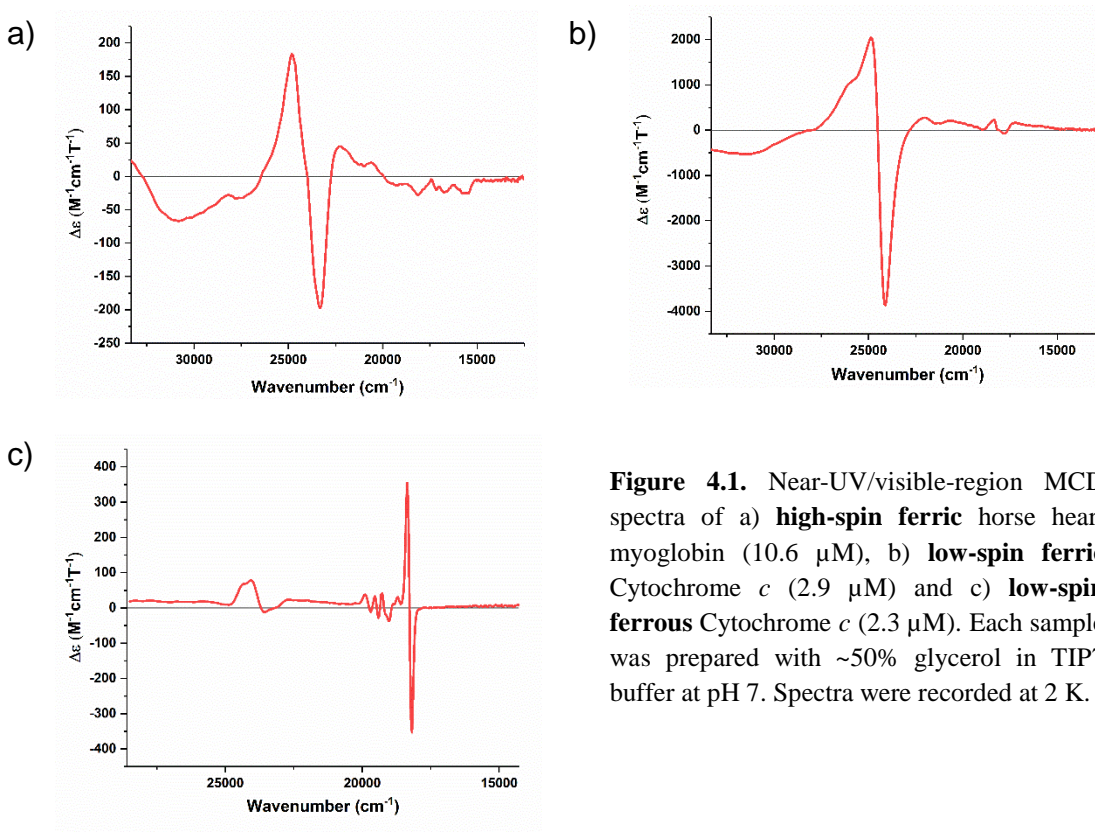


**Figure 4.1.** Near-UV/visible-region MCD spectra of a) **high-spin ferric** horse heart myoglobin (10.6  $\mu\text{M}$ ), b) **low-spin ferric** Cytochrome *c* (2.9  $\mu\text{M}$ ) and c) **low-spin ferrous** Cytochrome *c* (2.3  $\mu\text{M}$ ). Each sample was prepared with  $\sim 50\%$  glycerol in TIP7 buffer at pH 7. Spectra were recorded at 2 K.

MCD spectra of high-spin ferric myoglobin (metMb), low-spin ferric Cytochrome (Cyt.) *b*<sub>5</sub>, and both low-spin ferric and ferrous Cyt. *c* were taken in order to compare these benchmark spectra to the spectra of *NeCcP* and *SoCcP*. The heme in metMb is coordinated by the proximal His and a weakly-bound water molecule at pH 7. MetMb exhibits a positive band in the Soret region at 24830  $\text{cm}^{-1}$  and a negative feature at 23300  $\text{cm}^{-1}$  (**Figure 4.1a**). Less intense bands closer



to the Q-band region of the heme are also present at 22280 and 20640  $\text{cm}^{-1}$ , and in the 18770 to 15660  $\text{cm}^{-1}$  region. In comparison, the Soret band MCD features of the high-spin ferric heme in metMb are much less intense (by an order of magnitude) compared to the corresponding features of the low-spin ferric heme in Cyt. *c* (**Figure 4.1b**), as expected.<sup>21-25</sup> In the Soret region, bands are present at 24870  $\text{cm}^{-1}$  and 24100  $\text{cm}^{-1}$ , and less intense Q-band features are observed at 22000, 20710, 18360, and 17810  $\text{cm}^{-1}$ . The spectra for both Cyt. *b*<sub>5</sub> and Cyt. *c* are very typical for low-spin ferric hemes.<sup>24</sup> In contrast to this, low-spin ferrous Cyt. *c* is diamagnetic and exhibits only a very weak feature in the Soret region at 24070  $\text{cm}^{-1}$  (**Figure 4.1c**). A more intense MCD A-term signal that does not vary in intensity with changes in temperature is present at 18270  $\text{cm}^{-1}$ , which is assigned to the Q-band. To higher energy of the Q-band, smaller diamagnetic signals are observed at 19920, 19570, 19310, and 18730  $\text{cm}^{-1}$ , which are vibronic in nature and assigned to the Q<sub>v</sub> band.<sup>26</sup>

## 4.2 EPR Spectra of *NeCcP*

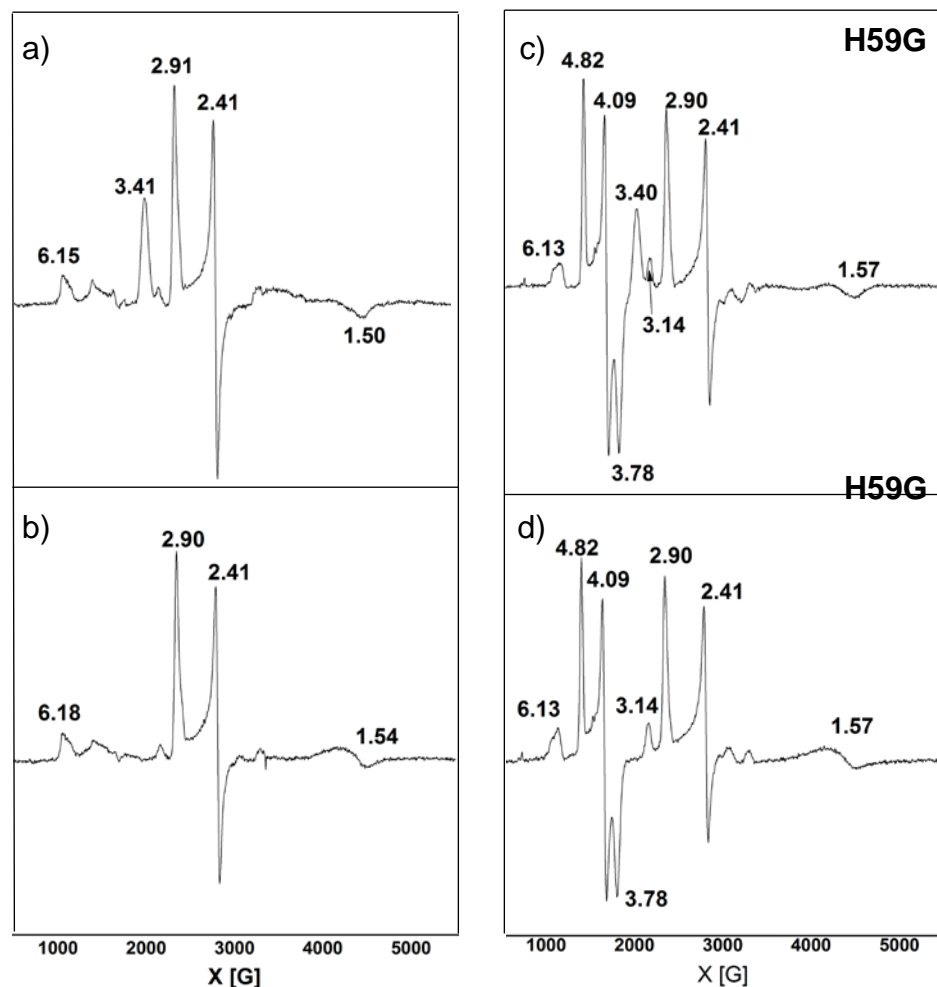


**Figure 4.2.** EPR spectra of a) 420  $\mu\text{M}$  diferric *NeCcP*, b) 490  $\mu\text{M}$  semi-reduced *NeCcP*, c) 419  $\mu\text{M}$  diferric *NeH59G CcP*, and d) 460  $\mu\text{M}$  semi-reduced *NeH59G CcP*. Experiments were conducted at 9.27 GHz, a power of 20 mW, and a temperature of 12 K.

EPR spectra were taken at 12 K for both the wild-type *NeCcP* and the H59G mutant of the enzyme (*NeH59G CcP*), where the distal His of the L-heme has been removed. Diferric *NeCcP* exhibits an anisotropic low-spin signal at  $g = 3.41$  that completely disappears upon reduction (**Figures 4.2a and b**). This signal must result from the H-heme, which is reduced to the ferrous state in the presence of ascorbate.<sup>13</sup> The L-heme exhibits dominant low-spin signals at  $g = 2.91$ , 2.41, and 1.50 at 12 K (**Figure 4.2b**). A very small amount of a putative high-spin ferric species

is also present that shows a signal at  $g = 6.15$ , which we tentatively assign to a small fraction of the L-heme that is in the high-spin state ( $< 5\%$ ). The EPR spectra of the mutant, *NeH59G CcP*, exhibit a similar signal for the H-heme at  $g = 3.40$ , and for the low-spin ferric L-heme at 2.90, 2.41, and 1.57. The putative high-spin component is also present with a signal at  $g = 6.13$ , again in a very small concentration. In addition to this, the spectra for *NeH59G CcP* exhibit signals at  $g = 4.82, 4.09, \text{ and } 3.78$  which likely originate from an intermediate-spin ferric heme with  $S = 3/2$ . It was our anticipation that the ferric L-heme in the mutant could potentially exist in the high-spin state, but the data show clearly that the L-heme is either able to attract another amino acid side chain as a ligand, or potentially a water molecule, or maybe a mixture of these two possibilities. The other form of the L-heme must be coordinated by a weak ligand, creating an intermediate strength ligand field at the heme that allows it to exist in the unusual  $S = 3/2$  state, at least at 12K. As shown below, this is a key difference between *NeCcP* and *SoCcP*. Upon reduction, the H-heme is reduced into the ferrous state, as evident from the disappearance of the  $g = 3.40$  signal, whereas there is little change for the L-heme – both the low-spin and the intermediate spin signals are still observed in roughly the same ratio.

### 4.3 Resonance Raman Spectra of *NeCcP*

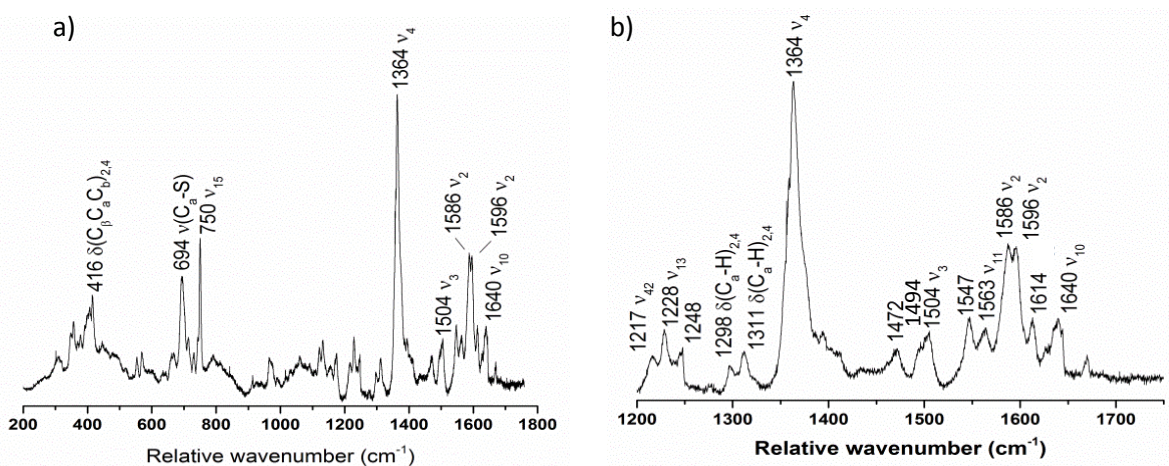


**Figure 4.3.** Resonance Raman spectrum of **diferric** *NeCcP* from a) 200 to 1750  $\text{cm}^{-1}$ , and b) enlarged view of the 1200 to 1750  $\text{cm}^{-1}$  region. The sample was 105  $\mu\text{M}$  with 50% glycerol in pH 7 TIP7 buffer. The sample was excited at 413.1 nm using a Krypton ion gas laser at 77 K.

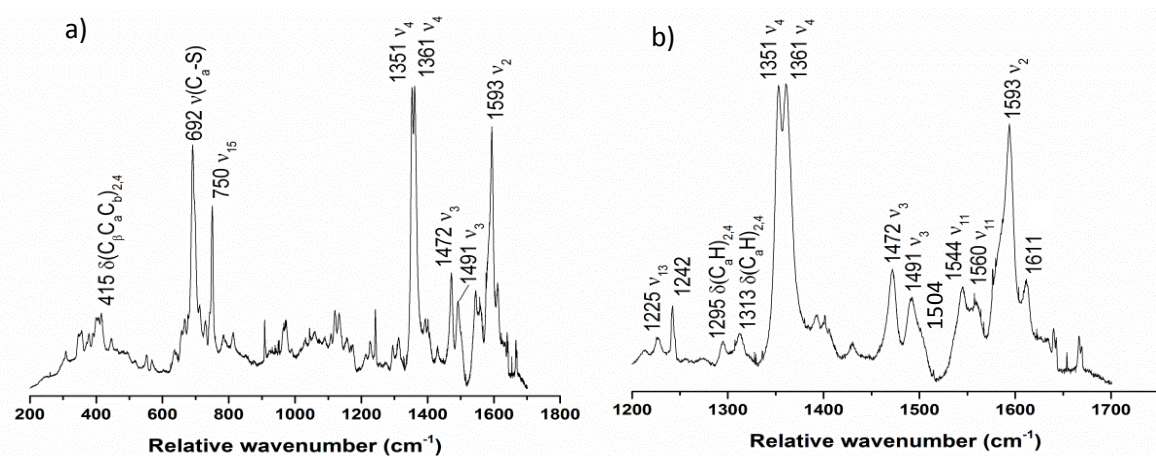


**Figure 4.4.** Resonance Raman spectrum of **semi-reduced** *NeCcP* from a) 200 to 1750  $\text{cm}^{-1}$ , and b) enlarged view of the 1200 to 1750  $\text{cm}^{-1}$  region. The sample was 160  $\mu\text{M}$  with 50% glycerol in pH 7 TIP7 buffer. The sample was excited at 413.1 nm using a Krypton ion gas laser at 77 K.

In resonance Raman (rRaman) spectroscopy, excitation of allowed electronic transitions leads to enhancement of vibrational modes that are coupled to that excitation, either via excited state displacements (A-term enhancement) or vibronic coupling (B- and C-term enhancement).<sup>27</sup> Heme proteins are typically excited with laser wavelengths that correspond to the intense Soret band of the heme or the less intense Q band features at lower energy.<sup>28-29</sup> Excitation of the Soret

band mostly enhances totally symmetric (polarized) vibrations according to the A-term mechanism, whereas excitation in the Q band region enhances non-totally symmetric (depolarized) and some anomalously polarized modes (via the B- and C-term mechanism).<sup>30</sup> In this work, the protein samples were excited at 413.1 nm (in the Soret region), leading to the observation of mostly polarized bands in the resonance Raman spectra, although some depolarized bands can also be observed. In previous work, the rRaman spectra of many simple heme proteins, including Cyt. *c*<sup>31</sup> and myoglobin,<sup>29, 32</sup> have been analyzed in detail and the different vibrational bands have been assigned and labeled using the  $\nu_n$  notation, which was first introduced by Kitagawa and coworkers.<sup>33</sup> Importantly, work by Kitagawa, Spiro and others has shown that certain porphyrin core vibrations are sensitive to the oxidation and spin state of the heme,<sup>34-35</sup> and can therefore be used to characterize intermediates in heme proteins.<sup>36</sup>

**Figure 4.3** shows the rRaman spectrum of diferric *NeCcP*. The single, intense “oxidation state marker band”  $\nu_4$  is observed at  $1364\text{ cm}^{-1}$ , and confirms that the enzyme is indeed in the diferric state. The “spin state marker band”  $\nu_3$  (which is actually sensitive to both the oxidation and spin state of the heme) is present at  $1504\text{ cm}^{-1}$ , and indicates that at least one heme is in the ferric low-spin state. Another spin state sensitive band,  $\nu_2$ , is observed at  $1586\text{ cm}^{-1}$ , which further supports the idea that the hemes are low-spin.<sup>32</sup> The presence of a high-spin ferric heme should manifest itself by the appearance of a  $\nu_3$  feature at  $\sim 1480\text{ cm}^{-1}$ , which is not observed. Bands at  $1547$  and  $1614\text{ cm}^{-1}$  ( $\nu_{11}$  and  $\nu_{10}$ , in this case) suggest that there may be some high-spin ferric heme present in the sample (in agreement with the EPR results). However, it should be noted that although these bands are present in high-spin metMb,<sup>29</sup> they also overlap with features that would be observed for a ferrous heme.<sup>34, 37</sup> A closer inspection of **Figure 4.3b** shows a lower energy shoulder of  $\nu_4$  as well as weak signals at  $1472$  and  $\sim 1494\text{ cm}^{-1}$  (the latter being a small shoulder

on the 1504  $\text{cm}^{-1}$  peak), which indicates the presence of small amounts of high-spin (1472  $\text{cm}^{-1}$ ) and low-spin (1494  $\text{cm}^{-1}$ ) ferrous heme. This ferrous heme would originate from the photoreduction of the H-heme in the presence of the laser light (which is therefore an artifact of the experiment). Note that low-spin ferric Mb also shows a weak signal around 1472  $\text{cm}^{-1}$  in the rR spectrum, indicating that the appearance of a weak signal at this energy in *NeCcP* by itself is not conclusive with respect to the presence of ferrous heme.<sup>38</sup> Based on all of these considerations, we therefore conclude that in diferric *NeCcP* both hemes are mostly in the low-spin ferric state, and that small amounts of ferrous H-heme (due to photoreduction) and potentially a small amount of high-spin ferric L-heme could be present. The data do not, however, support the paradigm that in the constitutively active *NeCcP*, the L-heme is dominantly in the high-spin ferric state.

Upon one-electron reduction (to the semi-reduced state), the  $\nu_4$  oxidation state marker band at 1351  $\text{cm}^{-1}$  appears, indicating that the H-heme has now been reduced (**Figures 4.3 and 4.4**). In addition, a decrease of the low-spin ferric marker band  $\nu_3$  at 1504  $\text{cm}^{-1}$  is observed (which has become a shoulder on the intense 1492  $\text{cm}^{-1}$  peak), concomitant with an increase in intensity for the  $\nu_3$  bands at 1471  $\text{cm}^{-1}$  and 1492  $\text{cm}^{-1}$ . These signals are attributed to high-spin and low-spin ferrous heme, respectively, again indicating H-heme reduction and suggesting that this heme can exist in a mixture of spin states (see below).<sup>34</sup> No  $\nu_3$  band around 1480  $\text{cm}^{-1}$  is observed, again indicating that the majority of the ferric L-heme is in fact in the low-spin state. The  $\nu_2$  marker band for a low-spin heme at 1586  $\text{cm}^{-1}$  decreases in intensity upon reduction, in agreement with the idea that some of the reduced (ferrous) heme is actually in the high-spin state. The band at 1560-1563  $\text{cm}^{-1}$  is present in both the diferric and the semi-reduced sample, though this band is not as easily assigned. The  $\nu_2$  band for a high-spin heme and the  $\nu_{11}$  band for a ferric heme overlap at 1560-1565  $\text{cm}^{-1}$  if both species are present in a single sample.<sup>34</sup> Bands at 1547 and 1614  $\text{cm}^{-1}$  are still

present in the spectrum, and these bands could result from either a high-spin ferric or a ferrous heme species.<sup>31, 34, 37</sup> The low-spin ferric  $\nu_{10}$  band at  $1640\text{ cm}^{-1}$  has almost entirely disappeared, which suggests that some high-spin ferric heme could be present (in agreement with the EPR data). Based on these results, it appears that in the semi-reduced form of *Ne*CcP, the H-heme has been reduced and appears to be in a mixed high-spin/low-spin state, whereas the L-heme is mostly low-spin ferric with potentially a small fraction of high-spin ferric heme present, like in the diferric enzyme. One potential issue with the EPR and rRaman experiments is that they were conducted at cryogenic temperatures, which leaves us with the possibility (playing devil's advocate) that the spin state of the L-heme could be temperature dependent. To help address this issue, resonance Raman data were further collected at room temperature (see below).

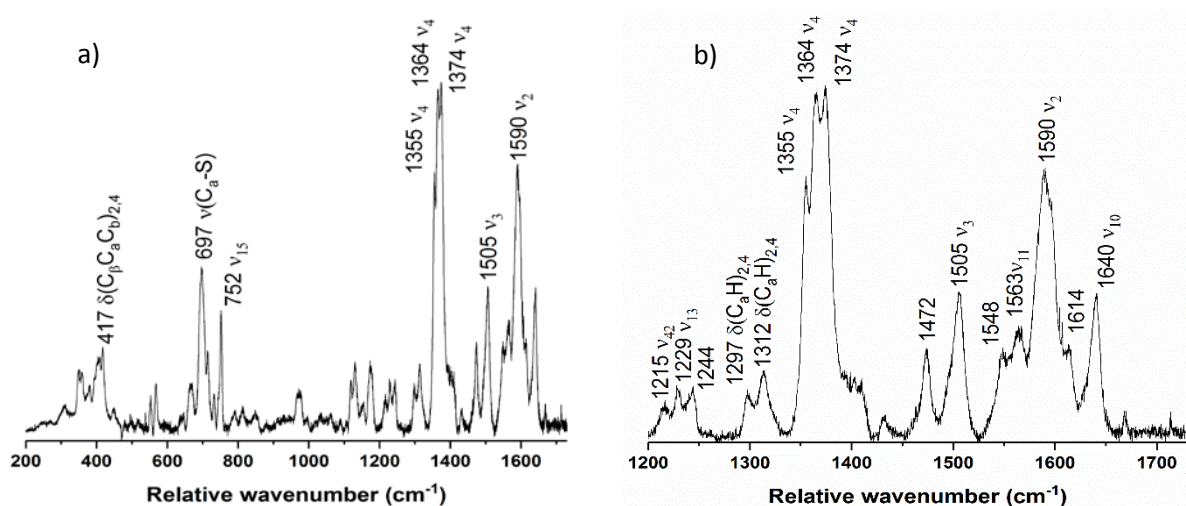


**Figure 4.5.** Resonance Raman spectrum diferric *Ne*H59G CcP from a) 200 to  $1750\text{ cm}^{-1}$ , and b) enlarged view of the  $1200$  to  $1750\text{ cm}^{-1}$  region. The sample was  $419\text{ }\mu\text{M}$  with 30% glycerol in pH 7 TIP7 buffer. The sample was excited at  $413.1\text{ nm}$  using a Krypton ion gas laser at  $77\text{ K}$ .



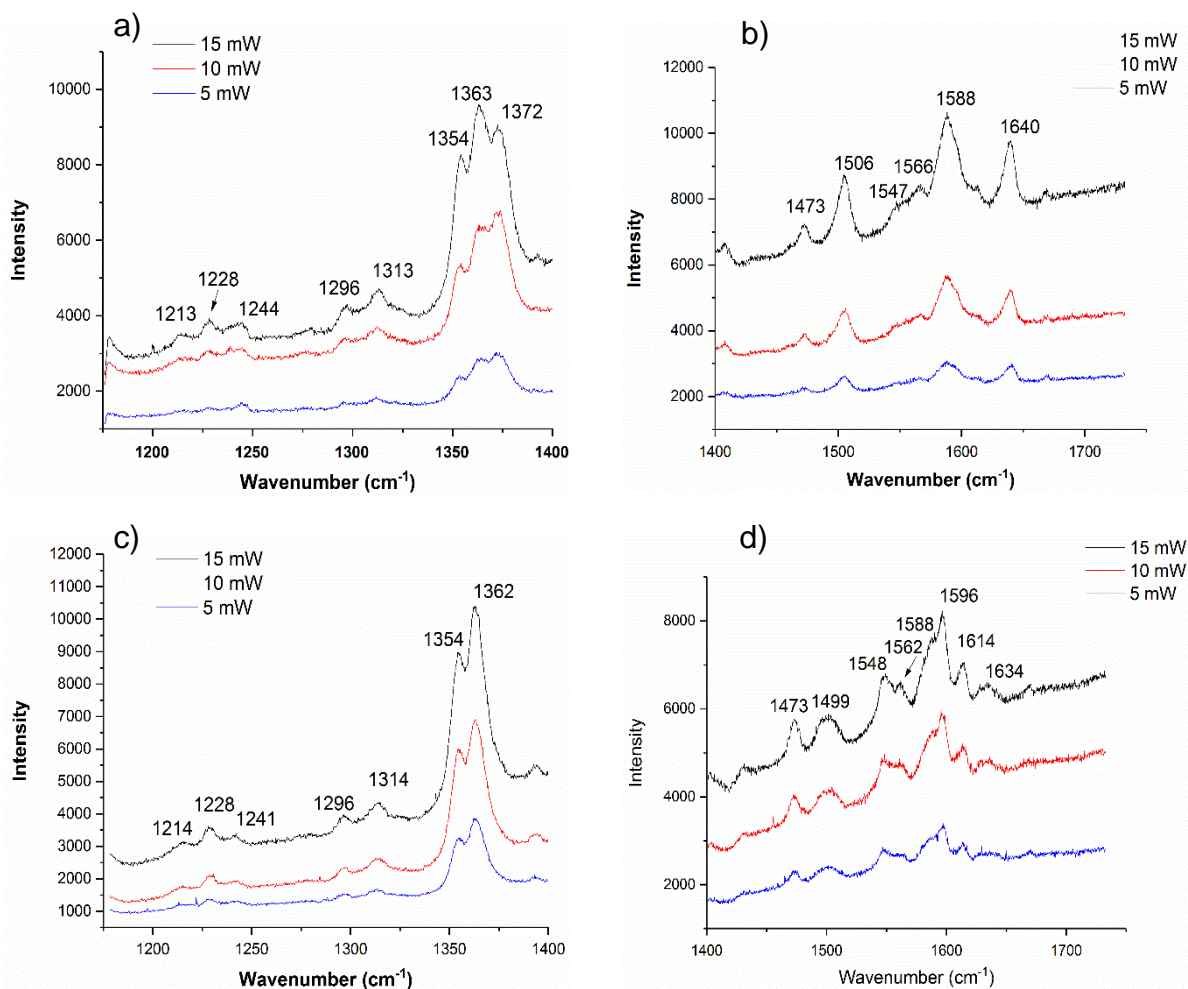


**Figure 4.6.** Power dependence resonance Raman spectra of diferric *NeH59G CcP* from a) 1150 to 1400  $\text{cm}^{-1}$ , and b) 1400 to 1750  $\text{cm}^{-1}$  and the power dependence spectra of semireduced *NeH59G CcP* from c) 1150 to 1400  $\text{cm}^{-1}$ , and d) 1400 to 1750  $\text{cm}^{-1}$ . The diferric sample was 419  $\mu\text{M}$  and the semireduced sample was 460  $\mu\text{M}$  both with 30% glycerol in pH 7 TIP7 buffer. The sample was excited at 413.1 nm using a Krypton ion gas laser at 77 K.

**Figure 4.5** shows the rR spectrum of the diferric variant *NeH59G CcP*. There are three  $\nu_4$  bands at 1355, 1364, and 1374  $\text{cm}^{-1}$ , though the band at 1355  $\text{cm}^{-1}$  is power dependent, and is therefore due to photoreduction of the H-heme during data collection (**Figure 4.6**). Compared to wild-type enzyme, the spectrum of the H59G mutant shows enhanced photoreduction of the H-heme. From 1400  $\text{cm}^{-1}$  to 1700  $\text{cm}^{-1}$ , the *NeH59G CcP* diferric spectrum is quite similar to the spectrum of wild-type *NeCcP*. The ferric low-spin marker band at 1505  $\text{cm}^{-1}$  is more intense in the



mutant, and the complete absence of a signal around  $1480\text{ cm}^{-1}$  indicates the absence of any high-spin ferric heme. Also, the  $\nu_3$  band at  $1472\text{ cm}^{-1}$  is now very pronounced, due to the increased photoreduction of the H-heme in the mutant, whereas no signal around  $1490\text{ cm}^{-1}$  is observed. This indicates that the photoreduced H-heme is predominantly in the high-spin state, and presumably five-coordinate. The  $\nu_2$  spin state marker band for a low-spin heme is present at  $1590\text{ cm}^{-1}$ , though this band is broad, and may overlap with another band at slightly higher energy. Potential high-spin ferric bands are present at  $1548$  and  $1614\text{ cm}^{-1}$ , potentially indicating the presence of a small amount of high-spin ferric heme (in agreement with the EPR results). Because these features are not power-dependent like the  $1355\text{ cm}^{-1}$  band, they should not be associated with the photoreduced, ferrous heme. Compared to the EPR data, the rRaman spectra do not indicate the presence of an unusual heme, like the intermediate spin heme observed by EPR. This indicates that the intermediate spin heme might only exist at lq. He temperatures, and that the fraction of intermediate spin L-heme becomes low-spin at higher temperatures. In addition, as mentioned above in the EPR section, it is surprising that the L-heme in the mutant does not adopt a predominant high-spin state.

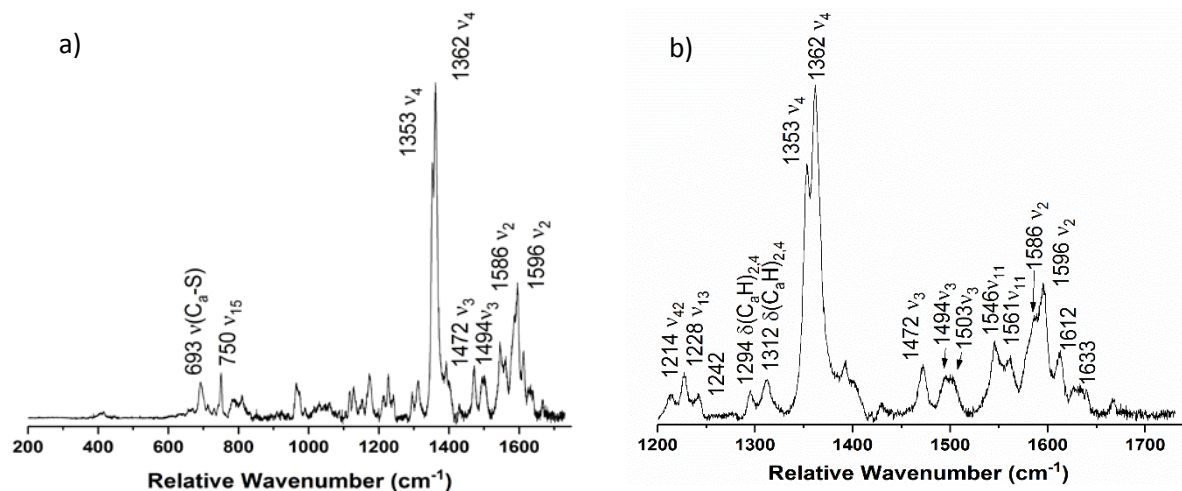


**Figure 4.7.** Resonance Raman spectrum of **semi-reduced NeH59G CcP** from a) 200 to  $1750\text{ cm}^{-1}$ , and b) enlarged view of the  $1200$  to  $1750\text{ cm}^{-1}$  region. The sample was  $460\text{ }\mu\text{M}$  with 30% glycerol in pH 7 TIP7 buffer. The sample was excited at  $413.1\text{ nm}$  using a Krypton ion gas laser at  $77\text{ K}$ .

Reduction of the H-heme in the *NeH59G* CcP mutant results in the disappearance of the  $\nu_4$  band at  $1374\text{ cm}^{-1}$  (compare **Figures 4.5b and 4.7b**), directly indicating that this feature is associated with the H-heme. Interestingly, in wild-type enzyme the H-heme shows the  $\nu_4$  band at  $1364\text{ cm}^{-1}$ , which emphasizes that the two hemes in *NeCcP* influence each other (since the H59G mutation affects the axial ligation of the L-heme). The rRaman spectrum of semireduced *NeH59G* CcP resembles that of semi-reduced wild-type enzyme (compare **Figures 4.4 and 4.7**). Two  $\nu_4$  bands are present at  $1353$  (reduced H-heme) and  $1362\text{ cm}^{-1}$  (ferric L-heme). Three different  $\nu_3$  bands are present at  $1472$ ,  $1494$ , and  $1503\text{ cm}^{-1}$  which can be attributed to high-spin and low-spin ferrous H-heme, and the low-spin ferric L-heme, respectively. Again, no signal is observed at  $\sim 1480\text{ cm}^{-1}$  that would be indicative of high-spin ferric heme. A  $\nu_2$  spin-state marker band is present at  $1586$ , which indicates the presence of low-spin heme. Bands at  $1548$  and  $1614\text{ cm}^{-1}$  remain, though once again these bands are difficult to immediately assign. Finally, it appears that the low-spin ferric  $\nu_{11}$  band at  $1640\text{ cm}^{-1}$  in the diferric sample has decreased significantly in intensity upon H-heme reduction, indicating less low-spin ferric heme in the sample.

Resonance Raman data were also collected at room temperature for *NeCcP* and *NeH59G* CcP while rotating the samples with an NMR spinner (**Figure 4.8**). The room temperature diferric spectra exhibit only one, broad  $\nu_4$  band at  $1368\text{ cm}^{-1}$  for the wild-type enzyme and at  $1360\text{ cm}^{-1}$  for *NeH59G* CcP. This indicates that photoreduction of the H-heme is suppressed in solution at room temperature, as no  $\nu_4$  band around  $1355\text{ cm}^{-1}$  is present in the spectra, rendering this an artifact in the low-temperature experiments in a frozen matrix. In addition, there is no band present at  $1472\text{ cm}^{-1}$  in the room temperature *NeCcP* and *NeH59G* CcP spectra (in contrast to the 77K spectra), in agreement with this. This result further indicates that the  $1472\text{ cm}^{-1}$  band in the low-temperature data also belongs to the photoreduced, ferrous H-heme. Low-spin ferric marker bands

are present in the room temperature spectra for both enzymes at 1500-1502  $\text{cm}^{-1}$  and 1636-1637  $\text{cm}^{-1}$ . The broad low-spin state marker band  $\nu_2$  is present at 1583-1584  $\text{cm}^{-1}$  for both samples and bands at 1543-1545  $\text{cm}^{-1}$  and 1608  $\text{cm}^{-1}$  also appear. These bands could have resulted from the presence of a small amount of ferrous heme in the sample for the low-temperature spectra, but since only one oxidation state marker band appears in each room-temperature spectrum, these bands must then originate from the presence of a different species in solution, likely a *small amount* of high-spin ferric heme, as indicated by the EPR data and the absence of any corresponding  $\nu_3$  band around 1480  $\text{cm}^{-1}$  (which is a direct marker for high-spin ferric heme).

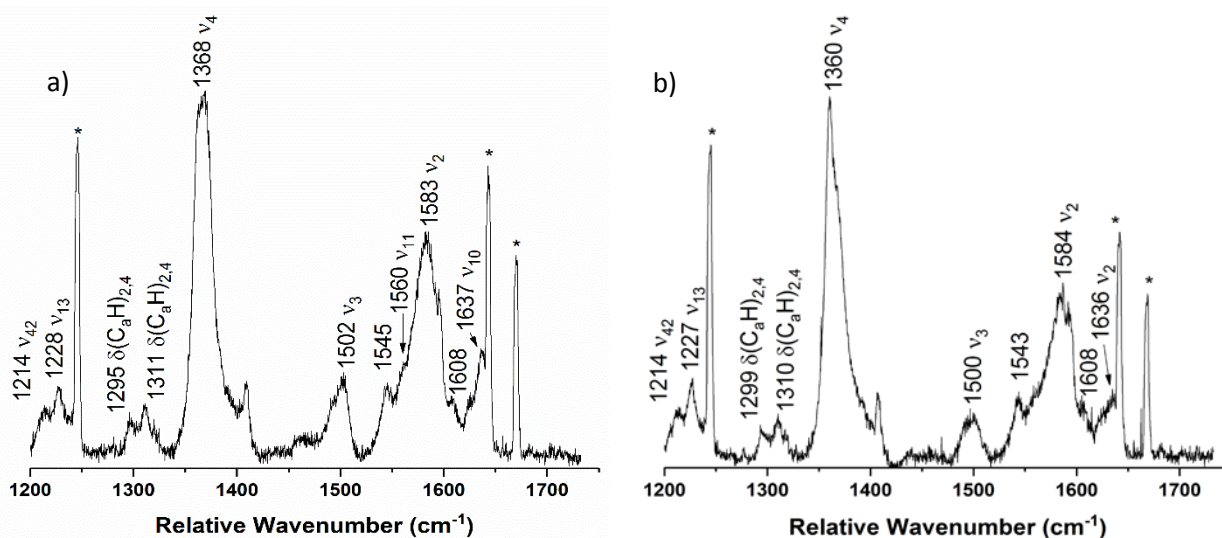


**Figure 4.8.** Room temperature resonance Raman spectrum of a) **diferric NeCcP** and b) **diferric NeH59G CcP**. The samples were  $\sim 420 \mu\text{M}$  with 30% glycerol in pH 7 TIP7 buffer. The samples were rotated and excited at 413.1 nm using a Krypton ion gas laser. Plasma lines are indicated with an asterisk.

## 4.4 Magnetic Circular Dichroism of *NeCcP*

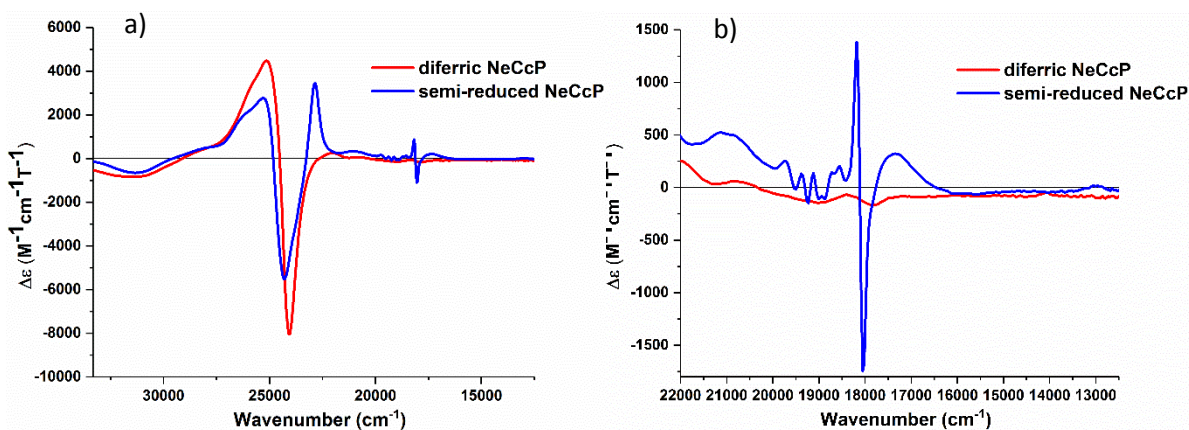


**Figure 4.9.** a) Near-UV/visible-region MCD spectra of the diferric and semi-reduced states of *NeCcP*, and b) a close-up of the Q-band region of the spectra. Samples were 20  $\mu\text{M}$  with  $\sim 50\%$  glycerol in a TIP7 buffer at pH 7. Spectra were recorded at 2 K.

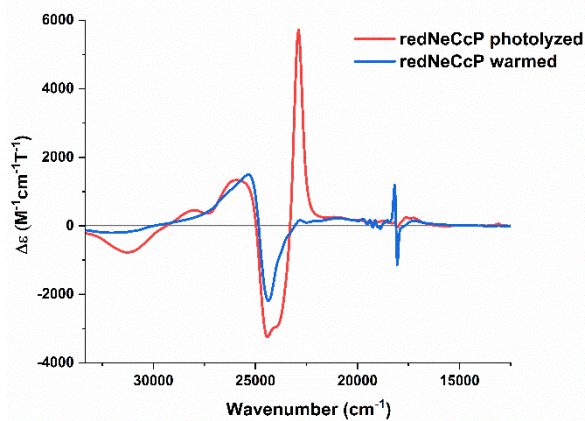


**Figure 4.10.** Near-UV/visible-region MCD spectra of a semi-reduced *NeCcP* sample that was photolyzed with a mercury lamp, and after warming the sample to 70 K in the dark and then cooling the sample back to 2 K. The sample was 3.1  $\mu\text{M}$  with  $\sim 50\%$  glycerol in a TIP7 buffer at pH 7. Spectra were recorded at 2 K.

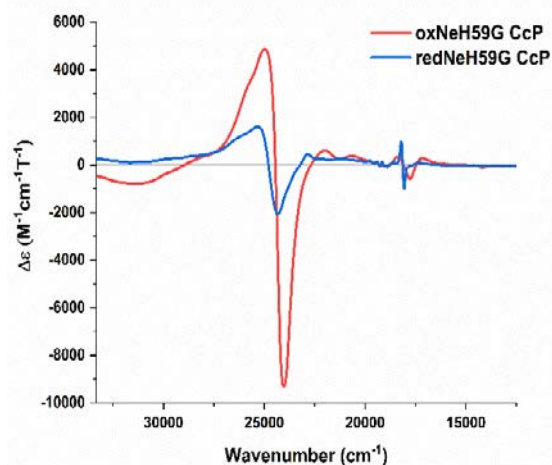


**Figure 4.11.** Near-UV/visible-region MCD spectra of the diferric and semi-reduced states of *NeH59G CcP*. Samples were 2-2.6  $\mu\text{M}$  with  $\sim 50\%$  glycerol in a TIP7 buffer at pH 7. Spectra were recorded at 2 K at pH 7. Spectra were recorded at 2 K.

Near UV-visible MCD spectra were recorded at lq. He temperatures for the *NeCcP* enzyme in both the diferric and semi-reduced states (see **Figure 4.9**). The diferric enzyme exhibits a typical MCD spectrum for low-spin ferric hemes with a positive signal at  $25130\text{ cm}^{-1}$  and a negative signal

at 24050  $\text{cm}^{-1}$  in the Soret band region as evident from **Figure 4.9a**. In addition, there are low-spin ferric signals in the Q-band region at 20800, 19000, 18490, and 17860  $\text{cm}^{-1}$  (see **Figure 4.9b**). Upon reduction, low-spin ferric signals in the Soret region, now at 25280  $\text{cm}^{-1}$  and 24300  $\text{cm}^{-1}$ , persist, which is in agreement with the idea that only one of the hemes is reduced. The observation that the ferric L-heme is low-spin is in agreement with the EPR and rRaman data. The small, sharp signals at 19720, 19380, 19120, 18720, 18550 and 18160  $\text{cm}^{-1}$  that appear upon reduction of the H-heme (**Figure 4.9b**) are markers for a diamagnetic (here low-spin ferrous) heme, and they are similar to the MCD signals observed for low-spin ferrous Cyt. *c* as shown in **Figure 4.1c**. The large positive signal at 22860  $\text{cm}^{-1}$ , on the other hand, originates from a fraction of the reduced H-heme that is in the high-spin state. In previous studies on *PaCcP*, it was shown by Foote and Co-workers that this signal results from the partial photolysis of the Fe-S<sub>Met</sub> bond of the reduced H-heme upon irradiation of the sample in the CD spectrophotometer.<sup>15</sup> We further investigated this issue in our own MCD experiments as shown in **Figure 4.10**. Here, the signal at 22860  $\text{cm}^{-1}$  increases upon photolysis of the sample with a mercury lamp at 2K, while at the same time the low-spin ferrous signal at 18160  $\text{cm}^{-1}$  decreases. This spectral change is reversed upon warming the sample to 70 K in the dark and then cooling the sample back to 2 K, with the low-spin ferrous signal reappearing. Compared to a ferrous Cyt. *c* standard, the low-spin ferrous signal in **Figure 4.9** represents ~62% of the H-heme, and thus the high-spin signal must correspond to the remaining ~38% of the H-heme in this sample. The observed mixture of high-spin and low-spin ferrous H-heme in the semireduced sample is directly supported by the rRaman data (see above). There is also a signal at 17,280  $\text{cm}^{-1}$  which originates from the high-spin ferrous H-heme. The MCD spectra of diferric and semi-reduced *NeH59G CcP* are quite similar to wild-type *NeCcP* (**Figure 4.11**). The diferric *NeH59G CcP* exhibits signals at 24970 and 24030  $\text{cm}^{-1}$  in the Soret band region and

at 22030, 20650, 18420, and 17140  $\text{cm}^{-1}$  in the Q-band region. The semi-reduced spectrum of *NeH59G* CcP exhibits signals at 25300 and 24320  $\text{cm}^{-1}$  in the Soret band region and sharp diamagnetic signals at 19740, 19410, 19150, 18760, 18570 and 18130  $\text{cm}^{-1}$  in the Q-band region.

#### 4.5 EPR Spectra of *SoCcP*

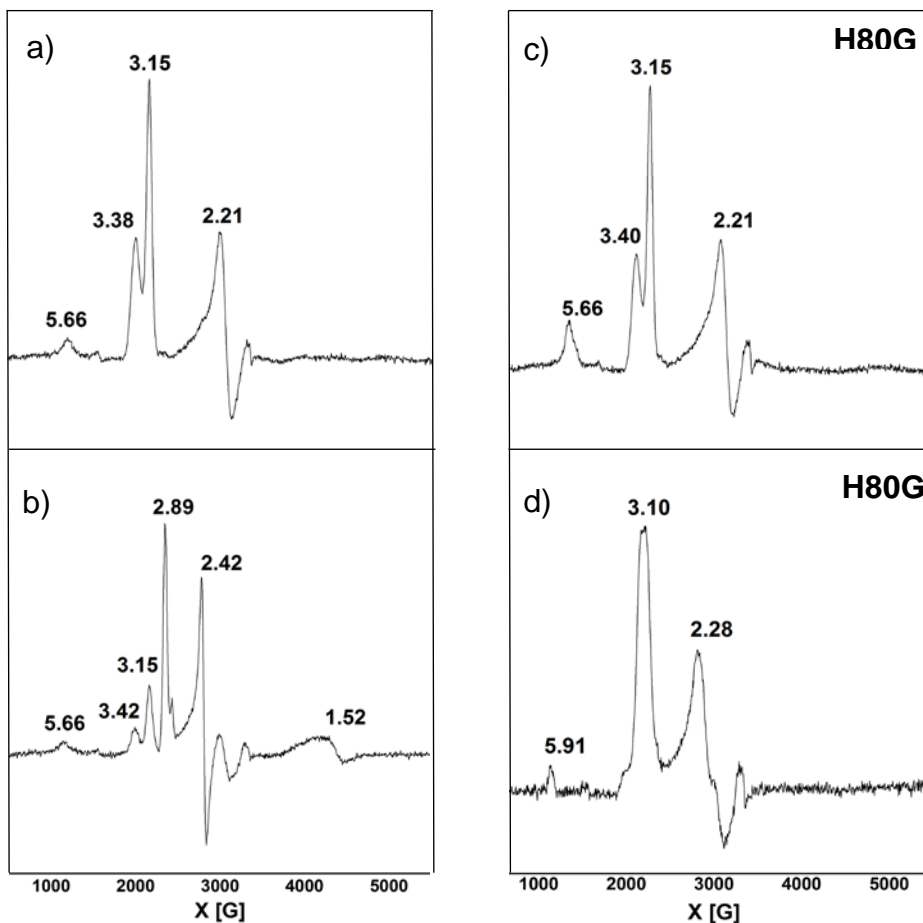


**Figure 4.12.** EPR spectra of a) 330  $\mu\text{M}$  diferric *SoCcP*, b) 230  $\mu\text{M}$  semi-reduced *SoCcP*, c) 280  $\mu\text{M}$  diferric *SoH80G* CcP, and d) 340  $\mu\text{M}$  semi-reduced *SoH80G* CcP. Experiments were conducted at 9.27 GHz, a power of 20 mW, and a temperature of 12 K.

EPR spectra for both the wild-type *SoCcP* and the H80G mutant of the enzyme (*SoH80G* CcP) were taken at 12 K. Diferric *SoCcP* exhibits an anisotropic low-spin signal at  $g = 3.38$  that disappears upon reduction (**Figures 4.12a and b**; a small residual signal is present in the

semireduced data). This signal must result from the H-heme which is reduced to the ferrous state in the presence of ascorbate.<sup>13</sup> The L-heme shows a strong low-spin signal at 12 K with  $g = 3.15$ , and 2.21 in the diferric enzyme. The origin of the weak signal at  $g = 5.66$  is not clear; it could presumably belong to a small amount of high-spin ferric L-heme, although the resonance position would be a bit unusual in this case. Alternatively, this could be due to an impurity. Curiously, in the semireduced sample the L-heme now exhibits strong signals at  $g = 2.89$ , 2.42, and 1.52 (the remaining, weak signals at 3.15 and 2.21 are due to the incomplete reduction of the H-heme). The latter resonance positions are similar to those of the L-heme in *NeCcP* (both diferric and semireduced), which indicates that the H-heme influences the properties of the L-heme in ways in *SoCcP* that are not observed in *NeCcP*. More specifically, the L-heme exists in a different state in diferric *SoCcP* and adopts the same properties as the L-heme in constitutively active *NeCcP* only after reduction, pointing to a potential difference between these two types of CcPs. Also, it should be noted here that the conversion from one low-spin L-heme species into a mixture of species upon reduction of the H-heme has previously been reported for *SoCcP*.<sup>13</sup> The EPR spectra of the diferric mutant *SoH80G CcP* exhibit similar signals for the H-heme at  $g = 3.40$  and for the L-heme at  $g = 3.15$ , 2.21 (low-spin heme). The somewhat mysterious signal at  $g = 5.66$  is also present in the spectrum of the diferric mutant, with an increased intensity compared to wild-type. Upon reduction, the  $g = 3.40$  signal disappears completely, indicative of complete reduction of the H-heme, but the signals of the L-heme remain at  $g = 3.10$ , 2.28 (**Figures 4.12c and d**). The shift of the L-heme resonances upon reduction are therefore only observed for wild-type enzyme, but not for the mutant, indicating that the mutation of H80 must influence the way that the two hemes interact. In semireduced *SoH80G CcP*, a very small amount of a high-spin ferric heme is observed, with a signal at  $g = 5.91$ . Finally, it is again noteworthy that mutation (removal) of the distal His

in *SoH80G* CcP does not lead to the formation of a high-spin ferric L-heme, just as in the case of the corresponding *NeCcP* variant. Again, the L-heme must be able to either recruit a different amino acid side chain as the 6<sup>th</sup> ligand to the heme, or bind a water molecule. However, in contrast to *NeCcP*, the His mutant does not give rise to the unusual intermediate spin heme in *SoCcP* (at low-temperature), indicating that there is a difference in the way that a six-coordinate L-heme is achieved in the *SoCcP* compared to the *NeCcP* mutant, or at least that a greater variety of species is present in *NeH59G* CcP. This point requires further study.

#### 4.6 Resonance Raman Spectra of *SoCcP*

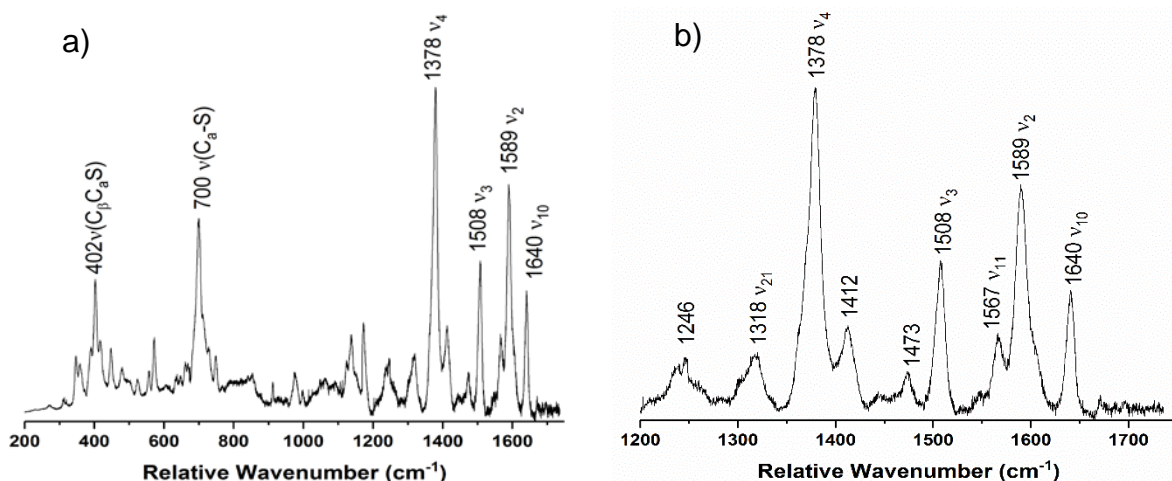


**Figure 4.13.** Resonance Raman spectrum of diferric *SoCcP* from a) 200 to 1750  $\text{cm}^{-1}$  and b) enlarged view of the 1200 to 1750  $\text{cm}^{-1}$  region. The sample was 105  $\mu\text{M}$  with 50% glycerol in pH 7 TIP7 buffer. The sample was excited at 413.1 nm using a Krypton ion gas laser at 77 K.

In the rRaman spectrum of diferric *SoCcP*, shown in **Figure 4.13**, the  $\nu_4$  oxidation state marker band is observed as a single peak at 1378  $\text{cm}^{-1}$ , which confirms that the enzyme is in the diferric state. Curiously, this band is shifted  $\sim 14 \text{ cm}^{-1}$  to higher energy compared to diferric *NeCcP*. Other marker bands indicative of low-spin ferric heme,  $\nu_3$  and  $\nu_{10}$ , are present at 1508 and 1640  $\text{cm}^{-1}$ , respectively. The  $\nu_2$  band at 1589  $\text{cm}^{-1}$  is analogous to the spin-state marker band for a low-spin heme observed at 1586  $\text{cm}^{-1}$  and 1596  $\text{cm}^{-1}$  for the diferric *NeCcP* sample. Interestingly, the



*NeCcP* sample shows two features for  $\nu_2$ , whereas only a single band is observed for *SoCcP*. This indicates that in *NeCcP*, the two hemes are more distinct with slightly different vibrational properties compared to *SoCcP*. A weak signal is also observed at  $1473\text{ cm}^{-1}$ , which might correspond to a small amount of photoreduction of the H-heme as discussed above. Alternatively, this peak could correspond to a different (unrelated) vibrational feature, as no accompanying ferrous  $\nu_4$  band is present in the spectrum of diferric *SoCcP*. As mentioned above, a corresponding feature is present in low-spin ferric Mb (see discussion for diferric *NeCcP*).<sup>38</sup> Note that there are no signals present in the spectrum of diferric *SoCcP* that correspond to the potential high-spin signals observed at  $1547$  and  $1614\text{ cm}^{-1}$  for diferric *NeCcP*, ruling out the presence of any measurable amounts of a high-spin ferric species in the *SoCcP* sample.

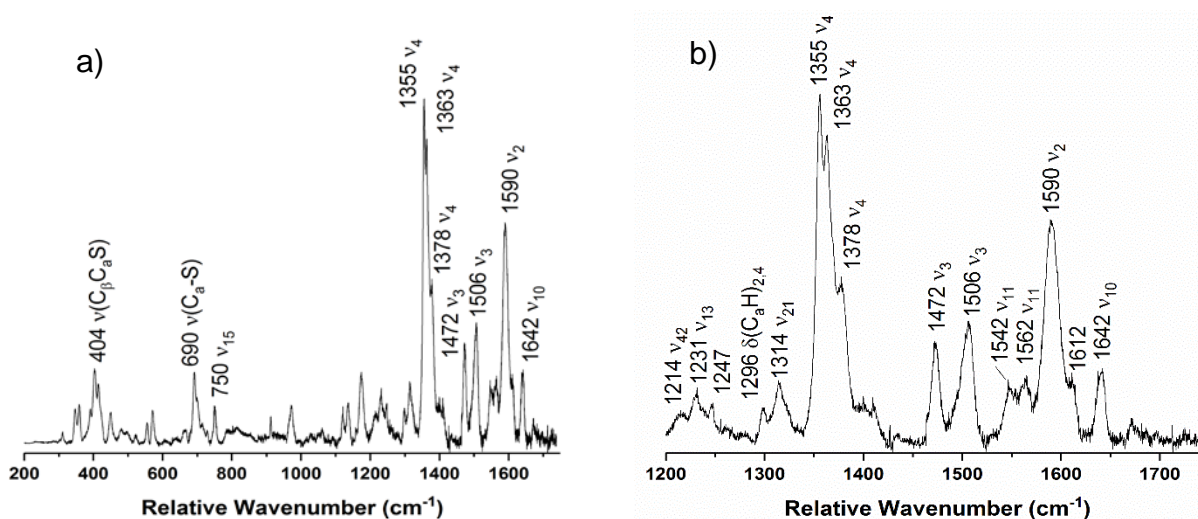


**Figure 4.14.** Resonance Raman spectrum of **semi-reduced *SoCcP*** from a) 200 to  $1750\text{ cm}^{-1}$  and b) enlarged view of the  $1200$  to  $1750\text{ cm}^{-1}$  region. The sample was  $160\text{ }\mu\text{M}$  with 50% glycerol in pH 7 TIP7 buffer. The sample was excited at  $413.1\text{ nm}$  using a Krypton ion gas laser at  $77\text{ K}$ .

Upon reduction of *SoCcP* to the semi-reduced state, two new  $\nu_4$  bands appear at  $1355$  and  $1363\text{ cm}^{-1}$ , indicating the reduction of the H-heme to the ferrous state (**Figure 4.14**; the residual band at  $1378\text{ cm}^{-1}$  is likely due to incomplete reduction – see EPR results, or a very small amount

of the L-heme that did not convert – see next). Interestingly, for the L-heme, a shift of the  $\nu_4$  band from 1378 (diferric) to 1363  $\text{cm}^{-1}$  (semireduced) is observed, which is further reflected by the change in the EPR parameters of the L-heme: here, the signals shift from  $g = 3.15, 2.21$  (diferric) to  $g = 2.89, 2.42, 1.52$  (semireduced). This indicates that the EPR properties of the L-heme and the energy of  $\nu_4$  are potentially correlated. Correspondingly, in *NeCcP*,  $\nu_4$  for the L-heme is observed at 1364/1361  $\text{cm}^{-1}$  with EPR parameters of  $g = \sim 2.9, 2.41, \sim 1.5$ , which is fully consistent with these ideas. In the semireduced state of *SoCcP*, the important spin state marker band  $\nu_3$  is observed at 1472  $\text{cm}^{-1}$ , indicating the presence of a high-spin ferrous heme. At the same time, the intensity of the low-spin ferric  $\nu_3$  band at 1506  $\text{cm}^{-1}$  decreases, but is still present in the semireduced form of the enzyme, in agreement with the idea that one heme remains ferric. However, this feature becomes asymmetric upon reduction, with a shoulder present around  $\sim 1490 \text{ cm}^{-1}$ . We believe that this shoulder corresponds to the  $\nu_3$  band of a small amount of the H-heme that is in the low-spin ferrous state. New bands at 1542 and 1612  $\text{cm}^{-1}$  appear in the semireduced form which likely result from the ferrous H-heme. These signals could also be evidence for the presence of a small amount of a high-spin ferric heme species at 77 K, but the complete absence of a corresponding  $\nu_3$  band around 1480  $\text{cm}^{-1}$  suggests that this is not the case (see discussion for semireduced *NeCcP* above). At the same time, the  $\nu_{10}$  marker band for a low-spin ferric heme at 1642  $\text{cm}^{-1}$  decreases in intensity upon reduction, but does not disappear, again indicating that the L-heme remains largely low-spin ferric in the semireduced form of *SoCcP*. This leaves us again with the contradiction that based on the mechanistic paradigm for reductively activated CcPs, the semireduced form should exhibit a five-coordinate, high-spin ferric heme, whereas experimentally, there is no evidence for such a claim. Again, one possible factor that could play a role here is

temperature, and correspondingly, the room temperature rRaman data of *SoCcP* were also analyzed (see below).

**Figure 4.15** shows the rRaman spectrum of diferric *SoH80G CcP*. The spectrum is almost identical to that of wild-type *SoCcP* with a ferric  $\nu_4$  band present at  $1378\text{ cm}^{-1}$ , and two low-spin ferric bands at  $1506$  and  $1640\text{ cm}^{-1}$  ( $\nu_3$  and  $\nu_{10}$  respectively). The low-spin  $\nu_2$  band at  $1589\text{ cm}^{-1}$  is also observed, as well as a ferric  $\nu_{11}$  band at  $1567\text{ cm}^{-1}$ . These results are in agreement with the EPR results that show that despite the removal of the distal ligand H80 from the L-heme, this heme remains low-spin in the ferric state with no indication for the presence of a high-spin ferric heme in the rRaman data. Reduction of the H-heme in *SoH80G CcP* results in a spectrum that is also similar to the semi-reduced wild-type *SoCcP* data (**Figure 4.16**). Two new  $\nu_4$  bands are present at  $1352$  and  $1360\text{ cm}^{-1}$  (the residual signal at  $1374\text{ cm}^{-1}$  is likely due to incomplete reduction, or incomplete conversion of the L-heme in the reduced form), indicating reduction of the H-heme, as in wild-type *SoCcP*. Here, the possible correlation between the  $\nu_4$  energy and the EPR resonances of the low-spin L-heme is not fulfilled; the reason for this is not clear. Two easily visible  $\nu_3$  bands are present at  $1472$  and  $1501\text{ cm}^{-1}$  which can be attributed to a high-spin ferrous (H-heme) and a low-spin ferric (L-heme) signal, respectively. The  $1501\text{ cm}^{-1}$  band is fairly broad and may conceal a low-spin ferrous  $\nu_3$  band  $\sim 1490\text{ cm}^{-1}$ , in agreement with the finding for wild-type enzyme that some of the ferrous heme might be in the low-spin state. A  $\nu_2$  spin-state marker band is present at  $1593\text{ cm}^{-1}$  and indicates the presence of low-spin heme. Two  $\nu_{11}$  bands are present at  $1543$  and  $1557\text{ cm}^{-1}$ , likely indicating the presence of ferrous and ferric heme in the sample. A  $\nu_{10}$  band is still present at  $1630\text{ cm}^{-1}$ , which is shifted compared to the other low-spin ferric  $\nu_{10}$  bands for the various *CcP* samples. The implication of this result is not yet clear. The more pronounced  $1608\text{ cm}^{-1}$  band in the diferric sample may result from either ferrous or a high-spin ferric heme species,

as in the other samples with signals in the 1608-1614  $\text{cm}^{-1}$  range. However, the absence of a  $\nu_3$  band around 1480  $\text{cm}^{-1}$  again indicates that most of the L-heme is in the low-spin state, as in the case of wild-type enzyme.

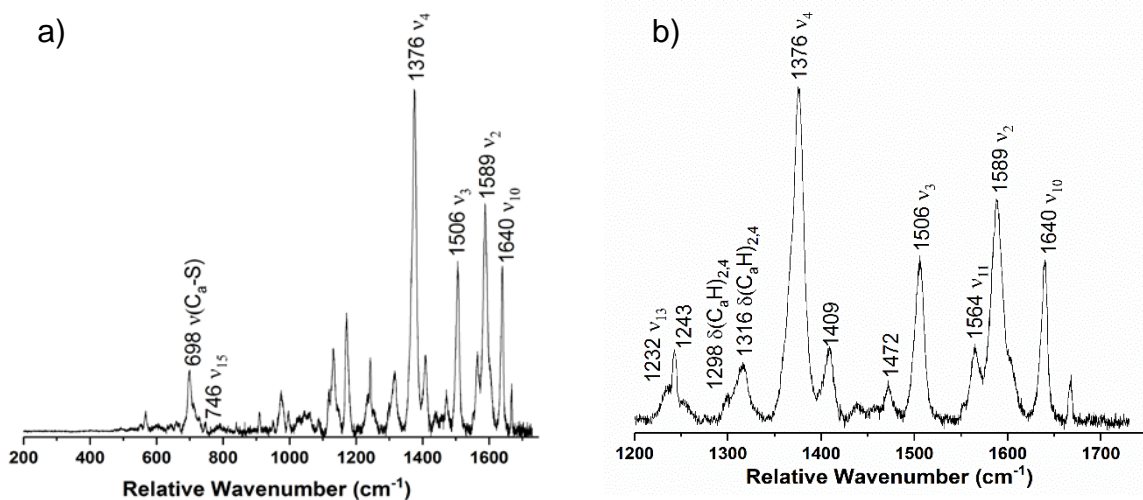


**Figure 4.15.** Resonance Raman spectrum of **diferric *SoH80G CcP*** from a) 200 to 1750  $\text{cm}^{-1}$ , and b) enlarged view of the 1200 to 1750  $\text{cm}^{-1}$  region. The sample was 280  $\mu\text{M}$  with 30% glycerol in pH 7 TIP7 buffer. The sample was excited at 413.1 nm using a Krypton ion gas laser at 77 K.

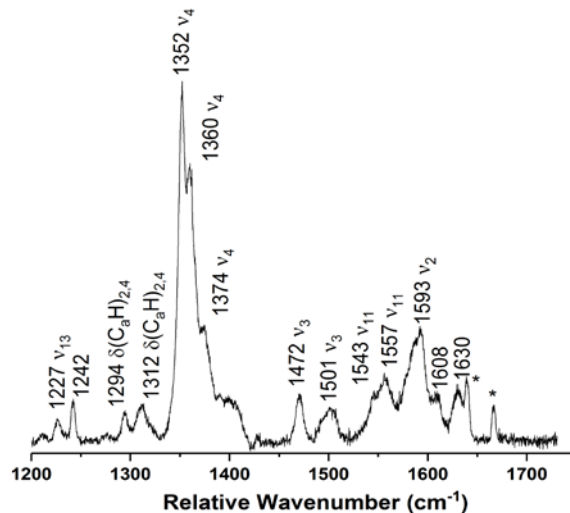


**Figure 4.16.** Resonance Raman spectrum of **semi-reduced *SoH80G CcP*** from 1200 to 1750  $\text{cm}^{-1}$ . The sample was 280  $\mu\text{M}$  with 30% glycerol in pH 7 TIP7 buffer. The sample was excited at 413.1 nm using a Krypton ion gas laser at 77 K.

Room temperature rRaman data were also collected for diferric *SoCcP* and *SoH59G CcP* (Figure 4.17). Both spectra are very similar to the resonance Raman data taken at 77 K for these enzymes. Only one  $\nu_4$  band is present at 1374-1375  $\text{cm}^{-1}$ . Bands at 1503-1505  $\text{cm}^{-1}$  ( $\nu_3$ ), 1563-1564  $\text{cm}^{-1}$  ( $\nu_{11}$ ), and 1638-1640  $\text{cm}^{-1}$  ( $\nu_{10}$ ) indicate that in both diferric *SoCcP* variants the H- and L-hemes are in the low-spin ferric state. Both spectra exhibit a weak band at 1467-1468  $\text{cm}^{-1}$ , which could originate from a small amount of photoreduction of the H-heme, but since no corresponding  $\nu_4$  bands are observed at  $\sim 1350 \text{ cm}^{-1}$ , it is more likely that these small bands are due to other, unrelated vibrations as discussed above (and as observed for low-spin ferric Mb).

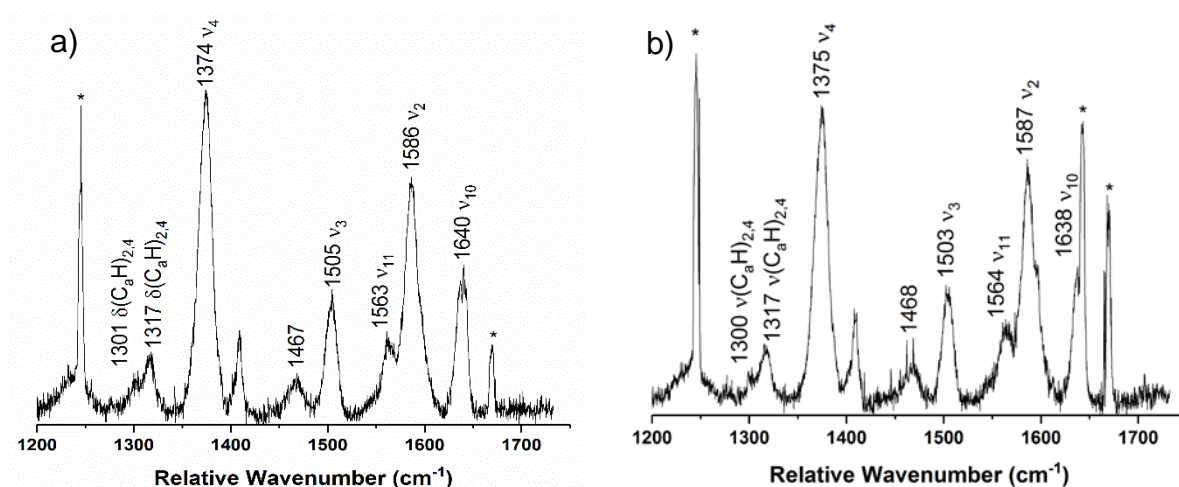


**Figure 4.17.** Room temperature resonance Raman spectrum of a) diferric *SoCcP* and b) diferric *SoH80G CcP*. The samples were 280-330  $\mu\text{M}$  with 30% glycerol in pH 7 TIP7 buffer. The samples were rotated and excited at 413.1 nm using a Krypton ion gas laser. Plasma lines are indicated with an asterisk.

## 4.7 Magnetic Circular Dichroism Spectra of *SoCcP*

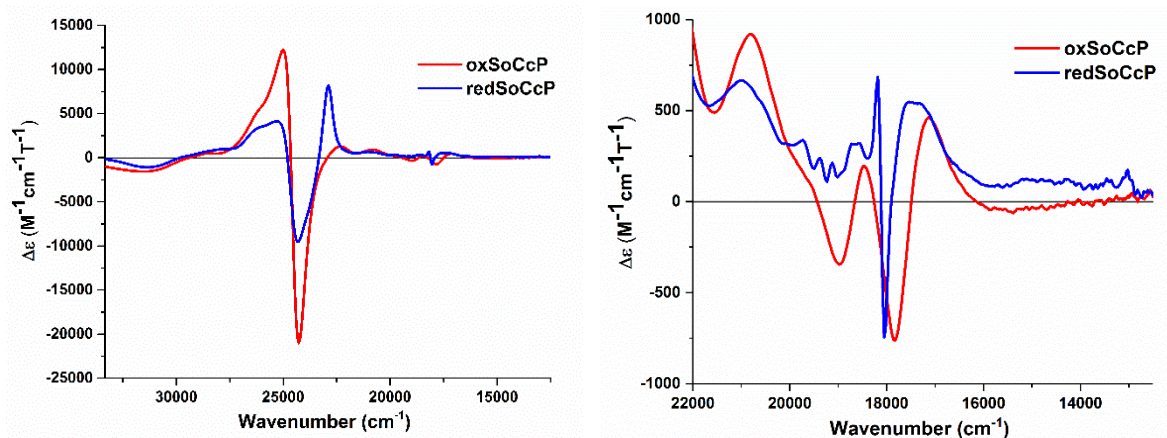


**Figure 4.18.** a) Near-UV/visible-region MCD spectra of the diferric and semi-reduced states of *SoCcP* and b) a close-up of the visible region of the spectra. The sample was 20 μM with ~50% glycerol in a TIP7 buffer at pH 7. Spectra were recorded at 2K.

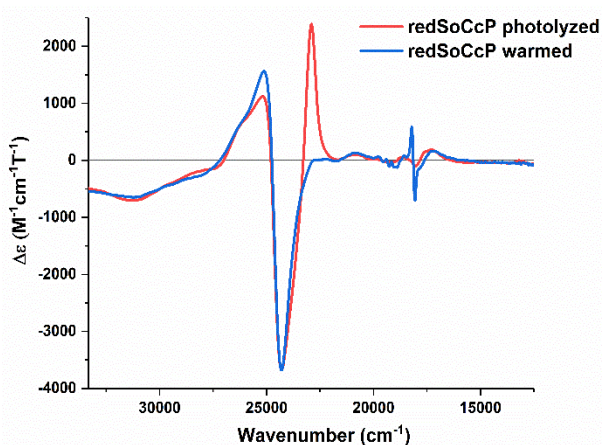


**Figure 4.19.** Near-UV/visible-region MCD spectra of a semi-reduced *SoCcP* sample that was photolyzed with a mercury lamp, and after warming the sample to 70 K in the dark and then cooling the sample back to 2 K. The sample was 2.0 μM with ~50% glycerol in a TIP7 buffer at pH 7. Spectra were recorded at 2 K.

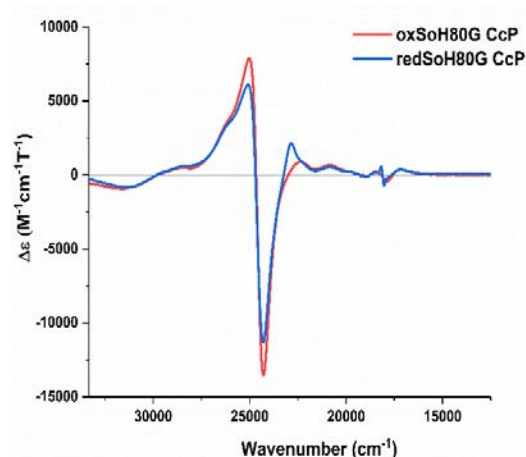


**Figure 4.20.** Near-UV/visible-region MCD spectra of the diferric and semi-reduced states of *SoH80G CcP*. The samples were 1.2-1.4 μM with ~50% glycerol in a TIP7 buffer at pH 7. Spectra were recorded at 2K.

Near-UV/visible MCD spectra at lq. He temperatures were recorded for the *SoCcP* enzyme in both the diferric and the semireduced states (**Figure 4.18**). The diferric enzyme exhibits a typical MCD spectrum for low-spin ferric hemes with a positive signal at 25000 cm<sup>-1</sup> and a negative signal at 24300 cm<sup>-1</sup> in the Soret band region. In addition, there are low-spin ferric signals present in the

Q-band region at 20870, 19050, 18510, and 17980  $\text{cm}^{-1}$ . This spectrum exhibits very similar features compared to the MCD spectrum of diferric *NeCcP* (**Figure 4.9**). Both of these peroxidases seem to possess low-spin ferric hemes at lq. He temperature. Upon reduction, the low-spin ferric signals at 25280  $\text{cm}^{-1}$  and 24310  $\text{cm}^{-1}$  are still present, though they have decreased in intensity significantly, in agreement with the idea that one of the hemes has become reduced. The large positive signal at 22880  $\text{cm}^{-1}$  results from the reduced H-heme in the high-spin state. As described before in the literature (for *PaCcP*)<sup>15</sup> and observed for *NeCcP* (**Figure 4.9**), this signal results from the partial photolysis of the Fe-S<sub>Met</sub> bond in the H-heme upon irradiation of the sample in the CD spectrophotometer. The H-heme continues to undergo photolysis over time, though some low-spin ferrous heme remains, which is evident from the sharp diamagnetic signals in the Q-band region of the semi-reduced form at ~18160  $\text{cm}^{-1}$ . Compared to a ferrous Cyt. *c* standard, the low-spin ferrous signal represents ~32% of the H-heme in the data shown in **Figure 4.18b**, and thus, the high-spin signal results from the remaining ~68% of the ferrous heme in this sample. Photolysis can be reversed by warming the sample to 70 K in the dark and then cooling the sample back down to 2 K (**Figure 4.19**), which also works for *NeCcP* (**Figure 4.10**). Both diferric and semi-reduced *SoH80G CcP* samples exhibit similar signals compared to wild-type *SoCcP*. The spectrum of diferric *SoH80G CcP* exhibits signals at 25010 and 24280  $\text{cm}^{-1}$  in the Soret band region and at 22330, 20820, 18490, and 17160  $\text{cm}^{-1}$  in the Q-band region (**Figure 4.20**). The spectrum of semireduced *SoH80G CcP* exhibits signals at 25080 and 24290  $\text{cm}^{-1}$  in the Soret band region and sharp diamagnetic signals at 19720, 19380, 19130, and 18090  $\text{cm}^{-1}$  in the Q-band region. A high-spin ferrous heme signal is present at 22850  $\text{cm}^{-1}$  due to some photolysis of the sample.

#### 4.8 Diferric *NeCcP* and *SoCcP*

In this study, EPR, resonance Raman, and MCD spectra were collected in order to elucidate the differences between the ‘constitutively active’ bCcP from *Nitrosomonas europaea* (*NeCcP*) and the ‘reductively activated’ bCcP from *Shewanella oneidensis* (*SoCcP*). In the literature, evidence from reactivity and crystallographic studies<sup>3, 18</sup> indicate that in the constitutively active enzymes, the L-heme is five-coordinate (5C) and in the high-spin state, whereas in the activatable enzymes, reduction of the H-heme is required for the L-heme to become 5C.<sup>2, 7</sup> Once the L-heme is 5C, it binds hydrogen peroxide to start the peroxidase reaction. In order to investigate this paradigm further, we studied the resting (diferric) and semi-reduced states of *NeCcP* and *SoCcP*.

In contrast to this expectation, the EPR spectrum of diferric *NeCcP* shows both the H-heme ( $g = 3.41$ ) and the L-heme ( $g = 2.87, 2.38, \text{ and } 1.50$ ) to be low-spin (at 12 K), and hence, six-coordinate. A small amount of high-spin ferric species is also present at  $g = 6.15$ , but this is only a very small percentage of the sample. This result is similar to previous EPR investigations on *NeCcP* that show one low-spin signal for the H-heme, and a major low-spin component and a small high-spin signal for the L-heme.<sup>3</sup> The low-temperature MCD data further corroborate these results. The MCD spectrum of diferric *NeCcP* shows only signals originating from low-spin ferric hemes. Since MCD signals from low-spin and high-spin ferric hemes sometimes overlap, and the signals from the low-spin form are much more intense,<sup>15</sup> the MCD results are less conclusive in ruling out a high-spin form for the L-heme compared to the EPR data. Nevertheless, the MCD data do not provide any evidence for a high-spin ferric heme either. Under cryogenic conditions, it is therefore clear that in diferric *NeCcP*, both the H-heme and the L-heme are low-spin, and correspondingly, these data do not support the notion that the L-heme in *NeCcP* is in the high-spin ferric state, as proposed for ‘constitutively active’ bCcPs. It may be noted that previous studies on *PaCcP* have



shown that the spin state of the L-heme is temperature-dependent,<sup>15-16</sup> and that at low temperature, the L-heme is mostly or completely low-spin. In order to further investigate this point, we then conducted rR studies on diferric *NeCcP* at 77 K, where the potential spin state change should not be an issue. In the rRaman data, a single  $\nu_4$  oxidation state marker band is visible at 1364  $\text{cm}^{-1}$ , and a single  $\nu_3$  spin state marker band is observed at 1504  $\text{cm}^{-1}$ , indicative of predominant low-spin ferric heme in the sample. This is further confirmed by the absence of a  $\nu_3$  signal at  $\sim 1480 \text{ cm}^{-1}$ , which is a hallmark of high-spin ferric heme.<sup>29</sup> Small signals at 1547 and 1614  $\text{cm}^{-1}$ , previously assigned as  $\nu_{11}$  and  $\nu_{10}$  for high-spin ferric myoglobin,<sup>29</sup> are the only indication that a small amount of a high-spin ferric heme could be present, but only as a minor species. A small amount of photoreduction of the H-heme is also evident from the data. Finally, we also collected room temperature rRaman data for diferric *NeCcP*, but again failed to detect any significant amounts of a high-spin ferric heme species. Interestingly, the photoreduction of the H-heme is suppressed when the rRaman measurements are conducted at room temperature in solution. In summary, our spectroscopic results obtained at 12 K, 77 K, and at room temperature do not support the previously proposed paradigm that the L-heme in diferric *NeCcP* is predominantly five-coordinate, and hence, high-spin.

We then investigated whether the L-heme in *NeCcP* could be “forced” to be five-coordinate if the distal His ligand of the heme would be removed. The EPR spectrum of the corresponding mutant, *NeH59G CcP*, indicates that the L-heme now exists as a mixture of the low-spin state ( $g = 2.90, 2.41, 1.57$ ; similar to wild-type) and a very unusual intermediate spin state ( $g = 4.82, 4.09, \text{ and } 3.78$ ;  $S = 3/2$ ). So surprisingly, there is still only an extremely small high-spin ferric heme signal observed in the sample, which indicates that the L-heme in the mutant is able to either recruit a different protein residue as the distal ligand, or has a water molecule coordinated as the 6<sup>th</sup> ligand.

The rRaman data of diferric *NeH59G* CcP are overall similar to those of wild-type enzyme, and again do not provide any evidence for the presence of significant amounts of a high-spin ferric heme. There are a couple of interesting differences to the wild-type enzyme though. First, *NeH59G* CcP shows an increased amount of photoreduction of the H-heme, and the  $\nu_4$  oxidation state marker band of this heme is shifted to  $1374\text{ cm}^{-1}$ . Considering that the mutation was performed on the distal ligand of the L-heme, these changes in the properties of the H-heme indicate that these hemes communicate in subtle ways that we do not fully understand yet.

There are some interesting differences between the spectral properties of diferric *NeCcP* and *SoCcP*. In the EPR spectrum of *SoCcP*, the H-heme shows the typical signal at  $g = 3.40$ , whereas the resonances of the L-heme are surprisingly different ( $g = 3.15, 2.21$ ). Just as in the case of *NeCcP*, there is no evidence for the presence of any significant amount of a high-spin ferric heme in the EPR data. The low-temperature MCD spectrum of *SoCcP* again supports the EPR results and shows only low-spin ferric bands. As mentioned above, it should be noted here that the presence of a smaller amount of a high-spin ferric heme species would be less noticeable in the MCD data compared to EPR. The rRaman spectrum of diferric *SoCcP*, taken at 77 K, shows one  $\nu_4$  ferric oxidation state marker band at  $1378\text{ cm}^{-1}$  and a single  $\nu_2$  low-spin marker band at  $1589\text{ cm}^{-1}$ . Important spin and oxidation state marker bands  $\nu_3$  and  $\nu_{10}$  are observed at  $1504\text{ cm}^{-1}$  and  $1640\text{ cm}^{-1}$ , again indicative of the presence of low-spin ferric heme. It is evident from these spectra that both hemes of *SoCcP* are exclusively low-spin in the diferric form of the enzyme, and no indication for a spin crossover is observed at higher temperatures, even in the room temperature rRaman spectrum of *SoCcP*, which is very similar to the data obtained at 77K.

In analogy to *NeCcP*, we also investigated the distal His mutant of *SoCcP*, *SoH80G* CcP, to determine whether a five-coordinate, high-spin ferric L-heme could be obtained in this way.

The EPR data of the mutant in the diferric state are essentially identical to that of wild-type *SoCcP* and show resonances at 3.40 (H-heme) and 3.15, 2.21 (L-heme), with both hemes in the low-spin state. No evidence for the formation of an intermediate spin heme is observed in this case, in contrast to *NeH59G CcP*. This indicates that in *SoH80G CcP*, the L-heme is again able to recruit a substitute 6<sup>th</sup> ligand. In *NeH59G CcP*, a mixture of two species with either two different axial ligands or different conformations of the same axial ligand is observed (indicating that the new distal ligand might not be that strongly bound). In contrast, this is not observed in *SoH80G CcP*, indicating that in this case the new distal ligand is strongly bound to the heme. It is also remarkable that the low-spin L-heme in both *NeH59G CcP* and *SoH80G CcP* shows similar EPR parameters as the corresponding wild-type enzyme despite the mutation of the distal His residue to glycine. It is unclear which ligand or residue is binding to the L-heme in *SoH80G CcP* that replicates the EPR parameters of the native enzyme so closely. No nearby His residue is available in lieu of His80, but the ligand that does bind still coordinates strongly to the heme. In addition, the rRaman spectra of *SoH80G CcP* at both cryogenic (77 K) and room temperature are very similar to those of wild-type enzyme and again show the presence of low-spin ferric hemes only, despite the removal of the distal His residue of the L-heme in the mutant. One interesting difference to *NeCcP* is the fact that no significant photoreduction of the H-heme is observed in the 77 K rRaman data of *SoH80G CcP*, whereas in *NeCcP* and *NeH59G CcP* the photoreduction of the H-heme is enhanced. This indicates that there are key differences in the communication between the H- and the L-heme in diferric *SoCcP* compared to *NeCcP*.

Since *SoCcP* is an activatable bCcP, the absence of any significant amount of high-spin ferric L-heme is still in agreement with the proposed mechanism of activation of these enzymes, where it has been proposed that reduction of the H-heme is required in order for the L-heme to

become activated. This aspect was further explored by investigating the semireduced states of *SoCcP* compared to *NeCcP*.

#### **4.9 Semi-reduced *NeCcP* and *SoCcP*.**

In the semi-reduced *NeCcP* sample, the EPR spectrum shows the disappearance of the anisotropic low-spin signal at  $g = 3.41$ . This low-spin signal is therefore assigned to the H-heme, which has been reduced in this sample. The low-spin signals of the L-heme are unchanged in the semireduced form, indicating that there is no significant change to this heme that would be caused by the reduction. The low-temperature MCD spectrum of semi-reduced *NeCcP* shows similar low-spin features when compared to the diferric enzyme, indicating that the L-heme is in the low-spin state. In addition, new features are observed at  $22860\text{ cm}^{-1}$  and a derivative-shaped, sharp signal occurs at  $18160\text{ cm}^{-1}$  (assigned to the Q-band), accompanied by a number of smaller, equally sharp peaks (the vibronic  $Q_v$  band). All of those new signals arise from the reduced ferrous H-heme. The sharp signals in the Q-band region are a hallmark of a diamagnetic heme, and correspond to low-spin ferrous heme. The feature at  $22860\text{ cm}^{-1}$  corresponds to ferrous heme in the high-spin state. This signal results from the photolysis of the Fe-S<sub>Met</sub> bond of the reduced H-heme,<sup>15</sup> which we further demonstrate here using photolysis experiments (see Results & Analysis section). Resonance Raman measurements were used to further corroborate these results. The spectrum of semi-reduced *NeCcP* exhibits two  $\nu_4$  oxidation state marker bands at  $1351$  and  $1361\text{ cm}^{-1}$ , confirming the presence of a ferric and a ferrous heme. The  $\nu_2$  band at  $1586\text{ cm}^{-1}$  decreases in intensity compared to the diferric form, which indicates a decrease in the concentration of low-spin heme in the sample. The decrease in intensity of  $\nu_3$  at  $1504\text{ cm}^{-1}$  and  $\nu_{10}$  at  $1640\text{ cm}^{-1}$  is in agreement with this, showing a loss in low-spin ferric heme upon reduction. At the same time, new

$\nu_3$  bands at 1472 and 1492  $\text{cm}^{-1}$  occur, which confirm the presence of a ferrous heme, both in the high-spin and low-spin heme state (the high-spin state results from photolysis during the rRaman experiment). As in the diferric enzyme, no  $\nu_3$  signal is observed at  $\sim 1480 \text{ cm}^{-1}$ , indicating the absence of any significant amount of a high-spin ferric heme. Small signals at 1544  $\text{cm}^{-1}$  and 1611  $\text{cm}^{-1}$  persist, which may indicate the presence of a small amount of high-spin ferric heme. So in summary, reduction of the H-heme has no significant effect on the spectroscopic properties of the L-heme in *NeCcP*. This makes intuitive sense, since in constitutively active bCcPs, like *NeCcP*, no reduction of the H-heme is required for catalysis, i.e. the L-heme is already in the active state. However, our data clearly show that this does NOT mean that the L-heme is statically five-coordinate and high-spin, as no significant high-spin ferric signals are observed in any of our spectroscopic data for *NeCcP*.

These conclusions also hold for the mutant *NeH59G CcP*. In the EPR spectrum of *NeH59G CcP*, the H-heme signal at  $g = 3.40$  disappears upon reduction, but otherwise, no change is observed for the low- and intermediate-spin signals of the L-heme. The rRaman spectrum of semi-reduced *NeH59G CcP* is very similar to that of wild-type semi-reduced *NeCcP*, with only slight shifts in the wavenumbers of the relevant bands. No significant amounts of a high-spin ferric heme are observed for semireduced *NeH59G CcP* either.

These observations are in contrast to the results for *SoCcP*. In the semi-reduced *SoCcP* sample, the EPR spectrum shows the disappearance of the low-spin signal at  $g = 3.38$ , similar to the observations for the *NeCcP* sample. This low-spin signal is therefore assigned to the H-heme. Importantly, the signals for the L-heme are shifted relative to the diferric enzyme: in diferric *SoCcP*, the L-heme resonances are observed at  $g = 3.15, 2.21$ , which shift to 2.89, 2.42, and 1.52 in the semireduced form. The latter resonance positions are almost identical to those of the L-heme

in *NeCcP* (both diferric and semireduced, see above). This provides direct evidence that the reduction of the H-heme leads to an activation of the L-heme in *SoCcP*, not by converting this heme into a five-coordinate (high-spin) heme, but by causing some other change in its coordination sphere.

One possible explanation for this finding is the deprotonation of one of the His ligands of the L-heme, leading to the formation of the corresponding imidazolate complex.<sup>13</sup> Using the crystal field parameters of Taylor,<sup>39</sup> the *g*-values at 2.89 and 2.42 correspond to an imidazolate classification, whereas the *g*-values at 3.15, and 2.21 correspond to an imidazole-bound heme. Hence, upon reduction of the H-heme in *SoCcP*, one of the His ligands of the L-heme becomes deprotonated to activate the enzyme. In contrast, in *NeCcP* the His ligand of the L-heme is already deprotonated in the diferric form. Hence, these results point towards a more subtle activation mechanism of reductively activated bCCPs than previously realized. The data do not support the idea that the L-heme becomes statically five-coordinate and high-spin upon reduction, as no corresponding signals are observed in the EPR data of semireduced *SoCcP*. The low-temperature MCD spectrum of semi-reduced *SoCcP* further supports this conclusion, as it exhibits low-spin ferric heme signals for the L-heme only, very similar to those observed in the MCD data of semi-reduced *NeCcP*. As in the latter case, the H-heme is reduced to the ferrous state, and exists as a mixture of high-spin and low-spin states (due to photochemical cleavage of the Fe-S<sub>Met</sub> bond). The rRaman spectrum of semi-reduced *SoCcP* exhibits two different signals for the oxidation state marker band  $\nu_4$  at 1353 cm<sup>-1</sup> (ferrous, H-heme), and 1361 cm<sup>-1</sup> (ferric, L-heme). Here, the reduced H-heme exists in both the high- and low-spin state, as evident from the appearance of peaks at 1472 (high-spin) and a weaker shoulder at 1496 cm<sup>-1</sup> (low-spin) for the spin state marker band  $\nu_3$ . This is again due to the photochemical cleavage of the Fe-S<sub>Met</sub> bond in the reduced H-heme.

Curiously, only one  $\nu_2$  spin state marker band at  $1590\text{ cm}^{-1}$  is present in the spectrum that indicates the presence of low-spin heme. In addition, low-spin ferric signals are still present at  $1506$  ( $\nu_3$ ) and  $1642\text{ cm}^{-1}$  ( $\nu_{10}$ ). No signal is observed for the spin state marker band  $\nu_3$  around  $1480\text{ cm}^{-1}$ , indicating that no significant amounts of a high-spin ferric heme are present in the sample. Weak signals appearing at  $1542$  and  $1612\text{ cm}^{-1}$  might indicate the presence of a small amount of high-spin ferric heme, but these signals could also arise from the reduced H-heme.

These results are further corroborated by investigations into the spectroscopic properties of the semireduced form of the mutant *SoH80G CcP*. As mentioned above, the EPR data of semireduced *SoH80G CcP* are very similar to those of wild-type enzyme, strongly indicating that the L-heme is able to recruit another ligand that binds strongly to the L-heme in the mutant. Importantly, upon reduction of *SoH80G CcP* to the semireduced state, only small changes in the EPR resonances of the low-spin L-heme are observed, i.e. the signals shift from  $g = 3.15, 2.21$  (diferric) to  $g = 3.10, 2.28$  (semireduced). This means that in the mutant, the new distal His ligand cannot be deprotonated upon reduction of the H-heme, in contrast to wild-type enzyme. More importantly, these data demonstrate that *it is in fact the distal His ligand, the one that is removed in the H80G mutant, which is deprotonated in wild-type enzyme upon reduction of the H-heme.* When this ligand, H80, is removed, the remaining His ligand of the L-heme can no longer be deprotonated when the H-heme is reduced. This finding has stark mechanistic implications as discussed below. On the other hand, the EPR data of semireduced *SoH80G CcP* do not show the presence of any high-spin ferric heme, and this is further supported by the MCD data. This latter conclusion is also confirmed by the rRaman spectrum of semireduced *SoH80G CcP*. As mentioned above, the diferric enzyme is completely low-spin ferric with bands at  $1376$  ( $\nu_4$ ),  $1506$  ( $\nu_3$ ),  $1589$  ( $\nu_2$ ), and  $1640$  ( $\nu_{10}$ )  $\text{cm}^{-1}$ . Despite the removal of the distal His residue adjacent to the L-heme,

semi-reduced *SoH80G* CcP still exhibits  $\nu_3$  and  $\nu_{10}$  low-spin ferric marker bands at 1501 and 1630  $\text{cm}^{-1}$ . The data do not provide evidence for the presence of any significant amount of a high-spin ferric heme. Hence, the previous proposal in the literature that the L-heme would become statically five-coordinate and high-spin upon reduction of the H-heme in activatable bCcPs, like *SoCcP*, cannot be confirmed by our spectroscopic data on both wild-type and H80G *SoCcP*.

#### 4.10 Mechanistic Implications

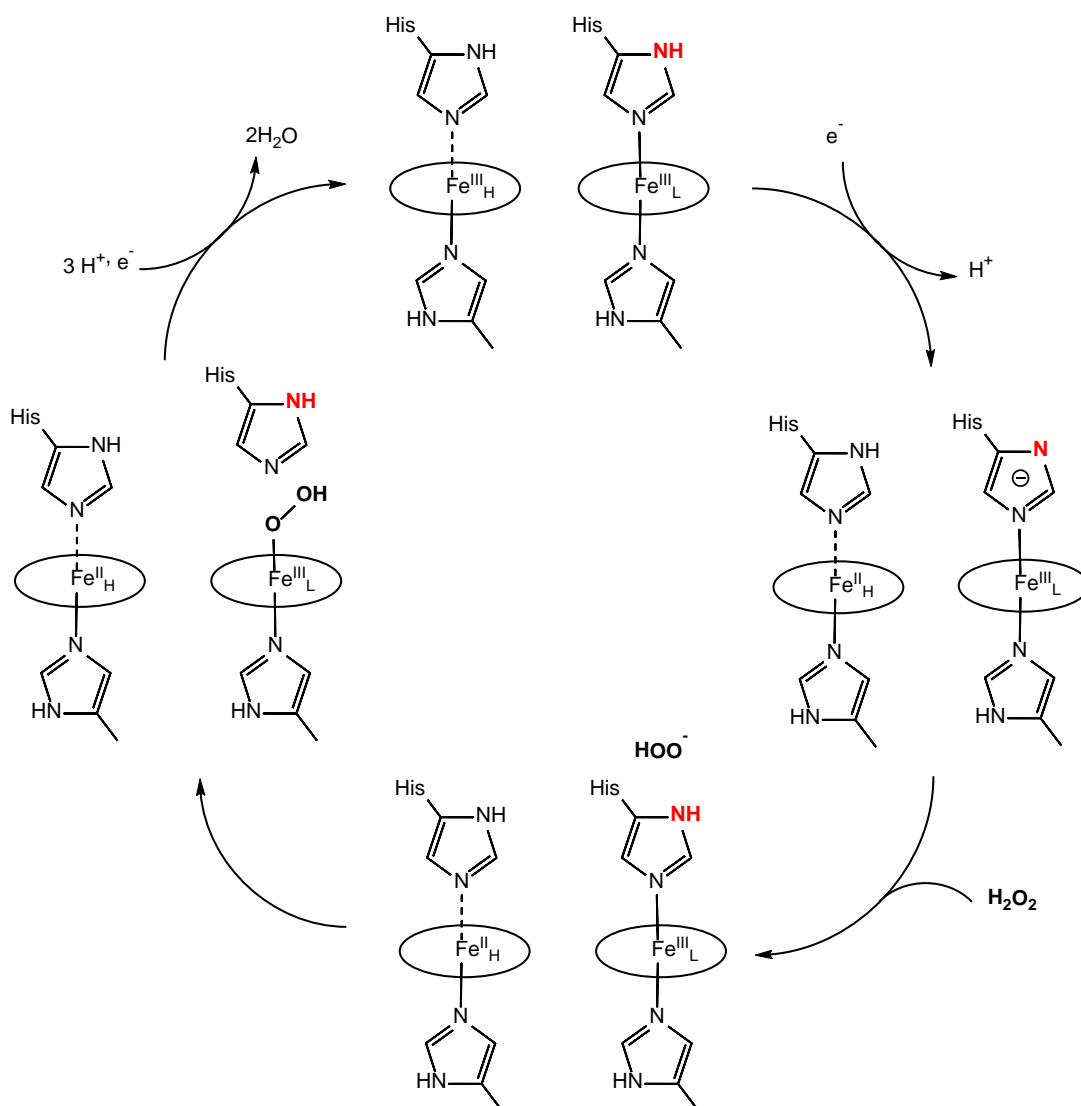
As described above in detail, our spectroscopic data for diferric and semi-reduced *NeCcP* and *SoCcP* do not support the general mechanistic paradigm of activation for bCcPs. In addition, although both enzymes are proposed to belong to the two different classes of bCcPs -constitutively active (*NeCcP*) and activatable (*SoCcP*) - they actually show very similar spectroscopic properties where both the H- and L-heme are in the ferric low-spin state in the diferric form of the enzymes, and upon reduction of the H-heme to the ferrous form (which co-exists in the high-spin/low-spin state), the L-heme remains low-spin ferric. All of our spectroscopic data - EPR, MCD and rRaman, determined at 12 K, 77 K and room temperature – only show the presence of small amounts of a ferric high-spin heme, if any at all. So in both cases, the L-heme does not exist in a static, five-coordinate high-spin ferric state in the active form of the enzyme (either diferric (*NeCcP*) or semireduced (*SoCcP*)) as proposed as a prerequisite for hydrogen peroxide binding. This points to a potentially different mechanism where in the activated form of the enzyme (diferric for constitutively active and semi-reduced for activatable enzyme) the L-heme does not reside in a statically five-coordinate form, but instead, the activation is more of a dynamic process. In this case, the enzyme could exist in a conformationally flexible state where one of the Fe-N(His) bonds of the L-heme has become weaker, such that the enzyme can sample through (multiple)



conformations with the L-heme being either five- or six-coordinate. These conformations would be in dynamic exchange at room temperature but the actual fraction of five-coordinate high-spin ferric L-heme at any given point in time would be small, and could then give rise to the weak rRaman signals that we observe in the 1540-1545 and 1608-1614  $\text{cm}^{-1}$  range, in particular for *NeCcP*. Upon cooling (and ultimately freezing) of the enzyme, entropic effects would then lead to a rebinding of the distal His, creating a six-coordinate low-spin ferric heme at lower temperatures. In this regard, the residual, small amount of high-spin ferric signal observed in the EPR data of *NeCcP* could then correspond to a small fraction of enzyme that for some reason was trapped in the five-coordinate state when the sample was frozen (but this signal could also be due to impurities and/or enzyme degradation). The fact that even the rRaman data taken at room temperature in solution do not show any evidence that the L-heme is now majorly converting into a five-coordinate ferric high-spin state argues against this model of a static, five-coordinate L-heme in the active state of bCcPs.

On the other hand, our spectroscopic results point to a completely different explanation for the activation process of bCcPs that is much more subtle. As described in detail above, our data show that in the constitutively activated *NeCcP*, the L-heme is coordinated by a deprotonated His in the distal position. In the case of the activatable bCcP *SoCcP*, the L-heme is initially coordinated by a protonated distal His in the diferric state, but this His becomes deprotonated in the semireduced form of the enzyme. This result therefore implies that in the activated state of bCcPs, the L-heme is coordinated by a deprotonated distal His. This could be mechanistically significant, as the deprotonated His could then deprotonate hydrogen peroxide when it enters the active site pocket of the L-heme, followed by a ligand exchange where the protonated His is subsequently released from the iron center, allowing the deprotonated hydrogen peroxide to bind to the ferric L-

heme in the first step of catalysis (**Scheme 4.2**). Future work will now focus on gathering further evidence for this new mechanism of activation for bCcPs.



**Scheme 4.2.** Possible mechanism for a reductively activated bCcP enzyme. The L-heme remains low-spin in each step of the mechanism prior to substrate release. EPR results suggest that the distal His bound to the L-heme is deprotonated upon reduction of the H-heme. This His residue may then deprotonate hydrogen peroxide before peroxide binds to the heme, displacing the same His residue.

## 4.11 Experimental Section

### Protein Expression and Purification of wt *So* and H80G

All proteins were expressed and purified in the Elliott laboratory at Boston University. Expression and purification of wild-type (wt) *So* and the H80G variant was performed as described previously.<sup>13, 19</sup> For semi-reduced samples, *So* samples were incubated on ice for 1.5 hr in the presence of 2 mM sodium ascorbate and 1 mM diaminodural. For oxidized samples, *So* was incubated with 1 mM hexachloroiridate on ice for 1.5 hr. The semi-reduced and oxidized states of *So* and H80G were verified by collecting their absorption spectra on a Cary50 UV-Vis spectrophotometer (Agilent). Final samples were exchanged into 100 mM TIP7 buffer with 30% glycerol before storing at -80°C until use.

### Protein Expression and Purification of wt *Ne* and H59G

The *Ne* gene was removed from the pMAL-Tev-NeCCP vector as previously described<sup>19</sup> by PCR with overhang ends that anneal outside the N-terminal Strep tag and C-terminal 6x-His tag of the pETSN vector.<sup>12</sup> PCR was carried out using Platinum High-Fidelity Super mix (Invitrogen) with the following primers: 5'-TTCGCTACCGTAGCGCAGGCCGGTAGTGGCAATGAACCGATAACAACCG (forward) and 5'-GGGCTTTGTTAGCAGCCGGATCTTACTCATACGGCTGAGAACGTGGTGTATC (reverse). The amplified PCR product was gel purified and used as the megaprimer in a QuikChange reaction with the pETSN vector as template (QuikChange Lightning II kit, Agilent). Insertion of the *Ne* gene was verified by sequencing (GeneWiz). *Ne-pETSN2* was co-transformed with a plasmid containing the Cytochrome *c* maturation cassette<sup>40</sup> into BL21(DE3) competent cells. Starter cultures of 5 mL were grown overnight at 37°C in 2x YT, supplemented with 100 µg/mL ampicillin and 35 µg/mL chloramphenicol. The culture was harvested and resuspended in

fresh media before inoculating it in a 1L flask of 2x YT for bulk expression at 37°C with 220 rpm until OD<sub>600</sub>=0.8 was reached. Cells were cooled and induced with 400 μM β-d-thiogalactopyranoside (IPTG, Bio-rad) for 17 hrs at room temperature with shaking at 150 rpm. Cell pellets were harvested by centrifugation, resuspended in 20 mM Tris, 1 mM PMSF, pH 8.2, and lysed by sonication. The lysate was clarified by centrifugation and the supernatant was loaded onto a Q-Sepharose anion exchange resin (GE) equilibrated with lysis buffer. The bound protein was washed extensively with 20 mM Tris, 20 mM NaCl, pH 8.2 before elution at 40 mM NaCl. Pooled fractions were concentrated in Amicon 30K MWCO and loaded onto an S-200 size exclusion column (GE) equilibrated in 50 mM HEPES, 100 mM NaCl, pH 7.8. Pure fractions were concentrated and exchanged into TIP7 buffer. The histidine residue at position 59 in *Ne* was mutated to a glycine using the QuikChange Lightning Mutagenesis Kit with the following primers: 5'-CGATAATATTACCACCTCGATCGGGGGCAAATGGCAGCAAGGCCCGATCAATGC (forward) and 5'-GACTTGATCGGGCCTTGCTGCCATTTGCCCCCGATCGAGGTGGTAATATTATCG (reverse). For semi-reduced samples, *Ne* protein samples were incubated on ice for 1.5 hr in the presence of 2 mM sodium ascorbate (Sigma) and 1 mM diamminodural. For oxidized samples, *Ne* was incubated with 1 mM hexachloroiridate on ice for 3 hr. The semi-reduced and oxidized states of *Ne* and H59G were verified by collecting their absorption spectra on a Cary50 UV-Vis spectrophotometer (Agilent). Final samples were exchanged into 100 mM TIP7 buffer with 30% glycerol before storing at -80°C until use.

### **EPR Spectroscopy**

Electron paramagnetic resonance spectra were measured on a Bruker X-Band EMX spectrometer equipped with an Oxford Instruments 3 S3 liquid helium cryostat. EPR spectra were

obtained on frozen solutions using 20 mW microwave power and 100 kHz field modulation with the amplitude set to 1 G. All samples were measured at 12 K.

### **Resonance Raman Spectroscopy**

Raman spectra were recorded in 3 mm diameter EPR tubes. Typical sample concentrations range from 0.1 to 0.16 mM. A SpectraPhysics BeamLok 2060-RS Krypton ion gas laser was used for excitation of the samples at 413.1 nm. The scattered light from the samples was focused onto an Acton two-stage TriVista 555 monochromator and detected by a liquid N<sub>2</sub>-cooled Princeton Instruments Spec-10:400B/LN CCD camera. Data were collected at liquid nitrogen temperature using an EPR cold finger to cool the samples, and at room temperature using an NMR spinner powered with compressed air. Typical laser powers were in the 15-30 mW range, and a spectral resolution of 0.3 cm<sup>-1</sup> was used.

### **Magnetic Circular Dichroism Spectroscopy**

Protein samples were prepared in 50 mM TIP7 buffer with 50-60% glycerol (a glassing agent) added to each sample. Typical sample concentrations range from 5 μM to 20 μM, depending on the spectral region of interest. Samples were placed between two quartz plate windows in an MCD sample holder. The samples were frozen in liquid nitrogen until a transparent glass formed. The MCD setup is comprised of an OXFORD SM4000 cryostat and a JASCO J-815 CD spectrometer. The SM4000 cryostat consists of a liquid helium-cooled superconducting magnet providing horizontal magnetic fields of 0-7 T. The J-815 spectrometer uses a gaseous nitrogen-cooled xenon lamp and a detector system with two interchangeable photomultiplier tubes in the UV-vis and NIR range. The samples were loaded into a 1.5-300 K variable temperature insert (VTI) which allows optical access to the sample via four optical windows made from Suprasil B quartz. The MCD spectra were measured in  $[\theta] = \text{mdeg}$  and manually converted to  $\Delta\epsilon$  (M<sup>-1</sup>cm<sup>-1</sup>T<sup>-1</sup>).

<sup>1)</sup> using the conversion factor  $\Delta\epsilon = \theta/(32980 \cdot cdB)$  where  $c$  is the concentration,  $B$  is the magnetic field, and  $d$  is the path length. The product  $cd$  can be substituted by  $A_{MCD}/\epsilon_{UV-vis}$ , where  $A$  is the absorbance of the sample measured by the CD spectrometer.<sup>23</sup> Complete spectra were recorded at different temperatures (2, 5, and 10 K) and magnetic fields (0, 1, 3, 5, and 7 T). For the photolysis experiments, a mercury lamp was used as a light source to illuminate the samples for 15 min before re-measuring the samples.

#### 4.12 References

- 1) Chandel, N. S.; McClintock, D. S.; Feliciano, C. E.; Wood, T. M.; Melendez, J. A.; Rodriguez, A. M.; Schumacker, P. T. Reactive oxygen species generated at mitochondrial complex III stabilize hypoxia-inducible factor-1 $\alpha$  during hypoxia: a mechanism of O<sub>2</sub> sensing. *J. Biol. Chem.* **2000**, 275 (33), 25130-8.
- 2) Pettigrew, G. W.; Echali er, A.; Pauleta, S. R. Structure and mechanism in the bacterial dihaem cytochrome c peroxidases. *J. Inorg. Biochem.* **2006**, 100 (4), 551-67.
- 3) Arciero, D. M.; Hooper, A. B. A di-heme cytochrome c peroxidase from *Nitrosomonas europaea* catalytically active in both the oxidized and half-reduced states. *J. Biol. Chem.* **1994**, 269 (16), 11878-86.
- 4) Ellfolk, N.; Ronnberg, M.; Aasa, R.; Andreasson, L. E.; Vanngard, T. Properties and function of the two hemes in *Pseudomonas* cytochrome c peroxidase. *Biochim. Biophys. Acta* **1983**, 743 (1), 23-30.
- 5) Pettigrew, G. W.; Prazeres, S.; Costa, C.; Palma, N.; Krippahl, L.; Moura, I.; Moura, J. J. The structure of an electron transfer complex containing a cytochrome c and a peroxidase. *J. Biol. Chem.* **1999**, 274 (16), 11383-9.
- 6) Pettigrew, G. W.; Pauleta, S. R.; Goodhew, C. F.; Cooper, A.; Nutley, M.; Jumel, K.; Harding, S. E.; Costa, C.; Krippahl, L.; Moura, I.; Moura, J. Electron transfer complexes of cytochrome c peroxidase from *Paracoccus denitrificans* containing more than one cytochrome. *Biochemistry* **2003**, 42 (41), 11968-81.
- 7) Ronnberg, M.; Ellfolk, N. *Pseudomonas* cytochrome c peroxidase. Initial delay of the peroxidatic reaction. Electron transfer properties. *Biochim. Biophys. Acta* **1978**, 504 (1), 60-6.
- 8) Echali er, A.; Goodhew, C. F.; Pettigrew, G. W.; Fulop, V. Activation and catalysis of the di-heme cytochrome c peroxidase from *Paracoccus pantotrophus*. *Structure* **2006**, 14 (1), 107-17.

- 9) Alves, T.; Besson, S.; Duarte, L. C.; Pettigrew, G. W.; Girio, F. M.; Devreese, B.; Vandenberghe, I.; Van Beeumen, J.; Fauque, G.; Moura, I. A cytochrome c peroxidase from *Pseudomonas nautica* 617 active at high ionic strength: expression, purification and characterization. *Biochim. Biophys. Acta* **1999**, *1434* (2), 248-59.
- 10) De Smet, L.; Pettigrew, G. W.; Van Beeumen, J. J. Cloning, overproduction and characterization of cytochrome c peroxidase from the purple phototrophic bacterium *Rhodobacter capsulatus*. *Eur. J. Biochem.* **2001**, *268* (24), 6559-68.
- 11) Timoteo, C. G.; Tavares, P.; Goodhew, C. F.; Duarte, L. C.; Jumel, K.; Girio, F. M.; Harding, S.; Pettigrew, G. W.; Moura, I., Ca<sup>2+</sup> and the bacterial peroxidases: the cytochrome c peroxidase from *Pseudomonas stutzeri*. *J. Biol. Inorg. Chem.* **2003**, *8* (1-2), 29-37.
- 12) Hoffmann, M.; Seidel, J.; Einsle, O. CcpA from *Geobacter sulfurreducens* is a basic di-heme cytochrome c peroxidase. *J. Mol. Biol.* **2009**, *393* (4), 951-65.
- 13) Pulcu, G. S.; Frato, K. E.; Gupta, R.; Hsu, H. R.; Levine, G. A.; Hendrich, M. P.; Elliott, S. J. The di-heme cytochrome c peroxidase from *Shewanella oneidensis* requires reductive activation. *Biochemistry* **2012**, *51* (5), 974-85.
- 14) Echalié, A.; Brittain, T.; Wright, J.; Boycheva, S.; Mortuza, G. B.; Fulop, V.; Watmough, N. J. Redox-linked structural changes associated with the formation of a catalytically competent form of the di-heme cytochrome c peroxidase from *Pseudomonas aeruginosa*. *Biochemistry* **2008**, *47* (7), 1947-56.
- 15) Foote, N.; Peterson, J.; Gadsby, P. M.; Greenwood, C.; Thomson, A. J. Redox-linked spin-state changes in the di-haem cytochrome c-551 peroxidase from *Pseudomonas aeruginosa*. *Biochem. J.* **1985**, *230* (1), 227-37.
- 16) Foote, N.; Peterson, J.; Gadsby, P. M.; Greenwood, C.; Thomson, A. J. A study of the oxidized form of *Pseudomonas aeruginosa* cytochrome c-551 peroxidase with the use of magnetic circular dichroism. *Biochem. J.* **1984**, *223* (2), 369-78.
- 17) Zahn, J. A.; Arciero, D. M.; Hooper, A. B.; Coats, J. R.; DiSpirito, A. A. Cytochrome c peroxidase from *Methylococcus capsulatus* Bath. *Arch. Microbiol.* **1997**, *168* (5), 362-72.
- 18) Shimizu, H.; Schuller, D. J.; Lanzilotta, W. N.; Sundaramoorthy, M.; Arciero, D. M.; Hooper, A. B.; Poulos, T. L. Crystal structure of *Nitrosomonas europaea* cytochrome c peroxidase and the structural basis for ligand switching in bacterial Di-heme peroxidases. *Biochemistry* **2001**, *40* (45), 13483-13490.
- 19) Frato, K. E.; Walsh, K. A.; Elliott, S. J. Functionally Distinct Bacterial Cytochrome c Peroxidases Proceed through a Common (Electro)catalytic Intermediate. *Biochemistry* **2016**, *55* (1), 125-32.
- 20) Bradley, A. L.; Chobot, S. E.; Arciero, D. M.; Hooper, A. B.; Elliott, S. J. A distinctive electrocatalytic response from the cytochrome c peroxidase of *Nitrosomonas europaea*. *J. Biol. Chem.* **2004**, *279* (14), 13297-13300.

- 21) Galinato, M. G. I.; Spolidak, T.; Ballou, D. P.; Lehnert, N. Elucidating the Role of the Proximal Cysteine Hydrogen-Bonding Network in Ferric Cytochrome P450cam and Corresponding Mutants Using Magnetic Circular Dichroism Spectroscopy. *Biochemistry* **2011**, *50* (6), 1053-1069.
- 22) Lehnert, N. Elucidating second coordination sphere effects in heme proteins using low-temperature magnetic circular dichroism spectroscopy. *Journal of Inorganic Biochemistry* **2012**, *110*, 83-93.
- 23) Paulat, F.; Lehnert, N. Detailed assignment of the magnetic circular dichroism and UV-vis spectra of five-coordinate high-spin ferric [Fe(TPP)(Cl)]. *Inorg. Chem.* **2008**, *47* (11), 4963-4976.
- 24) Vickery, L.; Nozawa, T.; Sauer, K. Magnetic circular dichroism studies of low-spin cytochromes. Temperature dependence and effects of axial coordination on the spectra of cytochrome c and cytochrome b5. *J. Am. Chem. Soc.* **1976**, *98* (2), 351-7.
- 25) Vickery, L.; Nozawa, T.; Sauer, K. Magnetic circular dichroism studies of myoglobin complexes. Correlations with heme spin state and axial ligation. *J. Am. Chem. Soc.* **1976**, *98* (2), 343-50.
- 26) Gouterman, M.; Snyder, L. C.; Wagniere, G. H. Spectra of Porphyrins 2. 4 Orbital Model. *J. Mol. Spectroscopy* **1963**, *11* (2), 108-&.
- 27) T. G. Spiro, R. S. C. Resonance Raman Spectroscopy. In *Physical Methods in Bioinorganic Chemistry: Spectroscopy and Magnetism*, Que, L., Ed. University Science Books: Sausalito, CA, 2010; pp 59-119.
- 28) Streckas, T. C.; Spiro, T. G. Resonance-raman evidence for anomalous heme structures in cytochrome c' from *Rhodospseudomonas palustris*. *Biochim. Biophys. Acta* **1974**, *351* (2), 237-45.
- 29) Hu, S. S., K. M.; Spiro, T. G. Assignment of protoheme resonance Raman spectrum by heme labeling in Myoglobin. *J. Am. Chem. Soc.* **1996**, *118*, 12638-12646.
- 30) Paulat, F.; Praneeth, V. K.; Nather, C.; Lehnert, N. Quantum chemistry-based analysis of the vibrational spectra of five-coordinate metalloporphyrins [M(TPP)Cl]. *Inorg. Chem.* **2006**, *45* (7), 2835-56.
- 31) Hu, S. Z.; Morris, I. K.; Singh, J. P.; Smith, K. M.; Spiro, T. G. Complete Assignment of Cytochrome-C Resonance Raman-Spectra Via Enzymatic Reconstitution with Isotopically Labeled Hemes. *J. Am. Chem. Soc.* **1993**, *115* (26), 12446-12458.
- 32) Kitagawa, T.; Kyogoku, Y.; Iizuka, T.; Saito, M. I. Nature of the iron-ligand bond in ferrous low spin hemoproteins studied by resonance Raman scattering. *J. Am. Chem. Soc.* **1976**, *98* (17), 5169-73.



- 33) Abe, M.; Kitagawa, T.; Kyogoku, Y. Resonance Raman-Spectra of Octaethylporphyrinato-Ni(II) and Meso-Deuterated and N-15 Substituted Derivatives .2. Normal Coordinate Analysis. *J. Chem. Phys.* **1978**, *69* (10), 4526-4534.
- 34) Spiro, T. G.; Streckas, T. C. Resonance Raman-Spectra of Heme Proteins - Effects of Oxidation and Spin State. *J. Am. Chem. Soc.* **1974**, *96* (2), 338-345.
- 35) Kitagawa, T.; Ozaki, Y.; Teraoka, J.; Kyogoku, Y.; Yamanaka, T. Ph-Dependence of Resonance Raman-Spectra and Structural Alterations at Heme Moieties of Various C-Type Cytochromes. *Biochim. Biophys. Acta* **1977**, *494* (1), 100-114.
- 36) Ruetz, M.; Kumutima, J.; Lewis, B. E.; Filipovic, M. R.; Lehnert, N.; Stemmler, T. L.; Banerjee, R. A distal ligand mutes the interaction of hydrogen sulfide with human neuroglobin. *J. Biol. Chem.* **2017**, *292* (16), 6512-6528.
- 37) Uno, T.; Nishimura, Y.; Tsuboi, M. Time-Resolved Resonance Raman-Study of Alkaline Isomerization of Ferricytochrome-C. *Biochemistry* **1984**, *23* (26), 6802-6808.
- 38) Bostelaar, T.; Vitvitsky, V.; Kumutirna, J.; Lewis, B. E.; Yadav, P. K.; Brunold, T. C.; Filipovic, M.; Lehnert, N.; Stemmler, T. L.; Banerjee, R. Hydrogen Sulfide Oxidation by Myoglobin. *J. Am. Chem. Soc.* **2016**, *138* (27), 8476-8488.
- 39) Taylor, C. P. S. Epr of Low-Spin Heme Complexes - Relation of T<sub>2g</sub> Hole Model to Directional Properties of G-Tensor, and a New Method for Calculating Ligand-Field Parameters. *Biochim. Biophys. Acta* **1977**, *491* (1), 137-149.
- 40) Arslan, E.; Schulz, H.; Zufferey, R.; Kunzler, P.; Thony-Meyer, L. Overproduction of the Bradyrhizobium japonicum c-type cytochrome subunits of the cbb(3) oxidase in Escherichia coli. *Biochem. Bioph. Res. Co.* **1998**, *251* (3), 744-747.

## Chapter 5

### Conclusions and Future Work

#### 5.1 Conclusions

Development of reactions that generate diverse organic products in industry necessitates the production of a wide variety of homogeneous and heterogeneous catalysts. Using less expensive and environmentally detrimental solvents and other reagents are important goals in developing sustainable catalytic systems in the chemical industry. Artificial enzymes are functional in water and have proven useful as stereoselective catalysts for a variety of organometallic reactions.<sup>1-4</sup> Heme proteins in particular are amenable to cofactor replacement and site directed mutagenesis.<sup>5-8</sup> Cytochrome P450<sub>BM3</sub>,<sup>8-9</sup> cytochrome *c*,<sup>10</sup> and myoglobin<sup>11-14</sup> have all been modified and used to catalyze carbene and nitrene transfer reactions to a variety of substrates including olefins, amines, and thiols, among others. Different transition metal porphyrins have long been investigated for these types of reactions,<sup>15-18</sup> and some work has recently examined the activity of different metals in myoglobin and cytochrome P450 for carbene transfer reactions.<sup>6-7</sup> Ruthenium porphyrins in organic solvents tend to be more active and less dioxygen sensitive catalysts compared to iron porphyrins and we hypothesized that higher activity towards carbene transfer reactions could be achieved by a ruthenium porphyrin reconstituted into myoglobin compared to native myoglobin.<sup>15, 19</sup> To investigate this hypothesis, the reactivity of ruthenium myoglobin (RuMb) and native myoglobin (FeMb) towards the N-H insertion of aniline and the cyclopropanation of styrene were studied in terms of catalytic yield, reaction rate, and catalyst

lifetime. Several His64 mutants were studied for both metals, modest substrate scope studies were conducted for both aniline and styrene derivatives, and catalytic decomposition was also investigated with the aim of better understanding the differences in catalytic activity between RuMb and FeMb.

Chapter 2 focuses on the comparison of carbene transfer activity between RuMb and FeMb and the investigation into catalyst decomposition. Several His64 mutants of Mb exhibit a less sterically-hindered active site and either increased hydrophobicity (H64A and H64V) or hydrophilicity (H64D) of the protein pocket; these mutants were reconstituted with RuMpIX(X) as well. Both RuMb and FeMb were moderately active for N-H insertion, catalyzing the reaction in 36% and 35% yield, respectively. At pH 7, all the catalysts studied achieve 30-60% yield, though 15% yield was also observed without any catalyst present. In contrast, catalytic activity towards the cyclopropanation of styrene is quite different between FeMb and RuMb. FeMb catalyzes the cyclopropanation of styrene in 25-30% yield and produces 92% of the *trans* cyclopropane isomer. RuMb is a poor catalyst for the cyclopropanation of styrene and only achieves 3% yield and produces 80% of the *trans* isomer. Other RuMb His64 variants also exhibit low yields for the cyclopropanation reaction, with the most effective catalyst (RuH64VMb) achieving up to 8% yield at pH = 3. Several different styrene derivatives were used as substrates in the cyclopropanation reaction and only 4-methoxystyrene demonstrates higher TON with RuH64AMb catalyzing up to 36% yield for the cyclopropanation of this substrate. This was due to the higher solubility of 4-methoxystyrene in water compared to styrene and other styrene derivatives.

In order to better understand the low cyclopropanation activity demonstrated by the RuMb variants, catalyst decomposition was investigated. UV-vis kinetics studies showed that the addition of ethyl diazoacetate (EDA) to Ru<sup>II</sup>Mb results in a rapid decrease in Soret band intensity over the

course of one hour. This indicates that the ruthenium-carbene ( $\text{Ru}=\text{CR}_2$ ) unit quickly inserts into the porphyrin ligand at the beginning of the reaction. Over the same period of time, a slight decrease in Soret band intensity was observed for  $\text{Fe}^{\text{II}}\text{Mb}$ , but insertion into the porphyrin occurs at a much slower rate. In addition, mass spectra of the  $\text{RuMb}$  cyclopropanation mixture after three hours indicate that the  $\text{Ru}=\text{CR}_2$  unit inserts into the protein backbone and that no significant amount of unmodified protein remains. In contrast, the mass spectra of  $\text{FeMb}$  three hours into the reaction show that while a significant percentage of the protein has been modified by one carbene unit, much of the protein scaffold remains unmodified. Therefore, the  $\text{Ru}=\text{CR}_2$  unit is quite reactive, but it inserts into both the porphyrin ligand and the protein backbone leading to catalyst decomposition before an appreciable amount of styrene can intercept the carbene and form cyclopropane. The  $\text{Fe}=\text{CR}_2$  unit is less vulnerable to decomposition, and achieves a higher yield for the cyclopropanation of styrene. Similar yields were observed for the N-H insertion of aniline due to the higher solubility of aniline in water compared to styrene, and therefore greater availability of this substrate to rapidly reaction with the metallocarbene unit.

In Chapter 3, catalyst lifetimes for the cyclopropanation of styrene and the N-H insertion of aniline are investigated for several  $\text{Fe}^{\text{II}}$  and  $\text{Ru}^{\text{II}}$  catalysts. For the cyclopropanation of styrene, all catalysts exhibit a much shorter lifetime compared to the typical 12-18 hour runtime for carbene insertion reactions.<sup>8, 12</sup>  $\text{Fe}^{\text{II}}\text{PpIX}$  exhibits a catalytic lifetime of two hours, and  $\text{Fe}^{\text{II}}\text{Mb}$ ,  $\text{Fe}^{\text{II}}\text{H64AMb}$ , and  $\text{Ru}^{\text{II}}\text{MpIX(X)}$  cease catalysis after 30 minutes.  $\text{Ru}^{\text{II}}\text{Mb}$  and  $\text{Ru}^{\text{II}}\text{H64AMb}$  are only active for mere minutes, and exhibit very low activity. These data align with the results from Chapter 2 demonstrating the rapid decomposition of  $\text{Ru}^{\text{II}}\text{Mb}$  in the presence of excess EDA. For all  $\text{Ru}^{\text{II}}$  catalysts studied, catalytic lifetimes for the N-H insertion of aniline are also short; catalysis ends in 30 minutes or less. Despite experimental error in some data collected for the N-H insertion

of aniline, Fe<sup>II</sup> catalysts generally exhibit short catalytic lifetimes as well, 30-120 minutes. For both reactions and all the catalysts studied, reactions take place on a relatively short timescale, with the Ru<sup>II</sup> catalysts decomposing faster and thus exhibiting shorter lifetimes.

Since RuMb exhibits a short catalytic lifetime due to rapid catalyst decomposition from insertion of the Ru=CR<sub>2</sub> unit into both the porphyrin and protein backbone, it was hypothesized that the application of more electron donating axial ligands (such as phosphines) could lower the electrophilicity of the Ru=CR<sub>2</sub> unit and make the carbene less reactive towards undesired decomposition reactions. To this end, the H93G mutant of Mb was prepared, RuMpIX was reconstituted into H93G Mb, and exogenous ligands were added to the protein. UV-vis studies clearly demonstrate that a variety of ligands including imidazole, phenol, tris(hydroxymethyl)phosphine, and several thiols bind to the Fe<sup>III</sup> center in H93G Mb, as previously reported.<sup>20</sup> However, no change in the UV-vis spectrum results from adding the same ligands to Ru<sup>III</sup>H93GMb. This is also the case when adding the ligands to Ru<sup>II</sup>H93GMb and Ru<sup>II</sup>H93GMb(CO). Addition of the ligands to the reaction mixture with Ru<sup>II</sup>H93GMb, styrene, and EDA did not improve catalytic yield; yields for the cyclopropanation of styrene remained between 0-3%. It is unclear if in these cases the ligands are actually bound to the Ru center, but if binding did occur it made little impact on activity, and decomposition likely remained swift. Addition of imidazole and phenol to Fe<sup>II</sup>H93GMb did not alter the yield for cyclopropanation, it remained close to 30%. The phosphine and thiol ligands added to Fe<sup>II</sup>H93GMb did lead to lower yields for the cyclopropanation of styrene, 15% and 11% yield, respectively. Though it is currently unclear why these lower yields result from the addition of phosphine or thiol ligands, we hypothesize that more electron-donating ligands push electron density into the metallocarbene unit

and make the carbene less electrophilic and less reactive with styrene. The studies on FeH93GMb seem to support this general concept.

The results in Chapters 2 and 3 demonstrate that different metal centers inserted into Mb result in varying catalytic activity and lifetimes. Despite the moderate activity achieved for the N-H insertion of aniline by both Ru and Fe centers in Mb, RuMb is a very poor catalyst for the cyclopropanation of styrene. Investigation into the catalytic lifetime of RuMb for carbene transfer reactions shows that the Ru=CR<sub>2</sub> unit is actually more reactive than Fe=CR<sub>2</sub>, but the carbene reacts with both the porphyrin ligand and the protein scaffold, leading to rapid catalyst decomposition. As further evidence of catalytic decomposition, the lifetimes of RuMb and RuH64AMb are also very short after the addition of EDA – activity largely ceases after a few minutes. Addition of exogenous ligands to RuH93GMb did not lead to improved yields for the cyclopropanation of styrene, though it is unclear if these ligands are actually bound to the Ru center in Mb. It is evident that the activity of RuMpIX inside Mb needs to be tuned in order to prevent or reduce undesired decomposition products that deplete catalytic function (see Section 5.2).

In Chapter 4, the mechanisms of constitutively active and reductively activated diheme bacterial cytochrome *c* peroxidases (CcPs) were investigated in collaboration with Dr. Sean Elliott at Boston University, using several spectroscopic methods. In the constitutively active peroxidase *Ne*CcP, the high potential heme (H-heme) and the catalytically-active low potential heme (L-heme) are both low-spin ferric in the diferric state of the enzyme. EPR and MCD spectra do not provide any evidence of a high-spin ferric heme despite previous isolation of a five-coordinate L-heme in the crystal structure of diferric *Ne*CcP.<sup>21</sup> Resonance Raman data show that there may be a small percentage of high-spin ferric heme present in the sample, but the absence of a band near 1480 cm<sup>-1</sup> seems to indicate that this is a minority species. The reductively-activated peroxidase

*SoCcP* exhibits low-spin heme signals for the diferric form of the enzyme by EPR and MCD spectra. *NeH59G CcP* and *SoH80G CcP* mutants were prepared by the Elliott group to remove the coordinating distal histidine for the L-heme to force the L-heme to be five-coordinate. Surprisingly, the diferric mutants exhibited similar low-spin ferric MCD and rRaman spectra, and only small percentages of high-spin ferric heme were observed in the EPR spectra. Thus, the L-hemes in *NeCcP* and *SoCcP* are not statically five-coordinate and the constitutively-active *NeCcP* likely exists in a more dynamic and conformationally-flexible state prior to peroxide binding.

Semi-reduced CcPs were also prepared by reducing the H-heme to the ferrous state. Signals for both high-spin and low-spin ferrous hemes could be detected by MCD and rRaman spectroscopy, suggesting that the H-heme exists in a mixed high-spin/low-spin state after reduction. MCD studies also show that the reduced high-spin ferrous signals result at least in part from photolysis of the Fe-S<sub>Met</sub> bond during the experiment. The L-heme in both *NeCcP* and *SoCcP* largely remain in the low-spin ferric state as evidenced by EPR and rRaman studies, even though *SoCcP* becomes catalytically active after reduction of the H-heme. Both the *NeH59G CcP* and *SoH80G CcP* mutants also exhibit a mostly low-spin L-heme, indicating that the L-heme must recruit a water molecule or a different ligand to coordinate at the distal side of the heme. As with *NeCcP*, the L-heme in *SoCcP* must exist in a dynamic state that could potentially oscillate between a five- and six-coordinate environments at room temperature, despite existing mainly as a six-coordinate site at low-temperature. This mechanism is different from the canonical ligand dissociation followed by peroxide binding and provides a new perspective with which to view different classes of bacterial CcPs.

## 5.2 Future Work

RuMb is a short-lived carbene transfer catalyst that only exhibits low product yields for the cyclopropanation of styrene. The low yield results from rapid catalyst decomposition, as the Ru=CR<sub>2</sub> unit is quite reactive towards both the porphyrin and protein scaffold. In order to overcome the facile decomposition of RuMb, we must further characterize the decomposition products after carbene insertion first. Arnold and coworkers determined that the Fe=CR<sub>2</sub> unit in a modified Cyt. P450 facilitates *N*-alkylation of the porphyrin and loss of Fe<sup>2+</sup> over time.<sup>22</sup> UV-vis data in Chapter 2 indicate that the Ru porphyrin is also modified after the addition of EDA as the Soret band decreases rapidly over a period of one hour. The decrease in the Ru<sup>II</sup>MpIX Soret band suggests that the aromaticity of the porphyrin is disrupted after the formation of Ru=CR<sub>2</sub>, which would not result from porphyrin *N*-alkylation. The carbene could be inserting into the *meso* position of the heme, and undergo further reactivity to alter the carbon backbone of the porphyrin and disrupt aromaticity (**Figure 5.1b**). Further mass spectrometry studies with free [RuMpIX(X)] should be undertaken to characterize the decomposition products and begin to develop a mechanism for heme porphyrin modification. In particular, fewer equivalents of EDA should be added to Ru<sup>II</sup>MpIX and the reaction should quickly be quenched prior to mass spectrometry analysis. Products may need to be separated by HPLC or column chromatography before determining the various species present by mass spectrometry. <sup>1</sup>H and <sup>13</sup>C NMR data could also be collected to aid in the identification of porphyrin decomposition products and to better understand the mechanism of decomposition.



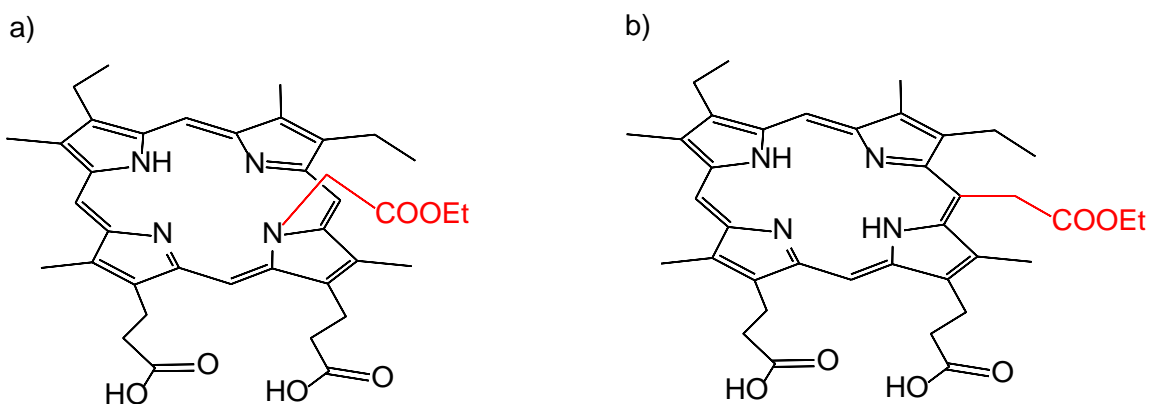


**Figure 5.1.** a) The product of *N*-alkylation of mesoporphyrin IX by  $\text{Ru}^{\text{II}}=\text{CHCOOEt}$  and loss of  $\text{Ru}^{\text{II}}$ , and b) the product of C-H insertion into the *meso* carbon of mesoporphyrin IX.

In addition to porphyrin modification, mass spectrometry results also indicate that the  $\text{Ru}=\text{CR}_2$  unit inserts into the protein scaffold (see Chapter 2). The distal His64 residue is a prime candidate for carbene insertion, but higher mass peaks also indicate that the carbene inserts into other residues. Crystallography of RuMb could help to determine if there were any significant differences in the interaction between RuMpIX and the nearby residues compared to native FePpIX that might lead to increased alkylation. To identify the residues alkylated by  $\text{Ru}=\text{CR}_2$ , a trypsin digestion of the protein after the addition of EDA followed by mass spectrometry analysis could point to the modification of specific peptides. Arnold and coworkers have previously taken this approach to identify residues modified in their Cyt. P450 catalyst.<sup>22</sup> Cysteine, serine, histidine, and lysine residues were all modified, even though these residues were 9-20 Å away from the metal center. Amino acid alkylation may also occur further away from the heme pocket in Mb. Once the alkylated residues are identified, Mb mutants could be prepared to substitute nucleophilic residues with nonpolar aliphatic amino acids. In this way, the reactivity of the metallocarbene towards the protein scaffold could be reduced and catalytic lifetime may be improved. On the other hand, porphyrin modification and degradation would still be significant, and without further

modifications to the metal cofactor, reactants, or reaction conditions, it is likely that the catalytic lifetime of RuMb would not improve significantly.

In order to improve the stability of RuMpIX, further investigations into H93G Mb should be conducted. IR spectroscopy of higher concentration Ru<sup>II</sup>H93GMb(CO) may indicate ligand binding to the metal center through shifts in the CO stretch, though ligand binding would likely occur in the distal pocket of the heme as CO likely binds on the proximal side. In addition, <sup>31</sup>P-NMR should be useful for indicating if tris(hydroxymethyl)phosphine binds to the metal center, and X-ray absorption spectroscopy could also be used to help determine ligand binding. The six different ligands added to RuH93GMb in this study did not lead to improved yields for the cyclopropanation of styrene, including the  $\sigma$ -donating phosphine. In organic solvents, strong  $\sigma$ -donating N-heterocyclic carbene ligands (NHCs) have proven effective for improving carbene transfer activity after binding to ruthenium porphyrins.<sup>23</sup> Preparing an NHC-bound ruthenium porphyrin prior to reconstitution into H93G Mb should lead to facile characterization inside the protein scaffold and could improve catalytic yields for the cyclopropanation of styrene. If yields for the cyclopropanation of styrene remain low for all ligands bound to the ruthenium porphyrin, other olefin substrates should be used to better understand the influence of different proximal ligands. The styrene derivative 4-methoxystyrene is more water soluble than styrene and exhibited higher TON with RuH64AMb as the catalyst as described in Chapter 2. The relatively high activity and solubility of 4-methoxystyrene may allow for greater insight into the differences in catalytic activity that result from different proximal ligand coordination, even if catalytic lifetimes remain low.

The stability of Ru=CR<sub>2</sub> could also be investigated using different carbene precursors. EDA is a common, commercially available carbene precursor that contains an acceptor group (-

COOEt). Acceptor groups “pull” electron density away from the carbene carbon and make the carbene more electrophilic and reactive towards nucleophiles. In the case of RuMb, the Ru=CR<sub>2</sub> unit is highly reactive towards a variety of different nucleophiles including protein residues and the porphyrin. Therefore, the introduction of donating groups to “push” electron density towards the carbene carbon could result in a less reactive metallocarbene unit and improve catalyst lifetime. Several carbene precursors with donor groups bound to the carbene carbon are shown in **Figure 5.2**. The carbene precursors with phenyl moieties may be less water soluble and require some synthetic modifications (such as sulfonation) prior to use. It is also likely that the Mb mutants with larger active sites such as H64A and H64V may be required for the formation of larger metallocarbene units such as Ru=CHPh. Of course, if the donor groups result in lower activity of the Ru=CR<sub>2</sub> unit, the metallocarbene may also be less reactive towards styrene or other desired substrates. The ideal carbene precursor would be less reactive towards carbene insertion into the protein and porphyrin but reactive enough to insert into styrene upon substrate approach towards the active site. More broadly, future work will also examine different metal cofactors such as corroles, different heme proteins as scaffolds such as P450s, Cyt. b<sub>5</sub>, and YFeX, and other reactions such as carbene insertion into less-activated C-H bonds with the goal of developing an array of artificial enzymes for different organometallic reactions.

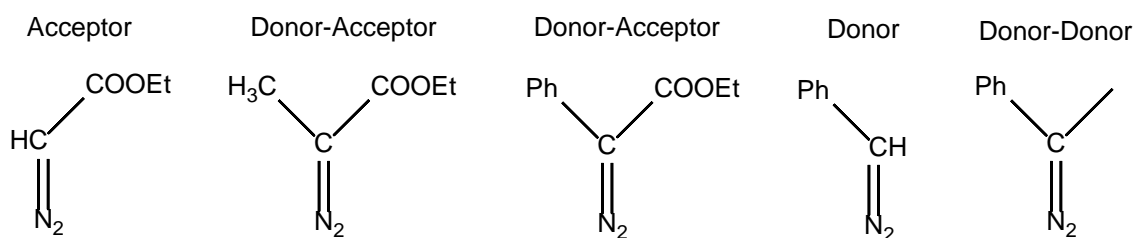


**Figure 5.2.** Several different carbene precursors with acceptor and/or donor groups that could be added to RuMb.

### 5.3 References

- 1) Hammer, S. C.; Knight, A. M.; Arnold, F. H. Design and evolution of enzymes for non-natural chemistry. *Curr. Opin. Green Sust.* **2017**, *7*, 23-30.
- 2) Rebelein, J. G. W., T. R. *In vivo* catalyzed new-to-nature reactions. *Curr. Opin. Biotech.* **2018**, *53*, 106-114.
- 3) Heinisch, T.; Ward, T. R. Artificial Metalloenzymes Based on the Biotin-Streptavidin Technology: Challenges and Opportunities. *Accounts Chem. Res.* **2016**, *49* (9), 1711-1721.
- 4) Steinreiber, J.; Ward, T. R. Artificial metalloenzymes as selective catalysts in aqueous media. *Coord. Chem. Rev.* **2008**, *252* (5-7), 751-766.
- 5) Sreenilayam, G.; Moore, E. J.; Steck, V.; Fasan, R. Metal Substitution Modulates the Reactivity and Extends the Reaction Scope of Myoglobin Carbene Transfer Catalysts. *Adv. Synth. Catal.* **2017**, *359* (12), 2076-2089.
- 6) Dydio, P.; Key, H. M.; Hayashi, H.; Clark, D. S.; Hartwig, J. F. Chemoselective, Enzymatic C-H Bond Amination Catalyzed by a Cytochrome P450 Containing an Ir(Me)-PIX Cofactor. *J. Am. Chem. Soc.* **2017**, *139* (5), 1750-1753.
- 7) Key, H. M.; Dydio, P.; Clark, D. S.; Hartwig, J. F. Abiological catalysis by artificial haem proteins containing noble metals in place of iron. *Nature* **2016**, *534* (7608), 534-537.
- 8) Coelho, P. S.; Brustad, E. M.; Kannan, A.; Arnold, F. H. Olefin Cyclopropanation via Carbene Transfer Catalyzed by Engineered Cytochrome P450 Enzymes. *Science* **2013**, *339* (6117), 307-310.
- 9) Coelho, P. S.; Wang, Z. J.; Ener, M. E.; Baril, S. A.; Kannan, A.; Arnold, F. H.; Brustad, E. M. A serine-substituted P450 catalyzes highly efficient carbene transfer to olefins in vivo (vol 9, pg 485, 2013). *Nat. Chem. Biol.* **2014**, *10* (2), 164-164.
- 10) Kan, S. B. J.; Lewis, R. D.; Chen, K.; Arnold, F. H. Directed evolution of cytochrome c for carbon-silicon bond formation: Bringing silicon to life. *Science* **2016**, *354* (6315), 1048-1051.
- 11) Tyagi, V.; Fasan, R. Myoglobin-Catalyzed Olefination of Aldehydes. *Angew. Chem. Int. Ed.* **2016**, *55* (7), 2512-2516.
- 12) Bordeaux, M.; Tyagi, V.; Fasan, R. Highly Diastereoselective and Enantioselective Olefin Cyclopropanation Using Engineered Myoglobin-Based Catalysts. *Angew. Chem. Int. Ed.* **2015**, *54* (6), 1744-1748.
- 13) Tyagi, V.; Bonn, R. B.; Fasan, R. Intermolecular carbene S-H insertion catalysed by engineered myoglobin-based catalysts. *Chem. Sci.* **2015**, *6* (4), 2488-2494.
- 14) Sreenilayam, G.; Fasan, R. Myoglobin-catalyzed intermolecular carbene N-H insertion with arylamine substrates. *Chem. Commun.* **2015**, *51* (8), 1532-1534.

- 15) Galardon, E.; LeMaux, P.; Simonneaux, G. Cyclopropanation of alkenes with ethyl diazoacetate catalysed by ruthenium porphyrin complexes. *Chem. Commun.* **1997**, (10), 927-928.
- 16) Wolf, J. R.; Hamaker, C. G.; Djukic, J. P.; Kodadek, T.; Woo, L. K. Shape and Stereoselective Cyclopropanation of Alkenes Catalyzed by Iron Porphyrins. *J. Am. Chem. Soc.* **1995**, *117* (36), 9194-9199.
- 17) Callot, H. J.; Piechocki, C. Cyclopropanation Using Rhodium(III)Porphyrins - Large Cis Vs Trans Selectivity. *Tetrahedron Lett.* **1980**, *21* (36), 3489-3492.
- 18) Anding, B. J.; Ellern, A.; Woo, L. K. Olefin Cyclopropanation Catalyzed by Iridium(III) Porphyrin Complexes. *Organometallics* **2012**, *31* (9), 3628-3635.
- 19) Che, C. M.; Huang, J. S. Ruthenium and osmium porphyrin carbene complexes: synthesis, structure, and connection to the metal-mediated cyclopropanation of alkenes. *Coord. Chem. Rev.* **2002**, *231* (1-2), 151-164.
- 20) Du, J.; Sono, M.; Dawson, J. H. The H93G myoglobin cavity mutant as a versatile scaffold for modeling heme iron coordination structures in protein active sites and their characterization with magnetic circular dichroism spectroscopy. *Coord. Chem. Rev.* **2011**, *255* (7-8), 700-716.
- 21) Shimizu, H.; Schuller, D. J.; Lanzilotta, W. N.; Sundaramoorthy, M.; Arciero, D. M.; Hooper, A. B.; Poulos, T. L. Crystal structure of Nitrosomonas europaea cytochrome c peroxidase and the structural basis for ligand switching in bacterial Di-heme peroxidases. *Biochemistry* **2001**, *40* (45), 13483-13490.
- 22) Renata, H.; Lewis, R. D.; Sweredoski, M. J.; Moradian, A.; Hess, S.; Wang, Z. J.; Arnold, F. H. Identification of Mechanism-Based Inactivation in P450-Catalyzed Cyclopropanation Facilitates Engineering of Improved Enzymes. *J. Am. Chem. Soc.* **2016**, *138* (38), 12527-12533.
- 23) Chan, K. H.; Guan, X. G.; Lo, V. K. Y.; Che, C. M. Elevated Catalytic Activity of Ruthenium(II)-Porphyrin-Catalyzed Carbene/Nitrene Transfer and Insertion Reactions with N-Heterocyclic Carbene Ligands. *Angew. Chem. Int. Ed.* **2014**, *53* (11), 2982-2987.